UNIVERSITY OF BIRMINGHAM

Note: Please sign this form and present it to the Bindery with your thesis, so that it can be bound at the front of the Library deposit copy

RESEARCH THESIS

Author's Declaration

Full name (block capitals, surname first): YANG REN

Full title of thesis/dissertation (block capitals): NUMERICAL INVESTIGATION ON HEAT TRANSFER PERFORMANCE ENHANCEMENT OF BINARY PCM SLURRY FLOW BOILING PROCESS IN MICROCHANNELS

College/School/Department (block capitals): COLLEGE OF ENGINEERING AND PHYSICAL SCIENCES / CHEMICAL ENGINEERING

Date of award of degree (leave blank):

1. I understand that one printed and one electronic copy of my thesis/dissertation (the Work) will be deposited in the University Library (the Library) and in a suitable electronic repository, for permanent retention.
2. Without changing the content, the Library or any third party with whom it has an agreement to do so, may convert either copy into a format or medium for the purpose of long-term retention, accessibility and preservation.
3. The Library will publish, and/or arrange with appropriate third parties for the non-exclusive publication of, a bibliographic description of the thesis/dissertation, and the author's abstract.
4. Unless arrangements are made to the contrary, (see paragraph 6. below), the Library is authorised to make the Work available for consultation in the Library, and via a recognised inter library loans system. The Library is authorised to make the electronic copy of the Work freely accessible to individuals and institutions - including automated agents - via the Internet.
5. Rights granted to the University of Birmingham through this agreement are entirely non-exclusive. I retain all my rights in the Work in its present version or future derivative works.
6. I understand that I may apply to the University to retain the right to withhold access to the content of my thesis/dissertation. Access to the paper version may be withheld for a period which shall not normally exceed four calendar years from the congregation at which the degree is conferred. The actual length of the period will be specified in the application, together with the precise reasons for making that application. The electronic copy may be withheld from dissemination via the web or other networks for any period.
7. I have obtained permission for any use made of substantial amounts of published or unpublished copyright material (text, illustrations, etc) where the rights are owned by a third party, other than as permitted under either The Copyright Designs and Patents Act 1988 (as modified by any related or successor legislation) or the Terms and Conditions of any Licence governing its use.
8. The content of the copies I shall deposit with the Library will be the final version of my thesis, as approved by the Examiners.
9. I understand that the Library and administrators of any electronic theses repository do not hold any obligation to take legal action on behalf of myself, or other rights holders, in the event of a breach of intellectual property rights, or any other right, in the material deposited.
10. I understand that, in the event of my thesis/dissertation being not approved by the Examiners, this declaration will become null and void.

Signature: Ren Yang **Date:** 27/10/2023

For Library use (please leave blank):

Classmark: **Accession number:** **Control number:**

eTheses Repository url:



UNIVERSITY OF BIRMINGHAM

NUMERICAL INVESTIGATION ON HEAT TRANSFER PERFORMANCE ENHANCEMENT OF BINARY PCM SLURRY FLOW BOILING PROCESS IN MICROCHANNELS

By

REN YANG

Thesis submitted to the University of Birmingham for the

Degree of Doctor of Philosophy

School of Chemical Engineering

The University of Birmingham

Edgbaston, Birmingham, UK

September – 2022

UNIVERSITY OF
BIRMINGHAM

University of Birmingham Research Archive

e-theses repository

This unpublished thesis/dissertation is copyright of the author and/or third parties. The intellectual property rights of the author or third parties in respect of this work are as defined by The Copyright Designs and Patents Act 1988 or as modified by any successor legislation.

Any use made of information contained in this thesis/dissertation must be in accordance with that legislation and must be properly acknowledged. Further distribution or reproduction in any format is prohibited without the permission of the copyright holder.

ABSTRACT

In this study, the escalating demand for efficient thermal management solutions in electronic devices and fuel cells, catering to their continuous operation under temperatures below 85℃, prompted the need for the effective heat dissipation. This necessity arises from the factors of work performance, reliability and material constraints in electronic component applications. Among various cooling methods, refrigerant flow boiling in microchannels holds promise due to its potential advantages over those conventional approaches. Nevertheless, it confronts challenges such as the elevated pressure drop, diminishing heat transfer efficiency along flow direction, and potential flow instability at high heat flux conditions. After comprehensive reviews and assessments, flow boiling of refrigerant-based functional fluids in microchannels is selected as the preferred thermal management approach.

The study utilizes numerical simulation method to enhance the comprehension of heat transfer between the melting phase change material (PCM) particles and boiling fluid. Subsequently, it delves into the multiphase flow heat transfer performance of pure and the zeotropic refrigerant fluids in microchannels. Moreover, it explores the influence of thermophysical properties of functional particles on the flow boiling heat transfer performance of refrigerant-based fluids under specific thermal operating conditions. These insights have implications for developing functional fluids for cooling electronic devices and fuel cells.

Accordingly, the heat transfer performance and the mutually influencing process are analyzed and evaluated qualitatively and quantitatively. The following findings are observed:

(1) The mutual interactions between a melting particle and the boiling coolant in a confined space were analyzed by using simulation methods, such as the dynamic meshing method. The research reveals that the heat-absorbing melting particle can significantly enhance local heat transfer under the same heat transfer conditions. However, it can also lead to a deterioration in heat transfer performance. This mainly depends on the vapor coverage rate on the surfaces, referred to as the vapor fraction on surfaces, during the multiphase flow heat transfer process. The analysis indicates that the attachment of some large-size bubbles to the heating surfaces not only reduces the bubble generation rate on hot walls, thus decreasing the evaporation heat transfer, but also hampers the transfer of heat from wall to coolant. It is well-established that

the thermal conductivity of gas is lower than that of liquid for the same material. Hence, the vapor fraction on wall surfaces is the primary factor that affects the heat transfer performance of multiphase flow in microchannels. This provides a viable direction for further enhancing heat transfer performance, such as incorporating the nanosize functional particles in coolants and utilizing non-isothermal phase change fluids.

(2) The effect of adding functional particles suspended in R134a on flow boiling heat transfer performance in microchannels was investigated comparatively. These particles could enhance the thermal properties of base fluid, such as thermal conductivity and the equivalent thermal capacity during the melting processes of PCM particles. The Volume OF Fluid (VOF) method, incorporating the LEE model and the equivalent physical properties approach, was validated with experimental data in literature. This method was then employed to simulate multiphase flow of R134a-based functional fluids in microchannels. The results indicate that, compared to R134a at the same thermal conditions, functional fluids with different types of particles can enhance flow boiling heat transfer coefficient (HTC) through various mechanisms. The high thermal conductivity particles increase the effective thermal conductivity of coolants, while the melting of PCM particles could shift the flow boiling pattern to one with a higher HTC value (e.g., from slug flow to nucleate flow) at the same inlet mass flux and wall heat flux. Additionally, the melting processes of PCM particles in R134a could decrease the vapor rate of R134a in the domain and result in a lower total pressure drop compared to pure R134a.

However, it is difficult to obtain nanoparticles with both high thermal conductivity and high heat melting rate in practice. Therefore, a systematic analysis was conducted to examine the mutual impact of the thermal conductivity and the melting heat of functional particles on heat transfer performance of R134a under the ideal conditions. It is found that there is a minimum matching data of particle thermal conductivity and the melting heat, at which the heat transfer coefficient of functional fluid is the same as that of R134a under the same conditions such as mass flow rate and heat flux. It provides support for the optimal selection and preparation of functional particles in practical applications.

(3) The heat transfer performance of NH_3/H_2O flow boiling in microchannels was extensively studied as it is a promising working fluid for cooling high-power electronic devices. It has the

largest boiling latent heat among available refrigerants within the operating temperature range of electronic components. Since the calculating method adopted in previous studies is only applicable for immiscible mixture, a new approach is proposed to simulate flow boiling heat transfer of zeotropic mixture in microchannels. It couples the multiphase VOF method with a modified LEE method and a quasi-ideal properties treatment of zeotropic mixture. Due to the lack of experimental data on NH_3/H_2O flow boiling in microchannels, this method is validated by experimental data of R134a and R245fa available in the literature.

The results indicate that there is a threshold data of the NH_3 concentration to achieve a certain heat dissipation rate at the same mass flux and heating wall temperature. For instance, when the inlet NH_3 concentration is 25%mol., it could dissipate the heat up to 0.8 MW/m^2 at a mass flux of 184 kg/(m^2·s) and a heating wall temperature of 50℃. The heat transfer capability of NH_3/H_2O in microchannels is remarkable. The overall heat flux is about 1.41 MW/m^2 with the maximum local heat flux up to 1.52 MW/m^2 at a mass flux of 552 kg/(m^2·s) and a heating wall temperature of 50℃.

(4) The multiphase flow and heat transfer performance of the NH_3/H_2O based PCM slurries in microchannels is assessed by adopting the same assumptions and methodologies as before. The effects of some major physical and operational parameters, such as inlet NH_3 and particle concentration, surface wettability and the melting latent heat of PCM particles are evaluated comparatively. Similar to R134a, the addition of PCM particles in the NH_3/H_2O mixture has both positive and negative effects on heat transfer performance. The larger melting latent heat of PCM particles and the better wettability of heating surfaces, the larger enhancement of the heat transfer performance. Conversely, the more and larger bubbles attaching to surfaces, the worse the performance degradation.

Since the evaporating latent heat of the NH_3/H_2O mixture is orders of magnitude larger than the melting latent heat of phase change materials available in applications, the positive effect is weakened significantly. In order to further enhance heat transfer performance, it is effective to improve flow boiling heat transfer performance of the NH_3/H_2O mixture in microchannels and ensure the suspended particles melted completely before they exit the heat sink. such as

the heating surface modification and the optimal matching of the operating parameters during the practical operations.

Overall, this study provides comprehensive insights into the intricate multiphase flow heat transfer process in microchannels, providing a valuable foundation for advancing functional fluids, and offering significant implications for enhancing the thermal management strategies in cooling the electronic devices and fuel cells

ACKNOWLEDGMENTS

First and foremost, I would like to express my heartfelt gratitude and sincere thanks to my supervisors, Dr. Yongliang Li and Professor Yulong Ding, for accepting me into research group. Their guidance and unwavering support have been invaluable throughout my life and studies at the University of Birmingham, especially in those exciting and promising research areas. Their encouragement, academic guidance, and invaluable advice will forever hold a cherished place in my memory.

I would also like to extend my gratitude to all my friends at the Birmingham Centre for their generous help, support, companionship, and encouragement at every stage of my research work. A special thanks goes to Dr. Yi Wang for his invaluable advice and genuine assistance throughout my research.

Furthermore, I would like to express my appreciation to my wife, Renjie Zhang, and my parents for their patience, dedication, and unwavering support throughout my studies. Last but not least, my deepest gratitude goes to my daughter, LingYu Yang, who has been a rock in my life.

CONTENTS

ABSTRACT..... I

ACKNOWLEDGMENTS.....II

CONTENTS..... VI

LIST OF TABLES.....XI

LIST OF FIGURES..... XIII

NOMENCLATURE..... XIX

LIST OF PUBLICATIONS.....XXI

Chapter-1 Background.....1

1.1-Introduction..... 1

1.2-Urgent requirement for high-level heat dissipation technologies.....2

1.2.1-Data centers and electronics systems.....2

1.2.2-PEM fuel cell and Li-ion battery systems..... 5

1.3-Different types of thermal management approaches..... 6

1.4-Enhancement methods for flow boiling in microchannel.....11

1.5-Aims and objectives.....15

Chapter-2 Literature review.....18

2.1-Introduction..... 18

2.2-Flow boiling heat transfer in microchannels..... 18

2.2.1-General heat transfer performance..... 18

2.2.2-Flow boiling instability.....22

2.2.3-Geometrical modification of channels.....26

2.2.4-Wettablility and roughness effects..... 31

2.2.5-Flow boiling of zeotropic mixture.....40

2.2.6-Flow boiling of nanofluids..... 43

2.2.7-Flow boiling of EPCM slurries.....49

2.3-Numerical simulation method for flow boiling..... 54

2.3.1-Flow boiling of pure fluids in microchannel..... 54

2.3.2-Flow boiling of binary mixture in microchannel.....60

2.3.3-Flow boiling of functional fluids in microchannel..... 62

2.4-Summary.....63

Chapter-3 Simulation methods for multiphase flow heat transfer..... 65

3.1-Introduction..... 65

3.2-General physical properties of coolants.....66

3.3-The multiphase VOF Method..... 70

3.4-Phase change model of evaporation..... 71

3.4.1-Pure fluids.....71

3.4.2-NH_3/H_2O.....72

3.5-Phase change model of melting..... 75

3.5.1-The melting and solidification method.....75

3.5.2-The equivalent heat capacity method..... 77

3.6-Dynamic meshing method..... 78

3.7-Initial and Boundary conditions..... 80

3.8-Summary.....81

Chapter-4 Flow boiling heat transfer of water with a PCM particle.....83

4.1-Introduction..... 83

4.2-Basical assumptions and treatments..... 85

4.3-Grid independence and model validation..... 86

4.3.1-Mesh independence test.....86

4.3.2-Simulation model validation.....88

4.4-Results and discussion..... 92

4.4.1-The overall heat transfer performance.....92

4.4.2-The local heat transfer performance..... 99

4.5- Summary.....106

Chapter-5 Flow boiling heat transfer of R134a based functional fluid..... 109

5.1-Introduction..... 109

5.2-Basical assumptions and treatments..... 110

5.3-Grid independence and model validation..... 112

5.3.1-Mesh independence test.....112

5.3.2-Simulation model validation.....113

5.4- Results and discussion..... 116

5.4.1-Effects of particle properties on the overall performance..... 120

5.4.2-Effect of heat fluxes on the overall performance..... 132

5.4.3-Effects of suspended particles on local performance..... 134

5.5-Summary.....136

Chapter-6 Flow boiling heat transfer of the NH_3/H_2O mixture..... 138

6.1-Introduction..... 138

6.2-Basical assumptions ad treatments..... 139

6.3-Grid independence and model validation..... 141

6.3.1-Mesh independence test.....142

6.3.2-Simulation model validation.....143

6.4-Results and discussion..... 145

6.4.1-Effect of inlet mass flux.....148

6.4.2-Effect of inlet concentration..... 156

6.4.3-Effect of heating temperature..... 167

6.4.4-General performance evaluation.....174

6.5- Summary.....176

Chapter-7 Flow boiling heat transfer of the NH_3/H_2O/PCM slurries..... 178

7.1 Introduction.....178

7.2-Basical assumption and treatment..... 178

7.3-Grid independence and model validation..... 179

7.4-Results and discussion.....180

7.4.1-Effect of the PCM melting temperature..... 180

7.4.2-Effect of the PCM melting latent heat.....189

7.4.3-Effect of surface wettability..... 191

7.5-Summary.....194

Chapter-8 Conclusion and future work.....195

8.1 General conclusions.....195

8.2 Future work.....199

Appendix-1 Flow boiling heat transfer in literature..... 201

Appendix-2 Calculation mathematical model of NH_3/H_2O mixture..... 207

A2.1-Vapor-liquid equilibrium and thermodynamic properties.....207

A2.2-Mixture critical temperature and pressure.....210

A2.3-Specific thermal capacity of saturated liquid mixtures at constant pressure.....210

A2.4-Thermal conductivity of liquid mixtures.....211

A2.5-Dynamic viscosity of liquid mixtures.....212

A2.6 Liquid Mixture density.....213

References.....214

LIST OF TABLES

Table.1 Sizes and heat dissipation of high-performance computer and desktop..... 4

Table.2 The main saturated thermophysical properties of some traditional coolants at 1bar 8

Table.3 Heat transfer performance of two-phase impingement methods in literature..... 9

Table.4 Heat transfer performance of flow boiling in microchannel in the literature 10

Table.5 HTC enhancement of H_2O-Al_2O_3 nanofluid single phase convection in microchannel.... 12

Table.6 Experimental researches of water flow boiling heat transfer in microchannel..... 21

Table.7 Experimental studies on the flow instability in microchannels..... 25

Table.8 Experimental investigations on the geometrical modification for flow instability..... 27

Table.9 Experimental studies of R134a, R245fa and NH_3 flow boiling in mini/microchannel..... 40

Table.10 Experimental studies of R134a/R245fa and NH_3/H_2O in flow boiling heat transfer..... 41

Table.11 Heat transfer performance and parameters of nanofluid flow boiling in microchannel.. 48

Table.12 Properties comparison of the organic and inorganic PCMs..... 49

Table.13 Properties of phase change materials available for electronic cooling applications.. 50

Table.14 Heat transfer performance of flow boiling heat transfer by VOF-LEE method..... 59

Table.15 The main operational conditions of different cases 92

Table.16 Boundary conditions of water flow boiling with a PCM particle in present work.... 93

Table.17 Main parameter data at 6ms and 11ms in different cases..... 95

Table.18 Thermophysical properties of R134a and PCM particles in present work..... 112

Table.19 Main boundary conditions of numerical simulations in Chapter 5..... 117

Table.20 The main properties of C18-based metal coated EPCM particles in literature..... 119

Table.21 The simulation conditions on flow boiling of NH_3/H_2O mixture in Chapter 6..... 146

Table.22 Physical properties of PCM and saturated NH_3/H_2O solution at 50℃ and 1bar..... 180

Table.23 Flow boiling heat transfer in microchannel (T_{wall} <85℃) 201

Table.24 Single phase convection in microchannel (T_{wall} <85℃)..... 202

Table.25 Heat transfer performance of water heat pipes (T_{wall} <85℃) 202

Table.26 Heat transfer of two-phase impingement (T_{wall} <85℃) 203

Table.27 Heat transfer of two-phase spray cooling (T_{wall} <85℃) 205

Table.28 Single-phase convection of air and water in microchannel (T_{wall} <85℃) 205

LIST OF FIGURES

Figure.1 The background, motivation and main research contents of this work..... 1

Figure.2 Composition of Energy consumption and carbon footprint in typical data centers..... 3

Figure.3 Distributions of local heat flux and temperature in the base of microprocessors 4

Figure.4 The classification of different cooling approaches available for the thermal management..... 7

Figure.5 Heat flux comparison of water single phase convection in microchannels 8

Figure.6 Thermal conductivity and specific heat capacity of fluids and nanoparticles 12

Figure.7 Thermal conductivity enhancement by adding Al_2O_3 and CNT nanoparticles 12

Figure.8 Relation of heat flux and pressure drop curve in boiling heat transfer 18

Figure.9 M-shape curve of flow boiling heat transfer in microchannels 19

Figure.10 Local flow boiling HTC and bubbles transition at a constant heat flux 20

Figure.11 Relations of local HTCs with vapor quality in different mass and heat fluxes 20

Figure.12 Channel aspect ratio effect of microchannel on flow boiling HTC and pressure drop. 21

Figure.13 Logic relation of flow boiling instability in microchannel and available treatments.....22

Figure.14 Inlet temperature effect on flow instability and three stages of bubble growth 24

Figure.15 Types of wall-liquid-bubble forces on bubbles in flow boiling in microchannels...25

Figure.16 Logic relations of Geometrical modification to ease flow instability in microchannel. 26

Figure.17 Geometry structures of microchannels with and without inlet restrictions 28

Figure.18 Geometry structures of microchannels with different constructions 28

Figure.19 Structure diagram of microchannels with different constructions 28

Figure.20 Structure diagram of different microchannels with the Ω-shaped reentrant cavities 29

Figure.21 Structure diagram of interconnected microchannel net 29

Figure.22 Structure diagram of microchannels with different shapes of pin fins 30

Figure.23 Effects of channel structures and geometrical parameters on flow boiling in microchannel (a) FC-72 (b) HFE7100 30

Figure.24 The main principles of surface modified treatment shown in boiling curve..... 31

Figure.25 Illustration of contact angle and wettability classification 32

Figure.26 Surface modification methods to enhance flow boiling heat transfer performance. 32

Figure.27 Mechanisms of superhydrophilic and superhydrophobic surfaces on flow boiling 33

Figure.28 The important performance of alternative surface modification treatment..... 34

Figure.29 Effects of solid materials on wettability and nanofluid deposition on wettability and roughness 35

Figure.30 Effects of contact angles on CHF in pooling boiling by surface modification methods36

Figure.31 Geometric structures of microchannels and contact angles of different surfaces ... 37

Figure.32 Definition of area ratio and the results of flow boiling heat transfer enhancement 38

Figure.33 Relations of contact angle with temperature on different material heating surfaces 38

Figure.34 Characteristics and mechanisms of zeotropic mixture flow boiling in microchannel... 41

Figure.35 Influences of suspended nano particles on refrigerants flow boiling in microchannel..44

Figure.36 Different results of nanofluid on flow boiling HTC in microchannel..... 46

Figure.37 Relation of thermal conductivity and encapsulation ratio of modified EPCM particles52

Figure.38 Illustration of subcooled flow boiling at a uniform heat flux condition.....56

Figure.39 The main assumptions and multiphase mass and heat transfer models in chapters. 65

Figure.40 Specific evaporation latent heat between the saturated liquid or gas mixture.....69

Figure.41 Thermophysical and transport properties of saturated liquid and gaseous NH_3/H_2O mixture at different pressure..... 69

Figure.42 Phase diagram of multiphase flow of NH_3/H_2O mixture at constant pressure..... 73

Figure.43 Latent heat of NH_3/H_2O mixture as functions temperature at 0.1MPa.....75

Figure.44 Rectangular profile of the equivalent heat capacity method for PCM melting..... 78

Figure.45 Research Description of the main numerical simulation cases in chapter 4.....84

Figure.46 Fixed-quadrilateral and dynamic re-meshing triangular grids for flow boiling with and without a physical PCM particle..... 86

Figure.47 Grid independence test of H_2O flow boiling in microchannel at 100 and 500 kW/m^2.. 87

Figure.48 Definition of major geometric parameters of cross-sectional area in microchannel 90

Figure.49 Heat flux versus flow time and the HTC versus exit vapor quality of the numerical and referenced cases 91

Figure.50 Relations of the overall heat fluxes, HTCs and pressure drops with flow time..... 94

Figure.51 Flow patterns of the vapor fraction at 6ms and 11ms in different cases..... 96

Figure.52 Relations of vapor fraction on hot walls and outlet velocity in different cases.....98

Figure.53 Relations of heat flux ratios (a) and vapor fraction on walls (b) with flow time... 100

Figure.54 Comparisons of the vapor fraction distributions near the PCM particle in cases...101

Figure.55 Relations of heat flux and vapor fraction on PCM particle surface with flow time102

Figure.56 Different types of forces on PCM particle in flow boiling in microchannel..... 103

Figure.57 Relations of velocity and liquid fraction of PCM particle with flow time in cases103

Figure.58 Comparisons of liquid PCM distributions inside the big PCM particle in cases... 104

Figure.59 The PCM particle effects on flow boiling heat transfer in domain..... 106

Figure.60 Schematic of numerical simulation construction and domain in Chapter 5..... 113

Figure.61 Grid independent test based on vapor fraction on inner hot surfaces of R134a 113

Figure.62 Relations of flow boiling heat transfer with an empirical factor r in LEE model...114

Figure.63 Comparisons of local HTCs and pressure drop of R134a between numerical and experimental results in micro/minichannel..... 115

Figure.64 Comparisons of heat transfer results between numerical and experimental cases for local HTCs of n-hexadecane/H_2O emulsion (with PCM melting) in a micro/minichannel....116

Figure.65 Effects of thermal conductivity and latent heat per unit melting temperature on the overall HTCs of R134a-based functional fluid in microchannel..... 122

Figure.66 Bubble distribution flow patterns of R134a based functional fluids near outlet in microchannel domain at mass flux 400 kg/(m^3·s) and heat flux 69 kW/m^2.....124

Figure.67 Effects of thermal conductivity and latent heat per unit melting temperature on the area-averaged surface vapor fraction in microchannel..... 125

Figure.68 Relations of flow boiling HTCs with vapor fraction on surfaces for R134a-based functional fluids in microchannel with different particle properties and mass fluxes..... 126

Figure.69 Effects of thermal conductivity and latent heat per unit melting temperature on the time-averaged pressure drop in microchannel..... 127

Figure.70 Effects of thermal conductivity and latent heat per unit melting temperature on the FOM in microchannel..... 129

Figure.71 Effect of particle concentrations on the FOMs of functional fluid flow boiling with different properties and mass fluxes in microchannel at 69 kW/m^2..... 130

Figure.72 Effects of heat fluxes on HTCs and pressure drops of R134a-based functional fluids flow boiling in microchannel..... 132

Figure.73 Bubble distribution flow patterns of R134a based functional fluids in microchannel at mass fluxes of 200, 400 kg/(m^2·s) and heat fluxes of 27, 69 kW/m^2 134

Figure.74 Comparison of local HTCs along the x-axis flow direction for R134a based functional fluids at 400 kg/(m^2·s), 69 kW/m^2, 15% vol..... 135

Figure.75 Schematics of bubble distribution in domain and local HTC values of water flow boiling in a channel at a uniform heat flux condition..... 135

Figure.76 Schematic of numerical simulation construction on NH_3/H_2O flow boiling.....141

Figure.77 Grid independent tests based on vapor fraction and heat flux on walls..... 142

Figure.78 HTC result comparisons among numerical and referenced experimental cases of R134a/R245fa mixture (70/30 by wt.%) in the microchannel..... 144

Figure.79 Comparisons of confined bubble and slug flow patterns of R134a/R245fa mixture (70/30 by wt.%) between the experiment and numerical simulation.....145

Figure.80 Simulation cases shown in saturated NH_3 solution properties plots at 0.1MPa..... 147

Figure.81 Relations of the area-averaged heat fluxes with flow time at different mass fluxes....147

Figure.82 Schematic diagram of boundaries and local positions in domain.....148

Figure.83 Effects of mass fluxes on the overall heat fluxes, vapor distribution in domain and overall HTC of NH_3/H_2O in microchannel at 50℃..... 149

Figure.84 Effects of mass fluxes on vapor fraction and the overall pressure drop of NH_3/H_2O in microchannel at 50℃.....150

Figure.85 Effects of mass fluxes on local heat fluxes, vapor fraction on local surfaces, fluid temperature in midsection and local HTCs of NH_3/H_2O in flowing direction at 50℃.....154

Figure.86 Effect of inlet concentration on the overall HTC, vapor fraction on surfaces, heat fluxes, vapor fraction in domain, outlet temperature and relative pressure drop ratio of NH_3/H_2O mixture in microchannel..... 159

Figure.87 Effect of inlet concentration on dynamic stable distributions of bubbles and fluid temperature in domain at 276 kg/ (m^2·s).....161

Figure.88 Effect of inlet concentration on local heat fluxes, local HTCs and local fluid temperatures in midsection at 184 and 276 kg/(m^2·s).....164

Figure.89 Effect of inlet concentration and mass flux on local heat flux near the entrance at a1 and the exit at a5 of microchannel..... 165

Figure.90 Effect of heating temperature on the overall heat flux, HTC, outlet temperature, vapor fraction on walls, pressure drop and vapor fraction in domain at various G_{in}..... 169

Figure.91 Effect of heating temperature on local heat flux, local HTC and fluid temperature in midsection at 276 kg/(m^2·s) 173

Figure.92 Effect of heating temperature on fluid temperature distribution and vapor fraction distribution of NH_3/H_2O flow boiling in microchannel at 276 kg/(m^2·s).....173

Figure.93 Local HTC with vapor fraction on wall surface of NH_3/H_2O in microchannel.....175

Figure.94 Effect of PCM melting temperature on the overall heat flux and HTC of single-phase convective heat transfer of NH_3/H_2O/PCM mixture in microchannel at 50℃..... 181

Figure.95 Effect of PCM melting temperature on flow boiling heat transfer NH_3/H_2O/PCM mixture in microchannel at heating temperature 50℃.....183

Figure.96 Effect of PCM melting temperatures on fluid temperature distribution of NH_3/H_2O/PCM mixture flow boiling in microchannel at heating temperature 50℃..... 184

Figure.97 Effect of inlet mass fluxes on fluid temperature, vapors and PCM distributions of NH_3/H_2O/PCM mixture flow boiling in microchannel at T_{wall} of 50℃.....186

Figure.98 The overall heat fluxes comparison of NH_3/H_2O/PCM mixture flow boiling with and without PCM melting in microchannel at a constant T_{wall} of 50℃..... 188

Figure.99 The overall heat fluxes comparison of NH_3/H_2O/PCM mixture flow boiling at different melting latent heat and inlet concentration of PCMs at a constant T_{wall} of 50℃..... 190

Figure.100 Effect of surface wettability on the overall heat flux, HTC and vapor fraction on surfaces of NH_3/H_2O/PCM mixture flow boiling in microchannel at T_{wall} of 50℃..... 192

Figure.101 Distributions of bubbles and PCM in domain at different surface wettability conditions..... 193

NOMENCLATURE

Nomenclature

A	area (m^2)
E	energy (J/kg)
FOM	figure of merit
$\vec{F}_{surf}$	*surface tension force (N/m3)*
H, h	Heat transfer coefficient (kW/(m^2·K))
h_m	total melting latent heat of EPCM particles (kJ/kg)
K	Thermal conductivity (W/(m·K))
k_{eff}	effective thermal conductivity (W/(m·K))
N	total number of individual time points
p	pressure (MPa)
ΔP	pressure drop (MPa)
q_{LH}	Latent heat (J/kg)
q_m	latent heat per unit melting temperature of EPCM particles (kJ/(kg·K))
q, q_{wall}	heat flux (kW/m^2)
r_i	relaxation factor during phase change process (m^{-1})
S_m	mass source term (kg/(m^3·s))
S_h	energy source term (J/(m^3·s))
t	time (s)
T	temperature (K)
ΔT_m	melting temperature range of EPCM particles (K)
$T_{backflow}$	mass-averaged back-flow temperature (K)
T_{sat}	saturated temperature of R134a (K)
$T_{melting}$	melting temperature of PCM (K)
u_x	velocity in the x direction at each grid cell (m/s)
$\vec{v}$	velocity (m/s)
x_{wall}	vapor fraction on heated surfaces (-)
x_{domain}	vapor fraction in the domain (-)
x, x_{exit}	thermodynamic equilibrium vapor quality (-)

X, X_{exit}	a new factor, seen in the eqn. (4-1) at page 90
x_{in} , x_{NH3}	the NH_3 concentration in liquid NH_3/H_2O mixture (by mol)
y, y_{PCM}	the NH_3 concentration in gaseous NH_3/H_2O mixture (by mol)

Greek symbols

α	volume fraction
κ	local interface curvature (m^{-1})
μ	dynamic viscosity (kg/(m·s))
ρ	density (kg/m^3)
σ	surface tension coefficient (N/m)

Subscripts

p, q	liquid and gas phases of fluid
sat	saturation
m, melting	Melting of PCM
local	local heat transfer performance
overall	overall heat transfer performance
in, out	inlet or outlet of a channel
wall	heating wall
L, R	left and right side of heating wall
l, r	left and right side of heating wall
fluid	fluid parameter

LIST OF PUBLICATIONS

The content of this thesis has been published in the following papers:

Journal articles:

[1] Jian X, Yi W, **Ren Y**, et al. A review of boiling heat transfer characteristics in binary mixtures. Int. J. Heat Mass Transfer, 2021 (164) : 120570.

[2] **Yang R**, Wang Y, Li Y. Numerical investigations on flow boiling heat transfer of ammonia water binary solution (NH_3/H_2O) in a horizontal microchannel.Int. J. Heat Mass Transfer, 2021 (171) :121091.

Conference papers and presentations:

[3] **Ren Yang**, Qinghua Yu, Jian Xu, Yulong Ding, Yongliang Li. Numerical simulation on flow boiling heat transfer behavior of microencapsulated phase change slurry in a microchannel.UK-China International Particle Technology Forum 2019 UK & Annual Particle Technology Forum, Edinburgh, 2019

[4] **Ren Yang**, Yi Wang, Yulong Ding, Yongliang Li. Numerical Simulation on Flow Boiling Heat Transfer of R134a Based Functional Fluids in a Microchannel. 7th Micro and Nano Flows Conference, London, 24-26 May 2021

[5] **Ren Yang**, Yi Wang, Yulong Ding, Yongliang Li. Numerical Simulation on Flow Boiling Heat Transfer of PCM-R134a Slurry in a Microchannel. 17th UK Heat Transfer Conference, University of Manchester,4-6 April 2022.

Chapter-1 Background

1.1-Introduction

This chapter provides a concise overview of the current research status and challenges in the thermal management for the electronic devices and fuel cells. It compares the performance of various advanced cooling approaches available and ultimately presents the main structure and objectives of this study. The main technical roadmap is illustrated in Figure.1 as follows.

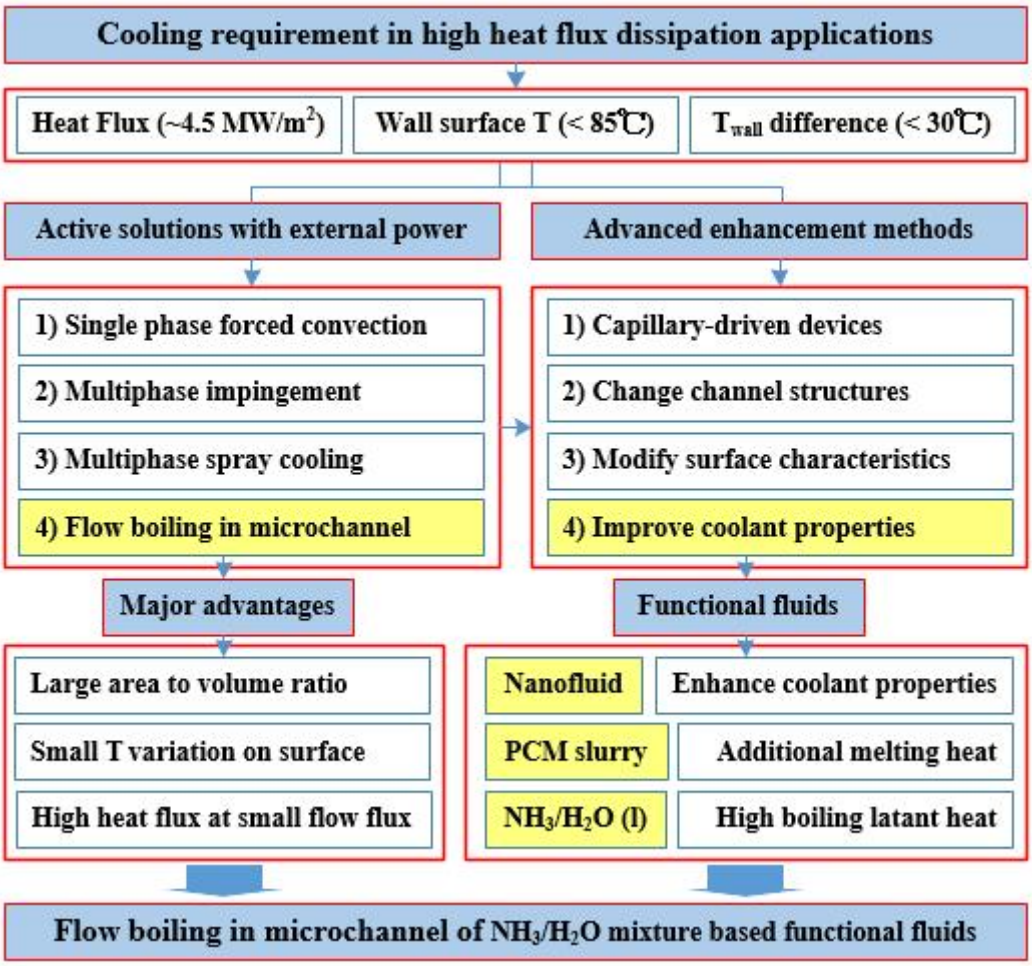


Figure.1 The background, motivation and main research contents of this work

Currently, there is an urgent requirement for advanced thermal management technologies to efficiently dissipate high-level heat generated in practical applications, such as the advanced electronic components in data centers, fuel cells, and Li-ion batteries in electric vehicles. It is predicted that in the future, the heat flux needed to be dissipated in advanced electronic devices will reach up to 4.5 MW/m² while operating in a maximum temperature of 85℃ and maintaining the largest temperature difference of less than 30℃.

Among various cooling methods available, flow boiling in microchannels is considered to be highly effective in the heat dissipation process. Furthermore, the use of functional fluids, such as nanofluids and PCM slurries that incorporate functional particles to enhance the physical properties of coolants, is expected to be a promising approach for further enhancing the heat transfer performance of flow boiling in microchannels.

Therefore, the main objective is to evaluate the heat transfer performance of functional fluids flow boiling in microchannels, such as R134a and the NH_3/H_2O mixture as well as functional fluids. Additionally, this research aims to identify the dominant factors and investigate their corresponding effects on the heat transfer performance.

1.2-Urgent requirement for high-level heat dissipation technologies

The ever-increasing demand for high-level heat dissipation in electronic devices and fuel cells has created an urgent need for highly effective thermal management solutions in various applications.

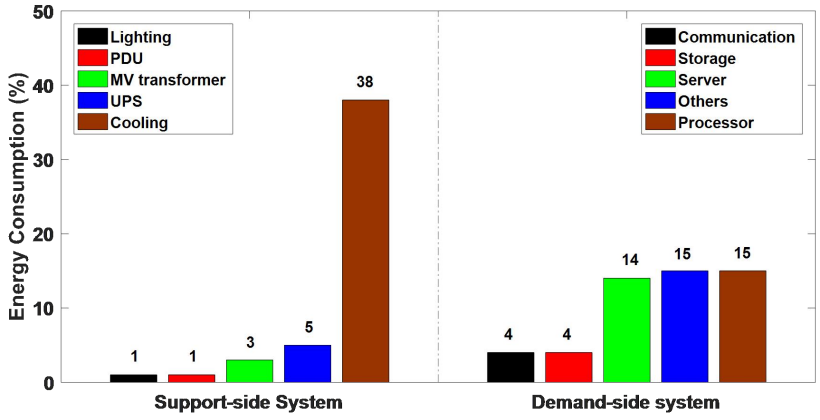
1.2.1-Data centers and electronics systems

There is a significant increase in the electricity consumption of data centers in recent years, mainly due to the the ever-increasing growth of data center market and the rapid development of electronic components. It is predicted that the annual increases in electricity consumption in data centers could reach as high as 15-20% [1], which is responsible for 3% of the global electricity use in 2017 and will rise to 4.5% in 2025 [2]. Remarkably, the CO_2 emissions produced by data centers are equivalent to those of the aviation industry, making the IT industry responsible for 2% of global CO_2 emissions [3].

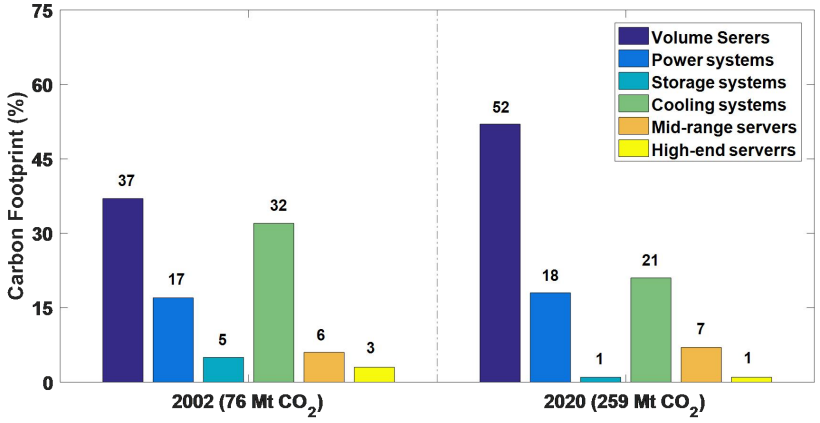
Figure.2 depicts the breakdown of energy consumption (a) and the carbon footprint (b) in a typical data center. The numbers located above the bars correspond to the respective values in each figure.

It is found that the cooling system accounts for the largest part of the total electronic power consumption, up to 38% of the support-side systems. This exceeds the energy consumption by the processors in data center systems [4]. Although the proportion of CO_2 emissions from cooling systems has decreased from 32% in 2002 to 21% in 2020, the CO_2 emissions in 2012 were approximately 2.2 times higher than those in 2002. This is attributed to the significant

increase in the total carbon emissions from data centers, which surged from 76 Mt CO_2 in 2002 to 259 Mt CO_2 in 2020 [5].



(a)



(b)

Figure.2 Composition of Energy consumption [4] and carbon footprint [5] in typical data centers

An efficient cooling management system is urgently needed to ensure the performance, safety, and longevity of electronic components in data centers. As discussed before, the majority of electricity consumed in data centers is converted into heat energy. Table.1 lists the sizes and heat fluxes of processors in high-performance computing devices. If this heat is not promptly removed, it may result in overheating, posing a threat to the safety of electronic devices and systems [3,6]. In order to maintain a safe operating temperature and humidity for electronic components, approximately 38% of electricity used in a data center is consumed for thermal management [3,4]. Therefore, the electricity assumption and CO_2 emissions of data centers could be significantly reduced by improving the efficiency of thermal management. This also directly impacts the overall performance of data centers.

Table.1 The sizes and heat fluxes of processors in high-performance computing devices [7,8]

Processor	Die size	Power	Heat flux	Heat flux in 2026	
ORACLE SPARC T4	403.0 mm^2	240W (2011)	0.60 MW/m^2 (2011)	800W	2.0 MW/m^2
i7-4790K	177.0 mm^2	88 W (2014)	0.50 MW/m^2 (2014)	800W	4.5 MW/m^2
i7-8700K	153.6 mm^2	95 W (2017)	0.62 MW/m^2 (2017)	800W	5.2 MW/m^2
i9-10900K	206.1 mm^2	125W (2020)	0.61 MW/m^2 (2020)	800W	3.9 MW/m^2

Furthermore, the heat dissipation density, also known as heat flux, of electronics like CPUs is significantly higher than the average value of a data center system [9]. For instance, the CPU dissipates 63% of the total electricity consumed in a computing node manufactured by 65nm technology [10]. According to Table.1, the heat flux of a processor has already reached 0.62 MW/m^2 [8]. It is also predicted that the power of high-end microprocessors will reach 800W by 2026, resulting in a maximum heat flux up to 5.2 MW/m^2 [7]. If the heat is not efficiently dissipated from the components, it can cause a rapid increase in chip temperatures, leading to decreased CPU performance and potentially jeopardizing the lifespan of devices.

The maximum local heat fluxes on electronic chips are larger than the average of electronic devices. Hot spots are common in processors due to the non-uniform arrangement of different components with varying heat on electronic chips. For example, the logic cells which only occupy 25% of the chip area can dissipate up to 90% of the total heat and generate local heat fluxes that are 6 to 10 times higher than the average [11].

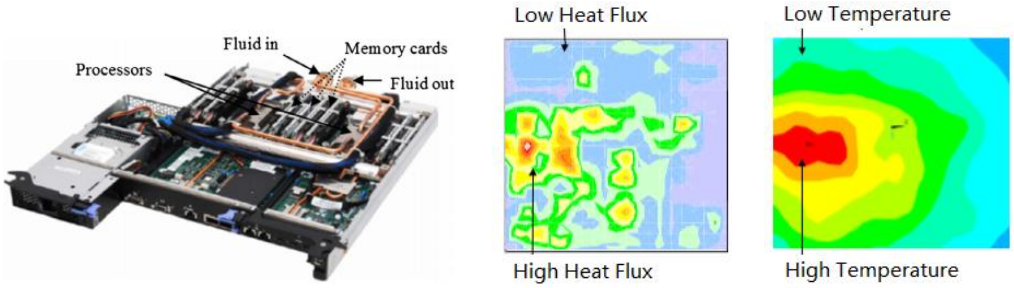


Figure.3 Distributions of local heat flux and temperature in the base of microprocessors [7,11]

For most of the electronic components, if the surface temperature exceeds the average value by 30℃, it can result in a decrease in calculating speed by more than 15% [12]. Furthermore, the operating temperature of electronic devices should be kept below 85℃ in order to ensure the performance, reliability and lifetime [13]. For example, when the temperature is reduced

from 100℃ to 70℃, the leakage power (namely power lost) of CPUs could be decreased by 50% [14] and enlarge the longevity of devices, accordingly.

Generally, there is a pressing need to investigate innovative and effective cooling solutions to dissipate high levels of the non-uniform heat from microprocessors in order to ensure that the peak temperature remains below 85 ℃ in advanced electronics applications in the future.

1.2.2-PEM fuel cell and Li-ion battery systems

Recently, the environment pollution, such as air pollution, has been worsening severely and rapidly. Road transport was responsible for around 80% of air pollution and almost 1/4 of the global GHG emissions [15]. Therefore, it is a great of interest to reduce air pollution focusing on the pollution sources, specifically power supply systems. When compared to the internal combustion engines (ICE), fuel cells and electric power supply systems offer great potential benefits in reducing these environmental issues.

Polymer electrolyte membrane (PEM) fuel cell is a promising option in the transportation and portable power fields due to its inherent advantages including the low operating temperature (less than 80C°), the zero emissions, high energy efficiency and fast responses [16]. However, the durability of PEM fuel cells is one of the main limitations to the commercial applications [17]. High temperature could lead to the membrane dryness, resulting in the increased ionic resistance and risks of material degradation [18]. Therefore, the development of effective heat dissipation techniques is crucial for maintaining the operating temperature of PEM fuel cells around 80℃.

The electricity storage system is an essential component of electric vehicles (EVs). Currently, there are several different electric storage techniques available for EVs, including flywheels, ultra-capacitors and batteries. Among them, the Li-ion batteries are commonly used mainly due to high power and energy density, long lifespan, and relatively low costs [19,20,21]. It is predicted that the annual demand for Li-ion batteries would be 408 GWh by 2025 and 1293 GWh by 2030 in EVs [22].

Thermal management system (TMS) is crucial to ensure the optimal performance of batteries. Typically, batteries account for about 75% of the total power cost in vehicles [23]. Similar to fuel cells, if this heat is not dissipated effectively, it can result in rapid temperature increases

and uneven temperature distributions, which can potentially lead to significant deterioration in performance and reduction in lifespan.

The optimal operating temperature range for a Li-ion battery is 15 to 35°C, in order to avoid the negative impacts on its lifetime, safety and performance [21,24]. It has high-risk to failure when the operating temperature exceeds 70°C [21,25]. Further rise in temperature causes the degradation of power and capacity and even the thermal runaway [20,26]. For example, a 1K increase in temperature can shorten the battery's lifetime by 2 months within 30~40°C [27]. A temperature difference of more than 5°C can result in a 10% degradation in power capability and a 25% increase in thermal aging [28].

In conclusion, it is crucial to address the challenges of local hotspots and temperature non-uniformity by implementing an effective thermal management system in PEM fuel cells and Li-ion batteries.

1.3-Different types of thermal management approaches

As mentioned before, it is necessary to adopt an effective thermal management to control the temperature within a proper range and ensure the temperature uniformity.

Different types of cooling approaches have been proposed and implemented in applications. These approaches can be classified based on either the heat transfer mechanisms or the type of coolants in Figure.4. The cooling approaches can be categorized into passive and active schemes. Passive systems rely on capillary force (such as heat pipes) or buoyancy force (such as air natural convection and liquid pool boiling) to circulate coolants. The active systems use fans, compressors (such as air forced convection), or pumps (such as forced convection and flow boiling) to achieve higher cooling capacity and optimize the performance of devices.

Compared to traditional macro-scale heat sinks, microchannels have significant advantages in enhancing both single-phase and multi-phase flow heat transfer capabilities due to their large surface area to volume ratio. For instance, a microchannel with a width of 40 μm and a depth of 200 μm has a surface area to volume ratio of 15,294 m^2/m^3, which is 23.5 times greater than that of a compact macro-scale heat sink with a ratio of 650 m^2/m^3 [29]. In this study, the heat transfer performance in microchannels will be compared with other cooling techniques.

The geometric parameters of heat sinks, operating conditions and heat transfer performance of different cooling approaches are listed in Appendix 1.

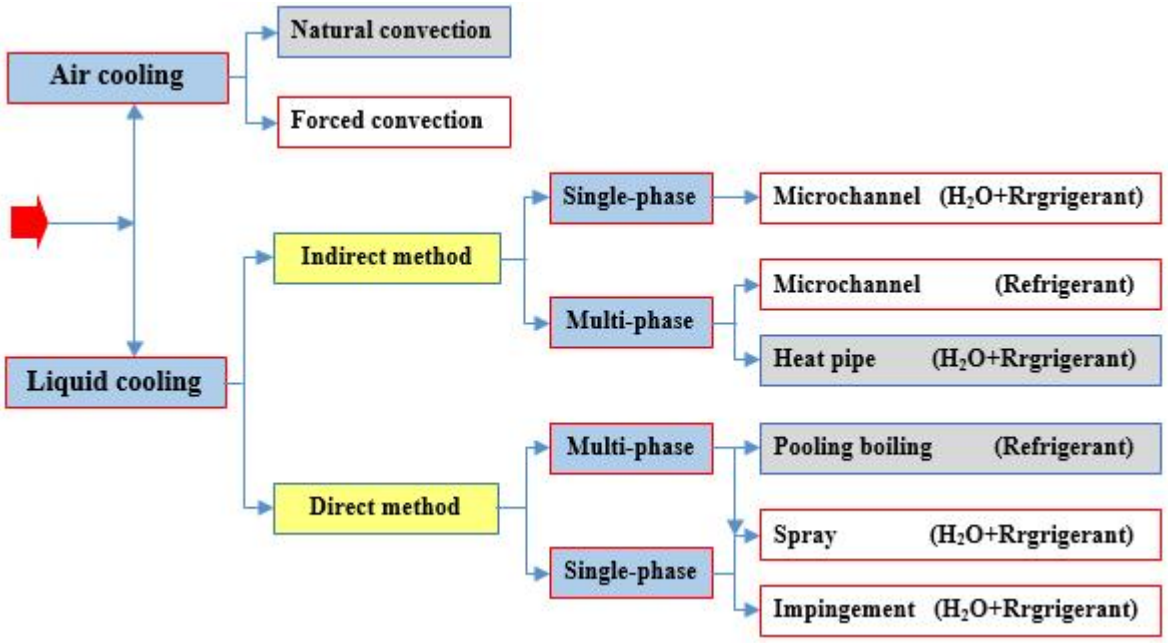


Figure.4 The classification of different cooling approaches available for the thermal management

Generally, passive cooling systems such as air natural convection, heat pipes, and liquid pool boiling have reached their maximum heat transfer capacities. However, it is not sufficient to meet the increasing demands for heat dissipation in the future. For example, the maximum capacity of natural air convection is about 0.15 MW/m^2 [30]. The cooling capacities of air forced convection in microchannels and miniature heat pipes are less than 1.5 [31] and 0.68 MW/m^2 [32], respectively. Wang et al. [33] investigated the cooling performance of a hybrid air-forced convection with heat pipes embedded in sink and found that the minimum thermal resistance was 0.15 ℃/W at 176 W and air velocity of 3 m/s. Pool boiling on porous graphite using HFE-7100 had a maximum critical heat flux of up to 0.7 MW/m^2 at a wall temperature below 85℃ [34]. Therefore, though the heat dissipation capacity of those passive systems has increased to some extent for cooling electronic devices, it still falls significantly short of meeting the ever-increasing requirements.

The active cooling methods include forced convection in microchannels, spray cooling, and impingement cooling. Table.2 presents the thermophysical properties of commonly used pure liquid coolants. It is evident that water is an optimal coolant for single-phase cooling due to its excellent specific heat capacity. According to experimental studies in the literature, the

heat flux achieved by forced convection of water in microchannels reached up to 7.9 MW/m^2, but at the cost of a high pressure drop of 214 kPa and a temperature rise of 71℃ between the substrate and inlet fluid [35,36]. Single-phase spray cooling using water could dissipate heat at a rate of 2.5 MW/m^2 with a pressure drop of 500 kPa [37]. The impingement method for single-phase water cooling could achieve a heat flux of 4.7 MW/m^2 with a pressure drop of 241 kPa [38] for cooling electronic devices. Figure.5 illustrates experimental results depicting the effects of mass fluxes and geometric parameters (e.g., shapes and sizes) on heat fluxes of single-phase water forced convection in microchannels, where the heating wall temperature is maintained below 85℃. It indicates that the heat fluxes can be enhanced by increasing mass fluxes, decreasing channel sizes and employing complex geometric shapes of microchannels. However, these come at the cost of large pressure losses. The details are listed in Appendix 1.

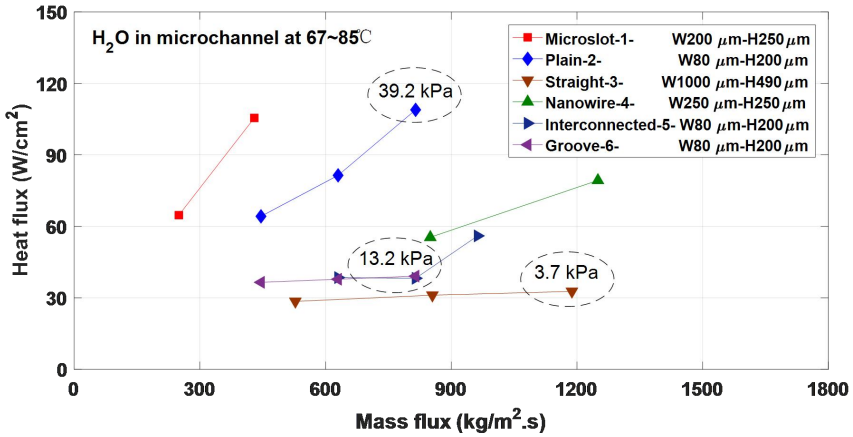


Figure.5 Heat flux comparison of water single phase convection in microchannels ([39,40,41,42,43])

Multiphase heat transfer methods, such as flow boiling in microchannels, spray cooling, and impingement cooling, are highly effective for cooling applications due to the heat absorbed in phase change processes. As mentioned earlier, It is crucial to select appropriate coolants with the saturated temperature lower than the maximum operating temperature of devices, such as fuel cells at 80℃ and electronic components at 85℃[12]. Therefore, water is not acceptable as a coolant for multiphase cooling of electronic devices, despite its excellent properties, such as high latent heat of evaporation. Table.2 Presents important physical properties of available coolants that have saturated temperatures below 100℃ at a pressure of 1 bar.

Table.2 The main saturated thermophysical properties of some traditional coolants at 1bar [44,45]

No.	Coolants	M	T_{sat}	ρ_{liq}	cp_{liq}	q_{LH}	λ_{liq}

/	/	g/mol	℃	kg/m^3	kJ/(kg·K)	kJ/kg	W/(m·K)
1	NH_3	17	-33.3	682.0	4.45	1369.5	0.666
2	R134a	102	-26.1	1377	1.28	217.0	0.104
3	R245fa	134	15.1	1365	1.30	196.0	0.091
4	FC-72	338	56.0	1680	1.10	88.0	0.057
5	HFE-7100	250	61.0	1520	1.17	125.0	0.061
6	NH_3/H_2O (19.5%mol)	/	50.0	981.0	4.21	1443.0	0.579
7	NH_3/H_2O (6.0%mol)	/	80.0	972.8	4.21	1719.0	0.642
8	H_2O	18.0	100	958.4	4.22	2256.5	0.679

The heat transfer performance of refrigerant multiphase impingement and spray are compared as follows. Table.3 presents representative experimental data from literature on refrigerants such as FC-72, R134a, R245fa, and HFE7100. The detailed data can be found in Appendix 1. In this table, T_{wall}, T_{in}, and T_{sat} represent the average surface temperature, inlet temperature, and saturated temperature of coolants, respectively. d_j denotes the diameter of jet nozzles and H represents the distance between the nozzles and the heating surfaces. Generally, refrigerant multiphase impingement and spray techniques have excellent cooling capabilities. The heat flux of impingement cooling on smooth surfaces is about 1.1 MW/m^2 [46]. While the micro-jet impingement on pin-fins and/or porous coated surfaces can enhance cooling capability, it also leads to significantly high pressure drops (up to 241 kPa [47]) and velocity (10 m/s [48]).

Table.3 Heat transfer performance of two-phase impingement methods in the literature (T_{wall} <85 ℃)

Surfaces	T_{wall}	T_{in}	T_{sat}	H	d_j	q	dP	year
	℃	℃	℃	mm	mm	W/cm^2	kPa	/
FC-72								
Smooth	68.9	47.0	50.0	5	0.24	40.8	241	2011 [47]
Submerged pin fins	75.2	21.0	56.0	/	/	166.5	/	2011 [49]
Microchannel	68.4	30.0	50.0	1.5	0.24	133.0	/	2014 [50]
HFE7100								
Smooth	68.0	56.0	61.0	20	0.76	69.0	210	2014 [51]

Pin fins & Porous	69.0	51.0	61.0	2.5	0.75	95.4	2.7	2015 [52]
Minichannel	81.6	0.0	/	3	0.3	285.6	16.7	2009 [53]
R134a								
Smooth	42.5	26.0	31.0	/	2.0	113.7	/	2012 [46]
Submerged micro jet	55.2	17.0	47.0	/	0.11	335.0	/	2010 [48]

Among those active cooling methods, forced flow boiling in microchannels stands out as a promising and efficient technique for cooling applications. This is mainly due to its compact size, relative low cost, high heat dissipation rate, and small coolant requirement [54,55]. For instance, the latent heat of R134a is approximately 170 times greater than its sensible heat for a 1 K temperature difference. Consequently, this method has the ability to reduce both the mass flow of coolants and pumping power required, while maintaining a small temperature difference on heating surfaces (only slightly higher than the coolant's saturation temperature). This also contributes to improved reliability by reducing thermal stress [56]. Moreover, when the channel diameter is less than 0.51mm, the stratified flow pattern disappears [13]. As a result, the risk of local dryout is reduced when compared to macrochannels. Therefore, flow boiling in microchannel is an effective method for the hotspot management and temperature uniformity.

Table.4 Heat transfer performance of flow boiling in microchannel in literature (T_{wall} <85 ℃)

Shapes	T_{wall}	T_{in}	T_{sat}	W×H-L	G	q	dP	year
/	℃	℃	℃	μm×μm-mm	kg/(m^2.s)	W/cm^2	kPa	/
FC-72								
Straight	81.0	23.3	56.5	220× 55-10	578	32.8	67	2019 [57]
Straight	83.2	23.3	56.5	220× 55-10	2311	65.7	109	2019 [57]
Oblique fins	70.7	26.5	56.5	300×1190-25	394	70.4	5.8	2016 [58]
HFE7100								
Straight	84.5	15.0	61.0	200×573-20	550	37.9	/	2021 [59]
Straight	83.1	0	63.0	260×1041-10	1682	278.3	7.4	2008 [60]
Micro cavities	74.4	18.0	61.0	200×250-10	1155	175.2	/	2018 [61]

				R134a				
Straight	34.8	15.0	25.0	100×500-15	400	30.5	/	2013 [62]
Straight	85.0	22.0	25.0	199×756-39	3000	197.7	/	2010 [63]

Table.4 lists some representative experimental results of FC-71, HFE7100 and R134a flow boiling in microchannel at T_{wall} less than 85 ℃. Flow boiling heat transfer of HFE7100 in straight microchannels could dissipate 2.78 MW/m^2 with 7.4 kPa pressure drop [60], where HFE7100 impinging cooling on a smooth surface achieved 69 W/cm^2 with 210 kPa pressure loss [51]. A hybrid cooling method with impingement on microchannels, could increase heat dissipation rate to 2.86 MW/m^2 with 16.7 kPa pressure loss [53]. Therefore, refrigerants flow boiling in microchannel is a promising method to cool electronic devices and fuel cells.

1.4-Enhancement methods for flow boiling in microchannel

Despite the mentioned advantages, flow boiling in microchannels still poses some challenges in applications such as high pressure drop, deterioration of heat transfer capability along flow direction and severe flow instability [55,64]. Additionally, the thermophysical properties of refrigerants such as FC72, R134a and R234fa are smaller than those of water. Therefore, it is necessary to take measurements to enhance refrigerant flow boiling heat transfer performance.

In order to suppress severe flow instability and further increase heat transfer performance in microchannels, different methods have been presented and experimentally investigated in the literature. These include improving thermophysical properties of coolants (e.g., nanofluid and EPCM slurry), modifying the surface morphology (e.g., surface coating and porous structures) and altering the channel structures (e.g., diverging cross-sections, pin fins and interconnected channel nets) [64,65,66]. Functional fluids also can be combined utilized with the surface and geometric modifications in practical applications.

Figure.6 presents the thermal conductivity and specific heat capacity of various representative fluids and nanoparticles as reported in the literature. It is evident that refrigerants exhibit low thermal conductivity compared to the metals, metallic oxides and carbon nanotubes. Figure.7 shows the enhancement of thermal conductivity by adding nanosize Al_2O_3 and CNT particles into water. It is clear that the thermal conductivity of coolant could be linearly increased with the increase of concentration. Moreover, the extent of thermal conductivity is influenced by

the nanoparticle sizes. The larger thermal conductivity and smaller sizes of nanoparticles, the more thermal conductivity enhancement of nanofluids.

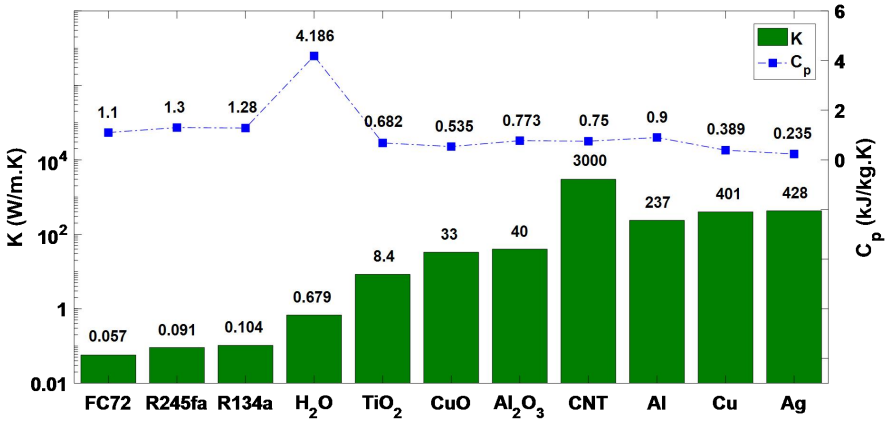


Figure.6 Thermal conductivity and specific heat capacity of fluids and nanoparticles [67,68,69,44,70]

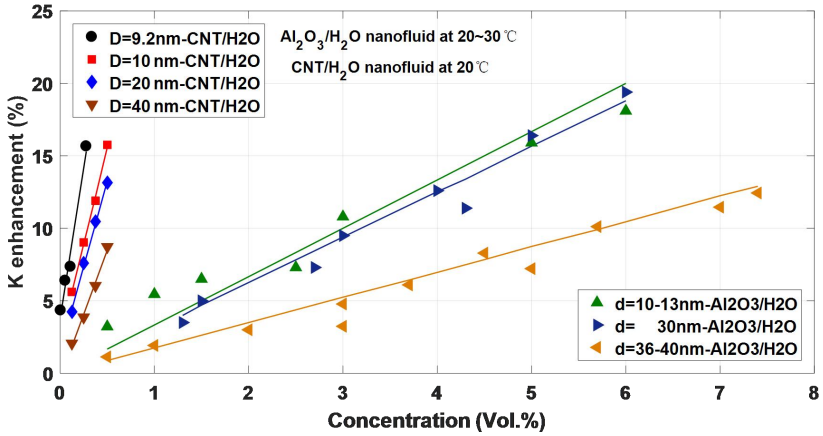


Figure.7 Thermal conductivity enhancement by adding Al_2O_3 and CNT nanoparticles (Al_2O_3/H_2O: 10-13nm [71,72], 30nm [72,73], 36-40nm [74,75,76]; CNT/H_2O: 9.2nm [77], 10~40nm [78])

Table.5 presents the enhancement of heat transfer coefficient (HTC) in the convective flow of single-phase Al_2O_3/H_2O nanofluid in microchannels [79-83]. It reveals that the addition of Al_2O_3 nanoparticles at low concentrations can enhance the HTCs by up to 70% compared to water in microchannels.

Table.5 HTC enhancement of water-Al_2O_3 nanofluid single phase convection in microchannel

Year	D_{in}	W×L	L	Size	φ_{Al2O3}	T_{in}	Re_{max}	HTC enhancement
/	μm	μm×μm	cm	nm	/	℃	/	%
2014 [79]	/	500×800	50	13	0.25%vol.	/	989	18.0
2013 [80]	500	/	120	20	0.77%vol.	18.0	2000	10.6
2014 [81]	/	400×560	50	20	1.0 %vol.	24.5	2000	49.0

2009 [82]	/	50×50	15	170	1.8 %vol.	21.0	300	32.0
2010 [83]	/	283×800	50	33	2.0 %vol.	32.6	1676	70.0

However, the effect of nanofluids on flow boiling in microchannels is inconsistent and even contradictory [84]. The heat transfer performance could either be enhanced [85,86,87] or weakened [88,89,90], depending on the nanoparticle concentrations and operating conditions [91]. For example, Xu et al. [86] indicated that the flow boiling HTC of Al_2O_3/H_2O nanofluid was enhanced due to local dryout inhibition and area enlargement of liquid film evaporation. However, Lee and Mudawar [88] pointed out that the Al_2O_3/H_2O nanofluid was unsuitable for flow boiling in microchannels due to a high risk of the disastrous failure by nanoparticle deposition on surfaces. Chehade et al. [87] showed that the HTC of Ag/H_2O nanofluid was enhanced by 162% at low concentrations, but with the enhancement decreased dramatically at high vapor qualities. Henderson et al. [92] found that the HTC of R134a/SiO_2 nanofluid was decreased by 55% compared with that of R134a. However, the HTC of R134a/POE/CuO nanofluid could be improved by 76% compared to that of R134a/POE mixture.

The phase change emulsion (PCE) and nano-size encapsulated phase change material slurries (PCMs) are also utilized to improve the single-phase convective heat transfer performance. It is found that the local Nusselt number of phase-change emulsion (e.g., n-hexadecane/water, 20%wt) was about 2.3-3.2 times that of water at the same operating conditions [93]. However, few studies were carried out on flow boiling heat transfer of PCE or EPCMs in microchannel. The main obstacles include the risk of liquid leakage and low thermal conductivity of PCM (less than 0.4 W/(m·K)) [94,95]. Recently, different materials and manufacturing methods have been investigated to improve the effective thermal conductivity of EPCM particles, as physical properties of EPCM particles mainly depend on the core/shell materials and particle sizes [96]. Taking n-octadecane as an example, it could be encapsulated with materials such as poly (ethyl methacrylate) and the metal-plated organic composite materials [97,98,99]. In those cases, thermal conductivity and the melting latent heat of particles are in ranges of 0.25-1.35W/(m·K) and 208.7-107.9kJ/kg respectively, compared to that of pure n-octadecane with 0.146 W/(m·K) and 227 kJ/kg, correspondingly.

Therefore, flow boiling of refrigerant-based functional fluid (e.g., nanofluid and PCM slurries) in microchannels represents a possible and promising approach to improve cooling capacity for thermal management of electronic components and fuel cells in the future.

Comparing to pure refrigerants, the zeotropic mixture such as R123a/R245fa and NH_3/H_2O, could better match the operating temperature with surface profiles due to the non-isothermal phase-change feature [100]. Furthermore, it can also delay serious dryout at high heat fluxes and significantly increase the critical heat flux (CHF) in microchannels [101,102]. Guo et al. [103] found that the R134a/R245fa mixture in a horizontal tube had lower pressure drop and higher HTC than pure R245fa. Dang et al. [104,105] conducted experimental studies on the R134a/R245fa mixture flow boiling in a rectangular microchannel. It had smaller HTCs than pure fluids, but could delay dryout at high heat fluxes and significantly increase the CHF.

The NH_3/H_2O mixture has been widely used as a working fluid in refrigeration systems for decades. According to Table.2, the evaporating latent heat of NH_3/H_2O mixture is larger than pure refrigerants. At a concentration of 20% by mass and a saturated temperature of 50℃, the NH_3/H_2O mixture has an evaporating latent heat of 1689 kJ/kg, which is higher than that of the R134a/R245fa mixture (167 kJ/kg) and the R123/R134a mixture (167 kJ/kg). However, most experimental studies in the literature are conducted in large-scale sinks and the heat transfer empirical correlations are not applicable to predict flow boiling heat transfer performance of the NH_3/H_2O mixture in microchannels. This is due to the difference in bubble dynamics and flow patterns [106]. Kærn et al. [100] evaluated flow boiling heat transfer correlations for the macro-scale NH_3/H_2O heat exchanger design, including two flow boiling correlations and three correlations modified based on pool boiling correlations. Taboas et al. [107,108] studied NH_3/H_2O flow boiling in a vertical plate heat exchanger with a hydraulic diameter of 4 mm. Arima et al. [109,110] investigated its performance in a vertical plate evaporator with a gap size of 2 mm. Bor et al. [111] found that the HTC of NH_3/H_2O in a single channel annulus with a hydraulic diameter of 0.4 mm increased with inlet vapor quality, mass and heat fluxes. Additionally, there are only a few numerical performance studies on NH_3/H_2O flow boiling in microchannels available in the literature.

In conclusion, the present study has identified flow boiling in microchannels as a promising thermal management solution for electronic devices and fuel cells, utilizing refrigerant-based

functional fluids such as R134a or the NH_3/H_2O mixture based nanofluid and PCM slurries. Additionally, numerical simulation is selected to evaluate the heat transfer performance of multiphase flow in microchannels.

1.5-Aims and objectives

The primary aim of this study is to advance the understanding of heat transfer during the flow boiling of functional fluids in microchannels, to investigate the impacts of coolant properties and the key parameters on heat transfer performance, and to explore effective approaches for enhancing thermal management in cooling electronic components and fuel cells in the future. The specific aims and objectives of this research are outlined as follows:

Chapter 1: Background

- **Objectives:** Briefly introduce the background and main challenges in thermal management for cooling the advanced electronic devices and fuel cells, as well as present the dominant restrictive conditions that govern the choice of cooling methods (i.e., the maximum tolerable temperature and temperature gradient on heated surfaces). Conduct a comparative analysis of the heat dissipation capacities of some available cooling approaches under those mentioned constraints. Present the core subjects of enhancing the heat transfer and set the context for the following chapters by highlighting the need for investigation and proper treatments.

Chapter 2: Literature review

- **Objectives:** Systematically summarize the latest research on the heat transfer theories, heat transfer characteristics, and prediction models of flow boiling heat transfer in microchannels. Conduct a comparative analysis of the primary factors affecting the heat transfer performance, identify the potentials, key trends and research methodologies of the promising enhancement approaches. Evaluate numerical models and computational approaches adopted for predicting flow boiling heat transfer performance in microchannels. Outline methods and approaches for the heat transfer enhancement, specifying the key parameters, evaluation criteria and research topics, as well as the numerical simulation models and computational approaches employed in the present work.

Chapter 3: Simulation methods for multiphase flow heat transfer

• **Objectives:** Briefly explain the computational models and simulation methods employed in this study to analyze transit subcooled multiphase flow and heat transfer in microchannels. It encompasses the mathematical models describing thermodynamic and transport properties of functional fluids, the mass and heat transfer models within multiphase interfaces (i.e., liquid boiling and solid melting), the initial and boundary conditions, and the specific computational methods utilized in each chapter.

Chapter 4: Flow boiling heat transfer of water with a PCM particle

• **Aim:** Explore the key factors and their impacts on the heat transfer performance between a melting and moving particle with the neighbor fluid and heated walls in this intricate physical process. Provide a reference for the subsequent analysis of functional fluids in microchannels.

• **Objectives:** Briefly introduce the research content, specify the assumptions and simulation treatment in this chapter, conduct the grid independence and the model validation. Investigate the effect of a PCM particle melting and moving on heat transfer performance of subcooled water flow boiling in a vertical microchannel. Reveal the effects of surface wettability and the particle density on the transient heat transfer performance and analyze the interactions between the particle and the surrounding fluid at different flow boiling patterns. Evaluate the mentioned methods and identify the key parameters for the subsequent investigation.

Chapter 5: Flow boiling heat transfer of R134a based functional fluid

• **Aim:** Conduct a parametric sensitivity analysis to understand the thermal properties effects of functional particles on the heat transfer performance of pure R134a in microchannels.

• **Objectives:** Provide a brief introduction to the research content, outline the assumptions and methodologies, perform the grid independence assessment and validate the calculating model. Investigate heat transfer performance of R134a-based functional fluids flow boiling in a horizontal microchannel. Explore the impacts of the functional particle properties such as thermal conductivity and the melting latent heat of PCM particles, as well as key parameters on heat transfer performance. Reveal the mechanisms responsible for enhancing flow boiling heat transfer performance of functional fluids by conducting an analysis of the heat transfer performance and the corresponding flow fields.

Chapter 6: Flow boiling heat transfer of the NH_3/H_2O mixture

• **Aim:** Evaluate the heat dissipation capacity and investigate the mechanisms of flow boiling heat transfer of the NH_3/H_2O mixture in microchannels, aiming to cool electronic devices and fuel cells.

• **Objectives:** Propose a modified VOF-LEE model and a corresponding simulation approach suitable for predicting the non-isothermal flow boiling heat transfer performance of zeotropic mixtures based on the theoretical analysis and reasonable simplifications. Conduct the grid independence assessment and the simulation model validation. Investigate the effects of the main thermal parameters such as inlet mass flux, inlet NH_3 concentration and heating wall temperature on the heat transfer performance and flow patterns of the NH_3/H_2O mixture flow boiling in microchannels. Evaluate the characteristics and potential of the NH_3/H_2O mixture for cooling electronic devices and fuel cells.

Chapter 7: Flow boiling heat transfer of the NH_3/H_2O/PCM slurries

• **Aim:** Explore the intricate behavior of multiphase flow heat transfer of the NH_3/H_2O/PCM slurries in microchannels and analyze their influence on enhancing heat transfer performance.

• **Objectives:** Explain those assumptions and simplification of adopted mathematical models and computational methods. Evaluate the heat transfer performance and the influence of the suspended PCM particles properties (e.g., the melting temperature and the melting latent heat) on heat transfer performance of the NH_3/H_2O mixture flow boiling under different conditions. Analyze the mechanism of interactions and mutual influences among different phases during the transient subcooled flow boiling process in microchannels. Assess benefits and challenges of enhanced heat transfer performance by adding PCM particles into the NH_3/H_2O mixture.

Chapter 8: Conclusion and future work

• **Objectives:** Summarize the main contributions and outcomes of simulation work focusing on enhancing heat transfer performance of various fluids flow boiling in microchannels for cooling electronic devices. Discuss the implications of the findings for the actual applications and advanced thermal management in the future. Propose potential areas and suggestions for future research, focusing on the experimental test and refined numerical simulation study.

Chapter-2 Literature review

2.1-Introduction

In this chapter, recent studies on flow boiling heat transfer performance in microchannels of pure refrigerants, the zeotropic mixture and functional fluids are reviewed, individually.

2.2-Flow boiling heat transfer in microchannels

2.2.1-General heat transfer performance

Flow boiling heat transfer is sensitive to various parameters, such as the physical properties of coolants, the geometrical shapes and dimensions of sinks, as well as operational conditions like inlet mass fluxes, degree of subcooling and heat fluxes, among others.

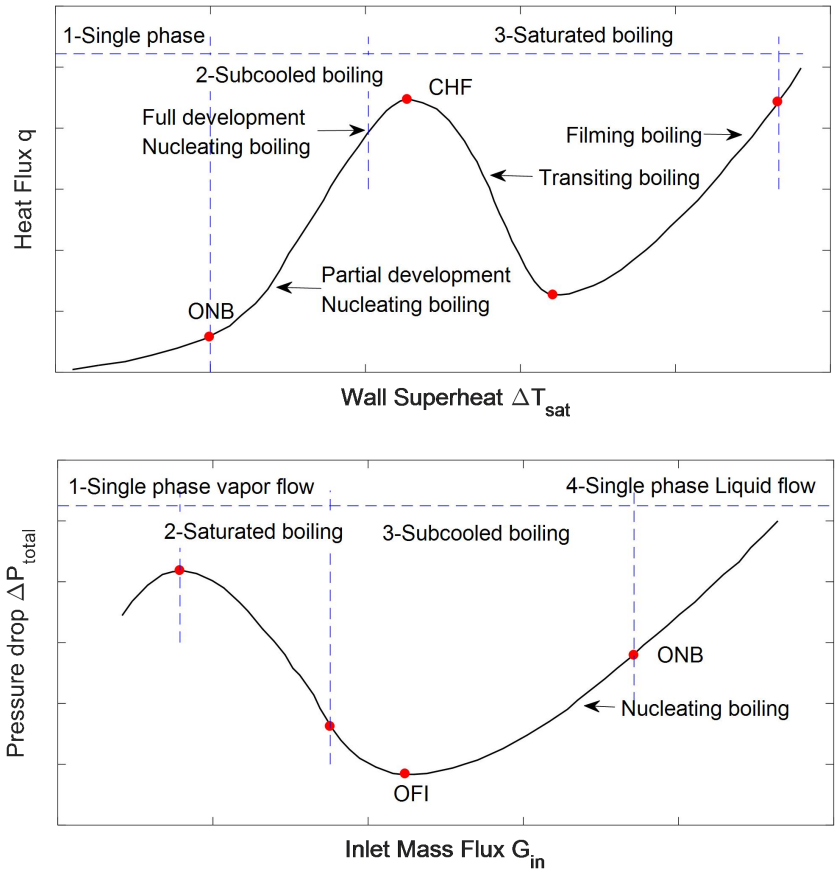


Figure.8 Relation of heat flux [112] and pressure drop curve in boiling heat transfer [113]

Traditional boiling curves of heat flux and pressure drop are shown in Figure.8. Once boiling phenomenon is triggered at onset of nucleating boiling (ONB) position, heat flux is improved significantly with continuously increasing of wall temperature at the same mass flux, leading

to the intense nucleate boiling processes. Owing to fast bubbles generations and insufficient liquid rewetting to surfaces, some large-size vapors will appear and give rise to decrease local heat transfer capability. Critical heat flux (CHF) is considered as a safety thread for boiling, after which heat flux begins to decrease sharply. Further increasing heating temperature, flow boiling will be changed to transiting pattern in which pressure becomes unstable [112]. The onset of flow instability (OFI) is another important criterion in safety applications. Pressure drop fluctuation could be exacerbated severely and trigger devastating damages to devices. The OFI is at the minimum point of pressure drops versus mass fluxes in macrochannels at the constant inlet temperature and heating fluxes [113].

The heat transfer curves for subcooled flow boiling in microchannels differ from traditional cases. For instance, Figure.9 illustrates M-shaped curves that show the relationship between heat transfer coefficients (HTCs) and vapor quality [114,115]. Vapor quality is defined as the mass ratio of saturated vapor in a two-phase mixture. For saturated flow boiling in Figure.10, it ranges from 0 to 1, where 0 represents a saturated liquid state and 1 represents a saturated vapor state. In subcooled flow boiling in Figure.9, the evaporation occurs in the liquid phase before reaching its boiling point. When the liquid starts to boil, the vapor is generated near the heat surfaced but rapidly condenses back into the liquid due to the lower temperature of surroundings. In this case, the value of a factor (X), which has the same formula of the vapor quality (x) is negative in order to differentiate it from the saturated liquid in Figure.9.

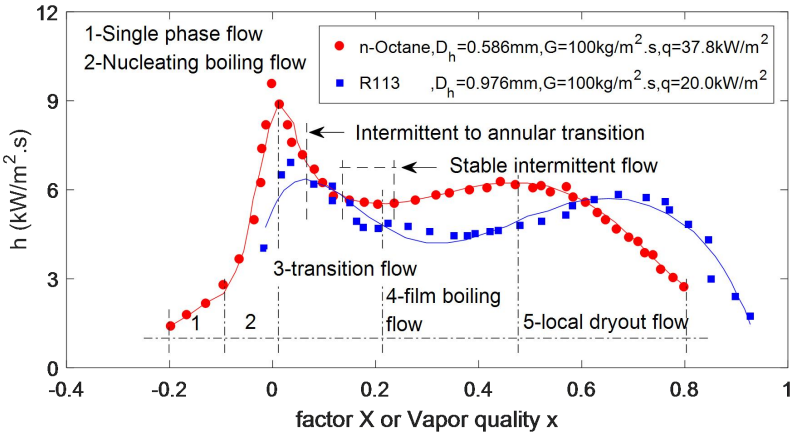


Figure.9 M-shape curve of flow boiling heat transfer in microchannels [114,115]

In a M-shape curve, there are two HTC polar points. The first point is at the transition from bubbly flow to intermittent flow, and the second point is at the turning point from moderate

to filming flow before local dryout. For example, the first polar of heat transfer coefficient (HTC) is found to be the maximum value for Octane or R113 in Figure.9, while the second polar is associated with the largest HTC for H_2O [116]. The research also noted that the flow boiling HTC of water in microchannels is degraded due to severe instability at high heat flux.

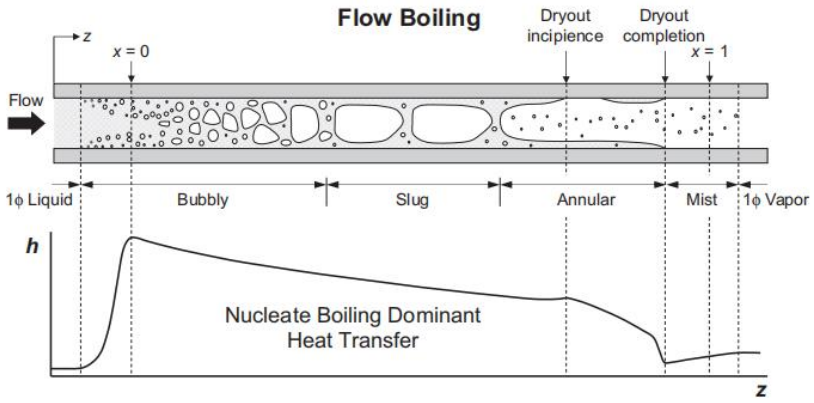


Figure.10 Local flow boiling HTC and bubbles transition at a constant heat flux [117]

The relation between the local HTC and flow patterns in a microchannel under constant heat flux was explained by Kim and Lee [117]. Firstly, the nucleation begins along the walls near the inlet, leading to the formation of small bubbles. As the evaporation continues, the bubbles increase in size and number, resulting in a bubbly flow. These bubbles then coalesce into the oblong shapes and trigger a transition to churn flow. Finally, the annular flow is formed when the elongated bubbles merge to create a continuous vapor with a thin liquid film near surfaces. It is also discovered that the location of the highest local HTC is influenced by the positions where the bubbles form [118]. Additionally, the diameters of the departing bubbles decrease as the mass flux increases [119]. The maximum HTC occurs near the onset of nucleation at the entrance, which differs from flow boiling in macrochannels shown in Figure.11 [120].

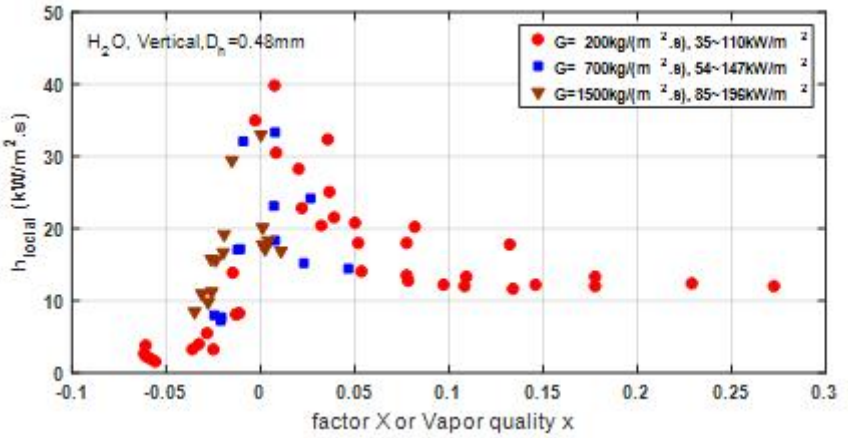


Figure.11 Relations of local HTCs with vapor quality in different mass and heat fluxes [120]

Qu and Mudawar [121] assessed eight classical flow boiling empirical correlations and found those correlations did not accurately predict trends with experimental data. This was attributed to the unique nature of flow boiling in microchannels and the actual conditions falling outside the ranges of the correlations. Additionally, the geometrical parameters such as aspect ratio, structures and surface textures of microchannels were identified as important factors in the heat transfer performance in microchannels. For instance, Markal and Aydin [122] experimentally investigated the effect of channel aspect ratio on water flow boiling in microchannels, while maintaining the same hydraulic diameter of 0.1mm. The results showed that the HTC increased with the aspect ratio up to 3.54, and then decreased at higher aspect ratios. The pressure drop increased with the heat flux due to the rise in evaporation momentum force, but no regular relations with the aspect ratio were observed.

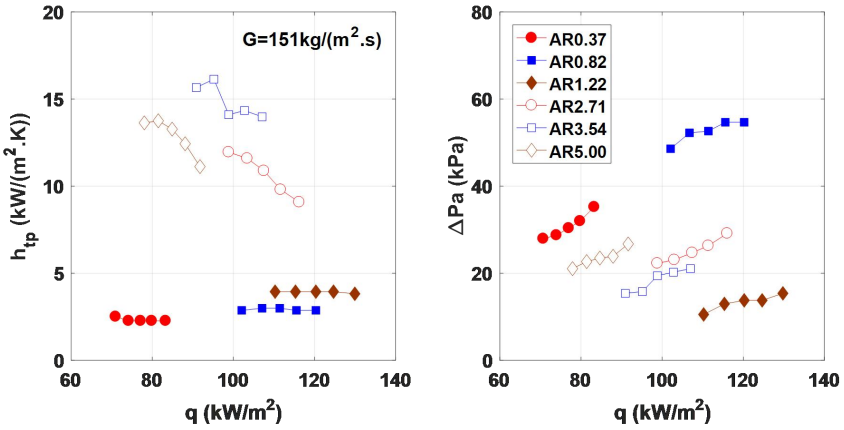


Figure.12 Channel aspect ratio effect of microchannels on flow boiling HTC and pressure drops [122]

Table.6 presents the main experimental data on water flow boiling heat transfer in rectangular microchannels. In this table, N_c, N_{hs}, and O denote the numbers of channels, heated surfaces, and the flow direction orientation, respectively.

Table.6 Experimental researches of water flow boiling heat transfer in microchannel

Ref	Microchannel		W×D×L	T_{in}	G	Q_{max}	h
/	Nc/Nhs/O/material		mm	℃	kg/(m^2. s)	kW/m^2	kW/(m^2.K)
2016 [118]	1/3/H	silicon	2.54×0.42×25.4	86	182/380	320	0-45
2017 [119]	1/1/H	silicon	5.01×0.52×80.0	90	200-400	250	0-15
2007 [120]	1/3/V	copper	0.807×0.346×330	40~50	200-1500	200	0-70

2012 [123]	1/3/H	copper	0.241×0.198×21.9	46~49	340-1297	2197	0-400
2016 [122]	29/3/H	copper	D_h=0.1, AR=0.37~5.0	50	151-324	131	0-20

In conclusion, there are four key parameters that characterize the performance of boiling heat transfer. These parameters include the superheat for the onset of nucleation boiling (ΔT_{ONB}), the heat transfer coefficient (HTC), the critical heat flux (CHF) and the related superheat (ΔT_{CHF}). Therefore, the main guideline for improving the heat transfer performance is to induce the onset of nucleation boiling at low heat flux cases, delay the CHF at high heat flux cases and promote overall and local heat transfer coefficients [124].

2.2.2-Flow boiling instability

According to the discussion in Chapter 1, refrigerants such as R134a, FC-72 and HFE7100 are chosen as potential coolants for cooling electronic devices and fuel cells. This is mainly due to the dielectric properties, chemical stability, electrical inertness and the saturation temperature below 85℃. The dielectric properties of coolants play a crucial role in the cooling of electronic components, as they directly affect the cooling efficiency, lifespan and safety under high loads and in complex environments. For example, Saums et al. [125] compared different pumped-supply cooling techniques for semiconductors in electric vehicles and found that the heat dissipation rate of R134a flow boiling was 96% and 125% greater than that of single-phase water and air cooling, respectively. Madhour et al. [126] studied R134a flow boiling heat transfer in microchannels for cooling the microelectronic CPUs and indicated that the local HTC could reach up to 270 kW/(m^2·K) with a maximum pressure drop of 94 kPa at 188 W/cm^2 and 1000 kg/(m^2·s) to keep the microchip under 85℃.

However, there are still some shortcomings that need to be addressed in practical applications, especially in cases of high-level heat dissipation where flow boiling instability might occur. The instability can lead to high pressure drop and severe deterioration of heat transfer capability along the direction. For pure refrigerants, they have problems in high-level heat application due to poor thermophysical properties such as small thermal conductivity, latent heat and high wettability feature [127,128]. Compared to water, refrigerants have super-wettability properties with small contact angles (e.g., 0°of FC72 and 62°of H_2O [129], 8°of R134a on copper surfaces [130]). Small contact angles could make fluids deep penetration

into surface cavities, leading to high surface superheat for nucleation. For example, You et al. [130] measured the superheat degrees of FC72 on different surfaces (e.g. Pt, SiO_2, and Al_2O_3) and found that the superheat was 18-51 C° at the incipient nucleation stage. Once the bubble nucleation occurs, the excessive superheat quickly dissipates, leading to the acute boiling process. Therefore, flow instability is a serious problem that needs to be effectively resolved as it can lead to severe fluctuations in pressure and temperature and even devastating dry out. The details of flow boiling instability are presented in Figure.13.

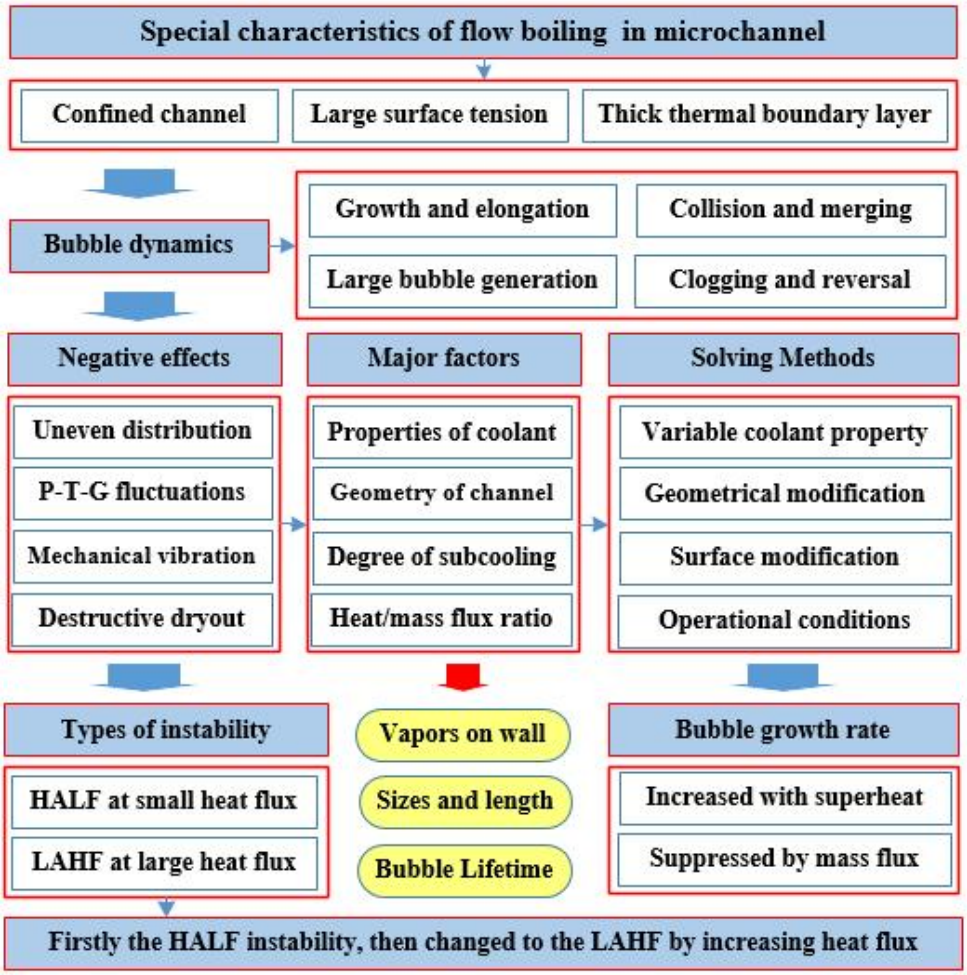


Figure.13 Logic relations of flow boiling instability in microchannel and available treatments

Flow instability is more pronounced in microchannels compared to macrochannels, primarily due to the combined effects of the strong surface tension forces and thick thermal boundary layers in confined channels [55]. The primary reason is an amount of vapor generated on the heated surfaces, which then moves into the channel domain. This leads to rapid growth and elongation of bubbles, bubble collision and merging, clogging and flow reversal at the inlet.

Several factors affect the extent of instability, including physical properties of coolants, the geometric parameters, microchannel structures, inlet subcooling and the heat/mass flux ratio.

Wang and Cheng [131] investigated the stability of subcooled water flow boiling in a microchannel. The unstable flow boiling occurred when the exit vapor quality was larger than 0.013. Lee and Liu [65] found that inlet orifices and expanding channels could alleviated the flow instability in microchannels. Edel and Mukherjee [132] found that the bubble growth rate increased with an increase in superheat and this growth was restrained by increasing the mass flux before the clogging process occurred.

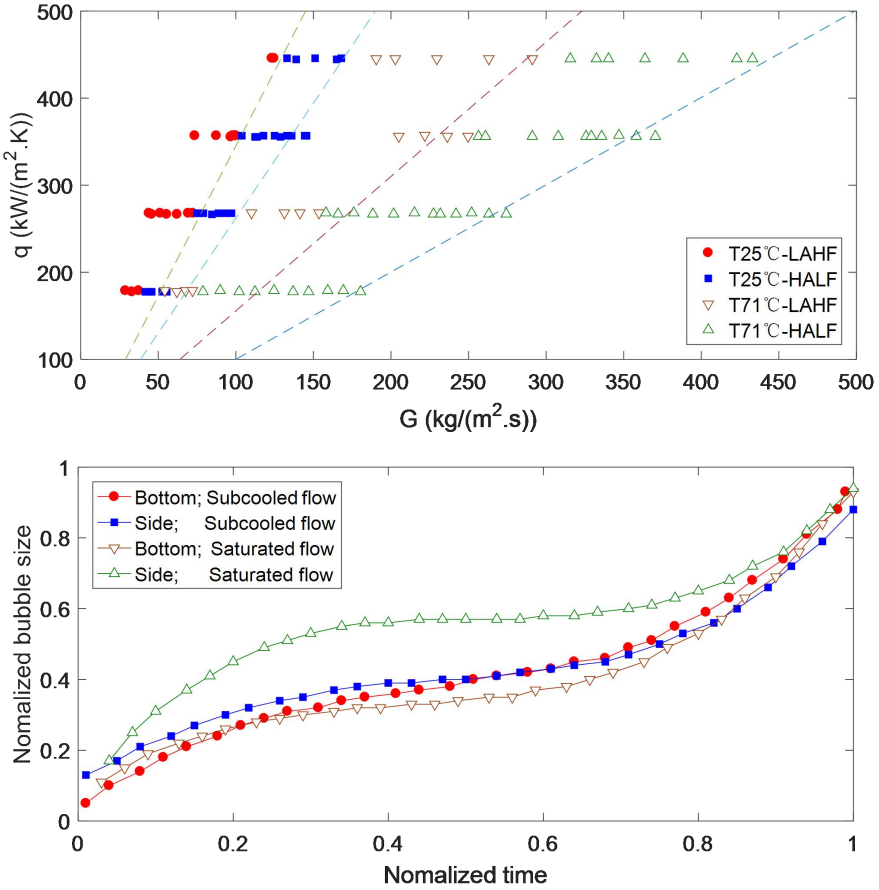


Figure.14 Inlet temperature effect on flow instability and three stages of bubble growth [133]

Bogojevic et al. [134] observed two types of instabilities in their study: the high-amplitude and low-frequency (HALF), as well as the low-amplitude and high-frequency (LAHF). These instabilities were found to be dependent on the heat/mass flux ratio and inlet temperature. In the HALF case, the frequency decreased with increasing heat fluxes or decreasing inlet mass fluxes, while a low inlet temperature resulted in high magnitudes of temperature fluctuations.

They also investigated instabilities under non-uniform hotspot cases [135] and found that at low heat fluxes, the fluctuation was HALF, which then changed to lower amplitude and higher frequency (LAHF) as the heat fluxes increased. In the HALF case, the fluctuation of the wall temperature was primarily driven by the oscillation of inlet mass flux. Additionally, it was observed that there are three stages of bubble growth: rapid growth, stagnation and accelerated growth [133]. As the bubble growth rate slows down and the bubble lifetime lengthens, the amplitude of fluctuations increases and the frequency decreases.

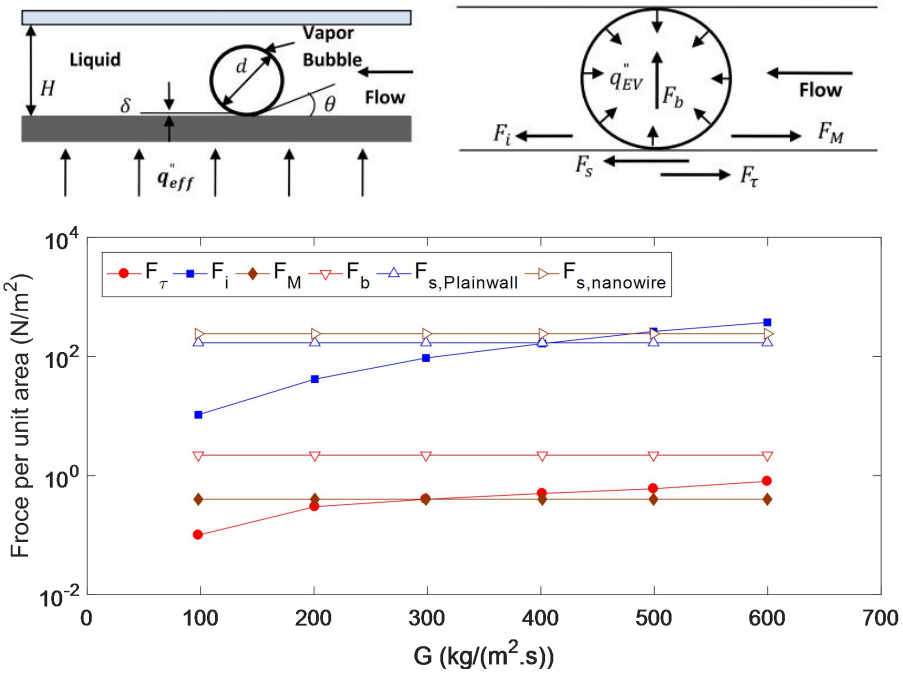


Figure.15 Types of wall-liquid-bubble forces on bubbles in flow boiling in microchannels [136] (F_b- buoyancy F; F_i- inertia F; F_M- evaporation momentum F; F_s- surface tension F; F_τ- shear F)

The wettability of heating surfaces has a significant effect on the flow instability. Alam et al. [136] investigated the effects of contact angles (e.g., 45.13° and 10.21°) on flow boiling in microchannels, respectively. It revealed that surface tension dominated the behavior at small to moderate mass flux, while the inertia force became the governing factor at high mass flux cases. Moreover, it was found that a nanowire surface with a smaller contact angle of 10.21° enhanced the critical heat flux due to higher surface tension force at the liquid-vapor interface. The main geometric parameters of microchannels and the experimental conditions are listed in Table.7.

Table.7 Experimental studies on the flow instability in microchannels

Year	Ref	Channel	material	D	W×D×L	T_{in}	G	Q

/	/	/	/	mm	mm	℃	Kg/m^2.s	kW/m^2
2010	[65]	48/H-Rec	silicon	0.353	0.235×0.710×20	70-95	25-114	60-380
2011	[132]	1/H-Rec	Brass	/	0.201×0.266×25	64/80/98	122/200	36-228
2013	[133,134]	40/H-Rec	silicon	0.194	0.15×0.273×15	25/71	42-433	138-537
2016	[136]	5/H-Rec	silicon	0.234	0.22×0.25×10	/	100-600	~3500

In general, several principal methods were studied experimentally to mitigate the instability and enhance the heat transfer capability of flow boiling in microchannels. These include the modification of coolant properties, the structures and geometric parameters of sinks and the heated surface morphology.

2.2.3-Geometrical modification of channels

In this part, some representative experimental investigations on the geometrical modification methods to ease flow instability in microchannel were analyzed and compared systematically. The general relations of basic principles and methods are listed in Figure.16.

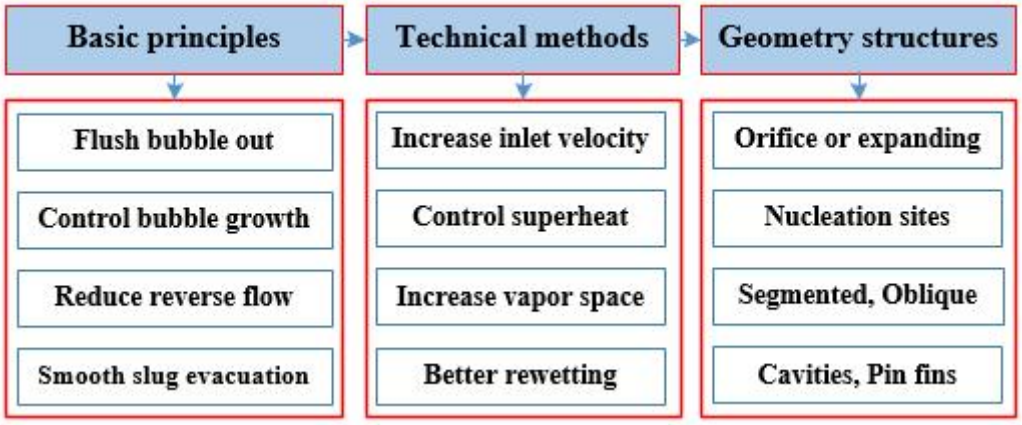


Figure.16 Logic relations of Geometrical modification to ease flow instability in microchannel

As discussed before, the primary strategies for addressing flow instability in microchannels involve the effective control and regulation of bubble generation in proximity to the heated surfaces, as well as the management of their dynamic evolution within the domain.

In general, the principles and treatments of alleviating flow instability are summarized in Figure.16, which include the following:

1. Flush large-size bubbles out of channels quickly before they block the domain (e.g., using inlet orifices to increase inlet velocity).

2. Control bubble growth rates to suppress confined bubbles in domain (e.g., increasing inlet subcooling, controlling surface superheat, and coating nano-size cavities on the surfaces to regulate nucleation sites).
3. Reduce reverse flow (e.g., using expanding channels to increase space for large bubbles near the exit and employing oblique fins to break bubbles into smaller pieces).
4. Smooth slug evacuation (e.g., expanding the downstream channel and applying rewetting surfaces to ensure thin liquid layers exiting between surfaces and slug/annular bubbles).

The main parameters of some experimental cases on H_2O flow instability in microchannel are listed in Table.8. The detailed results and main findings were introduced as follows.

Table.8 Some experimental investigations on the geometrical modification for flow instability

Ref	Shape/ Material	D	W×D×L	T_{in}	G	Q
		mm	mm	℃	$Kg/m^2.s$	kW/m^2
2007 [137]	Trap/Si	0.186	—×0.146×30	35	38.6-162	227-498
2008 [138]	Trap/Si	0.186	—×0.146×30	35	91-787	184-486
2011 [139]	Div/Si	0.120	—×—×26	28-48	99-297	0-500
2011 [140]	Expand/SS	/	0.3×1.153×25	90	100-133	0-1400
2013 [141]	Rec/Al	/	0.1×0.1×10	/	283-2370	/
2014 [142]	Rec/Si	/	0.22×0.25×10	40	160-404	500-6000
2015 [143]	Div/Cu	0.522	—×0.75×25.7	30	100-350	10-350
2015 [144]	Reen Ω/Cu	0.776	—×—×45	60/90	200/300	0-550
2016 [145]	Inter/Cu	0.400	—×—×45	30/60/90	100-250	100-900
2017 [146]	Inter Ω/copper	0.781	/	60,90	125-300	0-900
2017 [147]	Micro pin/copper	0.4(0.6) ×0.5(1.5)		90	500	83-593

Wang et al. [137] discovered that the isolated bubbles were pushed away by the incoming liquid in a stable state. They also observed that the amplitudes of pressures and temperatures in Type-B were smaller than those in Type-A, and no fluctuations were observed in Type-C under the same condition [138]. Szczukiewicz et al. [141] demonstrated that significant

temperature and pressure fluctuations were observed without any inlet restrictions. However, the utilization of inlet restrictions effectively prevented the fluctuations in Figure.17.

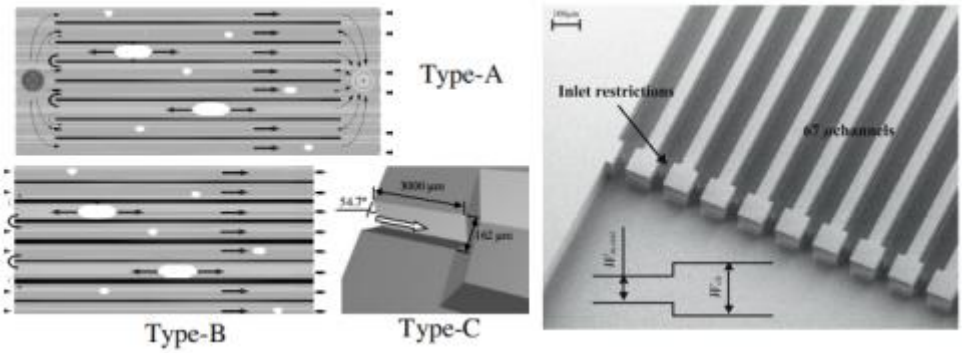


Figure.17 Geometry structures of microchannels with and without inlet restrictions [138,141]

Lu et al. [139] discovered that the hybrid effects of the artificial nucleation sites and diverging microchannels could reduce the wall superheat and also enhance the heat transfer performance. Balasubramanian et al. [140] found that the expanding channels exhibited lower pressure drop and higher heat transfer coefficients compared to straight channels. Prajapati et al. [143] found that the segmented channels demonstrated a higher HTC compared to other channel geometries. Although there was a slight increase in the pressure drop, the segmented channels could completely alleviate bubble clogging.

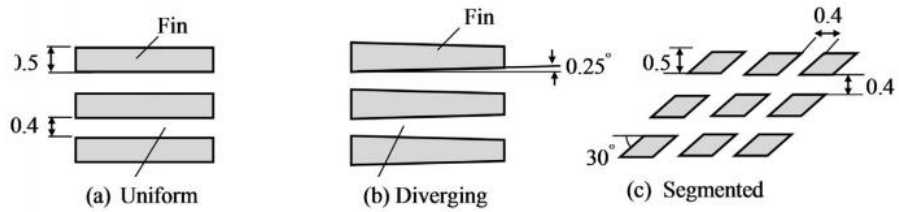


Figure.18 Geometry structures of microchannels with different constructions [143]

Yang et al. [142] found that the heat transfer coefficient and critical heat flux of inlet restricted nanowire microchannels were enhanced by up to 326% and 317% respectively, compared to those of the plain-wall microchannels. This was attributed to promoted nucleate boiling, induced film renewal, and improved film evaporation in Figure.19.

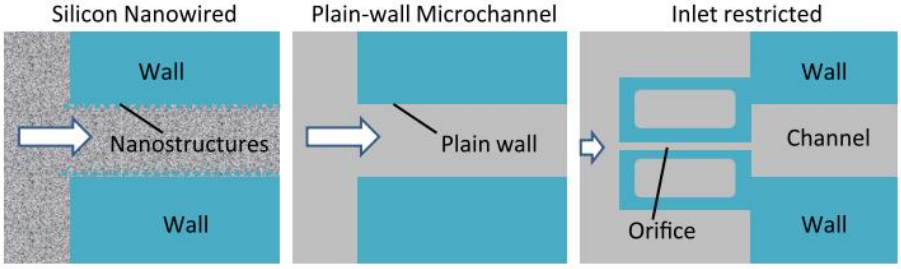


Figure.19 Structure diagram of microchannels with different constructions [142]

Deng et al. [144] found that the HTC enhancement of flow boiling in the Ω-shaped reentrant microchannels was up to 70% in large subcooling and moderate at high heat fluxes, while the pressure drop was close to 40% of that in rectangular channels. They [146] also found that the flow boiling heat transfer coefficient in interconnected reentrant microchannels of semi-closed Ω and transverse shapes could be improved up to 280% by providing more flow passages and diminishing confinement effects with the addition of transverse microchannels.

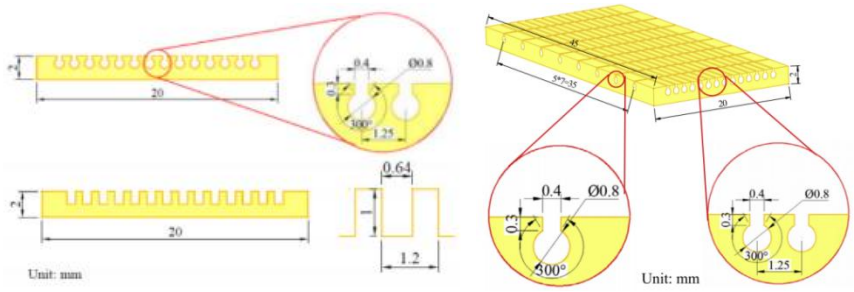


Figure.20 Structure diagram of different microchannels with the Ω-shaped cavities [144,146]

Zhang et al. [145] investigated flow boiling heat transfer in interconnected microchannel nets (IMN) and rectangular microchannels (RMC). The IMN microchannels exhibited higher heat transfer coefficient and lower pressure drop compared to the RMC at 180 kg/(m^2.s), but these trends were reversed at 250 kW/(m^2.s). However, the flow stability was compromised when the heat flux was increased to 250 kW/(m^2.s).

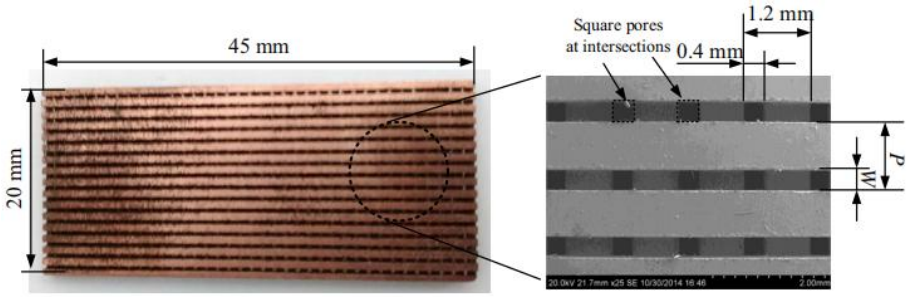


Figure.21 Structure diagram of interconnected microchannel net [145]

Wan et al. [147] compared the effects of different shapes of micro pin fins (e.g., square, circular, diamond and streamline) on flow boiling heat transfer performance. The shape of the fins did not influence the onset of bubble nucleation. However, the diamond shape resulted in the worst HTC and severe instability, whereas the square shape had the largest HTC due to its ability to hinder slugs and facilitate rewetting channels.

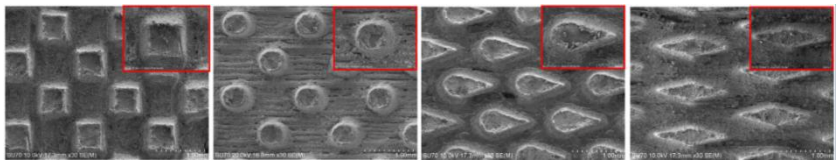
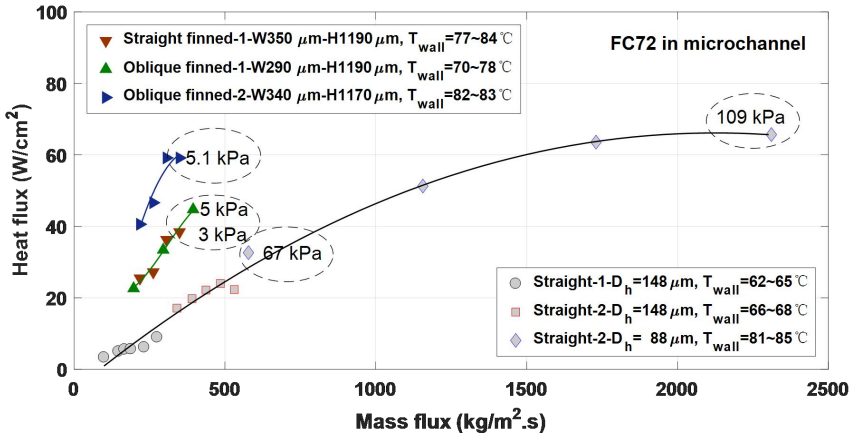
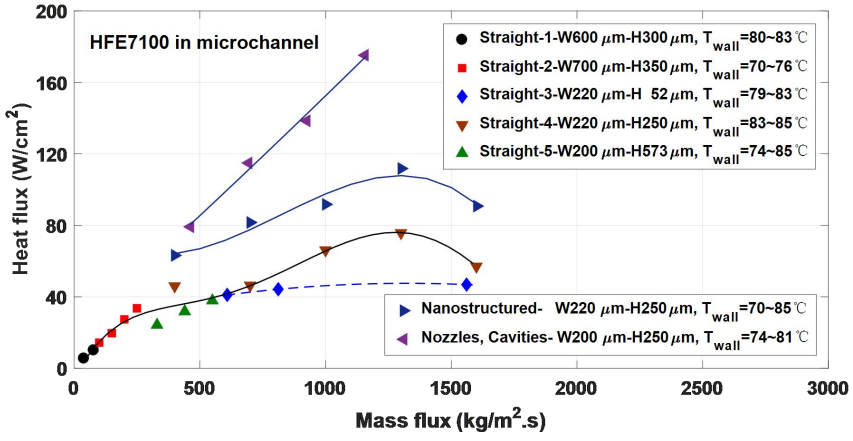


Figure.22 Structure diagram of microchannels with different shapes of pin fins [147]

Generally, the above discussions focused on the effects of channel geometry on the instability of flow boiling in microchannels. It is clear that an appropriate structure could mitigate the flow instability and enhance the heat transfer performance effectively. Figure.23 compares the effects of different structures and geometric parameters on flow boiling of refrigerants (e.g., FC72 and HFE7100) in microchannels with a wall temperature below 85℃.



(a)



(b)

Figure.23 Effects of channel structures and geometrical parameters on flow boiling in microchannel (a) FC-72 [148,57,58,149], (b) HFE7100 [150,151,152,59,153,61]

In Figure.23(a), the heat flux of FC72 exhibits nearly linear increase with the mass flux at low conditions, but the increment becomes small and tends to approach zero at the high mass flux cases. By utilizing microchannels with finned structures, such as straight and oblique

fins, the heat flux can be significantly intensified compared to that in straight microchannels at similar mass flux and wall temperature conditions. For example, in an oblique channel, a specific inlet mass flux of 349kg/ (m^2.s) and a pressure drop of 5.1kPa are required to achieve a heat flux of 59 W/cm^2. On the other hand, a straight channel necessitates a different inlet mass flux of 2311 kg/ (m^2.s) and a higher pressure drop of 109 kPa to achieve a heat flux of 66 W/cm^2.

Similarly, the heat flux of HFE7100 in the nanostructured channels shown in Figure.23(b) is considerably higher than that in straight microchannels with the same hydraulic diameter and inlet mass flux. Furthermore, by integrating flow boiling with multiple micro-nozzles and micro-cavities, the heat flux could be enhanced up to 175.2 W/cm^2, whereas the maximum values in the straight and nanostructured microchannels are 75.8 W/cm^2 and 111.8 W/cm^2, respectively.

2.2.4-Wettablility and roughness effects

As discussed before, the surface modification could enhance the heat transfer performance in microchannels, such as to reduce the superheat at the onset of nucleate boiling (ONB) and the critical heat flux (CHF), to improve the heat transfer coefficient at low heat loads and increase the CHF at high heat fluxes, as well as to alleviate dry out and instability under extreme high heat dissipation conditions, as illustrated in Figure.24.

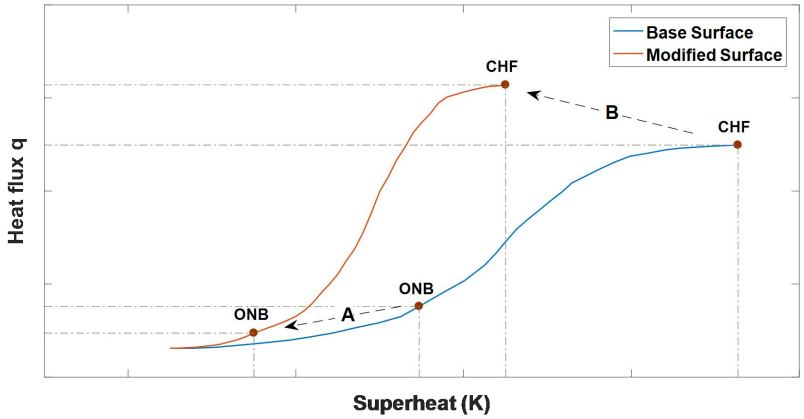


Figure.24 The main principles of surface modified treatment shown in boiling curve

The wettability represented by the solid-liquid contact angle and the surface morphology symbolized by surface roughness (Ra), are two crucial factors that can influence flow boiling in microchannels [154]. Recently, different definitions of contact angles have been proposed

for the static and dynamic situations. The equilibrium contact angle, which is the primary and widely used measure, is calculated by Young's equation under the assumption that the surface is ideally homogeneous, smooth and clean.

$$\gamma_{sv} - \gamma_{sl} = \gamma_{lv} \cdot \cos\alpha \tag{2-1}$$

Where γ_{sv}, γ_{sl} and γ_{lv} are the solid-vapor, solid-liquid and liquid-vapor interfacial tensions, respectively. α is the equilibrium contact angle shown in Figure.25.

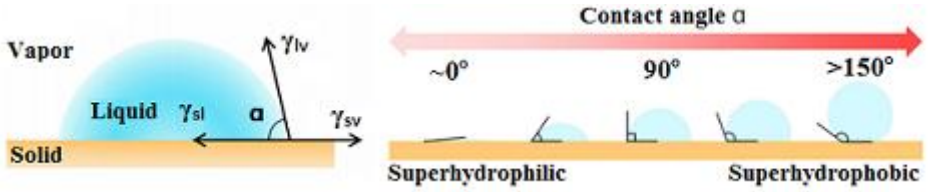


Figure.25 Illustration of contact angle and wettability classification [154]

While wettability primarily affects bubble departure diameter and frequency, as well as the liquid-wall contact area (expressed as the vapor area fraction on surfaces-x_{wall}), roughness can impact the effective heat transfer area, active nucleation sites, and capillary force on surfaces. Therefore, surface modification methods such as material coating, micro-cavities, and nano-structure treatments are expected to yield higher HTC and CHF of flow boiling compared to smooth surfaces, as illustrated in Figure.26. It is generally accepted that at low heat fluxes, the HTC can be improved by reducing wettability and roughening surfaces to decrease the ONB (Onset of Nucleate Boiling) point and increase the density of active nucleation sites on surfaces. On the other hand, increasing wettability and employing wicking structures can delay the CHF point in high heat dissipation scenarios, as they directly result in enhanced liquid affinity and rewetting on surfaces [155,156,127].

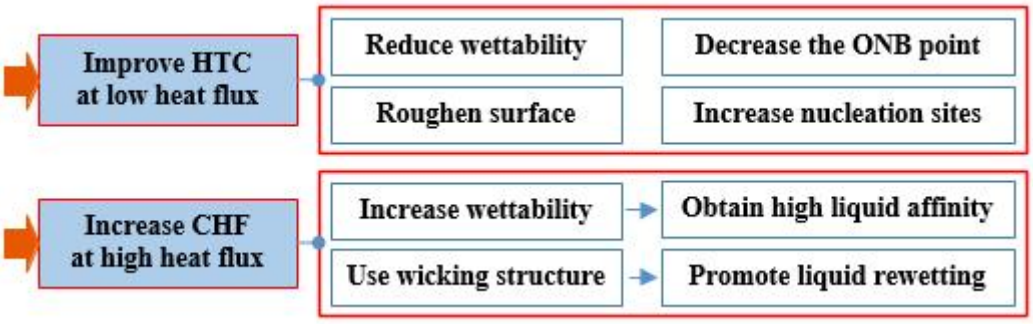


Figure.26 Surface modification methods to enhance flow boiling heat transfer performance

Surface wettability could be classified into superhydrophilic (contact angle ~0°), hydrophilic, hydrophobic and superhydrophobic (contact angle >150°) types in Figure.25. Generally, the

superhydrophilic surface could induce natural spreading to enhance capillary transport, while the superhydrophobic has merits of self-cleaning and reducing hydrodynamic drag. Hence, the superhydrophobic has features to promote bubbles attached on the surfaces and reduce the superheat for inducing nucleation boiling at low heat fluxes (i.e., decreasing the T_{ONB}). Differently, the superhydrophilic one could form a thin liquid film near hot walls till a severe evaporating phenomenon generated on surfaces (delaying the CHF point) in Figure.27.

In Figure 25, the surface wettability could be classified into four types: the superhydrophilic, hydrophilic, hydrophobic and superhydrophobic. The superhydrophilic ones could promote natural spreading and enhance capillary transport. On the other hand, the superhydrophobic surfaces have the advantage of self-cleaning and reducing hydrodynamic drag. Therefore, the superhydrophobic surfaces are beneficial for promoting bubble attachment and reducing the superheat required for nucleation boiling at low heat fluxes. In contrast, the superhydrophilic surfaces form a thin liquid film near the heated walls until a severe evaporating phenomenon occurs (thus delaying the CHF point) in Figure 27.

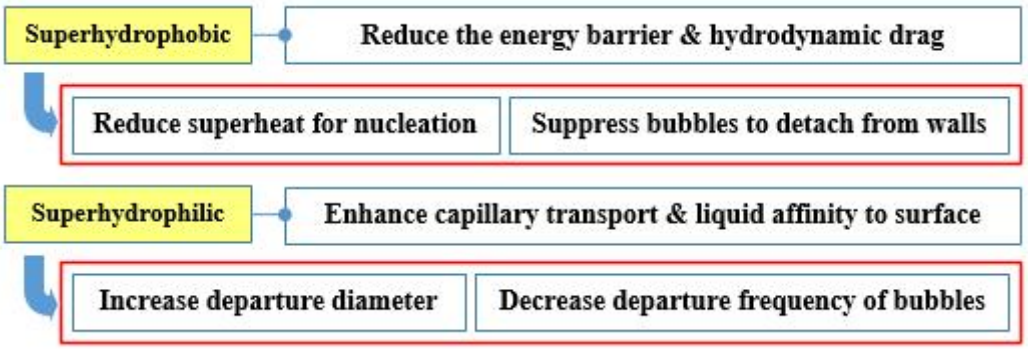


Figure.27 Mechanisms of superhydrophilic and superhydrophobic surfaces in flow boiling processes

Based on the discussions about the effects of wettability and roughness on flow boiling heat transfer, experimental studies have been conducted to investigate methods for improving the heat transfer performance. These encompass surface modification techniques, such as nano-structure and surface-roughening treatments, along with the utilization of biphilic wettability and smart material coatings on surfaces. as shown in Figure.28.

Generally, the heated surfaces could be modified to have superhydrophilic, superhydrophobic, and biphilic properties by fabricating nano-structures with special materials, shapes, sizes and manufacturing methods. Those specific materials with inherent characteristics of spontaneous

wettability change regulated by surface temperatures can be coated on surfaces to increase the heat transfer coefficients at low heat fluxes and the critical heat fluxes at high heat loads.

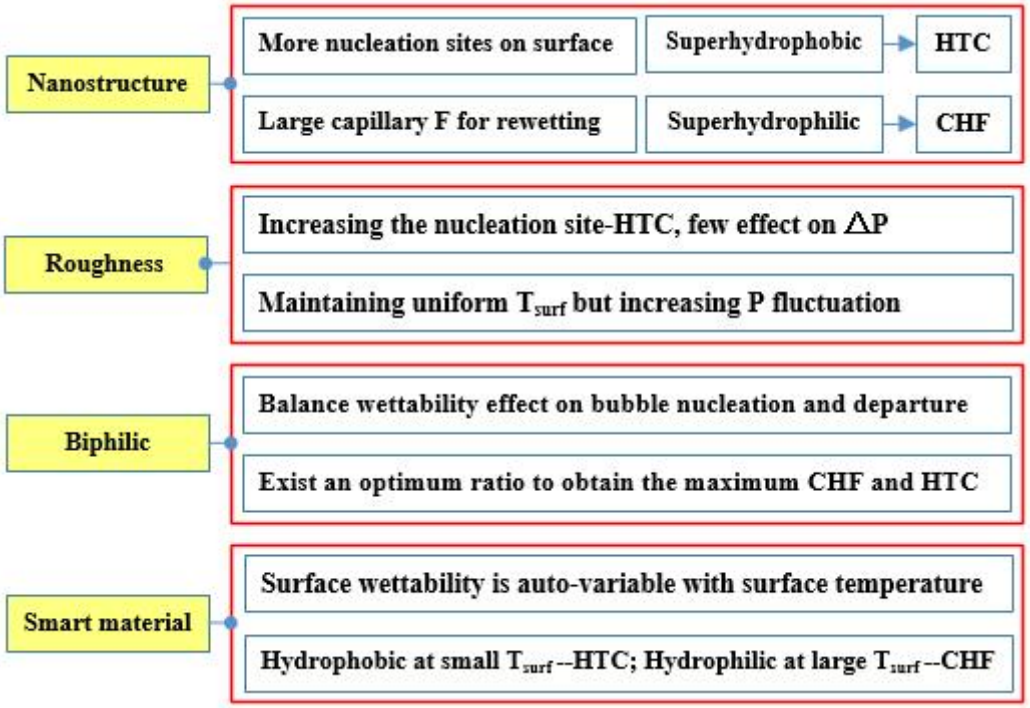


Figure.28 The important performance of alternative surface modification treatment

According to the Young's equation, it is evident that the contact angle of surfaces is related to the physical properties of the liquid and surfaces, which are determined by factors such as the material and the operating temperature. Figure.29 (a) presents the different contact angles of water on various surfaces, ranging from 22° to 112°. Therefore, the surface modification methods, including the chemical treatment, material and microstructure coating, nanoparticle deposition and coating, have been employed to expand the range of wettability in applications.

For instance, the effect of nanoparticle coating on the wettability and roughness of copper surfaces is shown in Figure.29 (b). Compared to copper, silica is hydrophilic and fluor silane is hydrophobic. By coating the nano-size SiO_2 or SiO2-fluorosilane particles, the wettability of copper can be altered from the superhydrophilic one (8°) to the superhydrophobic (155°). The higher particle concentration results in larger surface roughness and a higher density of active nucleating sites on the surfaces. Consequently, the heat transfer performance, such as pool and flow boiling in macro/microchannels, can be enhanced through appropriate surface modification treatments.

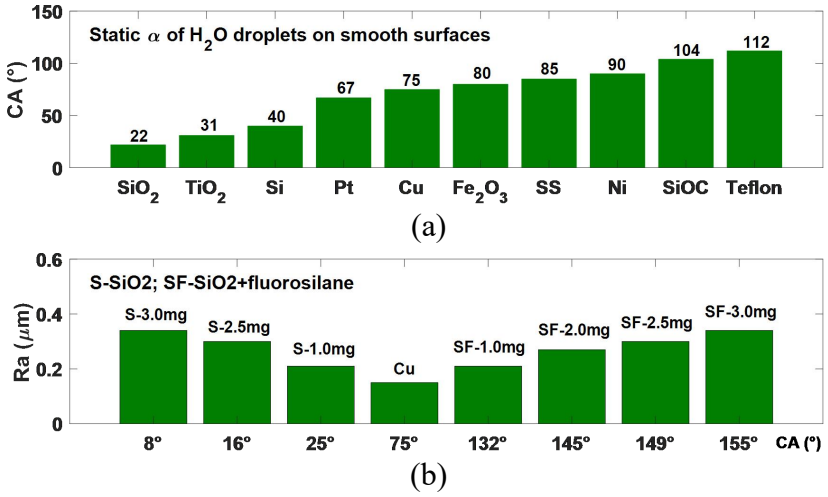


Figure.29 Effects of (a) solid materials on wettability and [157,158,159,160] (b) nanofluid deposition on wettability and roughness [157]

The wettability has a significant impact on pool boiling heat transfer performance. Phan et al. [158] found that the maximum heat transfer coefficients for pool boiling of water occurred when the contact angle was close to 0° or 90° at a constant heat flux. Hydrophobic surfaces can reduce the wall superheat necessary for bubble nucleation, but make it difficult for the bubbles to escape from the surface, resulting in large areas covered by vapor and a decrease in HTC at high heat fluxes. However, as the wettability increases, the departure diameter of the bubbles increases while the departure frequency decreases. Jo et al. [161] conducted a comparative study on water pool boiling heat transfer on surfaces with different wettability characteristics: hydrophilic surfaces with a contact angle of 54°, hydrophobic surfaces with a contact angle of 123°, and heterogeneous wetting surfaces. Result showed that hydrophobic surfaces exhibit an earlier onset of nucleate boiling, a higher heat transfer coefficient, but a lower critical heat flux compared to hydrophilic surfaces. This is attributed to the fact that the temperature at the onset of nucleate boiling (ONB) decreases as the contact angle increases, resulting in improved nucleation heat transfer on surfaces with lower wettability, especially at low heat fluxes.

Figure.30 compares the effects of surface modification on the CHF of pool boiling, including chemical treatment [159], the nano-cone array and nanowire treatment [159,160], and porous and nanoparticle coating methods [162,157,163,164,165]. In general, the CHFs increase as the wettability increases, and the increment is mainly dependent on those factors such as the modification techniques and materials. For the same materials such as Ni and NiCr, the CHF

enhancement by nano-structure modification is larger than that of chemical treatment at the same wettability. Furthermore, the treatment of nanoparticle/porous coatings could increase the wettability close to 0 and achieve the highest CHFs.

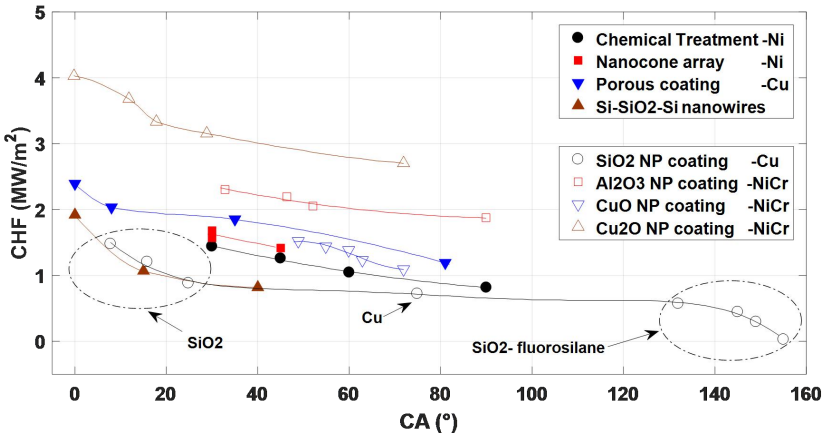


Figure.30 Effects of contact angles on CHF in pooling boiling by various surface modification methods [159,160,162,157,163,164,165]

Wettability also has an effect on flow boiling in microchannel. Choi et al. [166] indicated that in a hydrophobic microchannel with a contact angle of 105°, the HTC and pressure drop were larger than those in a hydrophilic microchannel with a contact angle of 25°. This difference was mainly attributed to the presence of active nucleation sites and the occurrence of unstable elongated bubbles/liquid film motions at high vapor qualities on the hydrophobic surfaces. Sadaghiani et al. [167] investigated the effect of mini/nano-structures with contact angles of 80.16°, 78.5°, 120.16° and 140.75° on water flow boiling heat transfer in a microchannel. The nanostructured surfaces (e.g., α=120.16° and 140.75°) exhibited higher HTCs compared to the base surface (α=80.16°) under the same mass and heat fluxes. This improvement was attributed to the more active nucleating sites, better uniform distribution of nucleation sites, and a larger effective surface area on the nanostructured surfaces. Liu et al. [168] investigated the effects of the wettability (with contact angles of 0°, 36°, and 103°) on flow instability in a microchannel. The study revealed that periodic temperature fluctuations were observed only on the hydrophilic (α=36°) surface, where the bubbles underwent the nucleation, growth and merging into confined shapes before flushed out by the inlet liquid.

Zhang et al. [169] investigated the effects of wettability and microstructure on the saturated flow boiling in microchannels. It is found that while the maximum HTC of 365 kW/(m^2.K) was obtained at the case of TS3 under low heat flux conditions, the highest CHF of 1627

kW/m^2 was achieved at the case of TS2, which were 6.3 and 1.6 times higher than that of plain surfaces, respectively.

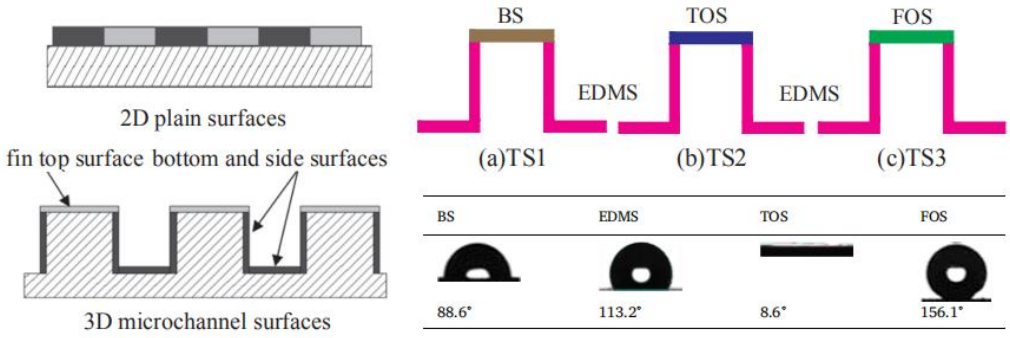


Figure.31 Geometric structures of microchannels and contact angles of different surfaces [169]

Surface roughness is an important factor affecting boiling heat transfer. Rough surfaces have a higher density of the active nucleation sites compared to smooth surfaces. Boiling on the smooth surfaces requires a higher superheat, which leads to a rapid bubble growth and large oscillations in pressure and temperature. Alam et al. [170] studied the effect of roughness on water flow boiling in a micro gap. It is found that the increasing of surface roughness could increase both the density of active nucleation sites and the heat transfer coefficient, while the pressure drop remained unchanged at the same conditions. Jayaramu et al. [171] investigated the roughness effects on water flow boiling in microchannels with different copper surfaces, a fresh one, an aged one and a cleaned one under the same conditions. The fresh surface had a higher HTC compared to the aged one, attributed to the greater wettability caused by thermal oxidation. The cleaned surface had a greater HTC than the fresh one due to an increase in roughness and the presence of more active nucleation sites.

To further improve the heat transfer performance in a wide range of conditions, surfaces with hybrid wettability have been investigated by researchers. Jo et al. [172] studied the effect of hybrid wettability on water pool boiling heat transfer by coating a hydrophilic substrate with hydrophobic dots. They found that the area ratio, defined as the hydrophobic area divided by the total surface area, had a significant effect on the critical heat flux, but a negligible effect on HTC. To achieve high CHF and HTC simultaneously, the hydrophobic dots (α=123°) needed to be manufactured at a microscale level on hydrophilic (α=54°) surfaces with a small area ratio. Betz et al. [173] found that a hybrid flat surface (α=7 and 110°) enhanced the HTC and CHF by 100% and 65%, respectively, compared to a hydrophilic surface.

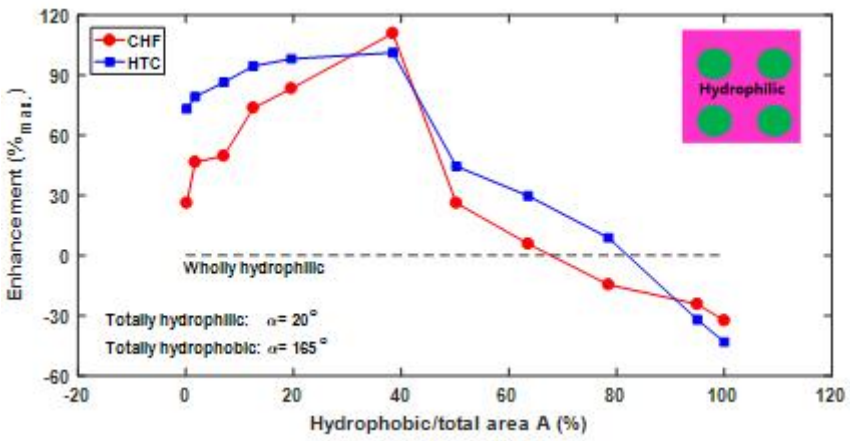


Figure.32 Definition of area ratio A and the results of flow boiling heat transfer enhancement [174]

Motezakker et al. [174] conducted a study on the effect of biphilic wettability for pool boiling. They aimed to determine the optimal surface ratio of hydrophilic (α=20°) and hydrophobic surfaces (α=165°). The results showed that the case with an area ratio of 38.46% exhibited the highest CHF of 1970 kW/m^2 and the HTC of 9 MW/ (m^2.K). It was observed that in cases with an area ratio greater than 38.46%, the earlier interactions of nucleated bubbles resulted in the formation of a vapor blanket, which led to lower CHF and HTC. When the area ratio exceeded 38.46%, the interaction of nucleated bubbles occurred earlier, causing vapor blanket formation and triggering CHF at lower heat fluxes.

Additionally, it is evident that the contact angle decreases with increasing temperature, as the interfacial tension is inversely dependent on temperature, as shown in Figure.33.

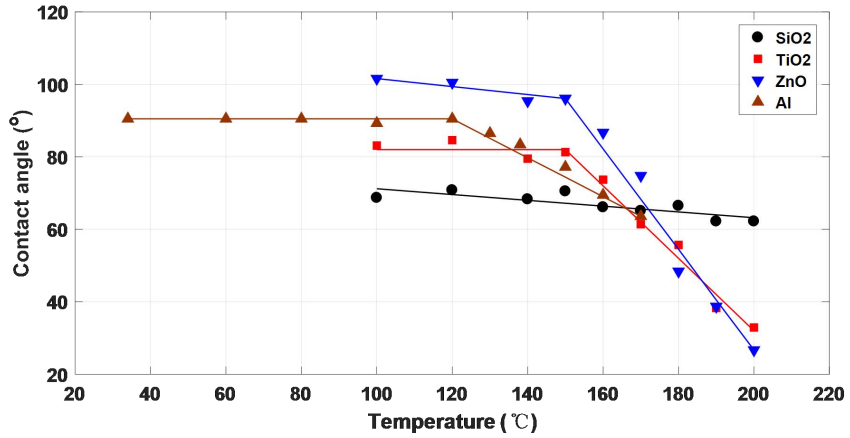


Figure.33 Relations of contact angle with temperature on different material surfaces [175,176]

Hence, smart materials with variable wettability that auto-adjust with temperature are another promising choice for improving the heat transfer performance in various applications. Kim et

al. [176] studied the effects of smart material (such as TiO_2 and ZnO) surfaces on water flow boiling heat transfer, which can naturally change the wettability with the surface temperature. For example, the contact angle of ZnO is decreased from 100° to 26°, when the temperature of surface is increased from 100 to 200℃. In comparison to SiO_2, the ZnO surfaces exhibited hydrophobic behavior at low temperatures, which facilitated nucleation and consequently led to increase the HTCs. However, for the high superheat cases, the ZnO surfaces became hydrophilic, allowing them to supply liquid to local dry-out regions and effectively delaying or inhibiting the degradation of critical heat flux (CHF).

In this study, flow boiling of water, R134a and the NH_3/H_2O mixture in microchannels was investigated by the CFD method. Contact angles of pure water and R134a were referenced in the literature. Since pure refrigerants are superhydrophilic (e.g., R134a and R22 with contact angles of 4-5° on the aluminum surfaces [177]), and the suspended nanoparticles can increase the wettability as shown in Figure.29, the contact angle of the NH_3/H_2O mixture was set as zero and the effect of particles on refrigerant wettability was neglected in this work.

The effect of surface roughness on R134a flow boiling in microchannels was investigated using experimental methods. For example, Mohamed et al. [178] and Karayiannis et al. [179] studied the roughness effect on R134a flow boiling in a welded and a seamless stainless-steel tube, respectively. In the case of the seamless tube, the heat transfer was primarily influenced by the nucleate boiling effects, with the heat transfer coefficient being dependent on the heat flux and unaffected by the mass flux and vapor quality. Conversely, there was no substantial impact on the HTC in the welded tube, but it elevated wall superheat levels at the onset of nucleate boiling. Ong and Thome [180] investigated R134a flow boiling in a stainless-steel mini-channel at a saturated temperature of 31℃. They found that heat flux had a stronger effect on the HTC at low vapor quality, while the mass flux had a relatively stronger effect at high vapor quality. Jafari et al. [181] investigated the roughness effect on R134a flow boiling in a copper microchannel at a saturated temperature of 10℃. Their observations revealed that the HTC increased by as much as 45% with an increase in surface roughness from 0.21μm to 2.38μm.

2.2.5-Flow boiling of zeotropic mixture

Selecting a working fluid with excellent thermophysical properties is one of the most crucial methods for enhancing the cooling performance. The fluid not only directly influences the heat dissipation capacity and operating conditions, but also interacts with the geometric and surface modifications [182].

Since the safe operating temperature of electronic components is less than 85℃, refrigerants such as NH_3, R134a and R245fa can be used as alternative coolants at pressures higher than atmospheric pressure. For example, R245fa has a saturated temperature of 25℃ at a pressure of 0.149MPa [183]. Some experimental studies on the refrigerants flow boiling are listed in Table.9. Madhour et al. [126] investigated R134a flow boiling in a microchannel for cooling the CPUs. It is found that the maximum value of the HTC could reach up to 270 kW/(m^2.K) with a maximum temperature gradient of 0.3℃/mm and the highest pressure drop of 94 kPa at a mass flux of 1000 kg/(m^2.s). Those related experiments were conducted on a CPU-based chip operating at 85℃.

Table.9 Experimental studies of pure R134a, R245fa and NH_3 flow boiling in mini/microchannel

	D or W×H	T_{sat}	p	G	Q_{max}	x_{max}	Ref
	mm	℃	MPa	kg/s	kW/m^2		
R134a	0.100×0.68	60~63	1.70~1.80	205~1000	1890	1.0	2011 [126]
R134a	0.100×0.50	25	0.68	400~1500	310	0.16	2013 [62]
R134a	0.382×0.47	13~23	/	150~600	127	0.92	2016 [184]
R134a	0.382×0.47	18,23,28	/	800~1200	460	0.6	2018 [185]
R245fa	0.233×0.68	23.7~43.9	0.14~0.27	281~1501	1900	0.78	2008 [183]
R134a,R245fa	0.381×0.95	8~30	0.13~0.75	20~350	220	0.9	2009 [186]
R134a,R245fa	ϕ0.40~2.00	31	0.79~0.18	100~900	226	0.75	2014 [187]
R134a,R245fa	ϕ0.38~2.32	21.5~58.3	0.40~1.20	49~2200	185	0.93	2016 [188]
R134a,R245fa	ϕ0.51~0.79	31	0.79	300~2000	200	0.8	2016 [189]
NH_3	ϕ1.22,1.70	23,33,43	/	100~500	355	1.0	2012 [190]
NH_3	ϕ0.98-2.16	30~60	/	75~225	/	0.8	2016 [191]
NH_3	1.00×1.10	27.5~47.5	1.00~1.54	66~148	12.2	0.01	2017 [192]

Refrigerant binary mixtures, such as R123a/R245fa and NH_3/H_2O, are potential coolants for dissipating heat in the electronic devices. These can align the operating temperature with the heated surface profiles, due to the non-isothermal phase-change feature [100]. The saturated temperature of a binary mixture is controlled by adjusting the pressure and the concentration. As the boiling occurs, the concentration of the volatile component in the mixture diminishes, resulting in a rise in the saturated temperature of coolants. This could impede the growth of bubbles and delay the dry-out, thus contributing to an enhancement in the CHFs [101,102]. Despite the HTCs of the mixtures are typically lower than those of pure fluids under the same conditions [100], flow boiling of the zeotropic mixture has attracted considerable attentions. Figure.34 illustrates the differences in flow boiling heat transfer between pure and zeotropic mixtures in microchannels.

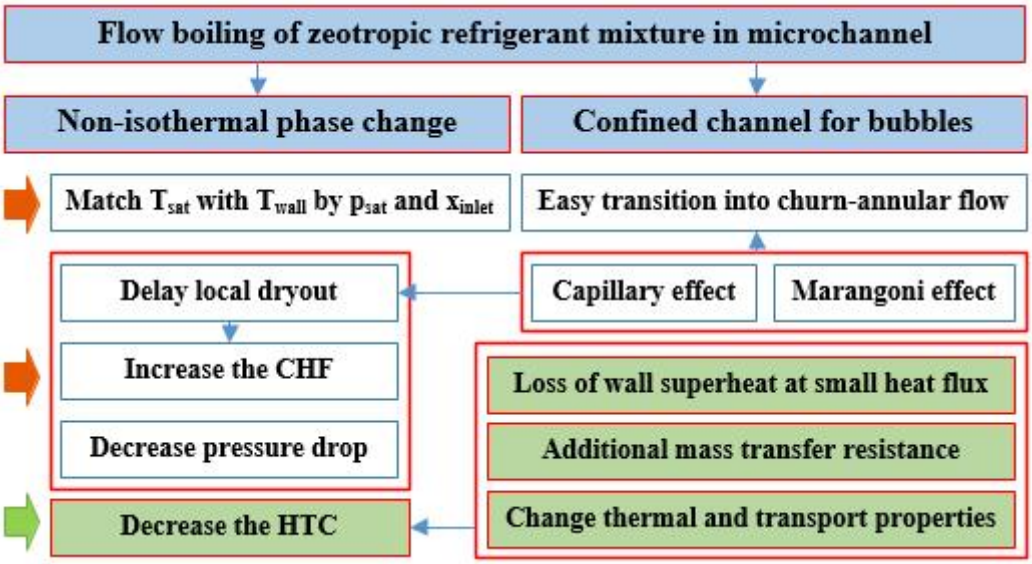


Figure.34 Characteristics and the mechanisms of zeotropic mixture flow boiling in microchannel

Table.10 documents experimental studies on flow boiling heat transfer of R134a/R245fa and NH_3/H_2O binary mixtures with the saturation temperature ranges of 18°C to 95°C.

Table.10 Experimental researches of R134a/R245fa and NH_3/H_2O in flow boiling heat transfer

Concentration	D	T_{sat}	p	G	Q_{max}	x_{max}	Ref
(by mass)	mm	℃	MPa	kg/s	kW/m2	/	
R134a/R245fa							
82/18	ϕ3	28~43	0.54~0.84	280~469	34	0.7	2016[103]
20/80, 27/73,43/57	ϕ3	28~32	0.4	300~800	69	0.8	2016 [193]

10/90, 30/70,70/30	1×1 single	18.5	/	60~1100	120	1.0	2017 [104]
10/90, 30/70,70/30	2×1 multi	26	/	300~400	350	1.0	2018 [105]
NH_3/H_2O							
39%~48%	ϕ25.8	/	0.88~1.24	4.2~9.0	18.1	/	1999 [196]
42%,55%,61%	ϕ6	70~90	0.15~2.0	707~2688	18.5	0.6	2005 [195]
42%~62%	D_h4 Plate	/	0.7~1.5	70~140	50	0.2	2010 [107]
90%	d_G2 Plate	18.5	0.7~0.9	7.5~15	23	0.4	2011 [110]

In general, the HTC of the R134a/R245fa mixture is significantly lower than that of R134a and similar to that of R245fa [193,104,105]. This is contrary to the findings in the ϕ3 tube, where the HTC is higher at a high concentration of R134a (i.e., 82% mass) [103]. The binary mixture has a lower pressure drop but a higher HTC compared to R245fa. At high saturation temperatures, the inlet mass flux and the concentration have less impact on the HTCs at large heat fluxes [105]. While R134a is more prone to local dry out than R345fa, the addition of a small amount of R134a to R245fa could enhance the CHF and the HTC at high heat fluxes [102, 105]. Furthermore, the segmented microchannel design does not improve the HTC of the mixture but can delay heat transfer degradation and enhance the CHF for both pure and zeotropic fluids [105].

The mechanisms of zeotropic mixture flow boiling in microchannels are different with that of pure fluids in microchannels, mainly due to the binary effects of confined channels and the non-thermal phase change feature on the bubble dynamics. For example, seven different flow patterns in the R32/R125/R134a mixture and five classic types in the R13a/R245fa mixture were observed in a microchannel, respectively [102,104]. Four patterns in the R134a/R245fa mixture were identified in a ϕ3mm circular tube [193].

The flow pattern transitions in the zeotropic mixtures are delayed and the degree of hysteresis is influenced by the concentration and temperature glide, which significantly affects the flow boiling heat transfer performance [104]. In the nucleating boiling region, the degradation of flow boiling HTC for zeotropic mixtures is mainly caused by the reduction of wall superheat and the additional mass transfer resistance [100,102,193]. In the convective flow boiling region, it is primarily caused by changes in the physical properties of fluids, such as the

increase of dynamic viscosity [182,194]. It is also indicated that the performance degradation of the zeotropic mixture is mitigated at high vapor quality due to the capillary and Marangoni effects [104].

Currently, the NH_3/H_2O mixture has been widely used as a working fluid in large industrial refrigeration systems due to its environmental-friendly nature and the high boiling latent heat. The latent heats of NH_3/H_2O, R134a/R245fa and R123/R134a (0.2/0.8 by mass) at a saturated temperature of 323.15 K are 1689 kJ/kg, 167 kJ/kg and 155.5 kJ/kg, respectively, which are calculated by REFPROP. Recently, the minimization design of cooling systems has reduced concerns about its toxicity, making it possible to use for cooling electronic applications [190].

The heat transfer correlations for the NH_3/H_2O mixture in the macro-scale cooling equipment have been assessed and the modified prediction models have been developed in the literature [100,195,196]. Additionally, the flow boiling of NH_3/H_2O in the mini-scale plate sink was experimentally investigated at inlet concentrations of 42%-90% and pressures of 0.7-1.5MPa shown in Table.10 [107,110]. In general, the overall HTC is highly dependent on mass fluxes and insignificantly affected by heat fluxes and pressure at large vapor quality from 0.1 to 0.22 [107,108]. Moreover, local HTC increases with the increase in vapor quality and mass fluxes but decreases with heat fluxes [109,110].

Therefore, flow boiling heat transfer of the NH_3/H_2O mixture in microchannels is an efficient and promising method to enhance the heat dissipation capability of thermal management for the electronic devices. However, the empirical correlations and calculating models developed for flow boiling in macrochannels are not applicable for that in microchannels due to the differences in the bubble dynamics and flow patterns [106]. It becomes crucial to investigate flow boiling of NH_3/H_2O in microchannels for the further understanding and improving heat transfer performances.

2.2.6-Flow boiling of nanofluids

As discussed before, refrigerants (e.g., R134a and R245fa) are suitable for cooling electronic devices. However, they also have shortcomings related to the poor thermophysical properties such as low thermal conductivity and the small boiling latent heat. Therefore, the addition of nanosize functional particles to refrigerants is an efficient approach to enhance single-phase

convective heat transfer in microchannels and is a promising method to improve flow boiling performance [7,54].

Nanofluid is a liquid mixture with nanosize high thermal conductivity particles suspended in a base fluid. While most studies show that nanofluids enable larger heat transfer coefficients for single-phase convection compared to the base fluids under the same conditions [197], the effects on heat transfer performance of flow boiling are inconsistent and even contradictory, which are summarized in Figure.35.

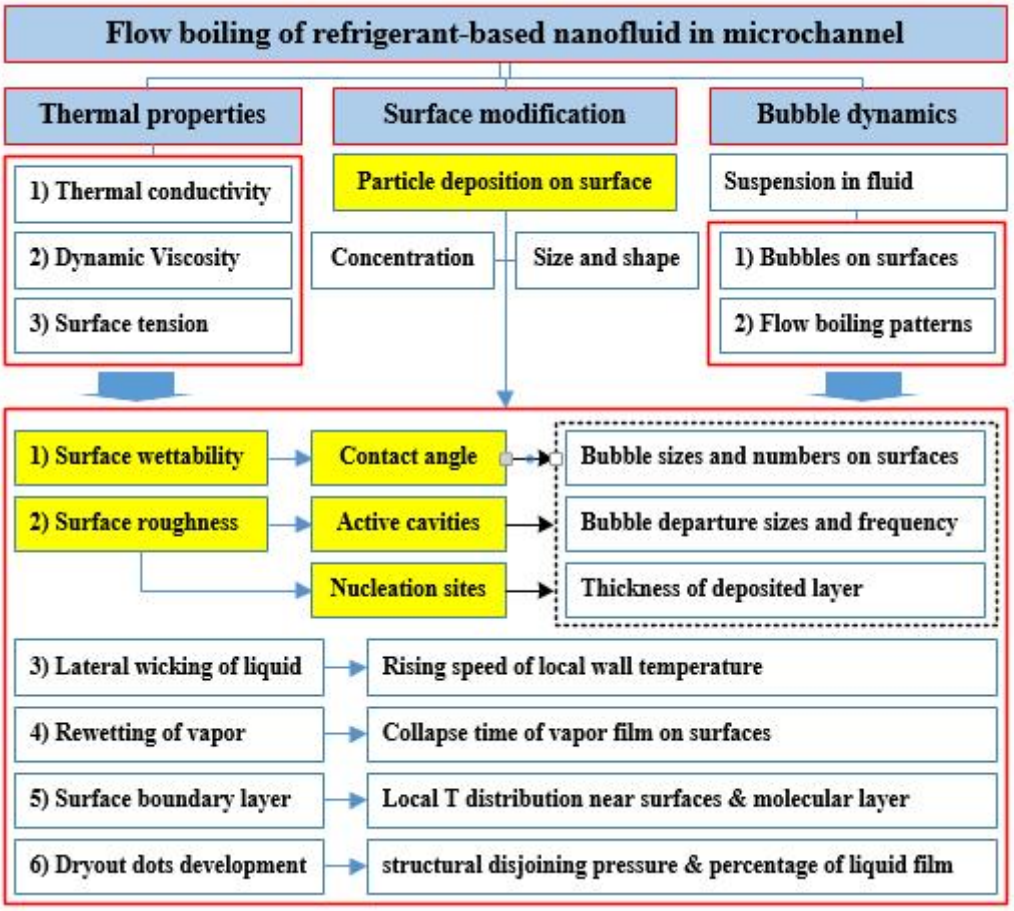


Figure.35 Influences of suspended nanosize particles on refrigerants flow boiling in microchannel

Generally, flow boiling heat transfer is affected by suspended nanosize particles through their effects on thermophysical properties (e.g., thermal conductivity and viscosity) of coolants, surface modifications (e.g., the wettability and roughness) and dynamic interactions (e.g., the thickness of boundary layer and flow boiling patterns). It is the mutual-coupling interactions that finally dominate the effects on the heat transfer performance in microchannels.

Compared to those base fluids, the HTCs of nanofluid flow boiling in microchannels could be either enhanced [85,86,87,202] or deteriorated [88,198,89,90,204], majorly depended on the physical properties of fluids and nanoparticles, geometrical parameters of channels and the operating conditions [91]. Some experimental cases are shown in Table.11.

Boudouh et al. [85] found that the HTCs of Cu/H_2O nanofluid flow boiling were increased mainly due to the higher viscosity compared to the base fluid. Xu et al. [86] found that the HTC was enhanced as the local inhibition of dryout and the enlargement of the liquid film evaporation area caused by the addition of Al_2O_3 nanoparticles into water. Chehade et al. [87] observed that the HTC enhancement of Ag/H_2O nanofluid was about 162% at a concentration of 50 mg/L, but the enhancement capability decreased dramatically at high vapor qualities. Additionally, the largest local HTC was observed at the entrance where the vapor quality was low, and the local HTC decreased along the flow direction. Duursma et al. [202] found that the maximum enhancement of HTC in Al_2O_3/ethanol flow boiling occurred at a nanoparticle concentration of 0.05%.

In contrast, Lee et al. [88] investigated single and multiphase flow heat transfer of Al_2O_3/H_2O nanofluid in microchannels and found that the nanofluid was not suitable for flow boiling due to the disastrous failure caused by the nanoparticle depositions on the heated surfaces. Once the nucleate boiling occurred, the nanoparticles began to deposit into large clusters, adhere to surfaces and quickly spread throughout the entire microchannel, leading to destructive failure. They also highlighted that the deposition was primarily caused by severe disturbance of the boundary layers, as well as the serious flow obstruction due to the localized evaporation and additional turbulence. Wu et al. [198] observed the depositions of Al_2O_3/H_2O nanofluids at a high wall temperature and a low concentration condition, especially at corners where the fluid velocity was low. Moreira et al. [89] investigated the effects of nanoparticle types (i.e., Al_2O_3, SiO_2 and Cu), concentrations and sizes on flow boiling heat transfer performance. The HTC decreased at a large concentration of 0.1 vol.%, and it also depended on particle sizes in small concentration conditions. The smaller particles (e.g., less than 30nm), the lower HTC values. This was caused by the heated surface modifications due to the deposition of nanoparticles: larger sizes of nanoparticles could generate a uniform texture similar to the original surfaces, but smaller particles could produce thin layers with notable peaks and valleys of oscillation.

Zhang et al. [90] found that the HTC of the graphene oxide/H_2O nanofluid was smaller than that of water and it was degraded by increasing the concentration. The generated non-porous deposition layer could block the active bubble nucleation sites and inhibit the heat transfer performance. It is the physical interactions of particles that trigger the particle depositions. Increasing the inlet mass flow, temperature and concentration could intensify the extent of the particle depositions.

Furthermore, Diao et al. [91] found an optimal concentration of the Al_2O_3/R141b nanofluid for the maximum value of HTC in microchannels. Compared to the HTC of R141b, that of the nanofluid was higher at a low concentration of 0.001vol.%, primarily due to the increased nucleation density on heated surfaces. However, the HTC was lower at a higher concentration of 0.1vol.% due to elevated thermal resistance by the particle deposition. Hence, the observed effect is attributed to surface modifications caused by nanoparticle deposition, rather than the dispersion of nanoparticles in the base fluid.

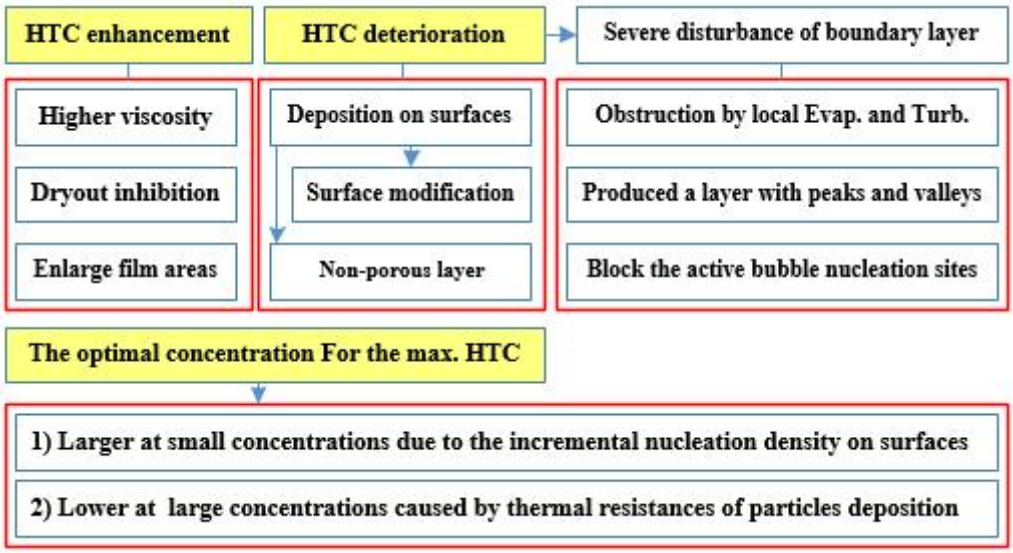


Figure.36 Different results of nanofluid on flow boiling HTC in microchannel

The CHF in microchannel could be significantly enhanced by adding nanoparticles into base fluids [88,199,200,201,90]. Comparing to that of water, the CHF of the Al_2O_3/H_2O nanofluid (i.e., 0.1%vol.) was improved by about 31% at 652 kg/(m^2.s) [199]. Furthermore, the CHF was enhanced by increasing inlet mass fluxes, initial subcooling and concentrations [199,201]. The enhancement could be attributed to the increase in surface wettability, bubble numbers in the microchannel and the decrease in bubble lifetime in the domain [88,200,90]. For example,

the contact angles were 85.9° of H_2O and 76.0° of the Al_2O_3/H_2O nanofluid (0.1%vol) on stainless steel surfaces [204]. Furthermore, Nascimento et al. [203] found that the effects of particle types (e.g., Al_2O_3, SiO_2), concentrations (e.g., 0.01,0.01%vol) and sizes (e.g., 10~80nm) on the CHF were negligible at high vapor qualities between 0.65 and 0.84.

The pressure drops in nanofluid flow boiling were greater than those in base fluids and were further amplified with higher concentrations. This is mainly attributed to the high viscosity of nanofluids and the formation of large nanoparticle clusters by the deposition [88,198,85,202]. However, Xu et al. [86] pointed out that nanofluids could reduce pressure drops compared to base fluids, mainly due to the inhibition of dry patch development and the existence of some miniature bubbles in the microchannel.

Xu et al. [86] found that the addition of Al_2O_3 particles could stabilize the flow boiling of water in microchannels without particle deposition. This stabilization is mainly caused by the sustenance of miniature bubbles in the domain and the inhibition of dryout on surfaces. Yu et al. [204] indicated that the Al_2O_3 nanoparticles in H_2O can delay the onset of nucleate boiling and suppress the onset of flow instability. This can be attributed to changes in the active nucleation site density and surface wettability mainly due to the particle deposition and the reduction in the thickness of thermal boundary layers. However, Vafaei et al. [199] found that the frequency and amplitude of inlet pressure and temperature oscillations in Al_2O_3/H_2O nanofluid flow boiling were larger than that of water due to changes of the surface wettability. Duursma et al. [202] pointed out that the pressure drop was unstable and the frequency and amplitude of fluctuations were dependent on nanofluid concentrations.

The effects of nanoparticles on the flow patterns and bubble dynamics are different and even controversial. Xu et al. [86] observed that the main pattern of water flow boiling in channels was the elongated bubbles, while the miniature bubbles in nanofluid were observed under the same conditions. However, Vafaei et al. [199] found that the Al_2O_3/H_2O nanofluids had more numbers of elongated bubbles than deionized water. The intensity of nanoparticle depositions increased with time and the concentrations once nucleation was triggered. The inconsistent or contradictory results of flow patterns can be attributed to the surface modification, which is a dominant factor [199]. The effects of nanoparticles on the surface modification and the flow boiling heat transfer performance in microchannels have been discussed in the previous work.

Table.11 Heat transfer performance and main parameters of nanofluid flow boiling in microchannel

Ref	Microchannel			Nanofluid Parameters				Operational condition		Performance		
	Channels	Material	Size (mm)	Fluid	Particle	Size(nm)	x (vol/wt)	T_{in}(℃)	G (kg/m^2.s)	h	CHF	ΔP
2007[88]	21	Cu	0.22W×0.82H	Water	Al_2O_3	36	1, 2%vol	30	2.15~5.55g/s	↓	↑	↑
2009[198]	8	Si	D_h0.195	Water	Al_2O_3	56	0.15,0.26%vol	35	40~280mm^3/s	↓		↑
2010[85]	50	Cu	2.0W×0.5H	Water	Cu	35	~0.0056%vol	64	167~616	↑		↑
2011[199,200]	1	SS	ϕ0.51	Water	Al_2O_3	25	0.001~0.1%vol	55	600~1650		↑	
2012 [86]	1	Si	0.1W×0.25H	Water	Al_2O_3	40	0.2%wt	20~27	171~401	↑		↓
2013[87]	50	Cu	2.0W×0.5H	Water	Ag	35	~0.000475%vol	60	87~653	↑		
2013 [91]	25	Cu	0.25W×0.5H	R141b	Al_2O_3	13	0.001~0.1%vol	/	50~800	↑↓		
2014 [201]	1	SS	ϕ0.51	Water	Al_2O_3	25	0.001~0.1%vol	20~55	600~1950		↑	
2015 [202]	1	/	D_h0.57~1.4	ethanol	Al_2O_3	50	0.01~0.1%vol	/	11.2~44.8	↑		↑
2017 [89]	1	SS	ϕ1.1×200L	Water	Al_2O_3 ,S_iO_2	15~80	0.001~0.1%vol	75	200~600	↓		
2017 [90]	5	Cu	2.5W×0.5H	Water	GO	2.3	0.005~0.05%wt	/	40,60mL/min	↓	↑	
2019 [203]	1	SS	ϕ1.1×200L	Water	Al_2O_3 ,S_iO_2	10~80	0.01~0.1%vol	100	133~494		→	
2015 [204]	1	SS	ϕ1.1×306L	Water	Al_2O_3	/	0.01~0.1%vol	80~91	680~3100	↓		
Symbol:	SS: Stainless steel; ↑: Performance enhancement; ↓: Performance deterioration; →: Performance stabilization											

2.2.7-Flow boiling of EPCM slurries

The nano/micro-size encapsulated phase change slurry (EPCM) is a type of functional fluids, in which the particles containing the phase change material inside are encapsulated by shells and dispersed in a base fluid. Compared to the base fluid, the EPCM particles have larger heat transfer areas, higher effective heat capacity and maintain nearly constant temperatures during the phase change process. The shells separate the PCM from the base fluid, increasing particle stability and allowing for a wider range of material selections [205]. Therefore, the addition of EPCM particles to base fluid is an effective and promising method to further enhance the heat transfer performance in microchannels [206].

Several critical principles should be considered when choosing a suitable PCM material. For instance, the melting temperature of the PCM should match the operational temperature, and the volume change rate during the melting process should be minimal. The shell material used to encapsulate the particles should possess excellent sealing properties, chemical stability, and mechanical durability for withstanding high temperatures and the pumping process. Moreover, the heat transfer performance of EPCM slurries depends primarily on the physical properties of PCMs and shells, the particle sizes and concentrations, as well as the operating conditions. Table.12 presents main properties of classic organic and inorganic PCMs, such as the melting latent heat, density and thermal conductivity.

Table.12 Properties ccomparisons of organic and inorganic PCMs［207, 208, 209, 210, 211, 212］

Properties	Organic PCM		Inorganic PCM	
/	Paraffin	Non-paraffin	Salt hydrates	Metal
$T_{melting}$ (℃)	9.9~84.2	7.8~81	8.1~80	10.7~72
Latent heat (kJ/kg)	60~273	85.7~259	68~377	25~90.9
Density (kg/m^3)	751.6~1304	830~1580	976~2194	>5903
Thermal conductivity (W(m·K))	0.14~0.75	0.097~0.36	0.46~1.34	10~54

Accordingly, the organic PCMs are acceptable materials for the EPCM particles suspended in refrigerants due to their advantages, such as the wide temperature ranges, high latent heat of melting, chemical stability and small subcooling, safety and recyclability, compatibility with conventional shell materials [213]. Furthermore, the densities of organic PCMs are similar to those of refrigerants (e.g., R134a and the NH_3/H_2O mixture in Table.2), which can prevent particle sedimentation caused by the gravity effects, even though the thermal conductivities are much smaller than those of salt hydrates and metals [214].

The phase change emulsion (PCE) and EPCMs have been demonstrated to improve the single-phase convection performance. F. Ma et al. [93] experimentally investigated the heat transfer of PCE (n-hexadecane/H_2O) in laminar flow and found that the local Nusselt number of PCE (20 % wt.) was about 2.3-3.2 times that of pure water under the same conditions. Ho et al. [215] investigated the single-phase heat transfer of H_2O-based EPCM slurries in a microchannel. The heat transfer effectiveness could be improved by 52% at Re of 133 and a latent-sensible heat ratio of 0.0472. Wang et al. [216] studied the single-phase convective heat transfer of mEPCM/ H_2O slurries in a microchannel. The Nusselt number of the EPCM slurry (2%vol.) could be increased by 34% compared to that of water due to its effect on destroying the thermal boundary layer and reducing the layer thickness. Wu et al. [217] experimentally studied the single-phase convection of poly-α-olefin (PAO)-based nanosize EPCM slurries in a microchannel. The HTC value of slurries with 30% indium nanoparticles was 47 kW/(m^2·K), twice as high as that of pure PAO. Hence, compared to the base fluid, the positive effect of EPCM melting processes was larger than the negative effect of poor thermal conductivity for single-phase convective heat transfer in a microchannel.

However, there are few studies in the literature regarding flow boiling of PCE or EPCMs in a microchannel. The main challenges might be the risks of the liquid leakage and low thermal conductivity of PCM (less than 0.4 W/(m·K)) [94,95].

Table.13 Thermal properties of phase change materials available for electronic cooling applications

Material/symbol	$T_{melting}$	Latent heat	Density	Thermal conductivity	Specific heat
/	℃	kJ/kg	kg/m^3	W/(m·K)	kJ/(kg·K)

Heptadecane	C17	19-23	164-240	760-778	0.21	/
Octadecane	C18	28	243-245	814-865	0.15-0.36	1.9-2.16
Nonadecane	C19	32	222	785	/	/
Eicozane	C20	37	247	788	0.15	2.46
Heneicozane	C21	40	200-216	758-791	/	/
P116-Wax	/	48-50	209	786	0.14-0.5	2.89

As mentioned before, the physical properties, such as latent heat and thermal conductivity of EPCM slurries are critical for the heat transfer capability in applications. These properties are primarily dependent on the core and shell materials, the particle sizes and concentrations [96]. Consequently, different PCM material and manufacturing techniques have been investigated to enhance the properties, particularly the effective thermal conductivity of EPCM particles.

The organic polymers, such as polystyrene (PS) and poly (methyl methacrylate) (PMMA), are popular utilized as shell materials due to their excellent sealing performance to avoid leakage. However, their thermal conductivities are fairly low compared to base fluids or metal/metal-oxide nanofluids. Hence, it is feasible to enhance effective thermal conductivities of EPCM particles by adding high-performance materials (e.g., CNT, Al_2O_3, TiO_2, SiO_2, graphene and metals in Figure.6) into organic materials.

For example, the thermal conductivity of 4wt.% MWCNTs-SA[1] modified EPCM particle was increased by 79.2% compared to that of the original EPCM particle (paraffin/UFR) [218]. The thermal conductivity of paraffin-based EPCM particle was improved from 0.244 to 0.382 W/(m·K) by adding nano-Al_2O_3 into shell materials (PMMA-MA[2]) [219]. Similarly, it could be increased from 0.232 to 0.363 W/(m·K) by adding modified Si_3N_4 powders [220] and from 0.192 to 0.3 W/(m·K) by adding the TiO_2 particles into PMMA [221] for encapsulating the microscale n-Octadecane (C18) particles. Zhang et al. [222] and He et al. [223] conducted a

[1] MWCNTs-SA: muti-wall carbon nanotube - stearyl alcohol. UFR: Urea form aldehyde resin.

[2] PMMA-MA: poly (methyl methacrylate)-co-methyl acrylate.

systematic investigation into SiO_2 encapsulation methods for C18-based EPCM particles. The particle thermal conductivity could be obtained from 0.375 W/(m·K) to 0.981 W/(m·K) when the encapsulating ratio of particle varied from 10.5 to 69.5%. When the encapsulation ratio of the C18/$CaCO_3$ EPCM particle was set at 22.44%, a remarkable enhancement of thermal conductivity up to 1.674 W/(m·K) was achieved with a melting latent heat of 46.93 kJ/kg [224]. Furthermore, graphene is a promising type of carbon materials for the EPCM particles due to its excellent thermal conductivity (5kW/(m·K)). Liu et al. [225] fabricated paraffin-based EPCM particles encapsulated by TiO_2/graphene hybrid shell materials, and the thermal conductivity was improved from 0.64 to 0.98 W/(m·K) with a melting latent heat of 160 kJ/kg. Wang et al. [226] found that the thermal conductivity of n-eicosane/SiO_2 PCM particles was increased by 193% when NaBH4 reduced the graphene oxide (i.e., 1wt.%) was added to the capsule shells. Al-Shannaq et al. [96] developed an innovative manufacturing approach for coating Ag on the RT21/PMMA micro-capsules. The thermal conductivity of particle could be improved up to 2.41 W/(m·K) compared to 0.19 W/(m·K) of non-material coated EPCMs.

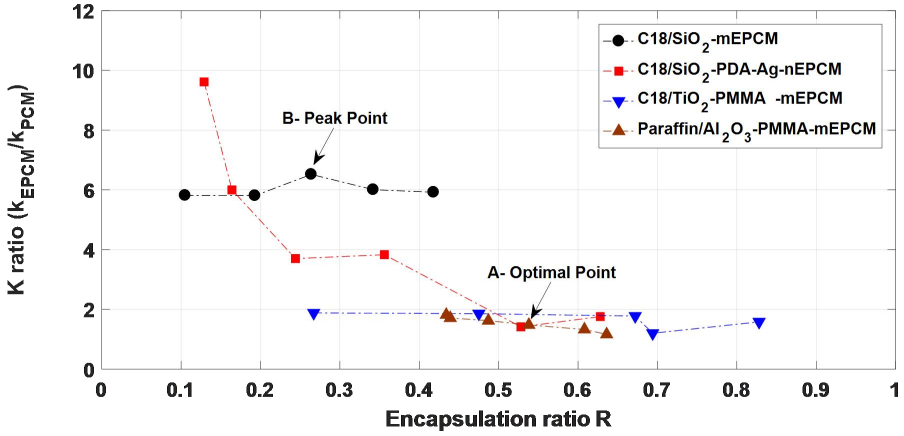


Figure.37 Relation of relative thermal conductivity and encapsulation ratio of modified EPCM particles [,99,221,219,223]

Compared to the micro-size EPCM slurries, the nanosize EPCM slurries have attracted much more attentions mainly due to larger specific surface areas, better dispersibility and improved mechanical properties in pumped heat transfer processes [227]. Therefore, it is important to further enhance heat transfer performance by increasing the thermal conductivities of nEPCM particles. For instance, Dhivya et al. [228] fabricated different types of nano-capsules with

metal coatings (e.g., cobalt, copper and silver) for ethyl esters fatty acid eutectic mixture/SiO_2 EPCMs, resulting in an increase of thermal conductivity from 0.257 to 0.713 W/(m·K). Zhu et al. [99] synthesized different silver-coated C18/SiO_2-PDA EPCM particles, and the thermal conductivity was significantly improved from 0.536 to 1.346 W/(m·K) compared to that of pure C18 of 0.146 W/(m·K). Additionally, Zhu et al. [229] found that the maximum thermal conductivities of C18/SiO_2 and C18/SiO_2/graphene EPCM particles were 0.642 and 1.494 W/(m·K), respectively.

In conclusion, the thermal conductivities of traditional organic-organic PCM particles can be enhanced up to ten times the original capsules, and even higher than that of base fluids by adding the materials with high thermal conductivity into the organic shells. As a result, these modified EPCM capsules have great potential to improve single-phase and flow boiling heat transfer performance of EPCM slurries in microchannels.

However, it is important to note that the enhancement of thermal conductivity in the modified PCM particles comes at the expense of reduction in the melting latent heat per unit, as shown in Figure.37. The encapsulation ratio, which represents the effectiveness of encapsulation, is defined as the ratio of the melting latent heat between encapsulated particle and pure phase change material. Generally, the addition of high-performance additives in shell materials leads to an increase in thermal conductivity but a decrease in the melting latent heat of the capsules. Both thermal conductivity and melting latent heat play important roles in the heat transfer of EPCM slurries. Therefore, there may be an optimal choice of modified EPCM particles based on the assessment of heat dissipation capability and cost. For instance, Jiang et al. [219] chose the case with R=53.81% and k=0.31 W/(m·K) in Figure.37 as the optimal point for the nano-Al_2O_3 modified EPCMs in the energy-saving building applications.

Therefore, in the present study, it is necessary to investigate the effects of thermal properties, such as thermal conductivity and melting latent heat of particles, on flow boiling heat transfer of refrigerant-based PCM slurries in microchannels. This can provide a clearer understanding and more engineering insights for heat dissipation applications in the future.

2.3-Numerical simulation method for flow boiling

Besides conducting experimental studies, computational fluid dynamics (CFD) methods have been widely accepted as an alternative approach to predict the heat transfer performance and investigate the basic mechanisms involved. This is due to the advantages of the CFD method, such as the ability to evaluate the multi-scale spatial and temporal distributions of the thermal parameters (e.g., velocity, temperature, and pressure) and flow patterns (e.g., bubble dynamics and transition) in complex flow and heat transfer processes. These capabilities can overcome the limitations of advanced dynamic visualization measurements in experiments, which are often affected by environmental conditions and equipment performance. For example, some numerical studies were conducted to study flow boiling heat transfer performance of different coolants (nanofluid [230], pure coolants [231] and binary fluids [232]) as well as single phase convection of functional fluids (e.g., nanofluid [233], PCE [93] and EPCM slurry [234]) in microchannels.

As mentioned in Chapter 1, the primary focus of this work is the flow boiling heat transfer of pure refrigerants and the NH_3/H_2O mixture with and without suspended functional particles (e.g., nanofluid and PCM slurries) in microchannels. Therefore, this section about numerical methods will be divided into three parts, including flow boiling of pure coolants, flow boiling of zeotropic mixture and the heat transfer performance of functional fluids in microchannels.

2.3.1-Flow boiling of pure fluids in microchannel

Comparing to single phase convective flow, it is challenging for multiphase flow to capture interfaces between different phases and calculate mass and heat transfer through interfacial surfaces. In principle, subcooled flow boiling heat transfer could be divided into two regions: a high-temperature region with heat flux partitioning near walls and a low-temperature region in domain with complex bubble dynamics flowed away from walls [235].

There are two types of multiphase models to simulate flow boiling heat transfer of pure fluids: the Eulerian-Eulerian model with the wall heat flux partitioning (EE-RPI) [235, 236] and the Volume of Fluid model coupled with the LEE method (VOF-LEE) [237]. The RPI model is a

mathematical framework developed by the Rensselaer Polytechnic Institute (RPI) to simulate the interactions between different phases in multiphase flow heat transfer. The VOF method is a numerical technique to track the interface between phases as they move and interact in a domain. It's often employed to accurately capture the behavior of fluid interfaces, including the deformation, breakup and coalescence.

In general, the EE-RPI method is well-suited for calculating near-wall heat fluxes, while the VOF-LEE method is focused on bubble dynamics and flow patterns to predict heat transfer performance. Specifically, the EE-RPI method is particularly suitable for highly subcooled flow boiling heat transfer in macrochannels, where nucleated bubbles occur near the heated walls but do not dominate the domain. On the other hand, the VOF-LEE model is appropriate for predicting slightly subcooled or saturated flow boiling heat transfer in mini/microchannels. This is due to its consideration of large-size bubble behaviors and flow patterns, allowing it to effectively simulate the heat transfer performance, especially at higher vapor qualities.

In the RPI model, the wall heat flux is divided into three separate components: single-phase convection (q_c), quenching (q_q), and evaporating (q_e) heat fluxes. These components depend on nucleation-related parameters such as active nucleation site density (N_a), bubble departure diameter (d_{bw}), and bubble departure frequency (f) in Figure.38 [238].

$$q_{w,RPI} = q_c + q_q + q_e \tag{2-2}$$

$$q_c = h_c \cdot (T_w - T_i) \cdot (1 - A_b)$$

$$q_e = N_a f \cdot \rho_v \left(\frac{\pi}{6} d_{bw}^3\right) \cdot h_{fg}, \quad q_q = \frac{2k_l}{\sqrt{\pi \lambda_l / f}} \cdot (T_w - T_i) A_b, \quad A_b = min\left(1, K \frac{N a \pi d_{bw}^2}{4}\right)$$

Where T_w and T_i represent the wall and liquid temperature, respectively. A_b denotes the area of influence, which indicates the fraction of heating surfaces covered by bubbles. h refers to the HTC of single-phase convective heat transfer. h_{fg} represents the latent heat. ρ_v is the vapor density. k_l and λ_l are the thermal conductivity and thermal diffusivity of liquid, respectively. In Figure.38, the onset of nucleate boiling (ONB) is defined as the point at which nucleated bubbles begin to form on hot surfaces, while the net of vapor generation (NVG) refers to the location where a large bubble escapes from the hot walls.

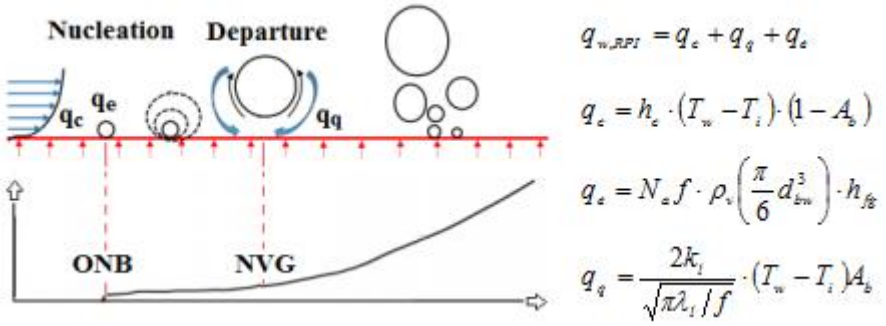


Figure.38 Illustration of subcooled flow boiling at a uniform heat flux condition

Due to the inherent complexity of boiling heat transfer on heating walls, these parameters are influenced by the operating conditions (e.g., subcooling, mass and heat fluxes), the properties of coolants (e.g., thermal conductivity and diffusivity) and heating surfaces (e.g., wettability). For example, there are many empirical correlations (e.g., 16 cases of N_a, 11 cases of d_{bw}, and 7 cases of f) developed and summarized in the literature [235]. However, it is difficult to find a combination of correlations that can accurately predict flow boiling heat transfer in a wide range of applications due to these limitations.

As discussed earlier, two crucial steps influence the accuracy of numerical simulation results: capturing interfaces between phases and calculating mass transfer at interfacial surfaces. For pure fluids, several methods have been proposed to track the interfaces, including Level Set, VOF, Lattice-Boltzmann and hybrid methods like CLSVOF. Moreover, various models for the mass transfer have been introduced, such as the Rankine-Hugoniot model, Schrage model and Lee model [237, 239].

Rankin-Hugoniot $$\dot{m}_g = -\dot{m}_f = \frac{\vec{n}\cdot(k_f \nabla T_f - k_g \nabla T_g)}{h_{fg}} \quad (2\text{-}3)$$

Schrage $$\dot{m}_g = -\dot{m}_f = \frac{2}{2-\gamma_c}\sqrt{\frac{M}{2\pi R}}\left(\gamma_c \frac{p_g}{\sqrt{T_{g,sat}}} - \gamma_c \frac{p_f}{\sqrt{T_{f,sat}}}\right) \quad (2\text{-}4)$$

Lee $$S_g = -S_f = r_i \alpha_f \rho_f \left|\frac{T - T_{sat}}{T_{sat}}\right|, \ T > T_{sat} \quad (2\text{-}5)$$

In summary, both the RPI model and the VOF method have their strengths and weaknesses to study multiphase flow and heat transfer. The selection among these methods depends on the specific research goals, desired level of accuracy, available computational resources and the nature of the multiphase flow. The VOF method is excellent at capturing fluid interfaces and tracking movements accurately, which is crucial in multiphase flow heat transfer. It is mainly due to its simplicity, computational efficiency and accurate mass conservation. Additionally, its limitation in accurately predicting interface profiles is alleviated by coupling the geometric reconstruction scheme in ANSYS [240].

While the Rankine-Hugoniot method (Eqn.2-3) is a physics-based model that relies on energy transferring across the vapor-liquid interface through thermal conduction, the Schrage model (Eqn.2-4) is linked to temperature and pressure based on the gas kinetic theory. However, the applicability of those methods is limited as the mass source term ($S_{vol.} = \dot{m}|\nabla \alpha_g|$) is non-zero at interfaces, indicating that the phase change only occurs at interfaces. Therefore, in order to broaden its scope, Lee [241] simplified the Schrage model by making assumptions that entail phase change taking place at a constant pressure and in a quasi-thermo-equilibrium state driven by the disparity between the local temperature and the saturated temperature. In other words, the VOF-LEE model can be adopted to simulate full-scale flow boiling heat transfer from subcooled to saturated boiling cases.

In present work, the VOF-LEE method was selected to predict the heat transfer performance of flow boiling in microchannels. Several simulation cases in the literature are summarized in Table.14. For example, Fang et al. [242] investigated the heat transfer performance of flow boiling in a microchannel featuring vapor-venting capabilities with the utilization of a porous membrane. The results revealed that this novel microchannel led to a significant reduction in pressure drop, prevention of flow instabilities, and mitigation of local dryout occurrences.

Wong and Chong [243] applied the VOF-LEE method to investigate the transition of water flow boiling from single-phase flow to the onset of nucleation in a microchannel. Cheng et al. [244] simulated the growth of individual bubbles and Wei et al. [245] studied the behaviors of multiple bubbles in subcooled flow boiling. Both studies compared the bubble growth rates

with experimental data and the correlations documented in literature. Prajapati et al. [246] conducted researches on the dynamic behavior of bubbles, the heat transfer performance and instability in a segmented microchannel. The bubble transition process predicted by the CFD method aligned well with the observed visual results. Furthermore, Luo et al. [247] studied the effect of different manifold arrangements on flow boiling of HFE-7100 in a microchannel. Their findings indicated that the H and U-shaped microchannels exhibited better heat transfer performance and lower pressure drop.

Furthermore, Kim et al. [248] investigated the effects of wettability and flow orientations on H_2O flow boiling heat transfer in a microchannel by a VOF method [249]. The results were consistent with experimental data, showing that the wall superheat at the boiling point was smaller in hydrophobic channels. Additionally, the CHF on hydrophilic surfaces was higher than on hydrophobic surfaces at mass fluxes below 100 kg/(m^2·s), but lower at mass fluxes larger than 200kg/(m^2·s). Subsequently, they [256] conducted further research on the effects of different heterogeneous wettability on flow boiling in microchannels by the VOF-LEE method. The parallel surface showed the lowest average surface temperature at mass fluxes less than 500 kg/(m^2·s) due to enhanced bubble movements. In contrast, the dotted surface had the best performance at mass fluxes larger than 500 kg/(m^2·s) because of a higher density of active nucleation sites at 350 kW/m^2. Additionally, an optimal value of hydrophobic area fraction was found, such as 0.165 for the crosswise pattern and 0.32 for the parallel pattern. A detailed analysis revealed that a smaller hydrophobic area could curtail the bubble nucleation density, while a larger hydrophobic area could impede the bubble movement away from the nucleation sites and stimulate the rate of bubble growth. Generally, the VOF-LEE method is capable to predict the heat transfer performance and bubble dynamic behaviors of multiphase flow in microchannel in present research.

The mathematical model is presented as follows.

$$S_g = -S_f = r_i \alpha_f \rho_f \left| \frac{T - T_{sat}}{T_{sat}} \right|, \quad T > T_{sat}$$

Where, T and T_{sat} represent local temperature and saturated temperature of coolants, while α and ρ denote the volume fraction and density in the calculating cell, respectively. Importantly,

r_i is an empirical relaxation factor, with a wide range from 0.1 to 10^6 s^{-1}, corresponding to the minimum saturation temperature deviation listed in Table.14.

Table.14 Heat transfer performance of flow boiling heat transfer by VOF-LEE method

Year	Fluid	/	Cross section	r_i	r_v	T_{sub}	G	Scheme
/	/	/	mm	/	/	K	kg/(m^2.s)	/
2015 [250]	Pentane	3D	D8.9	0.1	0.1	1	134	PISO
2019 [251]	Acetone	3D	D12	0.1	0.1	5	0.045	/
2019 [252]	H_2O	2D	W50	0.1	0.1	/	/	PISO
2017 [253]	HFE7100	2D	W6	1	1	5	20-210	PISO
2019 [240]	FC72	2D	W5	10	10	~34	446~2432	PISO
2020 [254]	FC72	3D	W2.5×H5	100	0.1	~36	176~2453	PISO
2008 [255]	R141B	3D	D6	100	100	8-10	120-180	PISO
2011 [245]	H_2O	3D	W2×H5	100	100	10	320	PISO
2010 [242]	H_2O	3D	W0.15×H0.3	100	100	3.5	270	PISO
2015 [243]	H_2O	3D	W0.22×H0.26	100	100	77	115	PISO
2020 [247]	HFE7100	3D	W0.05×H0.2	100	10^6	7	100~600	/
2020 [256]	H_2O	3D	W1.5×H0.7	100	100	0	100-800	PISO
2019 [244]	H_2O	2D	/	800	800	Pool boiling		PISO
2020 [257]	H_2O	3D	W0.315×H0.6	1000	1000	20	250-500	PISO
2018 [258]	R134a	3D	D8.38	5500	5500	Con	100-400	SIMPLE
2015 [259]	FC72	2D	D11.89	33315	33315	Con	184-459	PISO

Additionally, the r_i values for evaporation and condensation factors are based on assumptions of small subcooled, cross-section area and inlet velocity conditions [252]. Thus, a major challenge for applying the LEE model is choosing an appropriate value, as it greatly impacts predictions of surface temperatures and pressures, flow patterns and interfacial behaviors in microchannels [240]. Literature reviews indicate that the values depend on some factors such as the mesh sizes, computational time steps, channel geometries and operational conditions

[247]. While a small one can cause significant temperature deviations between interfacial and saturation temperatures, a large one led to the numerical convergence problems.

Therefore, the factor, r_i, should be validated by comparing the heat transfer performance and bubble dynamics with experimental data. For instance, Lee et al. [240] investigated the effect of r_i ranging from 5 to 80 on local wall temperature and bubble behaviors of subcooled flow boiling in a 2D channel at the same conditions. Finally, a value of 10 was chosen as the most appropriate compared to experimental results. Furthermore, Lee et al. [252] studied the shear-lift effect on highly subcooled flow boiling in a 3D channel and selected a value of 100 from 5 cases (in ranges of 10-1000) to predict the bubble formations, interfacial behavior and wall temperature with experimental data.

2.3.2-Flow boiling of binary mixture in microchannel

The literature review indicates that the VOF-LEE method is capable to conduct studies on the heat transfer of pure working fluids flow boiling in microchannels, due to its simplicity, low computational requirements and accuracy in maintaining mass conservation [258]. However, flow boiling heat transfer of the miscible mixture like the NH_3/H_2O mixture is more intricate compared to that of pure fluids [260]. For example, the mass and heat transfers, occurring at the interface between the liquid and gas phases in the miscible mixture, exhibit variability and dependence on several factors such as the variable saturated concentration of the more volatile component in the miscible mixture. Therefore, it is difficult to calculate by traditional models like the LEE model.

In order to simulate flow boiling heat transfer of the miscible mixture, the VOF model needs to be modified based on some specific assumptions in literature. For example, Banerjee [261] utilized the VOF method coupled with the effective diffusion model of the liquid mixture to simulate flow boiling of the ethanol/isooctane mixture in a 2D macro-scale stratified domain. Similarly, Zhang et al. [262] employed the same approach to investigate flow boiling of the isobutene/pentane mixture within a 2D macro-scale domain. Lima et al. [263] investigated the steady-state heat transfer performance of the NH_3/H_2O mixture in a 2D macro-scale plate by considering the gas and liquid mixture as the separate uniform phases. However, there have

been limited numerical investigations carried out on flow boiling heat transfer performance and bubble dynamics of the zeotropic mixture in microchannels. The NH_3/H_2O mixture is a complex zeotropic mixture, as it comprises more than two species such as $NH_3 \cdot H_2O$, NH_4^+, NH_2^-, OH^- and H_3O^+. Therefore, an exclusive mass diffusion model of the NH_3/H_2O mixture is essential to predict the heat transfer performance. Unfortunately, no such model is proposed or available for reference at present.

Moreover, it costs a tremendous of computing resources when the mass diffusion of multiple species is coupled with the VOF model in microchannels. For the cases of unsteady flow and heat transfer, it is essential to ensure that the maximum Courant number remains below one to maintain the stability and accuracy in simulations. In other words, the smaller the spatial size of a grid, the smaller the time step size. Therefore, it requires huge computational resources and time for simulating flow boiling in microchannels. Furthermore, the VOF method relies on solving the Navier-Stokes equations coupled with the continuity equation of the volume fraction. The interfaces among distinct species are tracked by monitoring the volume fractions of different fluid phases in each computational cell. Hence, when the variety of substances in fluid increases, the calculating workload will multiply significantly. Therefore, it is necessary to undertake a distinct modification of the original VOF-LEE method in order to simulate multiphase heat transfer of the zeotropic mixture based on reasonable hypothetical conditions.

In summary, the VOF-LEE method is one of the promising approaches for investigating the heat transfer performance and bubble dynamics of pure fluids in microchannels. Furthermore, though the original VOF-LEE method may not be directly applicable for the miscible mixture, this method can also be competent for multiphase heat transfer studies through the appropriate model adjustments under reasonable assumptions. Meanwhile, there are notable distinctions between flow boiling heat transfer of the NH_3/H_2O mixture and the conventional refrigerants. Therefore, special modifications are required for the original VOF-LEE method to investigate the flow boiling heat transfer of the NH_3/H_2O mixture in microchannels.

A new modified VOF/LEE model was proposed by the author [232] and employed to conduct the studies on flow boiling heat transfer of the NH_3/H_2O mixture in microchannels. Generally,

the NH_3/H_2O mixture is presumed to be a pure fluid with the same thermophysical properties of binary mixture in vapor and liquid states. Additionally, the mass transfer at the liquid-vapor interface of the NH_3/H_2O mixture is driven by the difference between local concentration and the saturation concentration of NH_3 in the liquid phase. This is in contrast to the case of a pure fluid, where the difference lies between the local temperature and the saturation temperature. The impacts of surface morphology, including factors like wettability, are taken into account in this modified method. It is achieved by selecting an appropriate factor as referenced in the literature [264]. The detailed mathematical model will be presented as follows.

2.3.3-Flow boiling of functional fluids in microchannel

As discussed before, there are two types of functional fluids available to enhance heat transfer performance in microchannels: nanofluids containing high thermal conductivity particles, and PCM slurries incorporating encapsulated phase change materials in base fluids. Furthermore, two approaches are utilized for simulating the convective heat transfer of functional fluids in the literature: the single-phase method and the two-phase method, including the VOF method [233,234]. In the single-phase method, the mixture is regarded as a homogeneous fluid with a set of averaged thermophysical properties. On the other hand, the two-phase method treats the liquid-particle mixture as comprising two distinct phases: liquid and solid, with each phase characterized by its own set of properties.

By comparing single-phase and two-phase models for simulating convective heat transfer of functional fluids, it is determined that the VOF model is a suitable choice for functional fluids with a high concentration of particles. Additionally, it demonstrates commendable calculating accuracy compared with experimental data, while maintaining acceptable computational costs [233, 265, 266]. Moreover, the effective heat capacity method has been employed in relevant simulations to consider the impact of EPCM melting on the heat transfer performance [267].

In conclusion, the integration of the VOF model with suitable phase change models appears to be a viable option for effectively simulating flow boiling heat transfer of functional fluids in microchannels. For example, Mohammed et al. [230] and Soleimani et al. [268] employed the VOF-LEE model to simulate flow boiling heat transfer of nanofluids including acetone/$ZnBr_2$

/ZnO and HFE-7100/Al_2O_3 in mini/microchannels. The nanoparticles were represented as a cloud-like phase, individually.

2.4-Summary

Flow boiling in microchannels is distinguished by a notable surface-to-volume ratio and high heat transfer performance, such as heat flux and HTC. This has attracted extensive attention owing to its capacity to meet the heat dissipation demands of electronic devices. However, its application faces several challenges including elevated flow resistance, deterioration of heat dissipation capacity along the flow direction and instability under high heat flux conditions. So far, a considerable number of solutions and approaches have been proposed and researched in the literature to mitigate flow instability and enhance the heat transfer performance of flow boiling in microchannels. These include the modification of coolant physical properties, the structures and geometric parameters of sinks, as well as the heat surface morphology. Among those methods, choosing a coolant with excellent thermophysical properties is one of the most important methods, as it not only directly impacts the heat dissipation capacity, but also could be interacted with the other approaches.

Theoretical analysis indicates that there are several physical properties of coolants that affect the heat transfer performance of flow boiling in microchannels, such as specific heat capacity, thermal conductivity, wettability and surface tension, latent heat of evaporating and melting, etc. Therefore, it is a potentially promising approach to enhance heat transfer performance by selecting coolants with high latent heat of evaporation and incorporating functional particles to increase thermal conductivity and effective specific heat capacity in cooling conditions.

Theoretical analysis indicates that various thermophysical properties of coolants influence the heat transfer performance of flow boiling in microchannels. These properties include specific heat capacity, thermal conductivity, wettability, surface tension, latent heat of evaporation and melting, etc. Hence, it presents a promising approach for enhancing heat transfer efficiency by opting for coolants with a high latent heat of evaporation (such as the NH_3/H_2O mixture) and incorporating functional particles (such as nanofluids and PCM slurries) to augment thermal conductivity and effective specific heat capacity within the cooling conditions. However, it is

worth noting that the addition of functional particles into coolants might potentially introduce adverse effects on flow boiling heat transfer in microchannels. These effects could increase pressure drop and reduce the heat transfer capability mainly due to the elevated viscosity and the deposition of particles on heating surfaces. Hence, there is an urgent necessity to conduct researches on the mutual effects of different physical properties of coolants on heat transfer performance under a wide range of operating conditions.

Numerical simulation is an effective and feasible method for conducting the aforementioned studies on flow boiling heat transfer performance and mechanism analyses. According to the literature review and practical assessment of simulation methods in this chapter, the VOF method is employed to analyze the heat transfer performance in microchannels. Additionally, specific simulation methods have been adopted to conduct the detailed performance analyses, tailored to various research subjects and objectives in different aspects.

Chapter-3 Simulation methods for multiphase flow heat transfer

3.1-Introduction

As mentioned previously, the multiphase VOF method is adopted to simulate the heat transfer performance of different coolants flow boiling in microchannels, including pure fluid, binary mixture and functional fluids. This chapter is to introduce the important numerical simulation methods utilized in this study. These methods encompass physical properties of the NH_3/H_2O mixture, the VOF method, the liquid-vapor and solid-liquid phase change methods, dynamic meshing method and boundary conditions. The mathematical models and methods utilized in different chapters are illustrated in the following diagram.

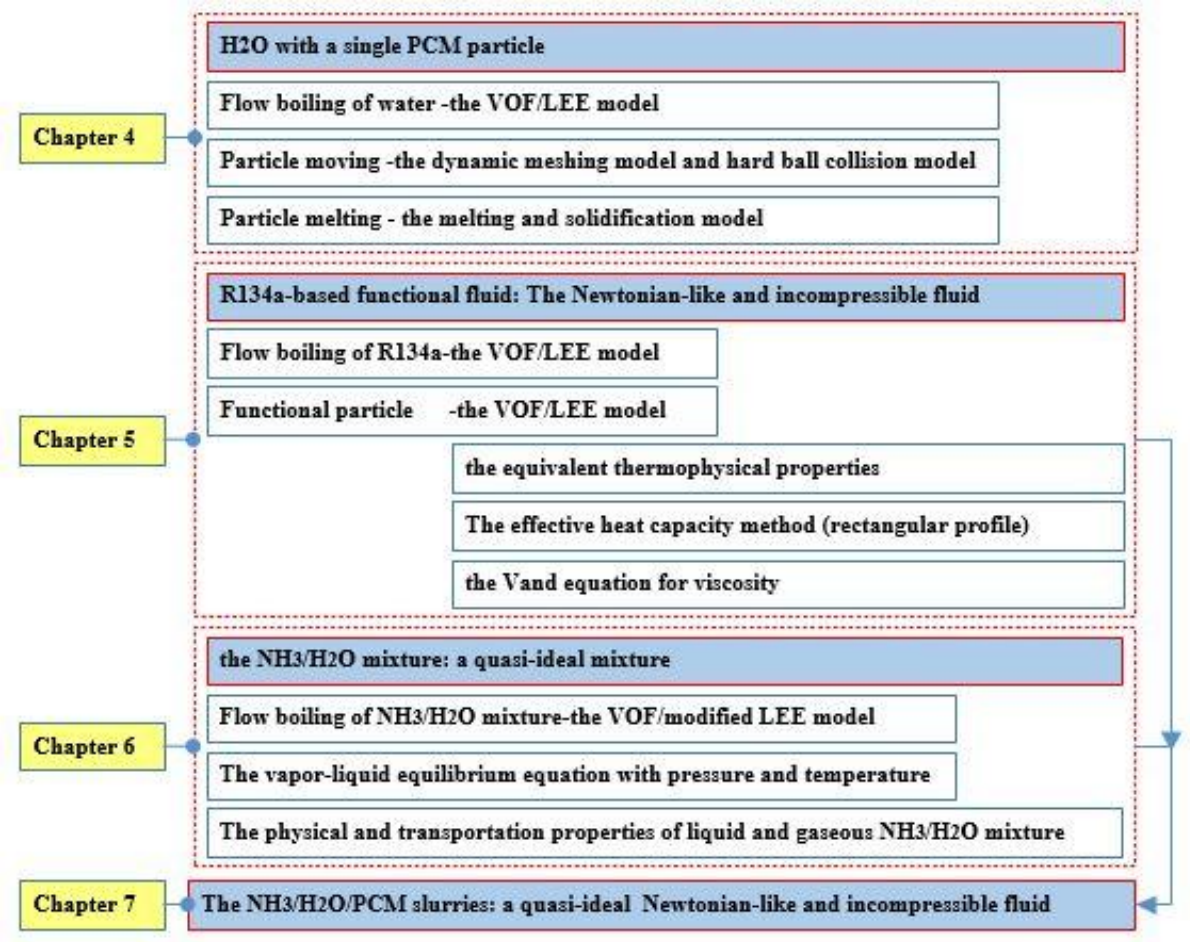


Figure.39 The main assumptions and multiphase mass and heat transfer models adopted in different chapters

As discussed before, the present work primarily focuses on studying the transient heat transfer performance of subcooled flow boiling in microchannels by using different functional fluids. More precisely, it includes the transitional processes from the single-phase laminar flow to the multiphase turbulent flow. In present work, the warm start approach is utilized to reduce the convergence process of transient simulations while providing accurate results. This approach involves using the convergent results of a steady-state single phase laminar flow as the initial conditions for the subsequent transient simulation of flow boiling heat transfer. This can help reduce the computing time and improve the accuracy of the transient simulations by starting from a state that closely resembles the realistic flow conditions [278].

In general, the realizable k-ε model is chosen as the turbulent calculation model for scenarios involving turbulent flow boiling processes. This model is well-suited for simulating subcooled flow boiling processes, encompassing the transition from laminar flow to turbulent boiling flow. Additionally, the coupling of pressure and velocity is achieved through the utilization of the PISO algorithm. The momentum and energy equations are discretized by a second-order upwind scheme. Furthermore, the pressure and volume fraction interpolations are performed by the PRESTO and the Geo-Reconstruct discretization methods, respectively.

To ensure the simulation stability, a variable time step is chosen with the maximum Global Courant number less than 0.25. The convergence criteria are achieved by setting the absolute residuals to a value of $1e^{-4}$. Those measures contribute to accurate and reliable simulations of flow boiling in microchannels.

3.2-General physical properties of coolants

In this study, a variety of fluids are chosen as coolants. These include pure water in Chapter 4, pure R134a and R134a-based functional fluids in Chapter 5, along with a zeotropic mixture of the NH_3/H_2O mixture and its functional fluids in Chapters 6 and Chapters 7. The multiphase VOF model is utilized for capturing the interfaces of different phases, such as vapors, liquids and suspended solid particles during flow boiling of liquids and the melting of phase change material in particles. Therefore, it is crucial to select an appropriate mathematical model for each phase to accurately calculate the physical properties in ANSYS by suitable methods.

Generally, the main physical properties of pure materials, such as H_2O, R134a, Al_2O_3, and n-Octadecane, are calculated by built-in methods in ANSYS software or set by reference data in the literature. However, there are no suitable calculation packages embedded in ANSYS for the properties of NH_3/H_2O mixture. Therefore, it is necessary to choose a set of mathematical equations and then compile them into the ANSYS by using User-Defined Functions (UDFs).

Different with pure fluids like water, the NH_3/H_2O mixture consists of more than one species in the liquid and gas phases. The properties play a dominant role in determining the accuracy and computational speed of simulations. Therefore, it is crucial to choose simple and efficient mathematical models to accurately calculate the physical and transport properties. Recently, some simplified formulations have been adopted to calculate the vapor-liquid equilibrium and physical properties of the NH_3/H_2O mixture in applications. These properties include density and thermal conductivity, the critical temperature and critical pressure, enthalpy and specific heat capacity, dynamic viscosity and surface tension [269,270,271,272].

The vapor-liquid equilibrium of the NH_3/H_2O mixture is as follows:

$$\begin{cases} T(p,x) = T_0 \sum_i a_i (1-x)^{m_i} \left[ln\left(\frac{p_0}{p}\right) \right]^{n_i} \\ T(p,y) = T_0 \sum_i a_i (1-y)^{m_i/4} \left[ln\left(\frac{p_0}{p}\right) \right]^{n_i} \end{cases} \tag{3-1}$$

$$y(p,x) = 1 - exp\left[ln\,(1-x) \sum_i a_i \left(\frac{p}{p_0}\right)^{m_i} x^{n_i/3} \right] \tag{3-2}$$

$$\begin{cases} h_l(T,x) = h_0 \sum_i a_i \left(\frac{T}{T_0} - 1\right)^{m_i} x^{n_i} \\ h_g(T,y) = h_0 \sum_i a_i \left(1 - \frac{T}{T_0}\right)^{m_i} (1-y)^{n_i/4} \end{cases} \tag{3-3}$$

The latent heat of the saturated NH_3/H_2O mixture:

$$\Delta h_{sat} = h_{g,sat}(p,T) - h_{l,sat}(p,T) \tag{3-4}$$

Where T and p represent the temperature (K) and pressure (Pa), respectively. The variables x and y denote the molar fractions of NH_3 in vapor and liquid phases, while h_g and h_l represent the enthalpies of the vapor and liquid mixture, respectively. Δh_{sat} corresponds to latent heat of evaporation (kJ/kg).

The critical temperature and pressure of mixture:

$$T_{c,m} = \sum_{i=0}^{4} a_i x^i \qquad p_{c,m} = \sum_{i=0}^{4} b_i x^i \tag{3-5}$$

The main thermophysical properties of the liquid mixture include:

$$c_{pm}(T^*, x) = x c_{p_{\mathrm{NH_3}}}\left(T^*_{\mathrm{NH_3}}\right) + (1-x) c_{pH_2O}\left(T^*_{H_2O}\right) \tag{3-6}$$

$$\lambda_m = x\lambda_{\mathrm{NH_3}}\left(\rho^+_{\mathrm{NH_3}}\right) + (1-x)\lambda_{H_2O}\left(T^*_{H_2O}\right) \tag{3-7}$$

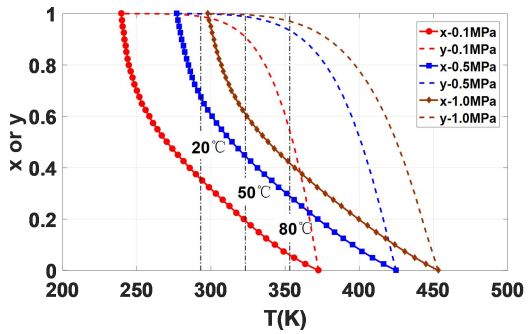
$$\ln\mu_m = x \cdot \ln\mu_{\mathrm{NH_3}}\left(T^*_{\mathrm{NH_3}}\right) + (1-x)\mu_{H_2O}\left(T^*_{H_2O}\right) + \Delta\mu_m(x) \tag{3-8}$$

$$\sigma_m = x \cdot \sigma_{\mathrm{NH_3}}\left(T^*_{\mathrm{NH_3}}\right) + (1-x)\sigma_{H_2O}\left(T^*_{H_2O}\right) + \Delta\sigma_m(x) \tag{3-9}$$

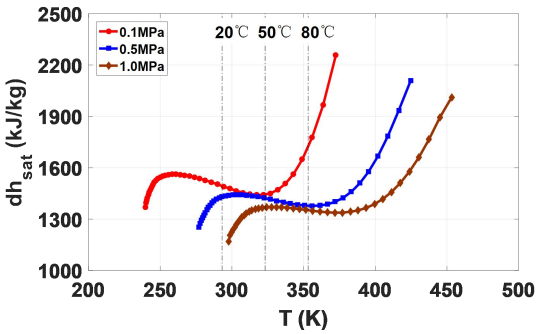
$$\rho_m = x \cdot \rho_{\mathrm{NH_3}}\left(T^*_{\mathrm{NH_3}}\right) + (1-x) \cdot \rho_{H_2O}\left(T^*_{H_2O}\right) + \Delta\rho_m(x) \tag{3-10}$$

Where, x and y represent the molar fractions of NH_3 in the liquid and vapor phases, while the variables h_l and h_g are specific enthalpies (kJ/kg) of the liquid and vapor phases, respectively. Δh_{sat} is the specific latent heat of evaporation (kJ/kg). $c_p, \lambda, \mu, \sigma$ and ρ are the specific heat capacity (kJ/(kg·K)), thermal conductivity (mW/(m·K)), dynamic viscosity (μPa·s), surface tension (mN/m) and density (kg/m³) of the mixture, respectively. The detailed mathematical models along with their corresponding coefficients can be found in Appendix-1.

These physical and transport properties, along with the NH_3 mole fractions in the saturated liquid and gaseous phases of the NH_3/H_2O mixture, are plotted as follows.

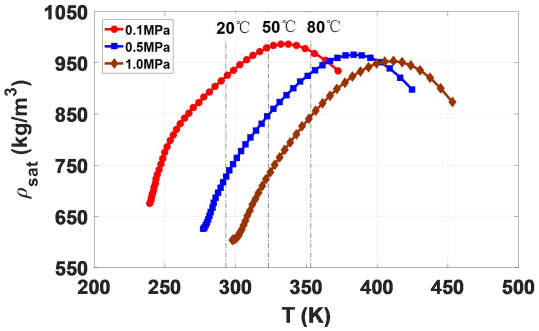


(a)NH_3 mole fraction

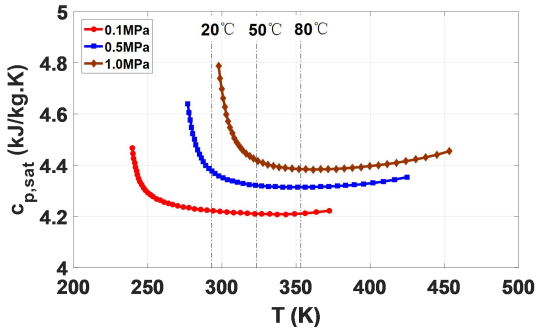


(b)Specific latent heat

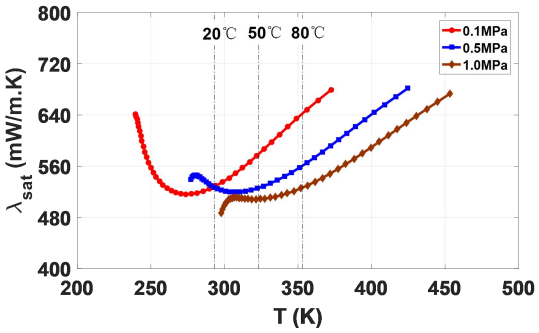
Figure.40 The specific evaporation latent heat between the saturated liquid or gas mixture



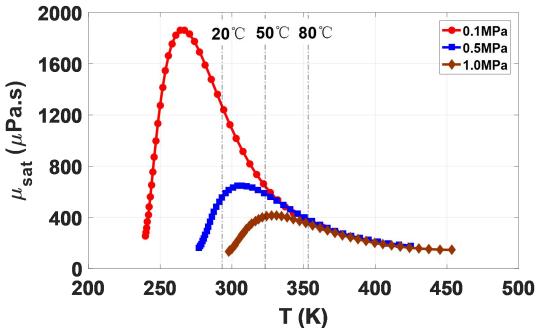
(a)Density



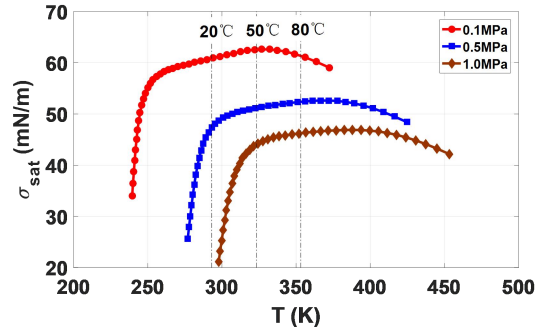
(b)Specific heat



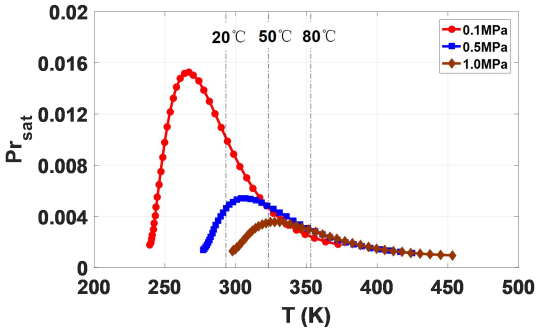
(c)Thermal conductivity



(d)Dynamic viscosity



(e)Surface tension



(f) Pr

Figure.41 The main properties of the saturated liquid and gaseous NH_3/H_2O mixture

3.3-The multiphase VOF Method

The volume of fluid (VOF) model is widely employed to study complex fluid interactions and multiphase flows, as it could accurately track the interfaces between liquid and vapor phases. It relies on solving a set of the Navier-Stokes equations coupled with the continuity equation for the volume fraction of different fluid phases in each computational cell [260]. It assigns a value between 0 and 1 to represent the portion of a cell occupied by a specific phase of fluids, thereby capturing the movement of liquid-gas boundaries during phase change processes.

For the short horizontal microchannel cases discussed in present work, the gravitational effect is neglected in the 2D domain. It has been observed that the gravity has a minimal impact on flow boiling in microchannels due to the increasingly dominant influence of surface tension, particularly when the channel size is less than 0.5mm [273].

The continuity equation for each phase is as follows:

$$\frac{\partial}{\partial t}\left(\alpha_q \rho_q\right) + \nabla \cdot \left(\alpha_q \rho_q \vec{v}_q\right) = S_{m,pq} \tag{3-11}$$

$$\sum_{q=1}^{n} \alpha_q = 1 \tag{3-12}$$

Whereα_q,ρ_q, and$\vec{v}_q$ denote the volume fraction, density, and velocity of phase q in each cell, respectively. $S_{m,pq}$ represents the mass source term (kg/s) from phase p to phase q, which can be calculated using the phase change model. Taking the case of R134a-based functional fluid as example, the mass transfer between the liquid and vapor phases of R134a is calculated by using the LEE model, while the values for the mass transfer between the particle cloud phase and the liquid and vapor phases of R134a are set to zero.

The momentum and energy equations for each phase are as follows:

$$\frac{\partial}{\partial t}(\rho\vec{v}) + \nabla \cdot (\rho\vec{v}\vec{v}) = -\nabla p + \nabla \cdot [\mu(\nabla\vec{v} + \nabla\vec{v}^T)] + \vec{F}_{surf} \tag{3-13}$$

$$\frac{\partial}{\partial t}(\rho E) + \nabla \cdot [\vec{v}(\rho E + p)] = \nabla \cdot (k_{\text{eff}}\nabla T) + S_h \tag{3-14}$$

Where densityρ, dynamic viscosityμ and effective thermal conductivityk_{eff} are the volume-averaged variables, energy E and temperature$T$ are the mass-averaged parameters in each cell.

$$\rho = \sum_{q=1}^{n} \alpha_q \rho_q \tag{3-15}$$

$$E = \sum_{q=1}^{n} \alpha_q \rho_q E_q \Big/ \sum_{q=1}^{n} \alpha_\rho \rho_q \tag{3-16}$$

Where E_q for each phase is based on the specific heat at a shared temperature in the cell, the surface tension force $\vec{F}_{surf}$ is considered a source in the momentum equation. It is calculated by using the continuum surface force method (CSF) as follows [274].

$$\vec{F}_{surf} = \sigma \frac{\rho \kappa \nabla \alpha}{(\rho_p + \rho_q)/2} \tag{3-17}$$

Where κ is the local interface curvature and σ is the surface tension coefficient.

3.4-Phase change model of evaporation

For coolants, two types of liquids are chosen in present work: pure fluids such as water and R134a, and a zeotropic binary mixture of NH_3/H_2O. Consequently, two mathematical models are adopted to calculate the mass and heat transfer during the evaporation.

3.4.1-Pure fluids

The Lee model, a simplified version of the Schrage model, is employed to calculate the rates of mass and heat transfer at the liquid-vapor interface of pure fluids. This model considers the quasi-thermo-equilibrium phase change occurring at a constant pressure. Mass transfer across the interfaces is driven by the deviation of the local fluid temperature from the corresponding saturated temperature of the fluid in the cells [275].

$$\begin{cases} S_g = -S_f = -r_i \alpha_g \rho_g \left| \dfrac{T - T_{sat}}{T_{sat}} \right|, & T < T_{sat} \\ S_g = -S_f = +r_i \alpha_f \rho_f \left| \dfrac{T - T_{sat}}{T_{sat}} \right|, & T > T_{sat} \end{cases} \tag{3-18}$$

$$S_h = S_g \cdot q_{LH} \tag{3-19}$$

Where q_{LH} represents latent heat of evaporation at the operating pressure, r_i is an empirical relaxation factor, also known as the mass transfer intensity factor, measured in units of s^{-1}.

The value of r_i ranges from 0.1 to 10^7 in the literature [237]. It is determined by factors such as the mesh sizes, time steps of numerical simulation, the operating conditions, geometric configurations and parameters of channels in specific cases [247,276]. Moreover, it has been observed that a small value of r_i may cause the temperature in interfacial cells to deviate from the saturation temperature, while a large one increases the difficulty to achieve convergence in the governing equations. Some simulation cases related to this aspect are listed in Table.14.

Generally, the selection of r_i values for various cases in present work should be validated by comparing simulation results with experimental data, such as the HTC and pressure drop. For instance, a r_i value of 100 was chosen for water in Chapter 4. This practice ensures that the chosen value accurately captures the characteristics of particular system under investigation.

3.4.2-NH_3/H_2O

As discussed before, the original Lee model is only applicable to pure fluids. For a zeotropic mixture such as NH_3/H_2O, the mass transfer of different components between different phases is crucial in the non-isothermal evaporating process. The mass diffusion of each component in the mixture, primarily characterized by the concentration gradients of respective species, is considered as a key factor affecting the heat transfer performance [104].

According to the detailed analysis presented in the section 2.3.2, it is essential to ascertain an efficient and feasible computational approach capable of accurately predicting flow boiling of NH_3/H_2O in microchannels. In this study, the VOF method is integrated with a modified LEE model and a treatment of the quasi-ideal properties of the zeotropic mixture, aiming to predict flow boiling of NH_3/H_2O in microchannels. This adapted LEE model, which was proposed by author [237], is employed for calculating the species transport in each phase at the interfaces in present work. The details are presented as follows.

(1) Species transport in the liquid and gaseous mixture. The NH_3/H_2O mixture is treated as two distinct homogeneous phases: the saturated liquid phase and the saturated gaseous phase. Consequently, the species diffusion of different components in the same phase is disregarded in this approach. To compensate this shortage, the effective properties of each saturated phase

were calculated by some industrial calculating correlations. Those thermophysical properties are correlated with local saturated concentration of the NH_3/H_2O mixture, which depends on local pressure and temperature.

(2) Mass transfer at the liquid-gas interfaces. The original LEE model is a widely-accepted version of Schrage model based on the kinetic theory of gases. It addresses the quasi-thermo-equilibrium phase changes under the constant pressure conditions, driven by the temperature deviation between the local temperature and the saturated value of pure fluid. Likewise, the phase change of the NH_3/H_2O mixture could be triggered by the NH_3 concentration deviation between the local concentration and the saturated value. Therefore, it is a feasible approach to modify the original LEE model for flow boiling of NH_3/H_2O in microchannels based on some reasonable assumptions and an analysis of phase change processes.

The non-isothermal phase change flow boiling process of NH_3/H_2O is described as follows:

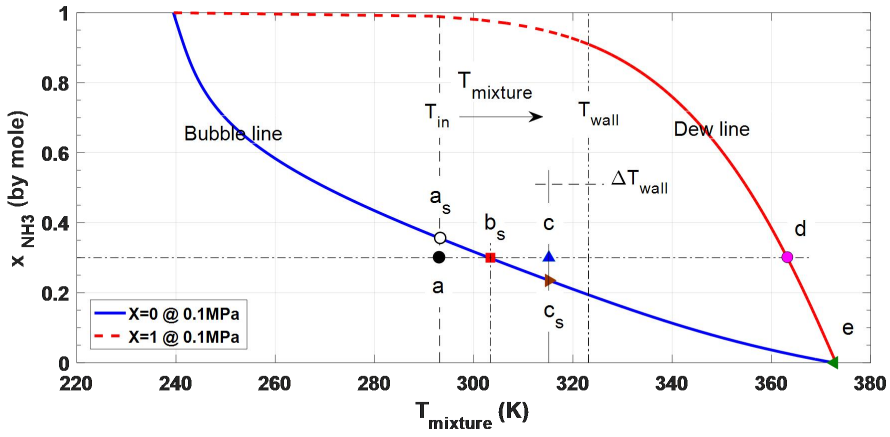


Figure.42 Phase diagram of multiphase flow of NH_3/H_2O mixture at constant pressure

In Figure.42, the inlet temperature and the concentration of the NH_3/H_2O mixture are denoted as T_a and x_a, respectively (at point **a**). As the inlet concentration x_a is lower than the saturated value x_{as}, the mixture remains in an undersaturated liquid state until reaching the bubble point $\mathbf{b_s}$. When the mixture temperature reaches the saturated temperature T_{bs} corresponding to the local pressure and concentration, the bubble nucleation occurs at the heating surfaces. Due to the non-isothermal phase change nature of the NH_3/H_2O mixture, the temperature of liquid saturated mixture increases gradually between T_{bs} and T_d (at dew point **d**), with the decrease

of the concentration of the liquid NH_3/H_2O mixture. As the evaporating process continues, the concentration of easily volatile component NH_3 in the liquid decreases, leading to an increase of the saturated temperature. For a given pressure, there is a one-to-one correspondence between the saturation temperature T_s and the saturation concentration x_s. Therefore, this non-isothermal boiling process can be explained in another perspective. When the fluid temperature increased to point **c**, the corresponding NH_3 concentration x_c is greater than local saturation concentration x_{cs} at a transient non-equilibrium evaporating state. Hence, the unmatched concentration Δx can be seen as the driving force for the evaporation [232].

Therefore, the primary driving force for mass transfer of the NH_3/H_2O mixture at interfaces is assumed to be the difference between the local concentration and the saturated concentration of NH_3/H_2O (which are functions of local temperature and pressure). Consequently, the mass transfer rate is considered to be proportional to the deviation in NH_3 concentration at the local level. Since the liquid and gas phases are initially treated as separate homogeneous phases, the concentration difference can be approximated as $\Delta x \approx x_a - x_{cs}$. Accordingly, the Lee model can be modified as follows:

$$\begin{cases} S_g = -S_f = -r_i \alpha_g \rho_g \left| \dfrac{x - x_{sat}}{x_{sat}} \right|, & x < x_{sat} \\ S_g = -S_f = +r_i \alpha_f \rho_f \left| \dfrac{x - x_{sat}}{x_{sat}} \right|, & x > x_{sat} \end{cases} \tag{3-20}$$

Where S_g represents the mass transfer rate at the liquid-gas interfaces, x and x_{sat} denote the inlet and local saturated concentration of the liquid, respectively. Similar to the original LEE model, the factor r_i is an empirical coefficient that is further optimized to better describe the mass transfer and diffusion phenomena of the mixture with experimental data available at the same conditions. In this work, a value of 100 is chosen for the NH_3/H_2O mixture flow boiling, referring to the literature on refrigerates flow boiling in Table.14., and validated in Chapter 6.

Boiling heat is the product of mass transfer and the latent heat of evaporation. Therefore, the corresponding heat rate Q_g can be calculated when the mass transfer rate S_g is determined. For the NH_3/H_2O mixture, the latent heat of evaporation q_{LH} is related to the local pressure and temperature, as shown in Figure 43.

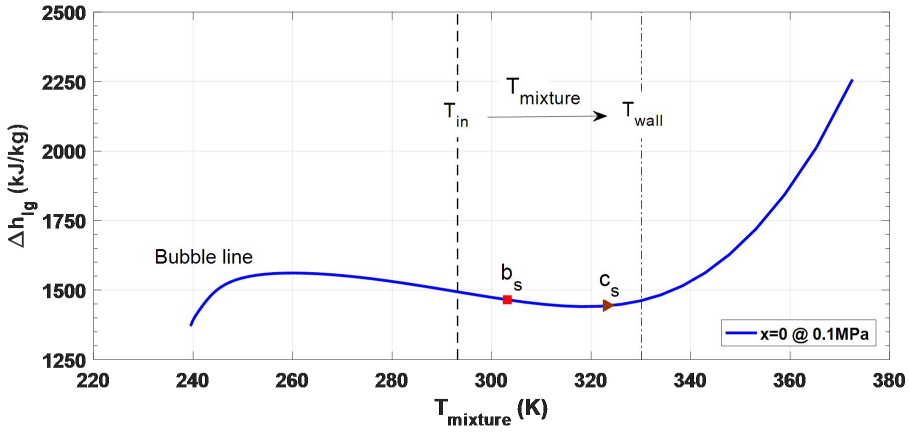


Figure.43 Latent heat of NH_3/H_2O mixture as functions temperature at 0.1MPa

3.5-Phase change model of melting

Two different models are adopted to simulate the melting and heat transfer processes of phase change material (PCM), including the melting and solidification method for a large-size PCM particle and the equivalent heat capacity method for a cloud of nanosized PCM particles.

3.5.1-The melting and solidification method

The melting and solidification of phase change material (PCM) is modelled by the enthalpy-porosity method in ANSYS Fluent. In this approach, the solid-liquid interface is not tracked explicitly, but considered as a mushy zone during the PCM melting process. Specifically, the mushy zone is treated as a "pseudo" porous zone with the porosity equal to the liquid fraction. The liquid fraction of each cell is calculated based on the enthalpy balance in each iteration, and is assigned a value of 0 for the solid phase and 1 for the liquid phase. Furthermore, this model could be utilized with the VOF model in ANSYS. Therefore, flow boiling heat transfer with a PCM particle melting in microchannels could be simulated by coupling this model with the VOF model and the dynamic meshing method in present work. The physical equations of this method are described in this section.

The energy equation is written as follows [260].

$$\frac{\partial}{\partial t}(\rho H) + \nabla \cdot (\rho \vec{v} H) = \nabla \cdot (k \nabla T) + S_{\text{melting}} \tag{3-21}$$

Where H, ρ, S_{melting} are the total enthalpy, density and source term, respectively. The total enthalpy is computed as the sum of sensible enthalpy$h$and latent heat content ΔH.

$$H = h + \Delta H = \left(h_{ref} + \int_{T_{ref}}^{T} c_p dT \right) + \beta L \tag{3-22}$$

Where$h_{ref}$and T_{ref} are the reference enthalpy and temperature, c_p,$\beta$and$L$are specific heat at a constant pressure, liquid fraction and latent heat of melting, respectively.

The liquid fraction β ranges between 0 and 1, with a value of 1 indicating pure liquid and a value of 0 representing the solid phase. It is defined as

$$\begin{cases} \beta = 0 & if\ T < T_{solidus} \\ \beta = 1 & if\ T > T_{liquidus} \\ \beta = \dfrac{T - T_{solidus}}{T_{liquidus} - T_{solidus}} & if\ T > T_{liquidus} \end{cases} \tag{3-23}$$

Where $T_{solidus}$ and $T_{liquidus}$ represent the starting and completion temperatures of PCM melting, respectively.

For the pure material, $T_{solidus}$ is the same as $T_{liquidus}$. In this case, the source term in the energy equation could be calculated based on specific heat, proposed by Voller [277].

$$S_{\text{melting}} = -\nabla \cdot (\rho \vec{v} \Delta H) \tag{3-24}$$

$$\begin{cases} \Delta H^{k+1} = \Delta H^{k} + h^{k} - c_p T_{pc} \\ \Delta H^{k+1} = max\,[\,0, \Delta H^{k+1}] \\ \Delta H^{k+1} = min\,[\,L, \Delta H^{k+1}] \end{cases} \tag{3-25}$$

Where$T_{pc}$is the melting temperature (K) of pure material and ΔH^{k+1} is the superscript referring to data of the next iteration.

The momentum equation is written as follows.

$$\frac{\partial}{\partial t}(\rho \vec{v}) + \nabla \cdot (\rho \vec{v} \vec{v}) = -\nabla p + \nabla \cdot \tau + \rho g + S_F \tag{3-26}$$

Where $\vec{v}$ and τ are the velocity of working fluid (m/s) and stress tensor, p and S_F are the static pressure (MPa) and source term respectively. The source term, caused by the reduced porosity in the mushy zone, could be calculated as the following equation.

$$S_F = \frac{(1-\beta)^2}{(\beta^3+\varepsilon)} A_{mush}(\vec{v}-\vec{v}_p) \tag{3-27}$$

Where ε is a small number to prevent the division by zero, A_{mush} is the mushy zone constant, $\vec{v}$ and $\vec{v}_p$ are the velocity of fluid and the extra force due to the pulling of solidified material out of the domain. In the present study, since an incompressible phase change material (PCM) is encapsulated in a rigid nanosize particle in present work, $\vec{v}$ and $\vec{v}_p$ are considered as zero, resulting in a source term of momentum that is also zero.

Moreover, in the case of a pure substance encapsulated in a constant-volume particle, phase change occurs at a uniform melting temperature. As a result, the impacts of species diffusion in the multiphase zones, along with the buoyancy effects stemming from variations in density due to alterations in temperature and species composition, are excluded from consideration.

3.5.2-The equivalent heat capacity method

As discussed before, the assessment reveals that it would require an unbearable consumption of computational resources and time for tracking all the nanosize PCM particles suspended in fluid within microchannels, along with accounting for the impacts of melting, movement, and mutual collisions on multiphase flow heat transfer. Therefore, it is needed to make a trade-off between computational accuracy and computation time. Consequently, a viable approach is to treat the suspended nanosize encapsulated particles as a pseudo pure fluid, resembling a cloud. This implies that the collision effects of particles on multiphase flow and heat transfer, as well as the melting time of PCM particles are not considered in this study.

The equivalent heat capacity method, often implemented with profiles like the rectangular and sinusoidal stepped profiles, is employed to simplify the thermal analysis of the encapsulated PCM particles. For example, the rectangular stepped profile divides the melting process into discrete segments characterized by a constant heat capacity. By doing so, a complex transient

simulation could be simplified while maintaining a reasonable level of accuracy. Therefore, the equivalent heat capacity method with the rectangular stepped profile [206] in Figure.44 is utilized to estimate the melting effect of the encapsulated PCM particles in microchannels.

The rectangular profile of the equivalent heat capacity of EPCM particles can be expressed as,

$$c_{p,p} = c_{p,c} + \left(\frac{T - T_1}{T_{mr}}\right) \cdot h_m \quad T_{mr} = T_2 - T_1 \tag{3-28}$$

Where $c_{p,c}$ and $c_{p,p}$ (J/kg·K) represent the specific heat capacities of PCM and EPCM particles, respectively. h_m denotes the melting latent heat of PCM. T_{mr}, T_1, and T_2 indicate the initial and final temperatures within the melting regions, respectively. The values depend on various factors, including the core and shell materials, shell thickness, and diameter of particles.

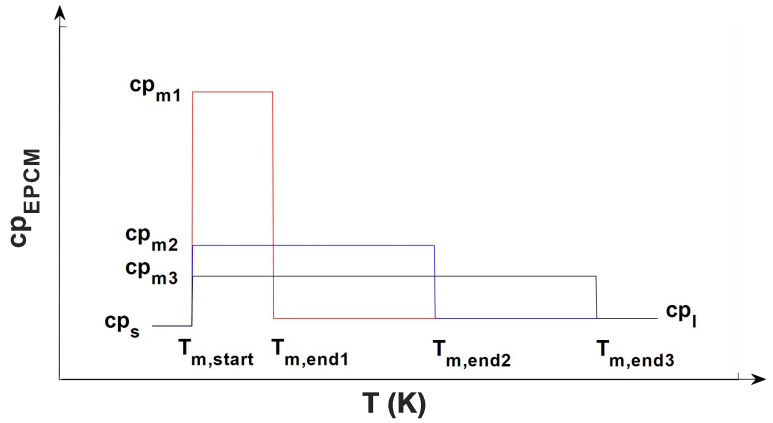


Figure.44 Rectangular profile of the equivalent heat capacity method for PCM melting

According to Figure.44, for an PCM particle with the same latent heat of melting, a narrower melting temperature range, indicates a greater absorption heat per unit temperature during the melting compared to a wider melting case. This leads to a larger enhancement of the apparent specific heat capacity c_p. In this study, the impact of the PCM melting heat absorption per unit temperature (referred to as the melting heat dissipation rate) will be investigated in relation to flow boiling heat transfer in microchannels.

3.6-Dynamic meshing method

The dynamic meshing method is commonly utilized in ANSYS for modelling the rigid-body flows in which the shape of domain changes with time due to the motion along the boundaries.

This motion could be an unprescribed motion, where the subsequent movement is determined based on the results at the current time. For example, the translation and rotational velocities could be calculated by the six-degree-of-freedom (six DOF) solver for the force balances on a solid body. The mesh is then automatically updated at each time step to generate a boundary. Furthermore, the dynamic mesh model is also applicable to multiphase flow.

This study initially investigates the impact of a melting and moving PCM particle on the heat transfer performance of pure fluid flow boiling in microchannels. In this section, the melting process of the phase-change material inside the particle is simulated by using the melting and solidification method, and the movement of the particle is calculated by the dynamic meshing method.

With respect to dynamic meshes, the conservation equation for a general scalar ϕ, applicable to all models in an arbitrary control volume, can be formulated as follows:

$$\frac{d}{dt}\int \rho\phi dV + \int \phi\left(\vec{u} - \overrightarrow{u_g}\right)\cdot d\vec{A} = \int \Gamma\nabla\phi \cdot d\vec{A} + \int S_\phi dV \tag{3-29}$$

Where ρ is the fluid density, Γ is the diffusion coefficient, S_ϕ is the source term, $\vec{u}$ and $\overrightarrow{u_g}$ are the flow velocity and the mesh velocity of the moving mesh, respectively.

The moving actions of the particle are determined by the forces and moments on the centre of gravity, including the translational motion in the inertial coordinate system and the rotational motions in the body coordinate system. These equations are solved by the six DOF solver.

In a 2D simulation case, they are calculated by the following equations [260].

$$\vec{a}_{vG} = \dot{\vec{v}}_G = \frac{1}{m}\sum \vec{f}_G \tag{3-30}$$

$$\vec{a}_{\omega B} = \dot{\vec{\omega}}_B = L^{-1}\left(\sum \vec{M}_B - \vec{\omega}_B \times L\vec{\omega}_B\right) \tag{3-31}$$

Where $m, L, \vec{a}_{vG}, \vec{a}_{\omega B}, \vec{v}_G$ and $\vec{\omega}_B$ represent the mass, inertia tensor, translational and angular acceleration, translational and angular velocity vector of the rigid EPCM particle, respectively. Additionally, $\vec{f}_G$ and $\vec{M}_G$ denote the overall force and moment vectors acting on the EPCM particle, respectively.

The moments are transformed from the inertial to body coordinates by following equations.

$$\vec{M}_B = \begin{bmatrix} cos\,\psi & sin\,\psi \\ -sin\,\psi & cos\,\psi \end{bmatrix} \vec{M}_G \tag{3-32}$$

Where ψ is the Eluer angles of the z-axis rotation.

After calculating the accelerations by solving the aforementioned equations, the translational and angular velocities are determined by the fourth-order Adams-Moulton integration method. These velocities are subsequently employed to compute the body's position for the purpose of dynamic meshing.

3.7-Initial and Boundary conditions

The present study employed the velocity-inlet and pressure-outlet conditions. To account for the potential occurrence of incomplete development and ensure fully developed flows at the outlet, the back-flow temperature was adjusted equal to the mass-averaged temperature of the forward flow at the previous time step. This adjustment was performed using a UDF code.

$$T_{\text{backflow}} = \frac{\sum_{i=1}^{m} (\rho_i u_{xi} A_i \cdot T_i)}{\sum_{i=1}^{m} (\rho_i u_{xi} A_i)}; u_{xi} > 0 \tag{3-33}$$

In this equation, $T_{backflow}$ represents the mass-averaged back-flow temperature, while ρ_i, u_{xi}, A_i, and T_i represent the density, velocity in the x-axis flow direction, area, and temperature of the mixture at the ith grid cell of the outlet boundary, respectively.

Since the inlet coolant of each case in present work is in a subcooled state (such as ΔT_{sub} >5K for water, ΔT_{sub} >1K for R134a and the NH_3/H_2O mixture), a steady single-phase flow field was simulated initially. The results obtained with a residual error of 10^{-5} were then employed as the initial condition for the subsequent flow boiling heat transfer simulation [278].

For subcooled flow of fluid in microchannels, the inlet Reynolds number (Re) is calculated by the following formula:

$$Re = \frac{\rho u D}{\mu} \tag{3-34}$$

Where ρ, u and μ represents the density, inlet velocity and the dynamic viscosity of the fluid, respectively. D is a characteristic length of the heat sink, commonly denoted as the hydraulic diameter of channels.

Under the same conditions, the inlet Reynolds number in microchannels is notably lower than that in macrochannels, primarily due to its much smaller hydraulic diameter. Consequently, in the majority of scenarios, the single-phase convective flow in microchannels is typically in a laminar flow process. However, this smooth laminar flow can be disrupted by the occurrence of the evaporation phenomena such as the bubble nucleation, flow pattern transitions, bubble detachment, liquid deposition, and even local surface dryout [195]. For example, the bubble generation and detachment phenomena occurring on the heated surface could create the local disturbances and then disrupt laminar flow. These processes have impacts on the heat transfer performance and fluid behaviors in microchannels.

To accurately simulate such complex flows with strong streamline curvature and vortices, the realizable k-ε model is adopted in present work according to references in the literature. This model has shown superior performance and has been validated in previous investigations on flow boiling heat transfer in mini/microchannels by other researchers [253,279].

In general, the transient VOF-explicit method was employed and integrated with other proper mathematical models to simulate multiphase flow boiling processes. The pressure-implicit splitting of operators (PISO) algorithm was chosen for pressure-velocity coupling, employing the second-order upwind discretization for the momentum and energy equations. Additionally, the PRESTO algorithm was employed for pressure interpolation, while the Geo-Reconstruct discretization was employed for the volume fraction interpolation. The variable time step was regulated to ensure the maximum Global Courant number below 0.25. The convergence was attained when the scaled residual for the continuity equation reached to 1×10^{-4}.

3.8-Summary

This chapter systematically introduces the hypotheses, the calculating theories, and utilization treatments of those simulation models adopted in this work. Generally, this work sequentially

investigates the mutual relations and heat transfer performance of a single functional particle melting and moving in water flow boiling, as well as numerous particles melting and moving in R134a and the NH_3/H_2O mixture flow boiling in microchannels.

Based on reliable simplification and assumptions, the calculating models and computational methods utilized in this study are determined by theoretical analysis and comprehensive assessment, including the vapor-liquid equilibrium state, the thermodynamic and transport properties of the NH_3/H_2O mixture, the capturing method of multiple interfaces (i.e., VOF), the mass and heat transfer models in the liquid-vapor interfacial surfaces (e.g., the LEE model for pure fluid, the modified LEE model for zeotropic mixtures), the melting of PCM materials (i.e., the enthalpy-porosity method and the equivalent heat capacity method), the initial and boundary conditions (e.g. dynamic meshing method and fully developed flows treatment at outlet). Furthermore, the warm start approach is utilized by using the convergent results of a steady-state single phase laminar flow as the initial conditions for the subsequent transient simulation of flow boiling heat transfer.

Chapter-4 Flow boiling heat transfer of water with a PCM particle

4.1-Introduction

Based on the detailed analysis before, flow boiling with suspended PCM particles melting in microchannels appears as a promising and effective approach for cooling electronic devices. However, there are still several challenges persisting in its implementation such as complexity, particle-related issues (e.g., agglomeration and setting) and the optimization considerations. Among them, the complexity resulting from the interactions between flow boiling and particle melting makes the optimization design and integration of system, material selection and PCM particle preparation more challenging.

Following the structural framework outlined in Chapter 1, this chapter primarily investigates flow boiling heat transfer of water with a PCM particle melting and moving in microchannels. The aim is to explore the key factors and their corresponding impacts on the local and overall heat transfer performance between the melting particle, the neighbour fluid and the hot walls within this intricate physical process. Additionally, considering the gravity effect of the PCM particle while avoiding the detrimental impact of the particle deposition on the dynamic grid reconstructions, this work studies the flow boiling process in a vertical microchannel. Taking into consideration of the geometric and temporal scales, which correspond to millimetre and millisecond orders of magnitude, respectively, the heating walls are maintained at a constant temperature condition [244, 262, 280]. The subject of study is illustrated in Figure.45.

As shown in Figure.45, this part employed a 2D single-channel vertical copper microchannel with dimensions of 6mm in length and 0.4mm in width. For cases with a single PCM particle, a particle with a diameter of 0.3mm was set at the bottom and moving with water towards the top of the channel. The inlet fluid temperature and the wall temperature are set at 95°C and 105°C, respectively. The saturation temperature of water is 100°C at 1 bar and the melting temperature of the PCM is chosen at 96°C, referencing to the original material Bi52Pb30Sn18 in the literature [283]. Furthermore, inlet mass flux of water is set at 50 kg/(m²·s) with inlet liquid velocity at 0.05m/s and the liquid Reynolds number at 40 in present work.

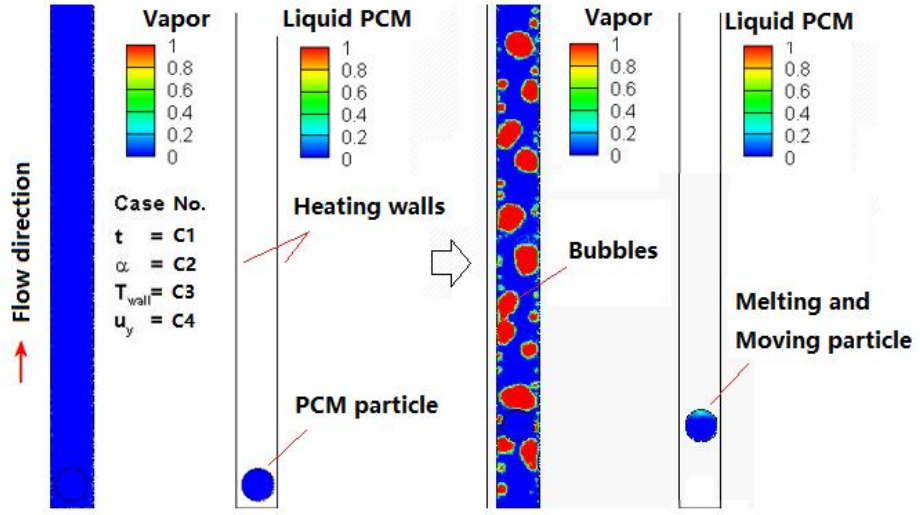


Figure.45 Research Description of the main numerical simulation cases in chapter 4

In this scenario, the single-phase laminar flow heat transfer of water firstly occurs at the inlet of the channel. As the heat is transferred from walls to the fluid, the temperatures of water and particle begin to rise. Upon reaching the phase change temperature, the material in the moving particle starts to melt and the water near the heated walls begins to evaporate quickly. When the flow and heat transfer processes continue, the bubbles nucleation and the disturbance near the walls become more intense. Consequently, the local laminar flow could transit into local turbulent flow. Taking pure water flow boiling at 11ms in this study as an example, while the inlet velocity of liquid is 0.05m/s, the maximum local velocity is up to 6.13m/s in the domain during the boiling process. Correspondingly, the local gas Reynolds number is in the order of magnitude of millions. Hence, it is necessary to choose a proper turbulence model that could accurately descript and predict the transitional region between laminar and turbulent flows.

Among those available turbulence models, the realizable k-ε model has been validated against experimental data as a tool for simulating the intricate flow boiling heat transfer behaviors in microchannels, contributing to the accurate and insightful analyses in applications [253,279]. the realizable k-ε model is an advanced turbulence model as it takes into account the physics of turbulence more accurately, leading to reliable and accurate predictions of flow patterns, velocity profiles and heat transfer characteristics, especially in regions with rapid changes in flow or near-wall interactions of flow boiling in microchannels. Furthermore, it is also a type of turbulence model that has been specifically developed to accurately capture the transition

from laminar to turbulent flow. Therefore, the realizable k-ε model is chosen as the turbulence model for predicting multiphase flow boiling process in microchannels in this work.

With the continuous growth and flow of bubbles, large bubbles start to detach from the walls and finally move out of the channel. In this process, those bubbles could collide with the neighbor particle and hot wall, further complicating the local flow and heat transfer within the confined space. Furthermore, four cases were conducted to investigate the effects of heating surface wettability and PCM density (which is used to account for different particle velocity) on the heat transfer performance.

4.2-Basical assumptions and treatments

In this chapter, the VOF-LEE method was employed to simulate flow boiling heat transfer of water, while the dynamic meshing and the melting method were utilized to predict the moving and melting process of the single PCM particle in a microchannel.

As analyzed in Section 4.1, when large bubbles detach from hot surfaces, they are potential to collide with the adjacent PCM particle. This collision could result in oscillatory motion of the particle between the opposing walls. In cases where the dynamic motions of bubbles on both sides of the particle are not synchronized, the collision between the particle and the wall may occur. In present work, a hard ball collision model is adopted to simulate the collision process between the particle and the walls when this scenario happens. In this model, the particle is considered as a rigid, non-deformable sphere, with no energy loss occurring during collision. More specifically, the velocity component in the flow direction remains unchanged, while the component perpendicular to the wall maintains a constant magnitude but changes direction.

In present work, the PCM particle is supposed as a rigid PCM particle and its moving process is simulated by dynamic meshing method. In order to avoid the negative grid-related issues arising during grid movement and deformation processes, the collision is considered to occur when the distance between the particle with each wall is three times the grid sizes.

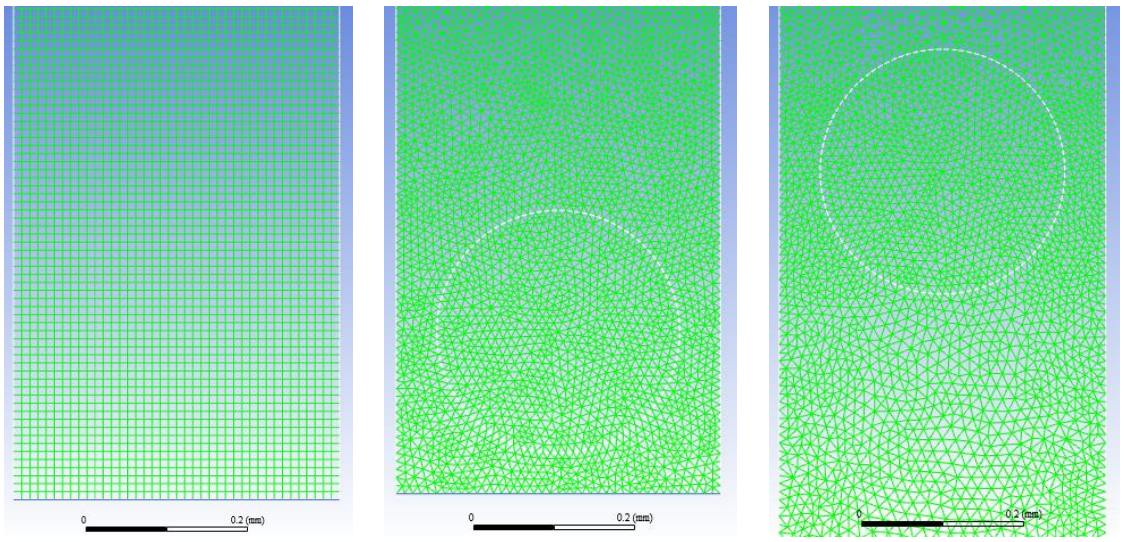
Generally, the effects of a single PCM particle melting on water subcooled flow boiling heat transfer performance, such as pressure drop, the overall and local HTCs, were investigated in this chapter. All cases were conducted under the same inlet mass flux condition.

4.3-Grid independence and model validation

In order to ensure the accuracy of the results, the mesh independence and model validations were firstly conducted in the same computational geometry of microchannel with a length of 6mm and a width of 0.4mm. Additionally, a convergent fully-developed single-phase flow field was calculated under a heating temperature of 99℃ and the result was adopted as the initial condition for unsteady flow boiling processes. This not only reduced the computational time significantly, but also provided realistic physical conditions for the simulation [278].

4.3.1-Mesh independence test

In the present work, two different types of calculation domains and their corresponding mesh structures were used for simulations with and without a PCM particle. The fixed-quadrilateral grids were employed for cases without a PCM particle, while dynamic re-meshing triangular grids were utilized for cases involving a PCM particle as shown in in Figure.46.



(a) (b, t=0ms) (c, t=10ms)

Figure.46 Fixed-quadrilateral (a) and dynamic re-meshing triangular grids (b,c) for flow boiling with and without a physical PCM particle

As discussed in the section 2.3, the performance simulation for flow boiling heat transfer in microchannels by the VOF method will cost huge computational resources and time. For the transient flow and boiling cases, in order to ensure the computational accuracy and stability, it is necessary to maintain the maximum Courant number at the order of magnitude of 0.25. The smaller size of a grid, the smaller time step size. In order to accurately capture the small-size

bubble nucleating and evolution in intense flow boiling process, the grid size is often chosen at the micrometer scale, accompanied by a corresponding time step in the microsecond range. Furthermore, in order to achieve the high-quality remeshing grids that meet the requirements for the accuracy and stability, it is imperative to carefully choose and finely adjust a series of dynamic meshing parameters based on specific cases. Those parameters include deformation limits, smoothing factors and remeshing frequency. This significantly increases the computing workload and cost of numerical simulations. For example, when utilizing a 32-core server in present work, it takes approximately one month to finish a simulating case.

The results of grid independence test are shown in Figure.47.

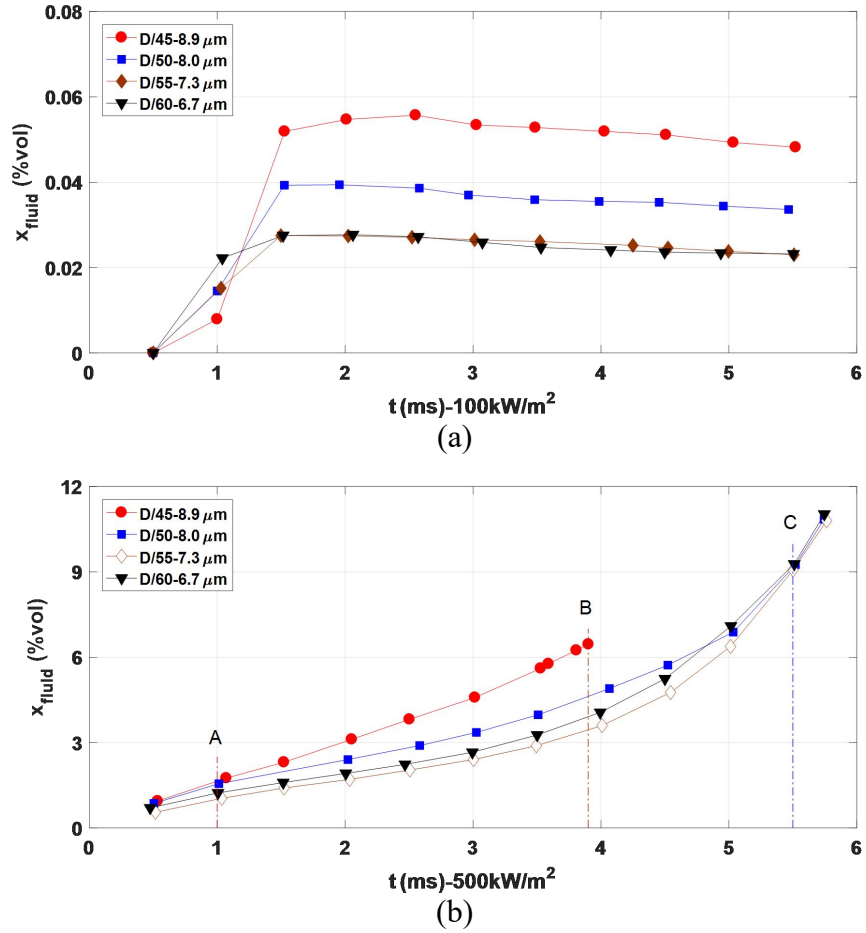


Figure.47 Grid independence test of water flow boiling in microchannel at (a) 100 and (b) 500 kW/m²

Considering the computational resources and the availability of experimental data conducted for water flow boiling in microchannels in the literature, the fixed-quadrilateral grid structure was selected to validate the mesh independence and the subsequent methods. Once validated,

the grid size was used as a reference to generate dynamic triangular grids for simulating flow boiling with a PCM particle, thereby optimizing computational efficiency.

Four different sizes of uniform quadrilateral mesh structures were tested under the same inlet mass flux and heating temperature: 150 kg/(m^2·s) and 95℃, respectively. The vapor fraction of water in the domain was computed and compared in unsteady flow. Furthermore, two cases with different heat fluxes were investigated to examine the size effects on the nucleation and growth processes of bubbles. As shown in Figure.47, the results indicate that a coarser mesh (e.g., 8.9μm) can increase the volume fraction of vapor during the bubble nucleation process, but these diminish when the bubble rate reaches a sufficient level at 500 kW/m^2 (e.g., point C in Figure.47 (b)). Finally, a mesh size of 7.3μm was chosen for the following simulation.

For the dynamic meshing cases, the average mesh size of the triangular grids was also initially set to 7.3μm. The minimum length scale was defined as 5μm and the maximum skewness was limited to 0.5 during the dynamic re-meshing processes.

4.3.2-Simulation model validation

Considering the available computational resources and research objectives in this chapter, the heat transfer performance simulation was conducted in a two-dimensional microchannel with dimensions of 6mm in length and 0.4mm in width. Due to the lack of experimental data under the same cases, the model validation was carried out by using published experimental data in the literature. The contact angle of water on copper material is assumed to be 86° [264].

Some experimental studies of subcooled water flow boiling in microchannels were conducted in the literature. For example, Prajapati et al. [281] compared the heat transfer performance of subcooled water flow boiling in a uniform cross-section microchannels with dimensions of 25.7mm in length, 0.4mm in width and 0.75mm in height. Qu and Mudawar [282] studied the saturated flow boiling heat transfer in a microchannels with dimensions of 44.8mm in length, 0.23mm in width and 0.71mm in height. Moreover, both studies have some experimental data acquired at the same inlet temperature of 30°C and an inlet mass flux ranging from 130 to 135 kg/(m^2·s). Therefore, those are chosen to validate the model and marked in Figure.49.

However, Qu and Mudawar [282] gave the variations of the saturated water flow boiling HTC against thermodynamic equilibrium quality, whereas Prajapati [281] depicted local HTCs near the channel outlet as a function of the effective heat fluxes. Furthermore, there exist notable differences in terms of the channel lengths, thermocouple placements and effective heat fluxes between the two experiments. Meanwhile, in this chapter, the heating surfaces for simulations are maintained at a constant temperature, as discussed in section 4.1. Therefore, it is necessary to select a universal and suitable parameter for conducting a comparative analysis of the heat transfer performance between the CFD simulations and experimental results.

For saturated flow boiling, the vapor quality, refers to the proportion of vapor in the saturated mixture, is a critical dimensionless factor to evaluate the heat transfer characteristics. A vapor quality of 0 indicates that the mixture is in a saturated liquid state. For subcooled flow boiling, the flow can be categorized into two regions, including the subcooled region near the entrance and the saturated region near the exit of microchannels, which can be divided by a location of zero thermodynamic equilibrium quality. This location is determined by using a heat balance calculation in Eqn. 4-1, assuming a uniform fluid temperature across the cross-section of the heat sink. The equilibrium is a state where various properties of liquid no longer change over time. Similar to that of saturated flow, a value of 0 indicates a fully liquid state.

In this section, subcooled flow boiling of water in a short microchannel is investigated under a large degree of subcooling. This microchannel is 6mm in length and the degree of subcooling is 70°C. In this scenario, it is insufficient time and heat transfer area for water to engage in heat exchange with hot walls. Hence, a distinct transitional region arises between single-phase flow and saturated boiling. In this region, heat transfer is in a state of incomplete development. More specifically, localized boiling and nucleation begin to occur, leading to the formation of tiny bubbles near the hot surfaces even though the temperature of bulk fluid is still below the saturation temperature. Additionally, the wall boundary condition in the simulation is defined as a constant temperature ranging from of 40 to 120°C, aligning with the conditions observed in the reference cases [281, 282]. Generally, there are three distinct flow regions present in the domain: single-phase flow, a transitional region and saturated flow in Figure.49 (b). Therefore, for the cases in this work, the fluid at the outlet may exist in three states: single-phase liquid state, the non-equilibrium gas-liquid mixture state and the saturated gas-liquid mixture state.

In summary, in order to better assess the accuracy of the simulation model across those three states, a new factor denoted as X_{exit} is introduced in present work, building on the concept of the exit thermodynamic equilibrium vapor quality x_{exit}. Specifically, in the cases of saturated flow boiling, it is equivalent to the vapor quality x_{exit}. For single-phase liquid flow, it assumes negative with a greater absolute value indicating a higher degree of subcooling at the outlet of channels. In transitional flow, it also remains negative, indicating that the average temperature of the bulk fluid at the outlet remains below the saturation temperature, while phase change occurs near the heated walls.

The formula for calculating the factor X_{exit} is identical to that of thermodynamic equilibrium vapor quality x_{exit}. The specific equation is shown as follows:

$$X_{\text{exit}} = \frac{q_{\text{wall}} \cdot (W_{\text{ch}} + 2H_{\text{ch}})L - GW_{\text{ch}}H_{\text{ch}} \cdot c_p \cdot (T_{\text{sat}} - T_{\text{in}})}{\dot{m} h_{\text{fg}}} \tag{4-1}$$

Where q_{wall}, m and G represent the heat flux (kW/m^2), mass flow rate (kg/s) and inlet mass flux (kg/m^2·s), respectively. c_p and h_{fg} are specific heat capacity (kJ/(kg·K)) and latent heat of evaporation (kJ/kg), W_{ch}, H_{ch} and L denote the width(m), height(m) and length(m) of channels, respectively.

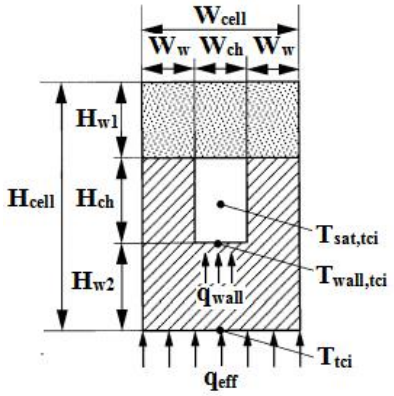


Figure.48 Definition of the major geometric parameters of the cross-section area in microchannels

Finally, X_{exit} is calculated by the following equivalence formula with the boiling number Bo, the subcooled temperature ΔT_{sub} and the hydraulic diameter D_e.

$$X_{\text{exit}} = 4B_o \frac{L}{D_e} - \frac{c_p}{h_{\text{fg}}} \Delta T_{\text{sub}} \tag{4-2}$$

$$B_o = \frac{q_{\text{wall}}}{Gh_{\text{fg}}} \qquad \Delta T_{\text{sub}} = T_{\text{sat}} - T_{\text{in}} \qquad D_e = \frac{4W_{\text{ch}}H_{\text{ch}}}{W_{\text{ch}} + 2H_{\text{ch}}} \tag{4-3}$$

For instance, the average heat flux (q_{wall}) at different cases were plotted as a function of flow time (t) in Figure.49(a). It can be considered a dynamic stable state when the heat flux (q_{wall}) fluctuated around a certain value (referred to as the stable point) regularly. The heat transfer coefficient (HTC) is then calculated as follows.

$$h_{\text{mid}} = \frac{q_{\text{wall}}}{T_{\text{wall}} - T_{\text{mid,m}}} \tag{4-4}$$

Where T and $T_{\text{mid,m}}$ are the wall temperature of channels and the mass average temperature (K) of fluid in the axial line of the bulk domain, respectively.

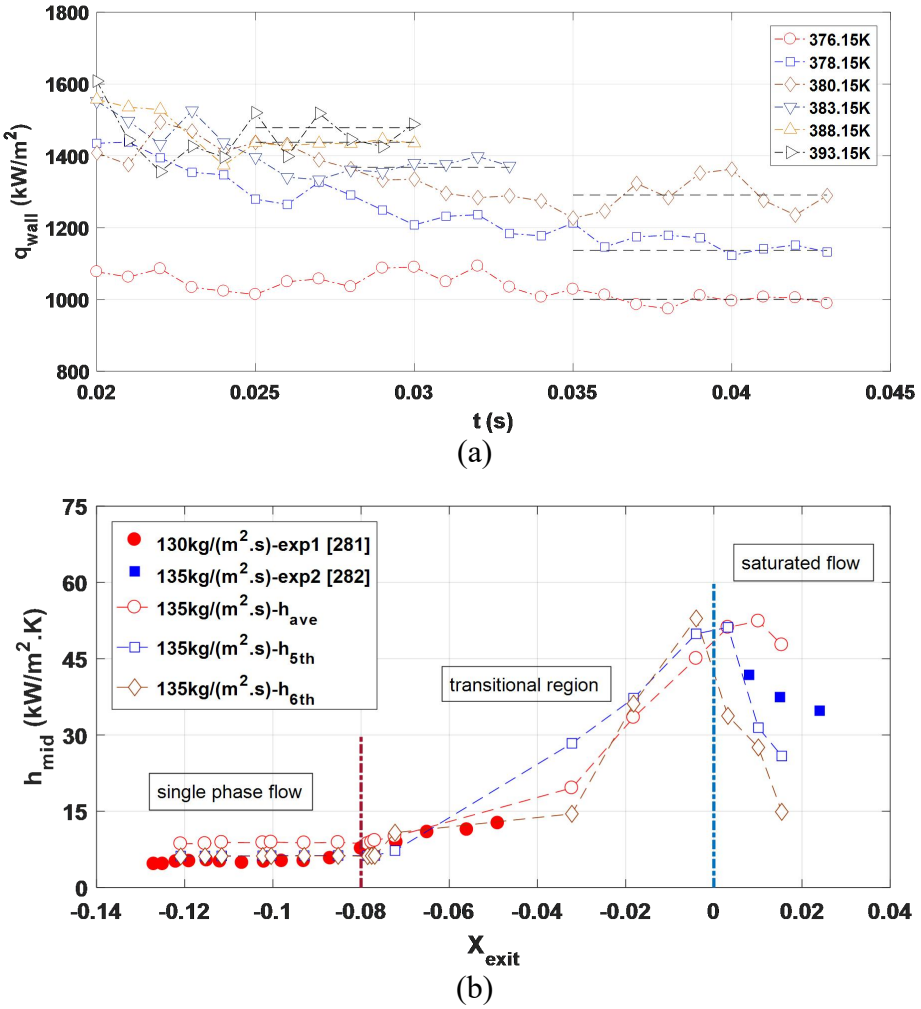


Figure.49 Heat fluxes (a) and the HTCs of the numerical and referenced cases (b). [281, 282]

The validation results are shown in Figure.49 (b), where the solid points denote experimental data in the literature and the connected hollow-dots for simulation results. h_{ave} is the overall flow boiling HTCs, while h_{5th} and h_{6th} are the coefficients in the 5th and 6th part close to the exit of the domain, in which the microchannel was divided into six parts along flow direction averagely.

The results demonstrate a favourable concurrence between the simulation results of subcooled flow boiling in the present work and the experimental data in the literature, exhibiting relative errors of approximately ±25%. Consequently, the simulation model utilized in this chapter is employed with confidence to predict the water flow and heat transfer process, spanning from single-phase flow to saturated flow boiling in microchannels.

4.4-Results and discussion

4.4.1-The overall heat transfer performance

In this chapter, six cases listed in Table.15 were conducted to compare the effects of a single PCM particle melting and moving on subcooled water flow boiling in a vertical microchannel. Additionally, the shell thickness of particles is neglected in present work.

Table.15 The main ooperational conditions of different cases. ρ is the original density of PCM

	Case0	Case1	Case2	Case3	Case4	Case5
Wettability (α)	86°	0°	86°	0°	86°	0°
No., density (ρ)	No	No	Single, ρ	Single, ρ	Single, ρ/2	Single, ρ/2

As discussed in Chapter 2, the wettability of heating surfaces is an important factor that could affect flow boiling heat transfer performance in microchannels. Therefore, the cases of water in a copper microchannel (with a contact angle of 86°) and a superhydrophilic channel (with a contact angle of 0°) were compared in this study. The surface wettability of the PCM particle is assumed to be congruent with that of hot walls. Meanwhile, the additional heat absorbed during the PCM melting process could enhance the heat transfer performance. Consequently, the cases of flow boiling with and without a PCM particle were simulated, individually. The material is referred to the original material of $Bi_{52}Pb_{30}Sn_{18}$ [283] (e.g., density of 9600kg/m^3, thermal conductivity of 24W/(m·K), the specific heat capacity of 0.167kJ/(kg·K), the melting

temperature of 369.15K and latent heat of 34.7kJ/kg). Additionally, the relative flow velocity between particles and the surrounding fluid is also one of the dominant factors influencing the convective heat transfer performance. In this context, a virtual PCM material was postulated and used to comparatively investigate the buoyancy effect of the PCM particles on the heat transfer performance. Except for the density, which is half that of the reference material, all other physical properties remain unchanged. The boundary conditions are listed in Table.16.

Table.16 Boundary conditions of water flow boiling with a PCM particle in present simulation

Inlet Temperature	Inlet mass flux	Wall temperature	Outlet pressure	Diameter of PCM
T_{in}	G_{in}	T_{wall}	P_{out}	ϕ
368.15K	50kg/(m^2.s)	378.15K	0.1MPa	0.3mm

Flow boiling heat transfer performance, including the heat fluxes, HTC, the vapor fraction on hot walls, the mass-averaged temperature in the midsection, the area-averaged outlet velocity and total pressure drop, are presented as a function of flow time. They are calculated by using the following methods.

$$X_{\text{wall,ave}}(t) = \frac{X_{\text{wall}}(t-0.5) + X_{\text{wall}}(t) + X_{\text{wall}}(t+0.5)}{3} \tag{4-5}$$

$$X_{\text{wall}}(t) = \frac{X_{\text{wall,left}}(t) + X_{\text{wall,right}}(t)}{2} \tag{4-6}$$

Where $X_{\text{wall,left}}(t)$ is the mentioned area-averaged parameter on left side heating wall.

$$h_{\text{mid,ave}}(t) = \frac{Q_{\text{wall,ave}}(t)}{T_{wall} - T_{mid,m}(t)} \tag{4-7}$$

Where $T_{mid,m}(t)$ is the mass-averaged temperature (K) in the mid section of channel.

Figure.50 illustrates the unstable transient relations between the overall heat fluxes, HTCs and pressure drops for the six cases. It is observed that the heat fluxes in Figure.50 (a) and HTCs in Figure.50 (b) on the superhydrophilic surfaces (such as Case1 represented by solid points) are higher than that on the copper cases (such as Case0 represented by hollow points) at the same conditions. Furthermore, the presence of a large PCM particle (such as in Case3 and 5) melting and moving in the domain could enhance the heat transfer performance. For instance, the time-averaged HTCs of Case 3 and Case5 with a PCM particle are about 60 kW/(m^2·K),

demonstrating a 50% increase compared to that of pure water in Case 1. However, it is worth noting that the magnitudes and average values of pressure drops in Figure.50 (c) are greater in superhydrophilic cases (solid points) than that in copper cases (hollow points).

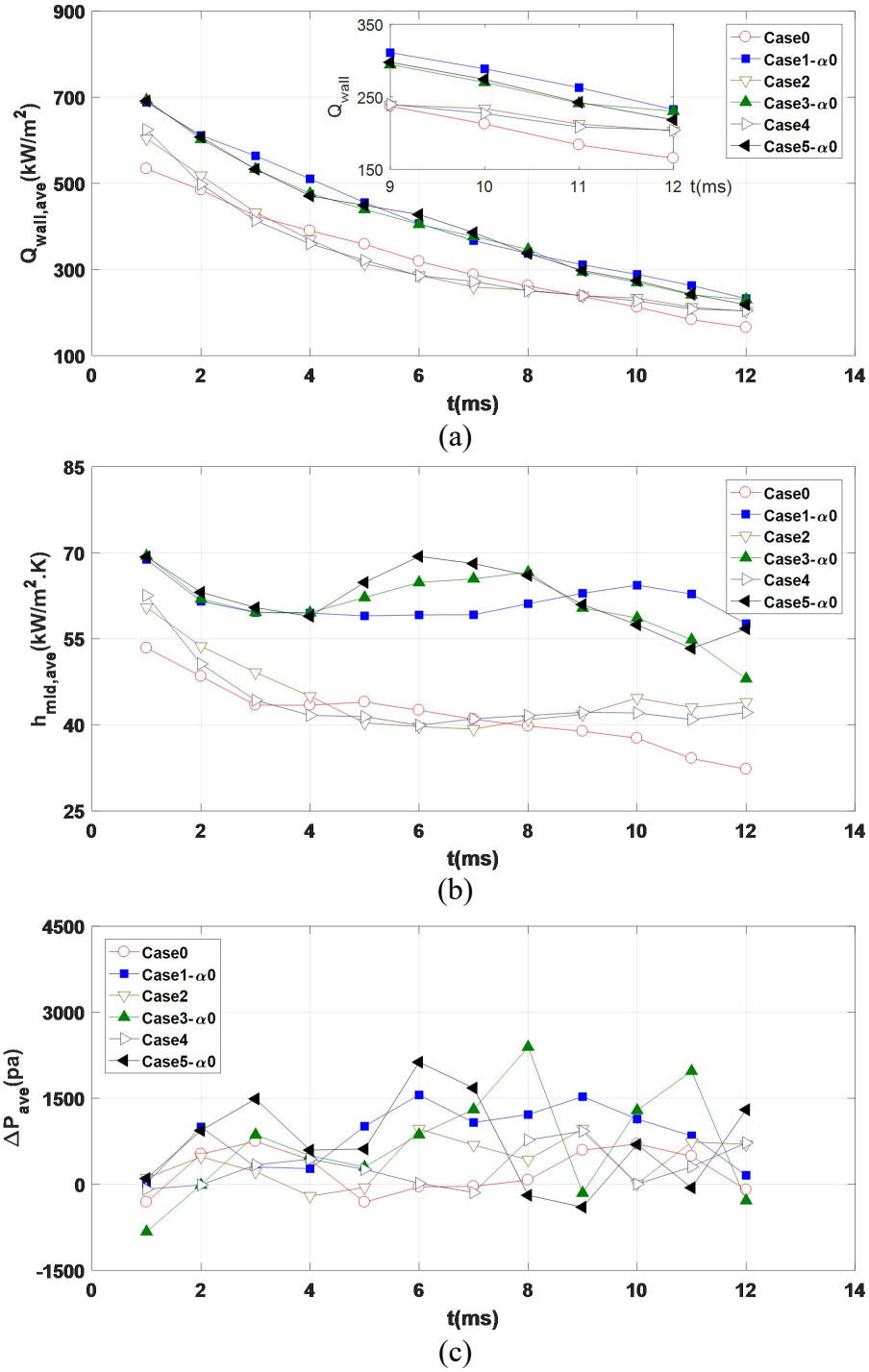


Figure.50 Relations of the overall heat fluxes, HTCs and pressure drops with flow time in 6 cases

Generally, these variations are related to the dynamic changes in bubble morphology and flow boiling patterns in microchannels. For example, the fluctuation of pressure drop observed in Figure.50(c), ranging from negative to positive values, can be attributed to the combination of multiple factors. These factors encompass flow pattern transitions, interactions between vapor and liquid phases, intermittent boiling, and even hydrodynamic instabilities. Specifically, the formation and collapse of bubbles, particularly near the heated walls of microchannels, can result in uneven pressure distributions and trigger the fluctuation in local pressure. As bubbles form, they momentarily reduce the flow area, causing a transient increase in local velocity and a subsequent pressure reduction. Conversely, when bubbles collapse, they can create pressure waves that increase the local pressure. Therefore, it is the intricate dynamics of complex two-phase flows in microchannels that leads to intermittent boiling and the associated oscillations in pressure drop. Flow patterns of different cases at 6ms and 11ms are compared in Figure.51.

Table.17 listed and compared the main heat transfer performance (e.g., the overall heat fluxes Q, heat transfer coefficient h and the relative rate R_E) at 6ms and 11ms in 6 cases.

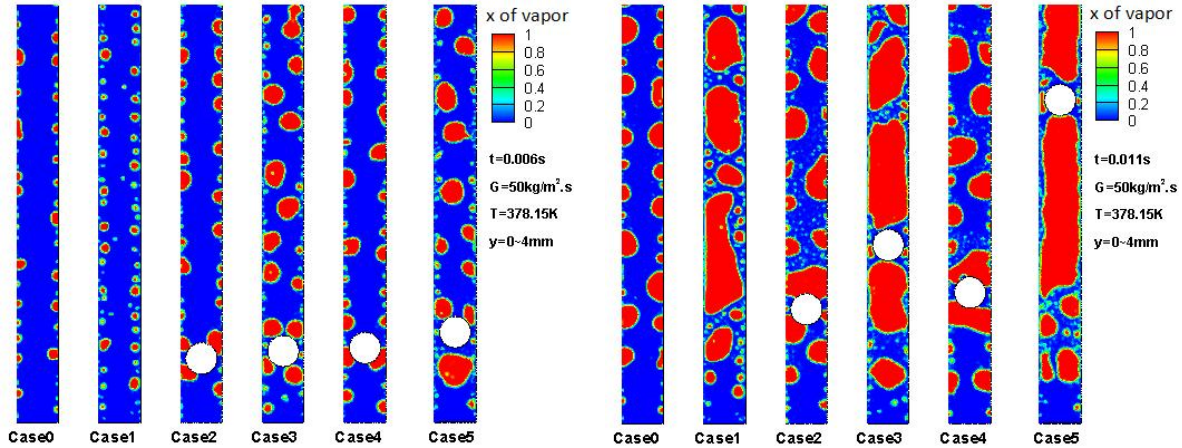
Table.17 Main parameter data at 6ms and 11ms in different cases

No.	t=6ms						t=11ms					
	Q	R_E	h	R_E	x_{wall}	R_E	Q	R_E	h	R_E	x_{wall}	R_E
	kW/m^2	%	$kW/(m^2.K)$	%	-	%	kW/m^2	%	$kW/(m^2.K)$	%	-	%
case0	318.8	-	42.56	-	0.329	-	183.6	-	34.15	-	0.539	-
case1	406.8	27.6	59.16	39.0	0.049	-85.0	262.7	43.1	62.81	83.9	0.074	-86.2
case2	286.4	-10.2	39.69	-6.7	0.441	33.9	212.4	15.7	43.03	26.0	0.498	-7.6
case3	404.9	27.0	64.82	52.3	0.075	-77.4	241.0	31.3	54.84	60.6	0.083	-84.6
case4	285.6	-10.4	39.93	-6.2	0.444	34.9	208.3	13.5	40.94	19.9	0.510	-5.5
case5	427.7	34.1	69.36	63.0	0.068	-79.3	242.4	32.1	53.33	56.2	0.083	-84.5

Comparing to the reference case (Case 0) of pure water flow boiling in a copper microchannel with an inlet mass flux of 50 $kg/(m^2 \cdot s)$ and a wall superheat of 5℃, the heat flux (and HTCs) in Case1 with a superhydrophilic channel could be increased by 27.6% (and 39%) and 43.1% (and 83.9%) at 6ms and 11ms, respectively. Morshed et al. [284] investigated water flow boiling in a microchannel with a hydraulic diameter of 0.672μm by experimental study and found that the HTCs could be enhanced by up to 56% when the contact angle of the heating surfaces was reduced from 97° to 56° using a surface nanowire coating method.

Furthermore, when a single PCM particle is added to a copper microchannel, such as in Case 2 and Case 4, the heat fluxes (and HTCs) initially decrease at 6ms and then increase at 11ms. In contrast, when a large PCM particle is added to a superhydrophilic microchannel, like in Case 3 and Case 5, the mentioned heat transfer characteristics are enhanced throughout the entire process. The maximum improvement in heat flux (and HTC) at 6ms is 34.1% (and 63%) in Case 5, while it is 43.9% (and 83.9%) at 11ms in Case1. Therefore, the surface coating treatment is considered as a primary approach for improving flow boiling heat transfer.

Moreover, it has been observed that the heat transfer performance, including heat fluxes and HTCs, can be significantly improved by reducing the vapor fractions on the heated walls. This reduction can be achieved either by coating the heating surfaces to decrease their wettability or by introducing a large PCM particle. Therefore, it is needed to further investigate the heat transfer performance in relation to flow patterns. The distributions of vapors in domain at 6ms and 11ms are exhibited in Figure.51.



(a)6ms (b)11ms

Figure.51 Flow patterns of the vapor fraction at 6ms and 11ms in different cases

Based on Figure.51, the dominant flow patterns observed in the microchannel were nucleating and bubbly flows at 6ms, as well as intermittent and elongated slug flows at 11ms. In general, the heat fluxes of the initial stage at 6ms were higher than those during the fully-developed stage at 11ms, despite having the same inlet mass flux and heating temperature.

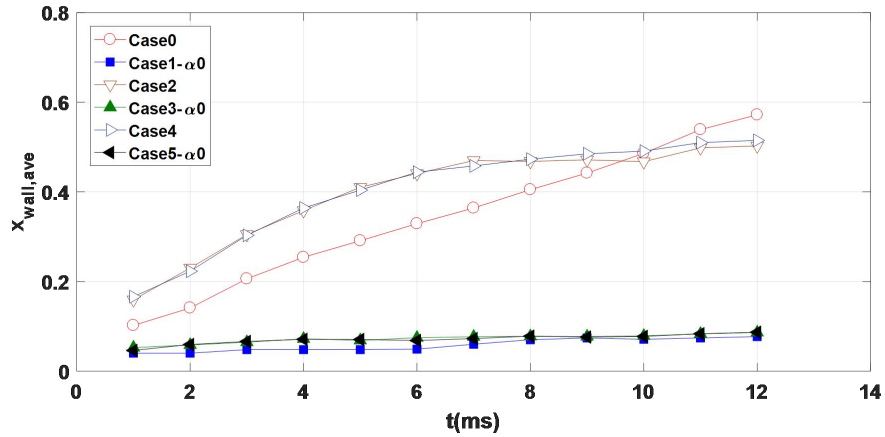
Comparing those flow patterns of six cases at 6ms in Figure.51(a), it is evident that the vapor fractions on the heated surfaces of the superhydrophilic channels (e.g., Case 1, 3 and 5) are

smaller than those of the copper channels (e.g., Case 0, 2 and 4). Additionally, the heat fluxes and bubble sizes in the former three cases are larger than those in the latter cases, respectively. As the previously discussion in Figure.50 and Table.17, for the same inlet mass flux and wall temperature, the superhydrophilic channel such as Case 1 results in the attachment of smaller-sized bubbles to hot surfaces. This attachment effectively inhibits thermal barriers caused by large bubbles, as the thermal conductivity of vapor is much smaller than that of liquid, which can occur between the hot surfaces and flow domain. Consequently, more heat is dissipated from the heated walls into the working fluid, and more liquid evaporates into vapor within the domain under the same conditions.

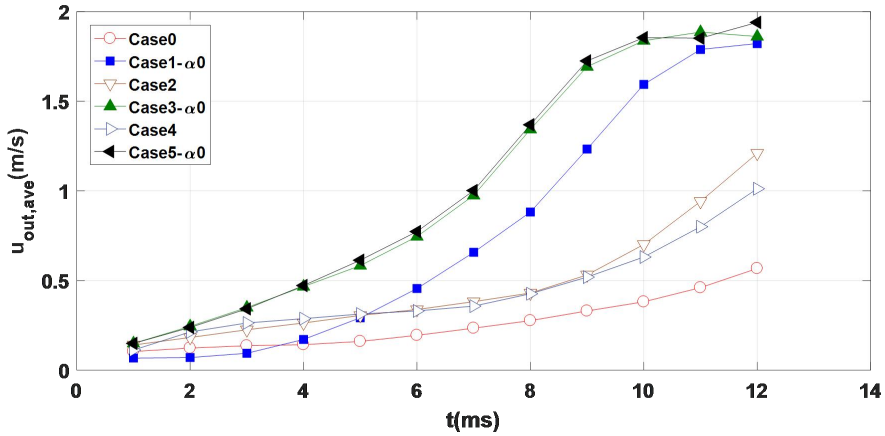
However, when compared to cases without a PCM particle in a copper channel (such as Case 1), the addition of a large PCM particle (such as Case 2 and 4) resulted in a decrease in heat fluxes by 10%. This decrease can be attributed to an increase in the vapor fraction on the heating surfaces by 33.9% and 34.9%, respectively. In contrast, although the addition of a large PCM particle also increased the vapor fraction on the superhydrophilic walls, as seen in Case 5 compared to Case 1, it actually improved the heat fluxes from 406.8 to 427.7 kW/m^2 in Table.17. This indicates that the heat transfer performance is optimal during the nucleating stage and the bubbly stage throughout the entire flow boiling process, as discussed earlier and shown in Figure.8 to Figure.10. Furthermore, it is noteworthy that the melting and movement of a PCM particle in the fluid could further enhance the heat transfer capability to some extent in a superhydrophilic microchannel.

Different flow patterns at 11ms are depicted in Figure.51(b). While the dominant flow pattern is bubbly flow with large isolated bubbles attached to the copper walls (e.g., Case 0, 2 and 4), it is the intermittent slug flow with elongated bubbles moving in the domain and a thin liquid layer observed near the superhydrophilic walls (e.g., Case 1, 3 and 5). As shown in Table.17, the overall heat fluxes (and HTCs) in the superhydrophilic channels (e.g., Case 1) are at least 31.3% (and 56.2%) higher than those in the copper channels (e.g., Case 0). Correspondingly, under identical conditions, higher heat fluxes result in the generation of larger vapor fractions within the domain. Therefore, an appropriate surface morphology treatment can significantly enhance the heat transfer capability in a specific application. Additionally, when compared to flow boiling of water in a copper microchannel (e.g., Case 0), the inclusion of a PCM particle

(e.g., Case 2 and 4) could increase heat flux (and HTC) near the particle by more than 13.5% (and 19.9%), according to the current numerical study under the same operational conditions. The particle has a diameter of 0.3mm and the length of microchannel is 6mm. Consequently, the addition of a melting and moving PCM particle in the domain has the potential to enhance the heat dissipation capacity near the particle. Furthermore, the coupled treatment, as seen in Case 3 and Case 5, could also enhance the heat fluxes (and HTCs) by as much as 32.1% (and 60.6%) in comparison to the reference Case 0. This involves surface morphology treatment on both the heated walls and PCM particle surface, each of which has a superhydrophilic feature.



(a)



(b)

Figure.52 Relations of vapor fraction on heating walls and outlet velocity in different cases

Additionally, when compared to the heat transfer performance of flow boiling in Case 0, Case 1 exhibits the most significant enhancement among the aforementioned cases in present study. According to Table.17, it is found that the enhancements of heat fluxes and HTCs are strongly related to the changes of vapor fraction on heated walls (x_{wall}) by those treatments. This could

be further supported by comparing the trends of the area-average vapor fraction on the heating walls (x_{wall}) in Figure.52 (a) with those of heat fluxes and HTCs in Figure.50, respectively.

Furthermore, the increments of heat fluxes also lead to an increase of the outlet velocity of the fluid, as shown in Figure 52(b), as more liquid is evaporated into vapor under the same inlet mass fluxes and heating temperature. In general, lower vapor fractions on the heating surfaces result in higher heat fluxes and HTCs at the same operating condition.

In other words, throughout the entire flow boiling process in a microchannel, which includes nucleating, bubbly, and slug flow regimes, the effects of adding a single PCM particle on heat transfer characteristics are primarily determined by its influence on flow patterns, particularly the vapor fraction on the heating walls. Consequently, it is crucial to investigate the local heat transfer performance in the vicinity of the PCM particle.

4.4.2-The local heat transfer performance

As mentioned earlier, this section will investigate the local heat transfer characteristics near the melting and moving PCM particle. The variation ratio of heat flux δQ_{wall} as well as the ratio of velocity in the vertical direction δu_y will be calculated using the following formulas.

$$\delta Q_{\text{wall}}(t) = \frac{Q_{\text{wall,local}}(t) - Q_{\text{wall}}(t)}{Q_{\text{wall}}(t)} \times 100\% \tag{4-8}$$

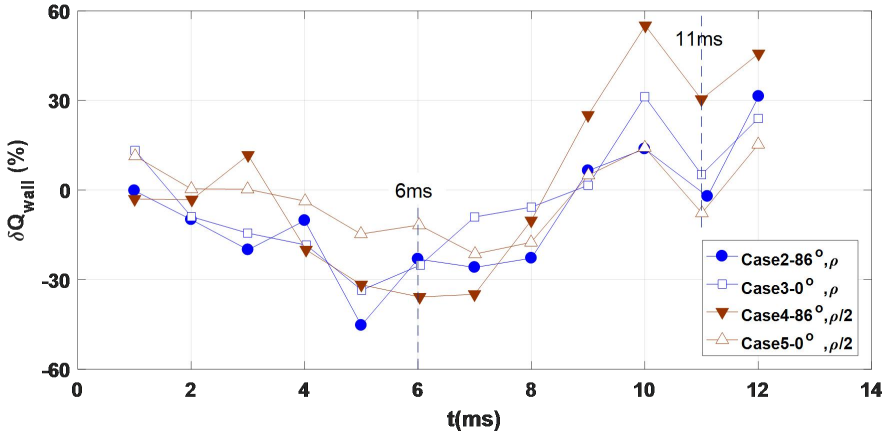
$$\delta u_y(t) = \frac{u_{ball,y}(t)}{u_{oulet,y}(t)} \times 100\% \tag{4-9}$$

Where Q_{wall} and $Q_{\text{wall,local}}$ are the area-averaged heat flux (kW/m^2) of entire heated surfaces and local surfaces near the moving PCM particle, respectively. Similarly, $u_{\text{ball,y}}$ and $u_{\text{outlet,y}}$ are the y-axis velocities of the PCM particle and the liquid-vapor mixture at the channel exit, respectively. As the Figure.53 demonstrates the correlations of the variation ratios of heat flux and the vapor fractions on heated walls with flow time, the corresponding vapor distributions near the PCM particle are depicted in Figure.54.

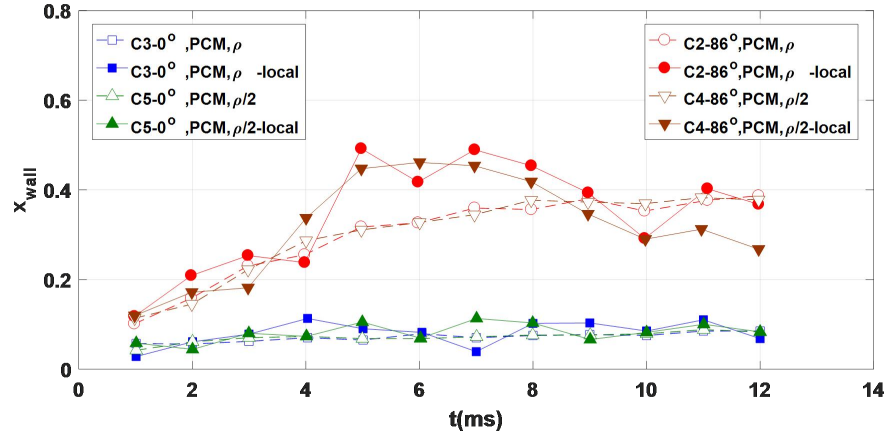
In general, the local heat fluxes on the walls near the PCM particle are lower than the overall heat flux values during the bubbly flow period (e.g., at 6ms). However, during the intermittent slug flow period (e.g., at 11ms), local heat fluxes exhibit larger values with some fluctuations, as shown in Figure.53(a). Correspondingly, the vapor fractions x_{wall} near the PCM particle, as

depicted in Figure.53(b), also exhibit more pronounced fluctuations in the copper cases (e.g., Case 2 and 4) compared to the superhydrophilic cases (e.g., Case 3 and 5). While local vapor fraction near the PCM particle is higher than the overall vapor fraction during the bubbly flow period from 4 to 8ms, it begins to fluctuate during the slug flow period after 8ms in the copper channels (e.g., Case 2 and 4). Hence, it is inferred that the variations in the vapor fractions on the heating walls caused by the melting and movement of the PCM particle play a significant role in determining local heat fluxes near the particle.

Additionally, the variations of δQ_{wall} and x_{wall} near the PCM particle are more pronounced in the copper cases (e.g., Case 2 and 4, especially the Case 4 with a smaller PCM density of $\rho/2$) compared to the superhydrophilic cases (e.g., Case 3 and 5), as shown in Figure.53. Therefore, it is needed to compare the vapor distributions near the PCM particle in Figure.54 and assess the complex influence of surface wettability and PCM density on heat transfer performance.



(a)



(b)

Figure.53 Relations of heat flux ratios(a) and vapor fraction on walls (b) with flow time

The vapor distributions near the PCM particle are depicted in Figure.54.

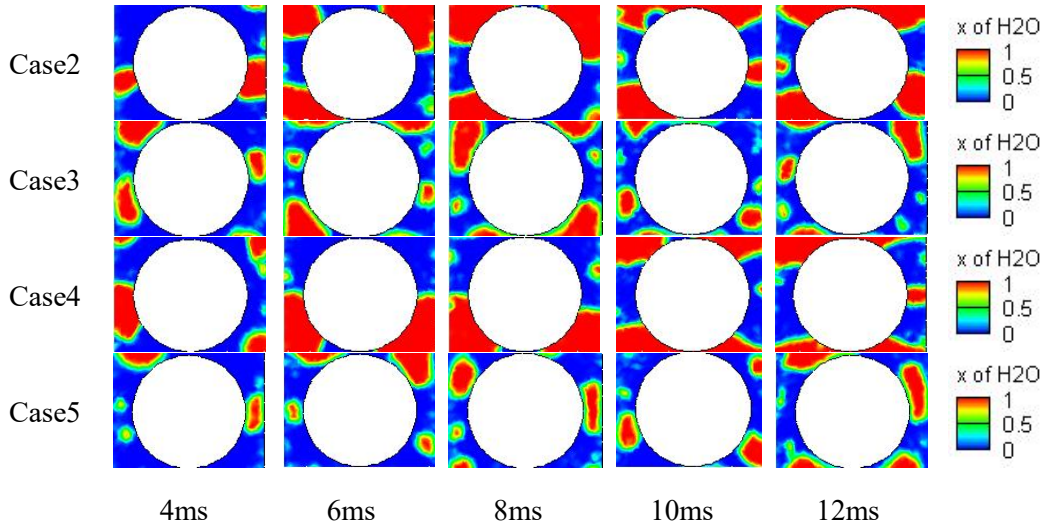
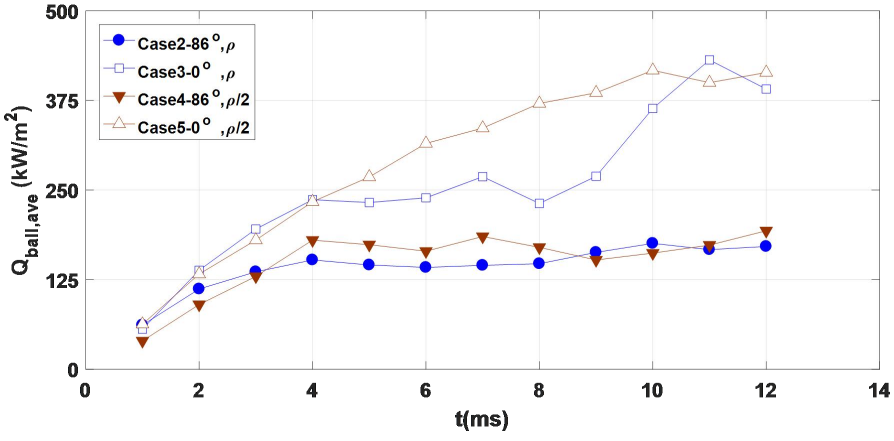


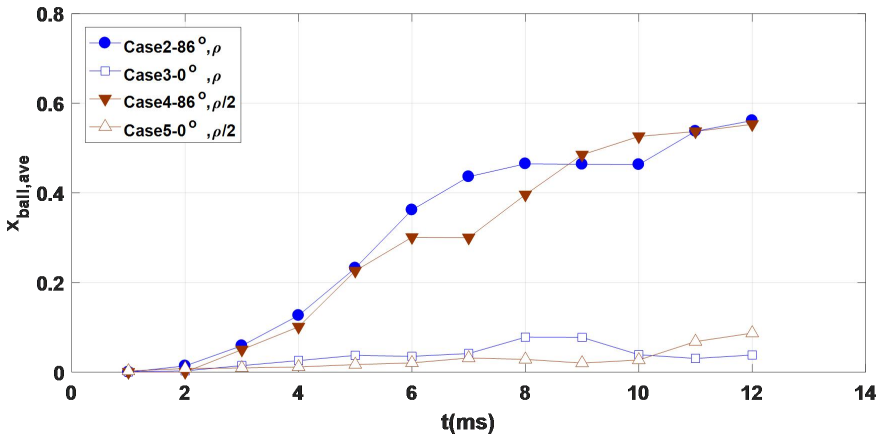
Figure.54 Comparisons of the vapor fraction distributions near the PCM particle in cases

The temporal variation of vapor fractions on the heated walls is illustrated Figure.53(b), along with the corresponding distribution of bubbles within the flow domain near the PCM particle, as depicted in Figure.54. It is clear that the existing of a big PCM particle within flow domain could hinder the nucleated bubbles detaching from the heated walls and moving into the main fluid near the PCM particle. In consequence, some big-size bubbles occur between the heating walls and the particle surface, leading to the obvious reduction of heat dissipation from local walls near the particle to the material inside the encapsulated particle. This adverse effect is more serious in copper cases (e.g., Case2) than in superhydrophilic cases (e.g., Case3).

The main parameters, including the area-averaged heat flux $Q_{ball,ave}$ and the vapor fraction on the PCM particle surface $x_{ball,ave}$ over flow time, are displayed in Figure.55.



(a)



(b)

Figure.55 Relations of heat flux (a) and vapor fraction (b) on the particle surface with flow time

As mentioned earlier in this chapter, the surface wettability of the PCM particle is assumed to be the same as that of the heating walls in the respective cases. Specifically, the contact angles of the PCM particle surfaces are set as 86° and 0° in the copper and superhydrophilic channels, respectively. Consequently, the values of $x_{ball,ave}$ in the copper cases (e.g., Case 2) are larger than those in the superhydrophilic cases (e.g., Case 3), resulting in smaller values of $Q_{ball,ave}$ in the former cases compared to the latter cases under the same conditions. Furthermore, for the same wettability, a lower density of the PCM material leads to smaller values of $x_{ball,ave}$ and larger values of $Q_{ball,ave}$ during the bubbly flow period between 4 and 8ms.

However, when the flow boiling process is developed to the interment slug flow period (such as that at 11ms in Figure.51), those mentioned parameters began to exhibit cyclic fluctuations. According to the results shown in Figure.57(a), it can be observed that the velocity along the flow direction (named as the y-velocity in vertical microchannels) of the PCM particle in cases with lower PCM density (e.g., Case 5) is larger than that with higher density (e.g., Case 3). Furthermore, it accelerates quickly during the flow boiling development, especially at the superhydrophilic cases, which is dominated by the unbalanced resultant forces along the flow direction during the dynamic flow along the flow direction shown in Figure.56.

$$F = \underbrace{\left(F_g + F_{buoyancy,y}\right)}_{\text{first item}} + F_{inertia,y} + \underbrace{\left(\sum F_{tension,y} + \sum F_{bubbles,y}\right)}_{\text{second item}} = 0 \tag{4-10}$$

Where F_g, $F_{buoyancy,y}$, and $F_{inertia,y}$ represent the gravity, buoyancy and inertia forces acting on the PCM particle, $\Sigma F_{tension,y}$ and $\Sigma_{bubbles,y}$ denote the net force along the flow direction between the PCM particle and the liquid, the bubbles attached to the PCM surface, respectively.

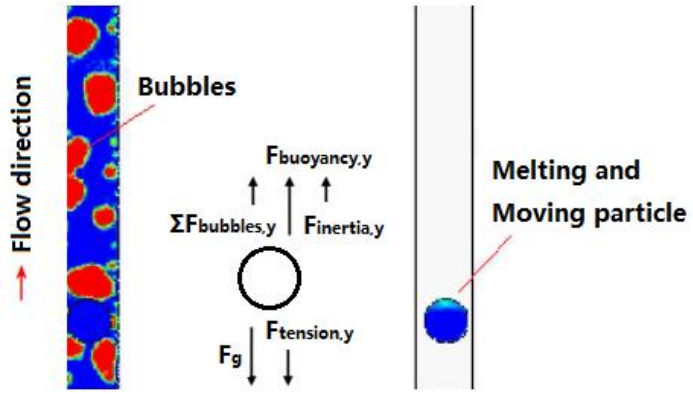


Figure.56 Different types of forces on the PCM particle in flow boiling in a vertical microchannel

Therefore, for a case involving a PCM particle in a vertical microchannel, the dominant factor affecting the first component in Eqn. 4-10 is the PCM density. A lower density results in a larger net force in the reverse flow direction.

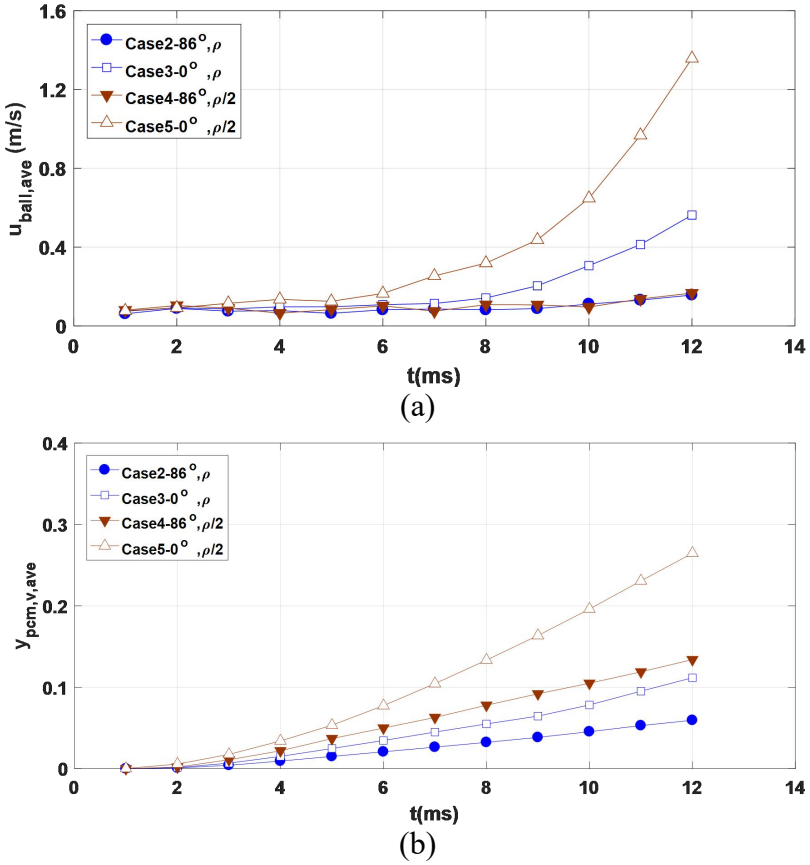


Figure.57 Relations of velocity (a) and liquid fraction of PCM particle (b) with flow time in cases

Additionally, the second component depends on the vapor fraction of bubbles in the domain. A smaller contact angle between the heated walls and the PCM particle surfaces lead to a larger net force in the flow direction. Specifically, a lower density of the PCM material and smaller contact angles of the surfaces contribute to a greater increase in the particle velocity along the flow direction, as illustrated in Figure.57(a). Moreover, the accelerated PCM particle has the capability to disrupt neighboring bubbles and carry them away from the heated walls. This phenomenon leads to the periodic fluctuations in local heat transfer performance (e.g., δQ_{ball}) during intermittent flow periods, as depicted in Figure.53(a). Furthermore, a lower wettability of the particle surfaces and faster speed of the PCM particle result in more heat being transferred to the PCM material, as also depicted by the larger liquid fraction of the particle, $y_{pcm,v,ave}$, in Figure.57(b).

The Figure.58 illustrates the distributions of liquid PCM material within the particle at various flow times in different cases.

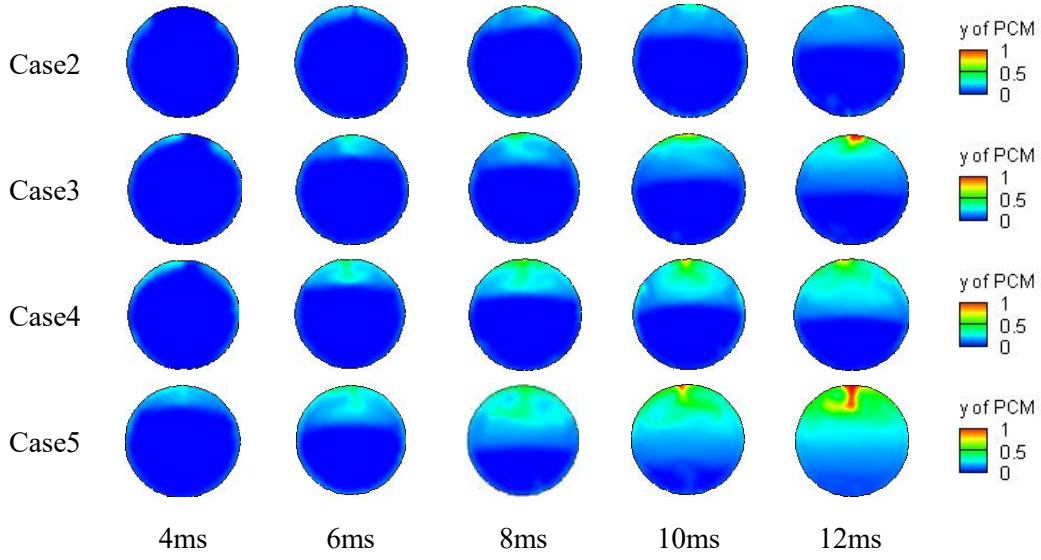


Figure.58 Comparisons of liquid PCM distributions inside the big PCM particle in cases

As explained before, the PCM particle is considered as a rigid particle moving in the domain. The melting of a pure substance inside the particle is treated as a pseudo-porous zone, where the porosity is equivalent to the liquid fraction. This fraction is calculated by an enthalpy balance in each cell. Specifically, the melting heat transfer process of an incompressible pure substance melting at a constant temperature is simulated in a fixed-volume zone. Hence, in this multiphase flow and heat transfer process, the heat absorbed from the heated wall

continuously accumulates along the flow direction, resulting in an increasing temperature of fluid along the flow direction until it reaches a steady heat transfer state. Since the PCM melting temperature is 96°C, which is lower than the boiling temperature of water at 100°C, the temperature of the upper part in the particle is higher than that of the bottom part prior to the complete melting. Therefore, the PCM melting in the particle progresses from the top to the bottom over time, as depicted in Figure.58. Meanwhile, the uneven distribution of the liquid phase within the particle is primarily attributed to the non-uniform heat conduction occurring around the particle and its interaction with the vapor-liquid mixture of water during the transient heat transfer process, as presented in Figure.51and Figure.54.

Furthermore, according to Figure.57 and Figure.58, it is important to notice that in the present study, the maximum velocity and liquid fraction of the PCM particle are 1.36m/s and 26.5%$_{vol}$ at 11ms in Case5, respectively. Hence, it is easy to deduce that the PCM particle in all cases undergoes the partial melting during the multiphase flow in this microchannel in Figure.51. In other words, the completed melting of the PCM particle takes the longer residence time in the heat exchange domain. Therefore, in order to fully utilize the endothermic melting process of the PCM material to enhance the heat dissipation capacity, some measures need to be taken to ensure that the PCM particle melt completely before exiting the microchannel by optimizing the geometric parameters and physical properties of the channel and the PCM particle.

Generally, the overall and local heat transfer performance of flow boiling in microchannels is dominated by flow patterns. Taking the mentioned cases in the present study as examples, the nucleating flow and bubbly flow occur in the initial stages, while the fully-developed stage is characterized by the intermittent slug flow. The heat dissipation capacity is determined by the combined effects of bubbles generated on the heated walls and the dynamic movement in the domain. Therefore, whether the addition of a PCM particle in fluid could enhance or weaken the heat transfer performance is dependent with the impacts on flow patterns in microchannels. For example, the morphology treatment of heating surfaces (e.g., the superhydrophilic case of Case1) promotes the rapid escape of generated bubbles from the heating walls, creating clear spaces for the nucleation of smaller bubbles on the heated walls. This allows for flow patterns characterized by a thin liquid layer between the heating surfaces and large bubbles in the bulk domain, thereby significantly enhancing the heat transfer performance.

In conclusion, the effect of the melting and moving PCM particle on flow boiling heat transfer performance near the particle is summarized in Figure.59.

$$\left.\begin{array}{l} Surface\ Wettability\ (\alpha)\downarrow \\ Density\ of\ PCM\ (\rho)\downarrow \\ Melting\ Heat\ (q_m)\uparrow \\ \cdots\cdot \end{array}\right\} \Rightarrow Flow\ Pattern$$

$$\Rightarrow \begin{cases} Vapor\ Fraction\ (x_{wall})\downarrow \\ Vapor\ Fraction\ (x_{domain})\uparrow \\ ParticleVelocity\ (u_{ball,y})\uparrow \\ \cdots\cdot \end{cases}$$

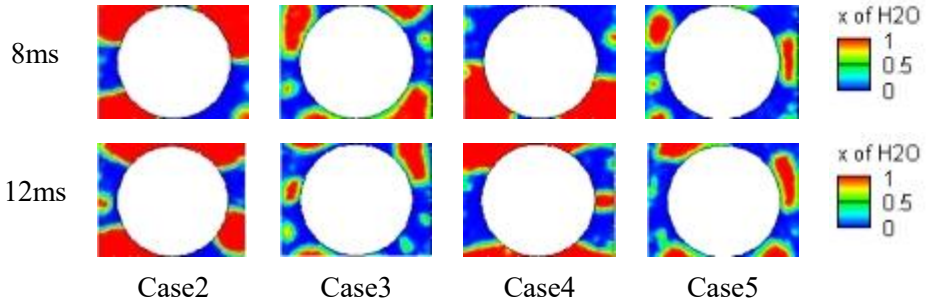


Figure.59 The PCM particle effects on flow boiling heat transfer in domain

Based on the aforementioned results, the presence of a PCM particle has positive and negative impacts on flow boiling heat transfer performance of water in microchannels. In general, the endothermal melting process directly absorbs the heat from the adjacent vapor-liquid mixture, resulting in increased heat dissipation from local heated walls compared to the case without a PCM particle. Furthermore, if it could inhibit the growth rate of large-size bubbles attached on the heated walls, it will further improve the heat transfer performance. However, if not or even hindering the bubbles escape from local heated walls due to the particle occupation near the domain, it will decrease the local heat transfer performance. Therefore, it is necessary to match the geometrical parameters and physical properties of particle for further enhancing the heat dissipation in applications.

4.5- Summary

In this chapter, the flow boiling heat transfer of water in a microchannel with a single PCM particle (e.g., the diameter of 0.3mm) melting and moving in a vertical microchannel (e.g., the width of 0.4mm and the length of 6mm) is investigated using hybrid approaches in ANSYS.

The VOF/LEE method is employed to simulate the water flow boiling phenomenon, while the Dynamic Meshing method as well as the Melting and Solidification method are utilized to predict the endothermal melting and moving effects of a single PCM particle on multiphase flow heat transfer in the microchannel. Initially, a grid independence test is conducted to ensure the accuracy, followed by the validation of the VOF/LEE method with some published experimental data of water flow boiling in microchannels. Finally, the study investigates the melting and moving effects of a PCM particle on overall and local heat transfer performance, including heat fluxes, HTCs and flow patterns. All the cases are carried out under identical conditions, including an inlet mass flux of 50 kg/(m^2.s), inlet temperature of 95℃ and heated wall temperature of 105℃.

According to those aforementioned analysis, the main results are found as follows,

(1) The calculation models and simulation methods used in present work could predict flow boiling process (e.g., single phase, nucleating and bubbly flow, intermittent slug flow) with a PCM particle melting and moving in microchannels. However, it costs significant computing resources and time.

(2) The surface wettability of heating walls has a dominant effect on flow boiling heat transfer performance. Comparing to the heat transfer performance in a copper microchannel, the heat flux and HTC in a superhydrophilic case exhibited the enhancements of by 27.6% and 39% in bubbly flow, along with the improvements of 43% and 83.9% in intermittent and slug flow. However, the aptitude of total pressure drop is increased by 45%.

(3) The presence of a melting and moving PCM particle has both advantage and disadvantage effects on heat transfer performance of water flow boiling in microchannels. On one hand, the additional heat of the PCM endothermal melting and the accelerated movement of the particle in the fluid could significantly increase local heat dissipation. On the other hand, the particle also could impede the movement of large bubbles attached on walls from entering the bulk flow and being carried away from the channel, resulting in a deterioration of the heat transfer performance near the particle.

(4) The melting degree of the phase change material, which is encapsulated inside the particle, is strongly influenced by both the residence time of the particle moving through the sink and the heat transfer capacity between the particle and the surrounding fluid. Therefore, in order to optimize the beneficial impact of the heat absorption through the PCM melting on the heat transfer capability, it is essential to take measures for ensuring the complete melting of PCM before the particle moves out of the channel.

Chapter-5 Flow boiling heat transfer of R134a based functional fluid

5.1-Introduction

As planned in the section 1.5, this chapter focuses on investigating flow boiling of functional fluid with suspended particles melting in microchannels using numerical methods for cooling the electronic devices. According to Table.2, R134a is a dielectric super-wetting fluid with a high boiling latent heat of 217 kJ/kg at 1bar, allowing for the evaporation in the appropriate temperature limits of the electronic components (e.g., below 85℃) [125, 285]. Hence, R134a is selected as the base fluid for this chapter.

In this chapter, the investigation of flow boiling heat transfer of R134a-based functional fluids in a horizonal microchannel is conducted by the numerical approach. It is carried out by using the VOF-LEE method and the equivalent properties approach, which encompasses factors like the specific heat capacity and viscosity of functional fluids.

Both the literature reviews in Chapter 2 and the simulation studies in Chapter 4 have indicated that there are some different and interrelated factors influencing the heat transfer performance of flow boiling in microchannels, including the structural and geometric parameters of heat sinks, the thermophysical properties of work fluids, as well as the operational conditions such as the temperature and pressure requirements in applications. Among them, the properties of fluids serve as the foundation for flow boiling heat transfer performance. Therefore, only clear understanding those heat transfer characteristics under given scenarios can the optimal design of the cooling systems, the selections of fluids and other related utilizations be achieved.

Specifically, the effects of physical properties of functional particles suspended in R134a (e.g., thermal conductivity and latent heat of melting), as well as particle concentrations and heat fluxes on heat transfer performance (e.g., HTCs, pressure drop and performance evaluation criteria (PEC)) are systematically studied in a 2D horizontal microchannel under the constant heat flux and mass flux condition. The microchannel possesses dimensions of 0.5mm in width, 20mm in length, and 0.05mm in thickness.

5.2-Basical assumptions and treatments

Flow boiling of functional fluid with the suspended PCM particles melting in microchannels is a complex heat and mass transfer phenomenon. To ensure the numerical convergence and strike a balance between computing resources and acceptable accuracy, the numerical model employed in present study is simplified based on the following assumptions and treatments:

(1) The R134a-based functional fluid is separated into three continuous phases for simulations: liquid R134a, vapor R134a and a suspended cloud of particles. It is assumed that the particles are uniformly mixed with the liquid R134a, which means that the behaviour and distribution of nanoparticles are treated as if they form a continuous and homogeneous medium, rather than being treated as discrete particles. This simplification allows for the usage of continuum fluid mechanics to describe the motion of both fluid and the suspended nanoparticles, as well as the heat transfer interactions between them. This approach is useful when the concentration of particles is relatively low and their impact on the overall fluid behavior is not dominant. However, this assumption might lead to some loss of accuracy, as it doesn't fully capture the discrete nature and interactions between individual nanoparticles.

(2) The inlet temperature of working fluid and the onset PCM melting temperature are set as 30 and 30.5℃, respectively. The saturated temperature of R134a is chosen as 31℃ at 8 bars. For simplicity, thermal radiation is ignored and the thermophysical properties of each phase are assumed to remain constant in Table 1, as the temperature change is minimal for the entire microchannel process. Additionally, the effective heat capacity method (rectangular profile) was employed to account for the PCM melting effect on thermal performance of fluids [206]. This method involves considering the PCM melting phase change as an effective change in heat capacity over a defined temperature range, represented by a rectangular profile. By doing so, this enables to consider the effects of the PCM phase transitions on heat transfer without explicitly modeling the intricate melting processes. Furthermore, the effective heat capacity method with a rectangular profile allows to simplify the complex melting behavior by treating it as a change in heat capacity, making it easier to incorporate into performance calculations.

(3) A R134a-based functional fluid with the nanosize particle volume concentrations of up to 25% is considered as a Newtonian-like and incompressible fluid, based on some experimental results in literature [286, 287]. Those relevant results demonstrate that, within this threshold concentration, the functional fluid's viscosity remains relatively constant over a range of shear rates, resembling the behaviour of a Newtonian fluid. Moreover, the dynamic viscosity of the fluid mixtures is computed by using the Vand's equation [288, 289], which takes into account the viscosities of individual components as well as the concentrations.

Furthermore, the literature review focused on nanofluid flow boiling heat transfer in chapter 2 has indicated that the maximum concentrations in most experimental studies are typically around 5% vol... Therefore, the majority cases in the subsequent numerical simulations are conducted with inlet concentrations not exceeding 5%. Only a few of cases are conducted at inlet concentrations larger than 5%vol. and they are considered as references.

(4) The VOF-LEE model is used to simulate the heat transfer process of R134a flow boiling in this part. It is postulated that the evaporation occurs at the positions where the local fluid temperature surpasses the saturated temperature of R134a. The degree of evaporation depends on the differences between local fluid temperature and the saturated temperature, along with the empirical relaxation factor "r" in LEE model, as depicted in the equation (3-18). The value of factor is selected through the validation of the numerical results against experimental data.

(5) The realizable k-ε model is chosen as the turbulent model for multiphase flow boiling in microchannels [253, 290], which has been explained in section 4.1. It is a refined turbulence model that could well predict flow patterns, velocity profiles and heat transfer characteristics, especially in regions with rapid changes in near-wall interactions of subcooled flow boiling in microchannels. Furthermore, it is also a valuable tool for accurately simulating complex flow process, such as those encountered during the transition from laminar to turbulent flows.

The investigated scenarios of subcooled flow boiling in microchannels are typical transitional flows involving both laminar and turbulent flow regimes. For the case with an inlet mass flux of 400 kg/(m²·s) and a heat flux of 69 kW/m², the inlet velocity of R134a is about 0.338 m/s and the average liquid Reynolds number is around 22 at the inlet of channel. Additionally, the

largest local velocity in the domain is approximately 1.69 m/s with a corresponding Reynolds number of 11287. Therefore, the realizable k-ε model is suitable for the present study.

The PISO algorithm is used for the pressure-velocity coupling and the second-order upwind discretization for the momentum and energy equations. The PRESTO and Geo-Reconstruct discretization methods are used for pressure and volume fraction interpolations. The variable time step is managed to maintain the maximum Global Courant number below 0.25, while the absolute residuals are adjusted to 1×10^{-4} to achieve numerical convergence.

(6) The main thermophysical properties are listed in Table.18.

Table.18 Thermophysical properties of R134a and PCM particles in present work

Properties	Unit	R134a [180,291]		PCM [98,292]
		liquid	gas	solid
T_{sat} and $T_{melting}$	℃	31	31	30.5 and 31.5
Latent heat of melting, H	kJ/kg	173	173	up to 208.7
Density, ρ	kg/m^3	1183.5	37.6	840
Specific heat capacity, c_p	J/(kg·K)	1451.1	1072.5	1900
Thermal conductivity, k	W/(m·K)	0.079	0.014	0.390

5.3-Grid independence and model validation

5.3.1-Mesh independence test

To capture small-size bubbles in viscous boundary layer, a non-uniform quadrilateral mesh refined towards the heating walls was employed in the computational domain, as shown in Figure.60.

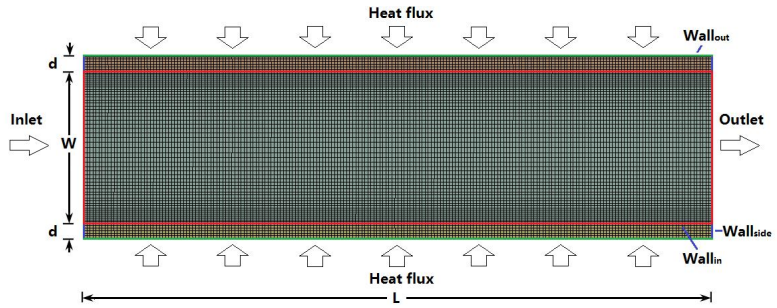


Figure.60 Schematic of numerical simulation construction and domain in Chapter 5

The objective of this chapter is to simulate the multiphase flow heat transfer of a R134a based functional fluid in a 2D horizontal stainless steel microchannel (with 0.5 mm width×20 mm length×0.05mm thickness) under a constant heat flux condition. A mesh independence test was conducted based on R134a flow boiling in the same domain. Four different mesh sizes were evaluated with an inlet mass flux of 200kg/(m^2·s) and a heat flux of 16kW/m^2. The area-averaged vapor fraction of R134a on inner walls in microchannels (x_{wall}) was used as the indicator for mesh independence. The results were plotted against the flow time revolution and the average grid size (i.e., d_1-d_4), as shown in Figure.61.

Accordingly, it is observed that when the grid size was below 10μm, the differences in vapor fractions among different mesh sizes were less than 3%. This indicates that the grid size was adequately refined to capture the formation of small bubbles on the heated surfaces. In other words, this grid size could accurately predict the local degree of saturation on the heated walls. Consequently, a size of 10μm was chosen for the subsequent simulations in this study.

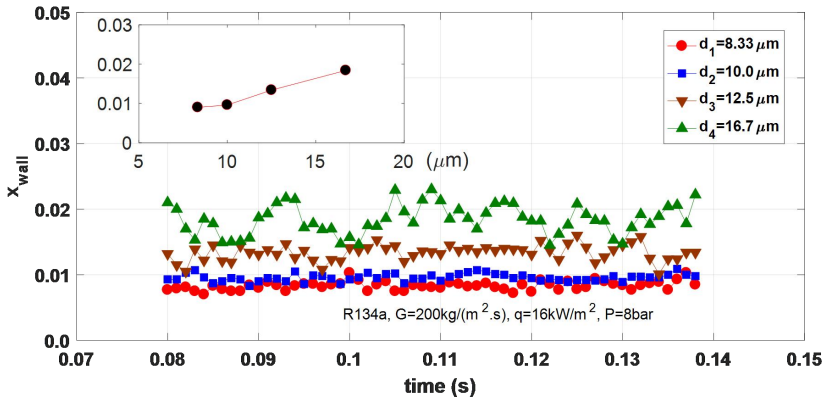


Figure.61 Grid independent test based on vapor fraction on inner heating surfaces of R134a

5.3.2-Simulation model validation

In the present study, the validation of those adopted numerical models was carried out in two separate steps due to the limited availability of experimental data for R134a-based functional fluid flow boiling in microchannels. Firstly, the multiphase VOF/LEE model for flow boiling was validated using experimental data of R134a flow boiling in a 1.1 mm diameter tube [293, 294, 295]. The contact angle and surface tension of R134a on stainless steel surfaces were set at 2° and 7.3×10^{-3} N/m, respectively [177]. Then, the VOF/the equivalent properties method

was validated based on single-phase convective heat transfer performance of functional fluids (i.e., 20% weight concentration of n-hexadecane in water) in a 2mm diameter tube [93].

(1) Validation of R134a flow boiling method (i.e., the VOF/LEE model)

As discussed in section 3.4.1, one of the challenges in adopting the LEE model as the mass and heat transfer model for flow boiling is to select an appropriate value r in Equation 9. This parameter significantly impacts the accuracy, such as the heated temperature, pressure drops, liquid-vapor interfacial behaviors and flow patterns in microchannels [240, 247]. For example, the effects of the factor on the heat transfer performance under the same operational condition is illustrated in Figure.62. the larger value of r, the higher HTC at the same conditions.

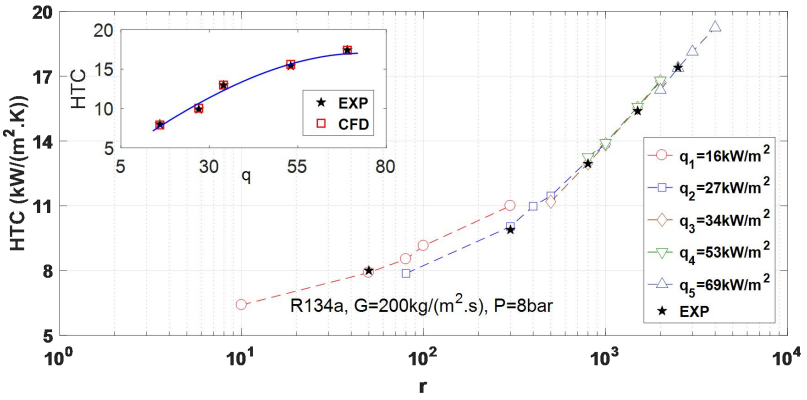


Figure.62 Relations of flow boiling heat transfer performance with empirical factor r in LEE model

Hence, the simulation results obtained by using the selected r values were compared with the corresponding experimental data for flow boiling HTCs and pressure drops in Figure.63. The results indicate that the numerical model and settings in this study can accurately predict both the HTCs within ±2.5% deviation and pressure drops within ±15% deviation of R134a flow boiling in channels, when the optimum values are set based on experimental data.

Additionally, the effect of suspended particles on the factor r of flow boiling is disregarded in the subsequent work due to a lack of reliable experimental data for the modification. Hence, the value r of R134a-based functional fluid is assumed to be the same as that of pure R134a in flow boiling under the identical conditions, which has been validated in the present section.

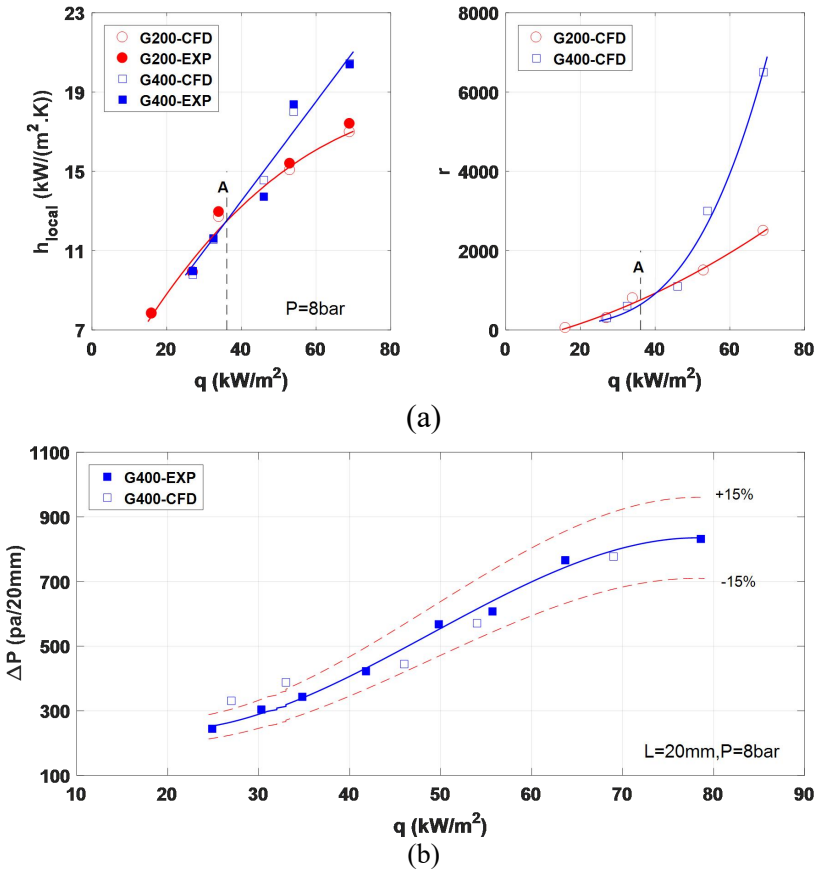


Figure.63 Comparisons of HTCs [293,294] and (b) pressure drop of R134a between numerical and experimental results in a microchannel [295]

(2) Validation of PCM melting method (i.e., the effective heat capacity method)

As mentioned before, there is few experimental data available of PCM slurries flow boiling in microchannels. Therefore, the equivalent heat capacity method for PCM melting is validated with experimental data from single-phase convective flow of n-hexadecane/H_2O emulsion in a mini-tube (D_h=2mm), as depicted in Figure.64. It is noteworthy that the simulation results of HTCs matched well with the experimental data with an error of ±15% in reference cases [93].

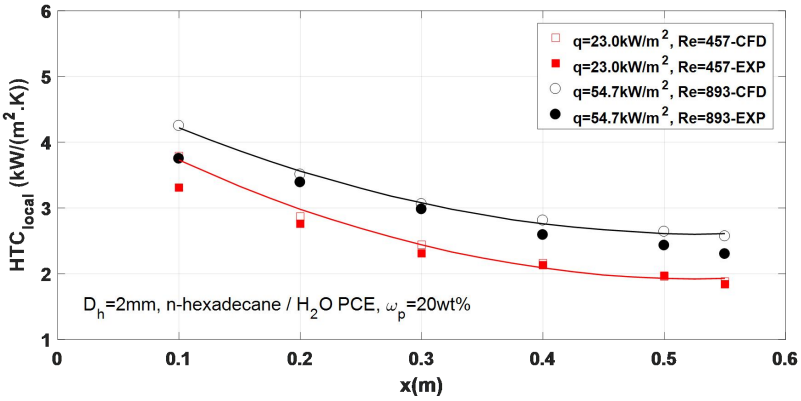


Figure.64 Comparisons of heat transfer results between numerical and experimental cases for local HTCs of n-hexadecane/H_2O emulsion (with PCM melting) in a mini-channel [93]

In general, the VOF-LEE-equivalent properties methods, which include the consideration of the equivalent properties such as heat capacity and viscosity, are considered acceptable for investigating the heat transfer performance of R134a-based functional fluids in microchannels.

5.4- Results and discussion

As mentioned in Section 2.2, the phase change materials are valuable in thermal management due to their ability to absorb the extra heat through melting process at a constant temperature. Additionally, in order to increase the heating area and prevent the leakage of the melted PCM into the surrounding fluids, the material could be encapsulated within shell materials to form the encapsulated phase change materials (EPCMs). Therefore, the purpose of this section is to investigate the properties effects of those encapsulated particles (e.g., the equivalent thermal conductivity and the latent heat of melting) on flow boiling heat transfer performance of R134a-based functional fluid in microchannel at a constant heat flux condition. The effects of particle concentration, mass and heat fluxes were explored in details.

As elaborated in the section 2.2.7, there are various factors that affect the equivalent physical properties of the encapsulated phase change material (EPCM) particles, such as the latent heat of fusion, the thermal conductivity and the temperature ranges of phase changing processes.

Specifically, the thermal conductivity ratio and the encapsulation ratio of the PCM particles are defined as the respective ratios of these parameters for the particle and the PCM material.

While a higher encapsulation ratio means that a larger heat absorbed during the phase change process, a higher thermal conductivity ratio leads to better heat transfer between the particles and their surroundings. From the heat transfer perspective, a higher thermal conductivity ratio combined with an appropriate encapsulation ratio of particles could enhance the overall heat transfer performance. However, it is a complex task to find the optimal balance between these ratios. It is not only dependent on the types of the core and shell materials, but also on those factors such as the diameters and the encapsulation layer thicknesses of particles, the practical constraints related to the material processing techniques and procedures. Consequently, even for the same PCM material, the properties of the PCM particles can exhibit notable variations due to the disparities in the preparation methods. Taking octadecane (C18) as an example, the thermal conductivity ratio of the particles ranges from 2 to 10 within the encapsulated ratio variation range of 0.1 to 0.8, as depicted in Figure.37. The main properties of the metal coated encapsulated particles of octadecane, including the thermal conductivity (k), the melting latent heat (h_m) and melting temperature range (ΔT_m), are listed in Table.19. Those are dependent on the size of capsules and the content of the PCM material in particles, which play critical roles in the cooling applications [96].

Table.19 The main properties of n-OD (C18) based metal coated EPCM particles in literature [96]

	Tm	h_m	ΔT_m	k	c_p	ρ
	℃	kJ/kg		W/(m·K)	kJ/(kg·K)	(kg/m^3)
n-OD/PMMA	31.1	208.7	12.8	0.390	1.900	840
n-OD/SiO_2	28.5	126.9	9.5	0.246	2.305	1184
n-OD/SiO_2-PDA-Ag (8)	28.0	72.0	8.8	0.536	2.525	1768
n-OD/SiO_2-PDA-Ag (16)	28.0	49.3	9.3	0.518	1.727	2306
n-OD/SiO_2-PDA-Ag (32)	27.8	33.2	8.6	0.840	1.579	3128
n-OD/SiO_2-PAD-Ag (48)	27.5	26.1	8.1	1.346	1.273	3916

Moreover, unlike the isothermal melting phenomena of most pure phase change materials, the melting process of the EPCM particles follows a non-isothermal phase transition pattern. This is mainly due to a combination of factors related to the heat transfer mechanisms, the material properties and external conditions, such as the thermal resistance caused by the encapsulation

layer surrounding the particles. As the discussion before, the PCM particles are presumed to behave as a pure fluid, and those impact on the isothermal flow boiling of R134a is studied in this chapter. Hence, it is crucial to consider the effect of the non-isothermal melting behaviour of the PCM particles. Therefore, the latent heat rate of PCM particles, quantified as the latent heat per the unit melting temperature (q_m) in the equation 5-1, is adopted to describe the non-isothermal melting feature.

$$q_m = \frac{h_m}{\Delta T_m} \tag{5-1}$$

Where, q_m is latent heat per unit melting temperature (kJ/(kg·K)), h_m is total latent heat (kJ/kg) and ΔT_m is the melting temperature range (K) of PCM particles.

In conclusion, this chapter primarily conducts a comparative study to investigate the effects of thermal properties (i.e., thermal conductivity and the latent heat per unit melting temperature and dynamic viscosity) and inlet concentrations of functional particles on the multiphase flow heat transfer performance of R134a flow boiling in microchannels under the same conditions [293-295]. The dynamic viscosity of functional fluids is related to the inlet concentrations and the properties of base fluid and functional particles. Drawing from the literature reviews and prospective advancement in the PCM materials and the associated encapsulation technologies, this study investigates the separate and interactive effects of the properties on the heat transfer performance across a wide range of thermal conductivity k from 0.08-10.0W/(m·K) and latent heat per the unit temperature q_m from 0-417.4kJ/(kg·K) by a predefined combination method. In particular, these include the materials that are currently feasible for production (e.g., pure n-Octadecane with k of 0.4 W/(m·K) and q_m of 208.7(kJ/(kg·K)), as well as the TiO_2 particle with k of 10 W/(m·K) and q_m of 0) and those that might become attainable in the future (e.g., the metal-coated EPCM particle with k of 1W/(m·K) and q_m of 41.74(kJ/(kg·K)). Furthermore, some virtual materials, which are impractical in actual applications, are also studied to assess the sensitivity of the properties regarding the impacts on the heat transfer performance. These include the PCM particle with a thermal conductivity similar to that of R134a (0.08W/(m·K)), as well as those akin to the thermal conductivity of TiO_2 particles (10W/(m·K)).

The relevant boundary conditions are listed in Table.20.

Table.20 The main boundary conditions of numerical simulations in Chapter 5

Parameters	Units	Values
Inlet temperature of functional fluid, T_{in}	℃	30
R134a boiling temperature (at 8 bar), T	℃	31
Latent heat per unit melting temperature, q_m	kJ/(kg·K)	0-417.4
Particle thermal conductivity, k	W/(m·K)	0.08-10.0
Mass fluxes, G	kg/(m^2·s)	200, 400
Heat fluxes, q_{wall}	kW/m^2	27-69
Inlet concentration of suspended particles, y	vol.	0-15%

Flow boiling HTCs, pressure drops and performance evaluation criteria (PEC) are determined to evaluate the heat transfer performance of flow boiling in microchannels. These results were calculated once the flow and heat transfer process reached a steady state, as a transient arithmetic model was utilized in this study.

For example, the overall HTC and pressure drop were calculated by

$$h_{\text{overall}} = \frac{\sum_{i=1}^{n}\left[\frac{q_{wall}}{T_{\text{wall,i}}-(T_{\text{in}}+T_{\text{out,i}})/2}\right]}{n} \tag{5-2}$$

$$\Delta P_{\text{overall}} = \frac{\sum_{i=1}^{n}\left|P_{in,i}-P_{out,i}\right|}{n} \tag{5-3}$$

Where, $h_{overall}$, $\Delta P_{overall}$ and q_{wall} are the overall HTC (kW/(m^2·K)), pressure drop (Pa) and heat flux (kW/m^2), while T_{wall}, T_{in} and T_{out} are the area-averaged channel inner wall temperature, mass-averaged inlet and outlet fluid temperatures (K) in microchannel, respectively. P_{in} and P_{out} are fluid pressure at channel inlet and outlet. The index "i" denotes an individual transient time point after thermal and hydrodynamic equilibrium state. A total number of "n" individual time points were considered for assessing the time-averaged performance at equilibrium state.

The performance evaluation criteria (FOM), a comparative ratio to demonstrate the advantage of one fluid/system over another in internal flow cooling applications, was calculated by [296]

$$FOM = \frac{h_{\text{mixture}}/h_{\text{R134a}}}{\Delta P_{\text{mixture}}/\Delta P_{\text{R134a}}} \tag{5-4}$$

Where, h and ΔP are the overall HTC (kW/(m^2·K)) and pressure drop (Pa) in microchannel. The subscripts "mixture" and "R134a" denote the improved R134a-based functional fluid and pure R134a fluid, respectively.

The local HTC was calculated by

$$h_{\mathrm{local,j}} = \frac{\sum_{i=1,j}^{n}\left[\frac{q_{wall}}{T_{\mathrm{wall,j}} - T_{\mathrm{fluid,j,i}}}\right]}{n} \tag{5-5}$$

where, h_{local} and q_{wall} are local HTC (kW/(m^2·K)) and heat flux (kW/m^2). The index j indicates the individual spatial locations for where the local HTC being evaluated. T_{wall} is local area-averaged channel wall temperature and T_{fluid} is the local mass-averaged bulk temperature (K) at corresponding individual evaluation points along channel wall.

5.4.1-Effects of particle properties on the overall performance

The present study examined and compared the effects of added particle properties, including enhanced thermal conductivity and latent heat on the overall heat transfer performance (such as HTC, pressure drop, and FOM) of R134a-based functional fluids. The investigation was conducted in comparison to pure R134a under a constant heat flux of 69 kW/m^2 and mass fluxes of 200 or 400 kg/(m^2·s). Various simulation cases were considered and the thermal conductivity and latent heat of the functional fluids were varied according to Table.19. For the analysis of thermal conductivity effects, the base case assumed that the added particles had no associated latent heat and possessed the same thermal conductivity as base fluid, pure R134a (0.08 W/(m·K)). When examining the impact of the melting latent heat, thermal conductivity of particles was set at 0.4 W/(m·K), based on the reference value for pure n-Octadecane.

5.4.1.1-Flow boiling HTC

Figure.65 presents the results of the overall HTCs in microchannels for functional fluids with different thermal conductivity and latent heat improvements. The evaluations were performed under the same conditions for two different mass fluxes and three particle concentrations.

As shown in Figure.65, the HTCs of the modified functional fluids in the microchannels were enhanced compared to those of pure R134a (represented by the solid dot lines). These trends were observed when the thermal conductivity and the melting latent heat per unit temperature increased due to the addition of particles with higher thermal conductivity and greater latent heat under the same conditions. Additionally, the HTCs exhibit a positive correlation with the inlet mass fluxes and particle concentrations.

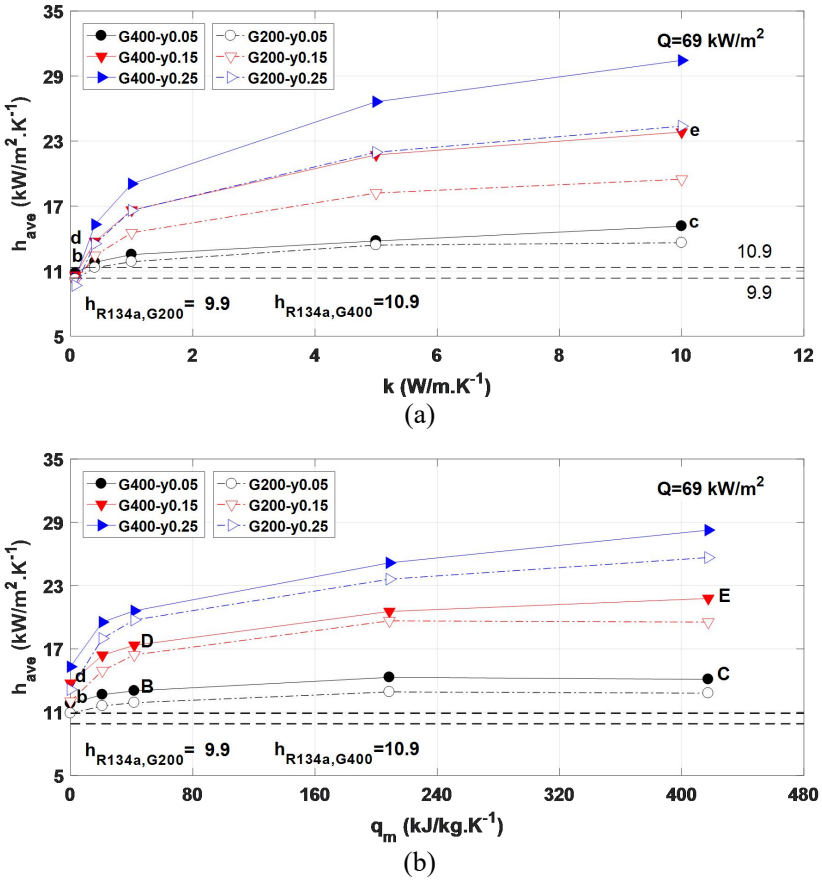


Figure.65 Effects of thermal conductivity(a) and latent heat per unit melting temperature (b) on the overall HTCs of R134a-based functional fluid in microchannel (G-mass flux (kg/(m²·s)), y-volume concentration)

Furthermore, for the same particle concentration, the increase in thermal conductivity and the melting latent heat per unit temperature of functional fluid leads to an increase in the HTCs. However, the rate of increase gradually diminishes as the thermal conductivity and latent heat values become higher. For instance, at a mass flux of 200 kg/(m²·s) and a concentration of 5% vol. (depicted by black chain-dotted lines) in Figure.65(a), the HTCs remain nearly constant when the thermal conductivity and the latent heat per unit temperature of particles exceed 5

W/(m·K) and 208.7 kJ/(kg·K), respectively. Generally, it can be observed that the HTC values reach 9.9 kW/(m^2·K) for pure R134a, 13.0 kW/(m^2·K) for R134a with particles of enhanced thermal conductivity, and 12.9 kW/(m^2·K) for R134a with particles of enhanced latent heat.

Furthermore, it is worth noting that the HTCs in the different thermal conductivity cases are a nearly similarity under the operating conditions of 400 kg/(m^2·s) and 15%vol., compared to the conditions of 200 kg/(m^2·s) and 25%vol. in Figure.65 (a). This suggests that the multiple factors, such as the mass flux, particle concentration and other parameters, can influence flow boiling HTCs. An optimal case of these factors may exist to achieve the maximum HTC for a specific practical application. To gain a better understanding of the particle property's effect on the HTCs in microchannels, the observations of flow boiling patterns (referred to as bubble distribution in the flow domain) and the area-averaged surface vapor fraction are presented in Figure.66 and Figure.67, respectively,

Figure.66 presents the flow boiling patterns in microchannels at 400 kg/(m^2·s) and 69 kw/m^2 for pure R134a, R134a-based functional fluids with higher thermal conductivity and larger melting latent heat particles, respectively.

Accordingly, under the same mass and heat flux conditions, the flow patterns observed in the microchannel at steady state are characterized by large bubbles and transitioning towards slug flow for pure R134a. In contrast, the flow patterns of R-134a based latent heating functional fluids (e.g., E1-E4) demonstrate that the addition of particles with higher latent heat, resulting in additional effective heat capacity in fluid, can shift the flow patterns from near-slug flow back to near-bubbly flow at the same particle concentration (e.g., 5%vol. and 15%vol.). This transition effect becomes more pronounced with increasing latent heat and concentration of the added PCM particles. Consequently, flow boiling HTC is enhanced by adding particles with higher latent heat, and it further increases with an increment in the effective latent heat, as also illustrated in Figure.65.

Nevertheless, when comparing the effects of adding particles with high thermal conductivity on flow boiling patterns, the influence is either insignificant or even reversed (e.g., N1-N4) in Figure.65. This can be attributed to two main factors: the improved overall effective thermal

conductivity of fluid and the deposition of particles on the heated surfaces [86]. Therefore, the enhancements in HTCs, resulting from the incorporation of functional particles with higher thermal conductivities in Figure.66, could be primarily interpreted from the perspective of the improved overall thermal conductivity in microchannels rather than the flow patterns.

Figure.66 presented bubble and particle distributions of R134a and different functional fluids flow boiling in microchannels at a mass flux of 400 kg/(m^2·s) and a heat flux of 69kW/m^2. As shown in subfigure R0, it illustrates a typical subcooled flow boiling heat transfer phenomena, encompassing the transition from single-phase convection flow at the inlet to the intermittent slug flow boiling heat transfer near the outlet. The subfigures N4 and Y4 depict the outcomes of the functional particle with the same properties and particle concentration.

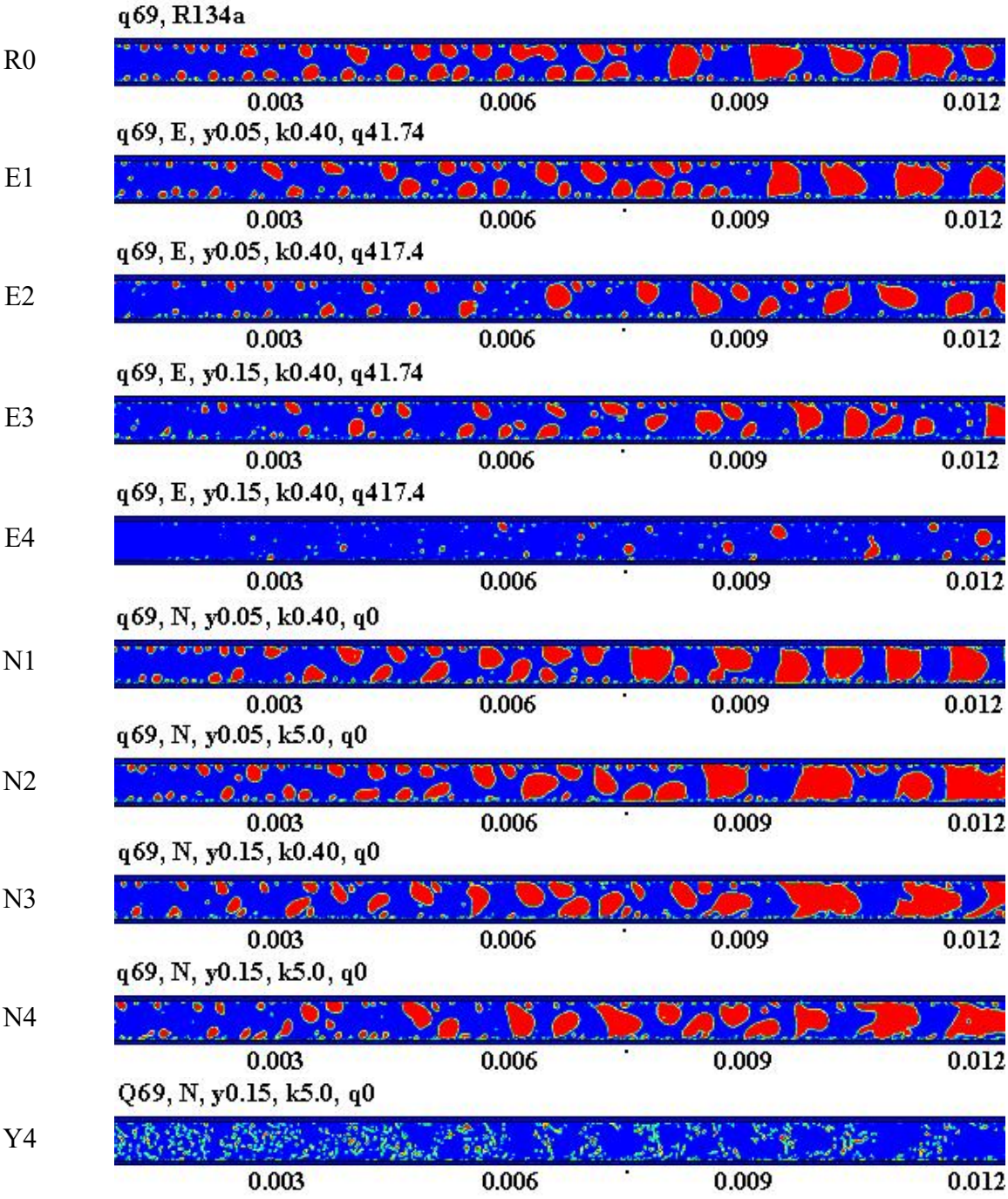
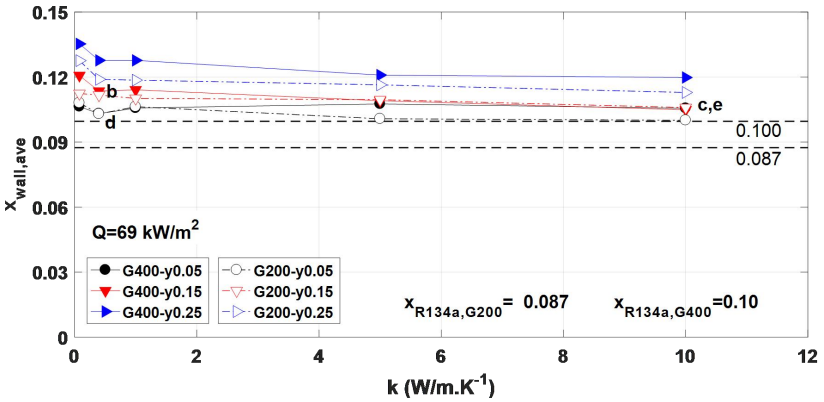


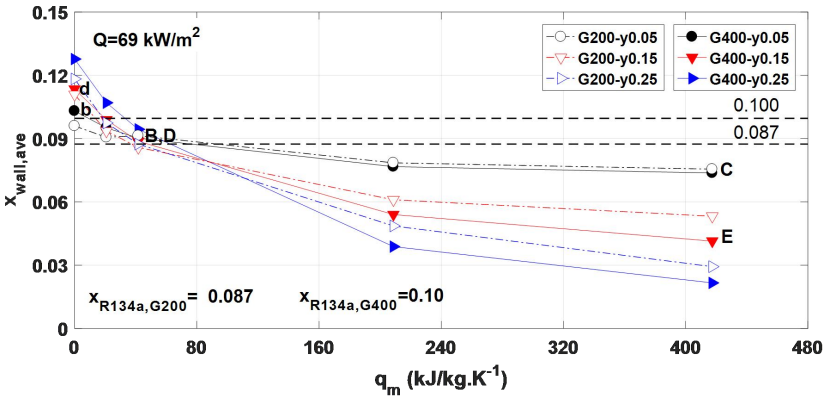
Figure.66 The bubble and particle distribution of R134a based functional fluids near the outlet of microchannels at a mass flux 400 kg/(m^2·s) and a heat flux 69 kW/m^2 (E: EPCM, N: Nanofluid)

Figure.67 illustrates the relations between the area-averaged vapor fraction on heated surfaces (i.e., $x_{wall,\ ave}$) and thermal properties (i.e., thermal conductivity k and the latent heat per unit

temperature q_m) of functional particles in microchannels under the mass fluxes of 200 and 400 kg/(m²·s) and a heat flux of 69 kW/m².



(a)



(b)

Figure.67 Effects of thermal conductivity(a) and latent heat per unit melting temperature (b) on the area-averaged surface vapor fraction in microchannels (G-mass flux (kg/(m²·s)), y-volume concentration)

According to Figure.67(a), it is evident that the addition of thermal conductivity functional particles could increase the vapor fractions on heated surfaces compared to pure R134a at 69 kW/m² (depicted by black dotted lines). Furthermore, as the thermal conductivity continues to increase, the surface vapor fraction values decline but do not ultimately converge to the values observed for pure R134a. This may be attributed to the tendency of bubbles to be retained on heated surfaces due to the particle deposition near the surfaces [88,90]. Notably, these solid particles that accumulate on the heated surfaces possess higher thermal conductivities. Similar trends can be observed in Figure.67(b), where the vapor fractions on heated surfaces decrease as more effective latent heat becomes available in the fluid through the addition of latent heat

functional PCM particles. This suggests that the addition of latent heat functional particles in R134a helps limit the accumulation of surface bubbles, thereby preventing the local dry-out at high heat fluxes [114, 282].

In order to explain the property effects of functional particles in R134a on flow boiling HTCs clearly and concisely, the relations of HTCs with the vapor fraction on the heated surfaces are plotted in Figure.68.

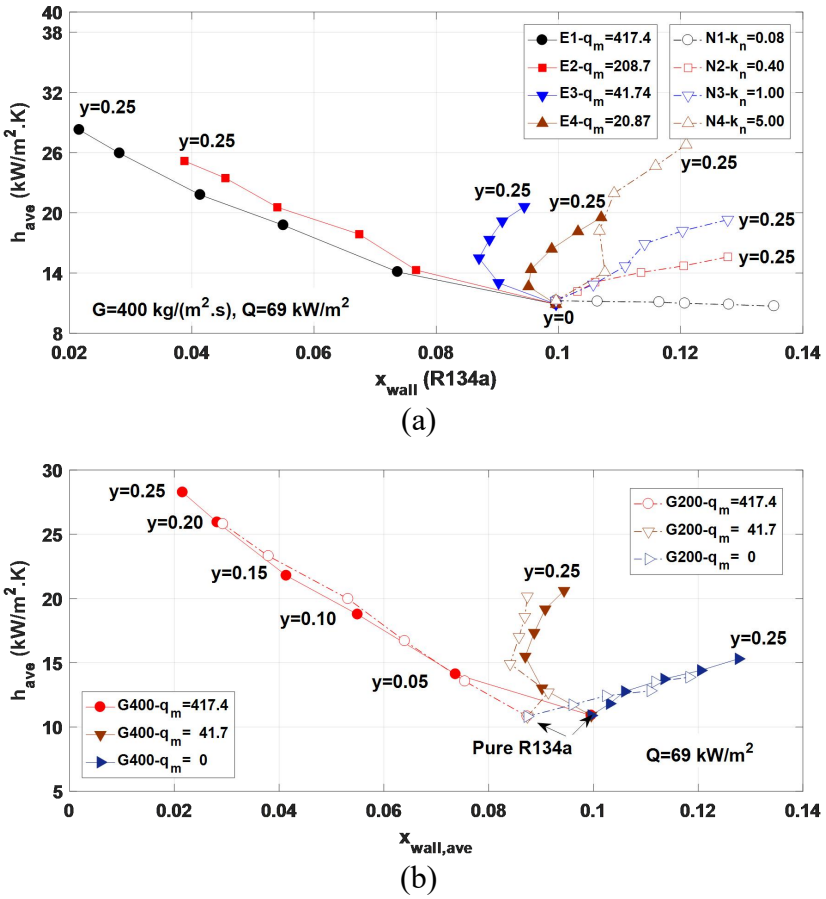


Figure.68 Relations of flow boiling HTCs with vapor fraction on surfaces for R134a-based functional fluids in microchannel with different (a) particle properties and (b) mass fluxes at 69 kW/m²

Compared to pure R134a flow boiling (i.e., inlet particle concentration y is 0) at 400kg/(m²·s) and 69kW/m², the addition of functional particles could enhance the HTCs based on different tendency of the vapor fraction on the heated surfaces with various thermal properties and inlet concentrations of functional particles in Figure.68 (a). While the facts of suspended particles aggregated and deposited near heated surfaces could increase the vapor fraction on the heated

surfaces, the effects of the extra endothermal heat and thermal conductivity enhancement of functional particles could decrease the values $x_{wall,\,ave}$ more or less. It is the balance of positive and negative effects, depended on properties and inlet concentrations of particles, that finally dominants the vapor fraction on the heated surfaces. This could explain the existence of the curved lines (e.g., E3, E4 and N4) in Figure.68 (a). Similarly, the inlet mass fluxes of coolants also affect change rules of the vapor fraction on the heated surfaces at 69 kW/m^2. The more mass flux means that there are the more particles melting and attached on the heated surfaces.

5.4.1.2-Pressure drop

The effects of adding higher thermal conductivity and melting latent heat functional particles to R134a on pressure drops in microchannel are illustrated in Figure.69.

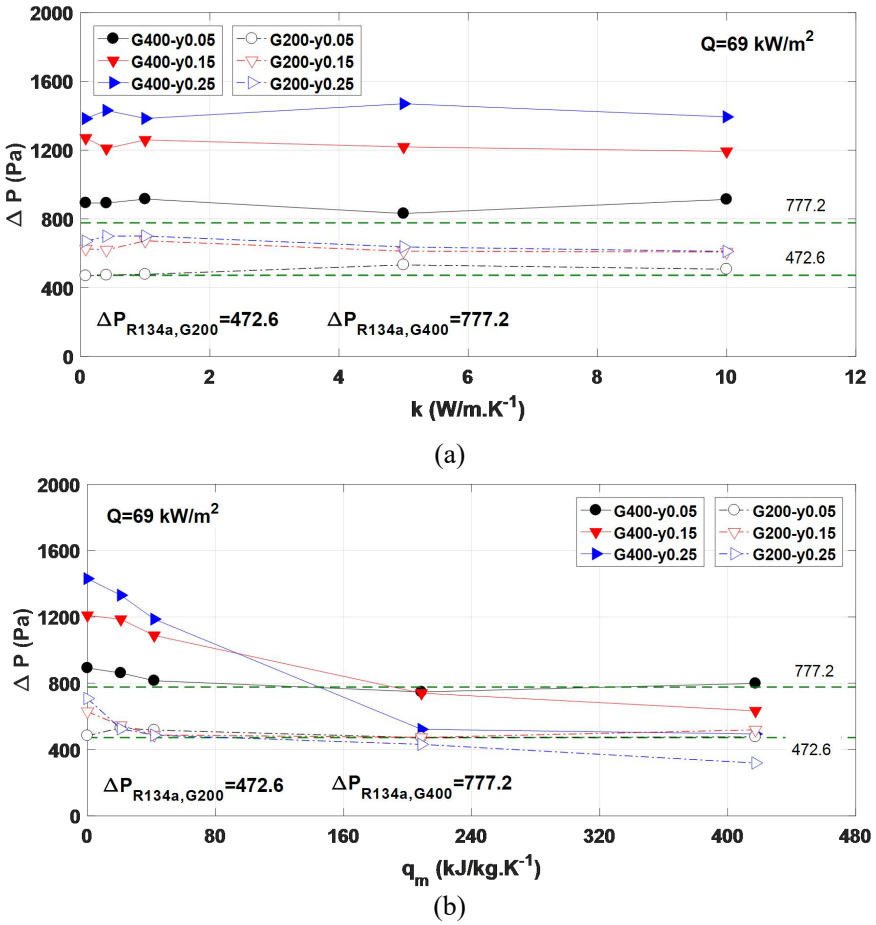


Figure.69 Effects of thermal conductivity(a) and latent heat per unit melting temperature (b) on the time-averaged pressure drop in microchannels (G-mass flux (kg/(m^2·s)), y-volume concentration)

Accordingly, it can be observed in Figure.69 that the addition of solid particles increases the pressure drops of R134a flow boiling in microchannels. For example, almost all of pressure drops in Figure.69 (a) are larger than the corresponding values for R134a, primarily due to the increased liquid viscosity resulting from the addition of solid particles in R134a. Furthermore, the pressure drop rises further as the particle concentration increases at a certain mass flux condition. It is also evident that the pressure drop values are greater for higher mass flow rates when comparing the values in Figure.69(a). The pressure drop is mainly influenced by the physical properties of the fluid and the added particles, such as the effective fluid viscosity and the possible aggregation of particles in the bulk fluid [88,202].

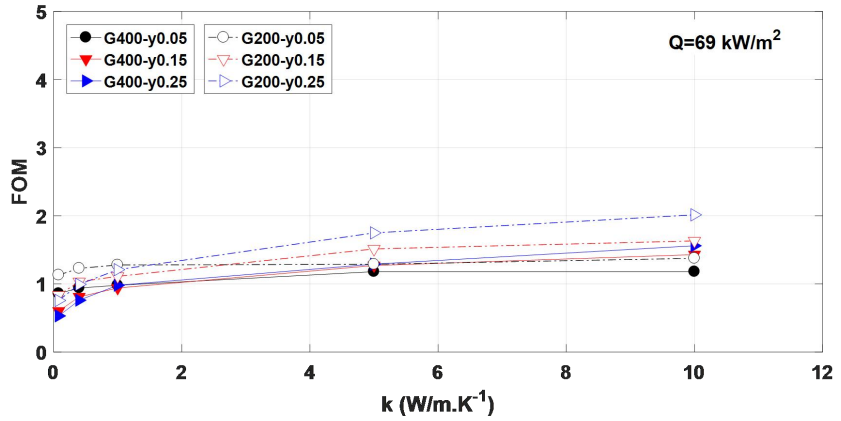
However, the property effects of functional particles on pressure drops in a microchannel are not the same. The pressure drops barely change with increased thermal conductivity, as shown in Figure.69(a). This implies that changes in thermal conductivity of particles and the fluid have limited impacts on pressure drops under the same mass and heat flux conditions (equally at the same vapor quality). On the other hand, increasing the latent heat of the added particles results in a decrease in pressure drop, which can be attributed to the additional heat absorbed during the particle phase-changing process in Figure.69(b). In other words, the endothermic PCM melting process reduces the vapor fractions of R134a in the bulk fluid under the same operational conditions. This shift in flow patterns and attenuation of turbulent flow resistance can be observed in Figure.66 and Figure.69.

5.4.1.3-Figure of Merit

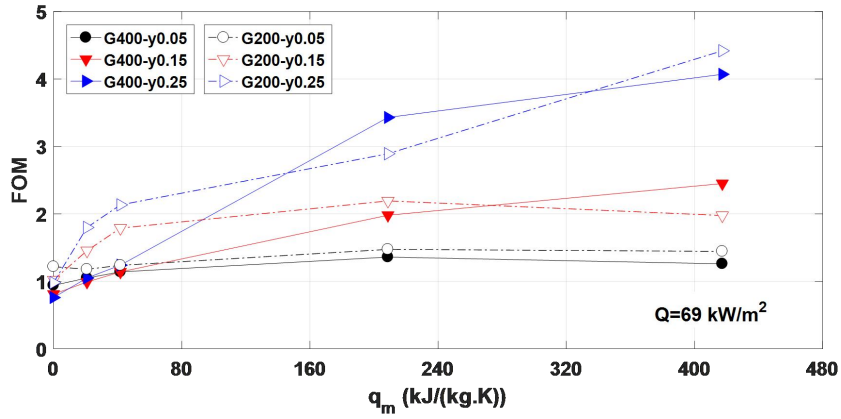
In order to evaluate the overall heat transfer performance in microchannels and compare the effects of adding functional particles to R134a, the Figures of Merit (FOMs) are calculated by the equation (5-4) and plotted in Figure.70, based on the corresponding HTCs and pressure drop results obtained before. The thermal conductivity and latent heat properties of R134a are 0.08 W/(m·K^{-1}) and 173 kJ/kg, respectively.

The overall indicator (FOM) is defined as the ratio between the heat transfer ratio (modified over the base fluid) and the pressure drop ratio (modified over the base fluid). It is commonly

used to provide a general assessment of the overall benefits of a specific treatment (such as fluid modification) for enhancing heat transfer.



(a)



(b)

Figure.70 Effects of thermal conductivity(a) and latent heat per unit melting temperature (b) on the FOM in microchannels (G-mass flux (kg/(m²·s)), y-volume concentration)

Generally, it is clear in Figure.70 that the FOMs increase and tend to stabilize as the thermal conductivity (k) increases in Figure.70 (a), and as the melting latent heat per temperature (q_m) increases in Figure.70(b), for the added functional particles at the same concentration, mass, and heat fluxes. This indicates that the mentioned fluid modification treatments have positive effects on improving the heat dissipation capacity, as assessed by the combined evaluation of flow boiling heat transfer coefficients (HTCs) and pressure drops.

Furthermore, it is observed that the enhancement level of the FOM for latent heat functional particles in Figure.70(b) is greater than that for pure improved thermal conductivity particles

in Figure.70 (a), especially when considering the maximum values (the final stable state of the curves) under the same conditions. For example, the largest FOMs are 2 in Figure.70(a) and 4.4 in Figure.70(b), respectively. This can be explained by the results obtained from the HTCs in Figure.65 and the pressure drops in Figure.69. The HTCs increase with the properties and the concentrations of added latent heat functional particles and enhanced thermal conductivity particles under the same conditions. However, pressure drops decrease due to the additional endothermal heat induced by PCM particle melting processes, while they increase in the cases of improved thermal conductivity solid particles.

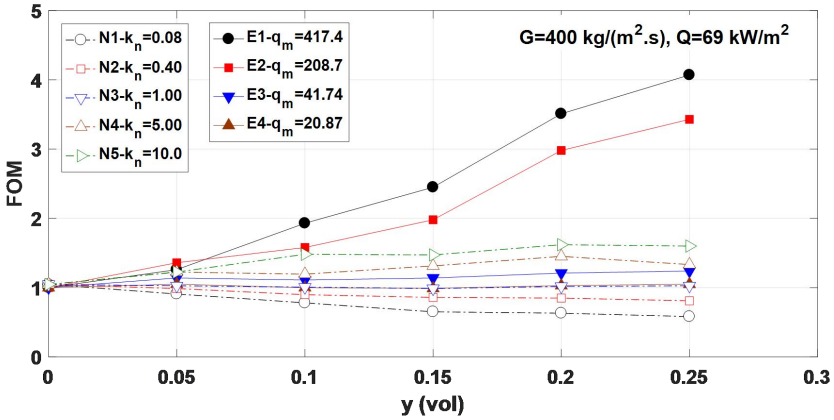


Figure.71 Effect of particle concentrations on the FOMs of functional fluid flow boiling with (a) different properties and (b) mass fluxes in microchannel at 69 kW/m²

Specifically, the FOMs are less than one in cases where the thermal conductivity is smaller than that of pure R134a (i.e., 0.08 W/(m·K)) or when the melting latent heat is negligible. For example, taking the cases without melting (e.g., points on the y-axis) in Figure.70(b), the

FOMs are smaller than 1. This indicates that adding particles to the base fluid could worsen the heat transfer performance in these cases.

According to the aforementioned reviews on nanofluid flow boiling in section 2.26 and Table 11, it has been pointed out that the suspended particles can block the active bubble nucleation sites, inhibit heat transfer from surfaces, and ultimately deteriorate heat transfer performance in microchannels. This is primarily due to the surface modification caused by the deposition of particles on heated surfaces [88,90,198]. Hence, in order to counteract the adverse effects of added particles on the flow boiling heat transfer, it is necessary to select particle materials with higher thermal conductivity than the base fluid or with a certain melting latent heat. For instance, to ensure that the FOM is greater than 1 in Figure 71(a), the thermal conductivity of particles without the melting effects (e.g., N3-N5) should be larger than 1 W/(m·K), while the latent heat per temperature of particles (e.g., E1-E4) with 0.08 W/(m·K) needs to be greater than 20.87 kW/(m²·K). The properties of R134a are 0.08 W/(m·K) and 173 kJ/kg, respectively.

The effect of inlet mass flux on the FOM is complex. In the cases of coolants with improved thermal conductivity particles in Figure.70 (a) and small latent heat particles in Figure.70 (b), increasing inlet mass flux results in a smaller FOM value under the same condition. This is because a higher inlet mass flux leads to more particles being suspended in the domain and attached to heated surfaces. However, for cases with particles having a large latent heat, an increase in inlet mass flux means that more additional heat is absorbed by the PCM melting process. This reduces the evaporation degree (indicated as the vapor fraction in the domain) of R134a, which can transform the large-size bubbles into small bubbles as shown in Figure.66 and ultimately increase the HTC while decreasing the pressure drop. Consequently, the FOM is larger than that without melting in Figure.70 (b).

In conclusion, the FOMs of R134a-based latent heat functional fluids are higher than unity 1. This is primarily due to the balances between the advantages and disadvantages arising from the effects of properties (e.g., thermal conductivity and latent heat per unit temperature) and suspended particles on flow boiling in microchannels. For the improved thermal conductivity

functional fluid, the thermal conductivity of particles needs to be significantly higher than that of the base fluid in order to achieve FOM values greater than unity 1.

5.4.2-Effect of heat fluxes on the overall performance

In the previous section, the impact of functional particles on flow boiling of R134a-based functional fluid was evaluated at a constant heat flux of 69 kW/m². In this section, the effect of heat fluxes on the heat transfer performance of functional fluid has been investigated at a particle concentration of 15% vol., as depicted in Figure.72. To facilitate a better comparison of the property effects, the thermal conductivity of the latent heat functional particles was set to be the same as that of the pure thermal conductivity functional fluid (0.4 W/(m·K)). The latent heat rate of the PCM particles was set as 417.4 kJ/(kg·K).

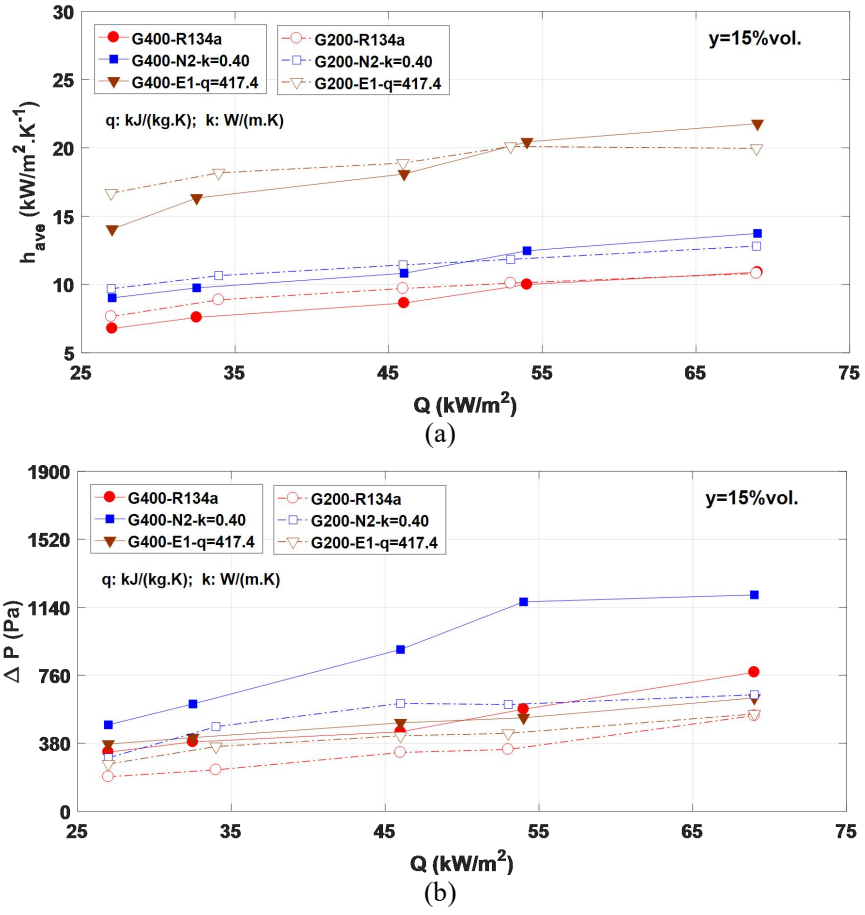


Figure.72 Effects of heat fluxes on (a) HTCs and (b) pressure drops of R134a-based functional fluids flow boiling in microchannel

As observed in Figure.72 (a), the HTCs of R134a-based functional fluids, whether thermal conductivity or latent heat functional types, are increased with higher heat fluxes on heated walls. This indicates that the heat flux, which contributes to the nucleation process in flow boiling, has a positive effect on R134a flow boiling heat transfer in the range of 27-69 kW/m² for both types of investigated functional fluids.

Furthermore, when the inlet mass flux is increased from 200 to 400 kg/(m²·s), the HTC values decrease at low heat fluxes (e.g., 27 kW/m²) but increase at high heat fluxes (e.g., 69 kW/m²), particularly for latent heat functional fluid. This is because at low heat fluxes, which are far from slug flow and critical heat flux, nucleation (i.e., bubble formation) enhances flow boiling heat transfer. However, at higher flow rates, there is less time for the fluid to interact with the heating surfaces, which can deteriorate the nucleation and the HTCs [117]. This phenomenon becomes more pronounced with the addition of latent heat functional particles, which could shift the flow pattern of R134a rom slug flow to bubbly flow. Conversely, for flow boiling heat transfer primarily governed by convection under high heat flux conditions, the excessive nucleation could lead to local bubble accumulation and subsequent the dry-out [114]. Hence, a higher flow rate is preferred to enhance convection and diminish the bubble accumulation on the heated surfaces at a high heat flux condition. The results in Figure.72(a) can be better attained by examining the corresponding bubble distribution in microchannels, as illustrated in Figure.73.

The pressure drops of R134a-based functional fluids with a 15%vol. particle concentration are plotted against various heat fluxes in Figure.72(b). It is indicated that the pressure drops increase with higher heat fluxes due to the induction of increased vapor quality and escalated turbulence resistance, as also illustrated in Figure.73. Additionally, the pressure drops also rise with an increase of mass flux due to the elevated flow resistance.

Moreover, functional fluids containing particles with enhanced thermal conductivity exhibit the highest pressure drops, surpassing those of the R134a base fluid. This rise in pressure drops is attributed to the increase in viscosity caused by the addition of particles. However, the pressure drops of functional fluids with latent heat functional particles are much lower,

and in fact, lower than those of pure R134a, especially under high heat flux conditions. One possible explanation, as discussed earlier, is that the additional available heat capacity in the bulk can delay the development of flow boiling (i.e., moving towards slug flow) and reduce the flow resistance in the domain. A clearer understanding of the findings in Figure.72 (b) can be attained in conjunction with the corresponding bubble distributions depicted in Figure.73.

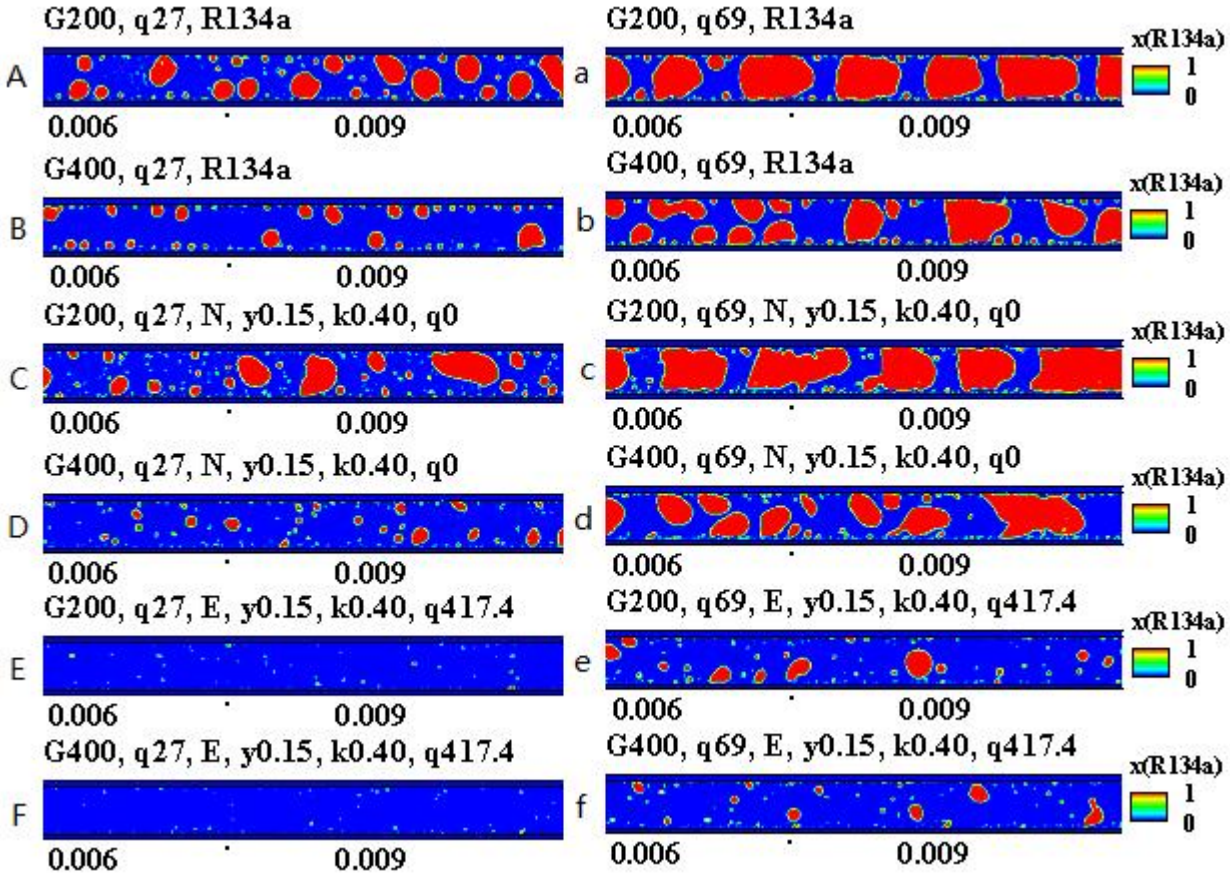


Figure.73 Bubble distribution flow patterns of R134a based functional fluids in microchannel at mass fluxes of 200, 400 kg/(m^2·s) and heat fluxes of 27, 69 kW/m^2 (left A-F: 27 kW/m^2 right a-f: 69 kW/m^2)

Therefore, the overall heat transfer performance of R134a-based functional fluids multiphase flow in microchannels ultimately depends on the balance among the nucleation, convection, particle interactions and latent heat absorption.

5.4.3-Effects of suspended particles on local performance

In order to further investigate the heat transfer mechanisms of R134a-based functional fluids during flow boiling in a microchannel, the results of local heat transfer coefficients (HTCs)

along the x-axis flowing direction at a mass flux of 400 kg/(m²·s) and a heat flux of 69 kW/m² are presented in Figure.74.

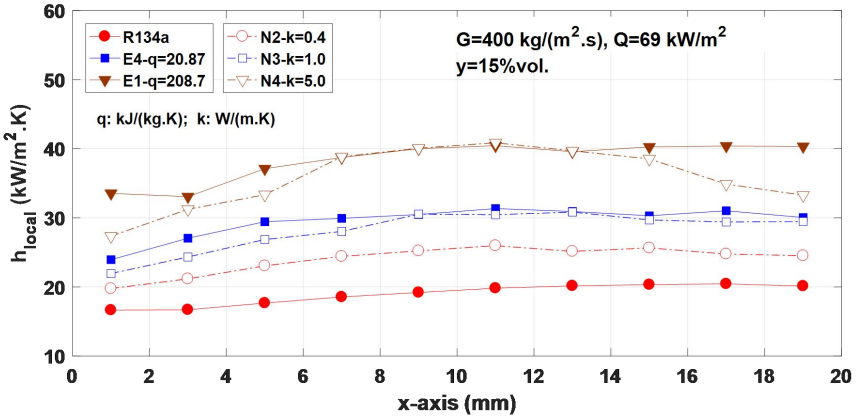


Figure.74 Comparison of local HTCs along the x-axis flow direction for R134a based functional fluids at 400 kg/(m²·s), 69 kW/m², 15% vol.

According to Figure.74, the local HTC f pure R134a initially increases and then maintains almost a constant value near the exit of the microchannel. This local HTC curve for R134a differs from the typical curve observed for water flow boiling in a channel, which shows an initial rise followed by a decline after reaching a maximum value, as depicted in Figure.75. The main reason is likely the distinct surface wettability of pure R134a compared to water, as R134a exhibits a superhydrophilic feature [254,297, 298]. Furthermore, it can be observed that the addition of functional particles enhances flow boiling heat transfer, as indicated by all local HTCs of functional fluids exceeding those of pure R134a under the given conditions.

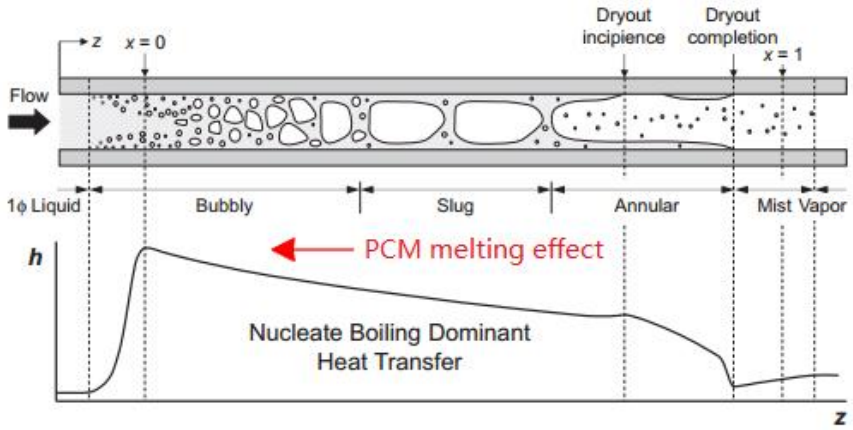


Figure.75 Schematics of bubble distribution in domain and local HTC values of water flow boiling in a channel at a uniform heat flux condition [117].

Nonetheless, the mechanisms of flow boiling differ between thermal conductivity and latent heat functional particles introduced to R134a, despite their shared characteristic of being solid particles integrated into pure R134a, which in turn elevates the fluid's viscosity. In Figure.74, it becomes evident that the local HTC near the channel exit of the functional fluid, containing suspended particles with enhanced thermal conductivity of 5 W/(m·K), experiences a decrease (e.g., at 10-20 mm in the direction, marked by the brown dotted line with a reversed triangle). This reduction is a consequence of flow boiling evolving towards slug flow at the exit and the gradual inhibition of nucleate boiling due to particle deposition, as depicted in Figure.66. However, this diminishment is averted in all functional fluids containing latent heat functional particles (represented by the brown solid line with a reversed triangle in these figures). The presence of particles with significantly higher latent heat within the bulk fluid may reshape the original bubble distribution through additional heat absorption (where the total heat Q_{wall} is equal to the sum of the melting heat $Q_{R134a,\ boiling}$ and the boiling heat $Q_{PCM,\ melting}$), thereby promoting enhanced flow boiling heat transfer (indicated by the red arrow in Figure.75).

5.5-Summary

In this study, numerical simulations were conducted to investigate heat transfer performance of R134a-based functional fluids flow boiling in a horizontal microchannel. The functional fluids were modified by adding particles with higher thermal conductivity and melting latent heat into the base fluid of R134a. The simulations were performed under a constant heat flux condition. The VOF-LEE model was employed to simulate R134a flow boiling, while the effective heat capacity method was used to model the melting of PCM particles. The validity of the numerical model was confirmed by comparing the simulation results with experimental data in the literature. The effects of some factors, such as the properties of particles, particle concentration, mass and heat fluxes on the heat transfer performance in microchannels were thoroughly evaluated by the validated numerical model. The main remarks are as follows:

(1) Adding functional particles with improved thermal conductivity or the effective latent heat could enhance R134a flow boiling heat transfer in microchannels. However, the mechanisms between the heat transfer enhancements by adding different suspended particles are different.

Latent heat functional particles could provide base fluid R134a with additional heat capacity but more importantly help shift flow patterns to be in favor of flow boiling heat transfer (e.g., transform slug flow to bubbly flow). While high thermal conductivity particles contribute to flow boiling heat transfer performance mainly through the enhancement of equivalent thermal conductivity and heat conduction of coolants.

(2) Pressure drops of R134a flow boiling in microchannels may be presumed to increase due to the addition of suspended solid particles. Indeed, the pressure drop was found increased when the latent heat functional particles added to base fluid. This suggests that the improved thermal conductivity has little impact on pressure drops in microchannels, and that pressure drops are mainly influenced by the increase in fluid viscosity. However, significant reductions in flow boiling pressure drop were observed in the microchannel when latent heat functional particles were added to the base fluid R134a. This can be attributed to the favorable shift in flow patterns induced by the additional available heat capacity in the bulk fluid, resulting from the presence of latent heat functional particles.

(3) The flow boiling FOMs of non-melting functional fluids such as high thermal conductivity nanofluids suspended in microchannels are barely above or even lower than 1, primarily due to the significant increase in pressure drops caused by the addition of particles. On the other hand, the FOMs of latent heat functional fluids (such as the PCM emulsions and slurries) are always greater than 1, indicating that there are thermal performance benefits from the addition of particles with the endothermal heat absorption. This results in enhanced heat transfer while reducing the penalty of pressure drop.

(4) The local flow boiling heat transfer characteristics of R134a in microchannels differ from those of water. Therefore, it is important to consider the differences in fluid properties, such as the wettability on heated surfaces. For example, the R134a exhibits superhydrophilicity on stainless steel surfaces, whereas water does not. The results of the current study also suggest that the addition of latent heat functional particles can improve the distribution of bubbles in the channel. This is achieved through the additional available heat capacity provided by the particles, which helps prevent local dry-out on heated surfaces, especially at high heat fluxes.

Chapter-6 Flow boiling heat transfer of the NH_3/H_2O mixture

6.1-Introduction

In this chapter, a novel simulation method (i.e., the VOF-modified LEE model) is adopted to investigate heat transfer performance of the NH_3/H_2O mixture flow boiling in microchannels for enhancing heat dissipation capability in electronic cooling applications.

Flow boiling of the zeotropic mixture is a non-isothermal phase changing phenomenon under a constant pressure condition, which is different with that of pure fluid. This feature holds the potential to mitigate irreversibility of heat transfer in heat exchangers and enhance the energy efficiency of phase change-related thermal applications. Moreover, the properties, such as the saturation temperature of the zeotropic mixture can be flexibly adjusted by manipulating the inlet concentrations of the more volatile component. This adjustability confers advantages in multiphase applications that have stringent limits on the maximum operating temperatures, as seen in electronics industry. For instance, while water cannot evaporate at 50℃, an NH_3/H_2O mixture can accomplish this when an appropriate NH_3 concentration is selected at 1 bar.

As discussed in Chapter 1, the NH_3/H_2O mixture has been widely used as a zeotropic mixture in industrial refrigeration systems for several decades. One of its primary advantages lies in its high latent heat of evaporation. For instance, the NH_3/H_2O mixture exhibits an evaporating latent heat value of 1689 kJ/kg at a saturation temperature of 323.15 K, in contrast to that of 167 kJ/kg for the R134a/R245fa mixture and 155.5 kJ/kg for the R123/R134a mixture under the same saturated temperature. Therefore, the NH_3/H_2O mixture is selected for this section.

However, it has been observed that the majority of experimental studies in the literature were conducted in large-scale heat exchangers, and the empirical correlations derived from those studies may not be applicable for predicting the heat transfer performance of the NH_3/H_2O mixture flow boiling in microchannels. This is dominantly due to the differences in the bubble dynamics and flow patterns that occur in microchannels. Furthermore, there are only a limited number of numerical studies available that specifically investigate the NH_3/H_2O mixture flow

boiling in microchannels. Therefore, it is of great significance to conduct dedicated numerical studies to investigate flow boiling of the NH_3/H_2O mixtures in microchannels.

In general, numerical simulations were conducted to investigate the impacts of inlet mass flux, the NH_3 concentration at the inlet, and heated wall temperature on the overall and local heat transfer performance of NH_3/H_2O mixtures in a single horizontal microchannel (i.e., with 0.4 mm width and 6 mm length) under a constant wall temperature condition.

6.2-Basical assumptions ad treatments

As discussed in Chapter 2, numerical performance simulations of the NH_3/H_2O mixture flow boiling present huge challenges due to its complex phenomena, making it computationally demanding and time-consuming. Unlike those pure fluids such as H_2O and NH_3, the NH_3/H_2O mixture contain multiple species (e.g., $NH_3{\cdot}H2O$, NH^{4+}, NH^{2-}, and OH^-) with distinct physical properties (e.g., density and viscosity) in both the liquid and gaseous phases. Currently, there is a lack of dedicated mass diffusion models available specifically tailored for the NH_3/H_2O mixture. Additionally, the original multiphase VOF model and the phase change LEE method are not suitable for accurately simulating the non-isothermal flow boiling process. Therefore, it is necessary to identify an appropriate method and simplify the simulation models based on reasonable assumptions.

Generally, the effective physical and transport properties of the NH_3/H_2O mixtures, as well as a modified LEE model incorporated into the VOF model, are adopted based on the following assumptions.

(1) The binary zeotropic mixture of NH_3/H_2O is treated as two separate homogeneous phases: the saturated liquid and gaseous phases. Therefore, the species diffusion effect is not directly considered in individual phases. During the phase change processes of the zeotropic mixture, the vaporization of a fluid with a higher content of the more volatile component leads to the development of a concentration gradient in the liquid phase near the interfaces (e.g., the liquid becomes richer in the less volatile species). These gradients are responsible for mass transport near the interfaces. To address this issue, the effective thermophysical and transport properties

in each phase are considered and obtained based on the practical correlations. This approach ensures that the local saturation concentration of the NH_3/H_2O mixture is taken into account in the aforementioned properties, which are all related to local pressure and temperature. The detailed models are presented in section 3.2.

(2) A modified LEE model is employed to calculate the mass and heat transfer in interfaces, considering the difference in local concentration compared to the saturated NH_3 concentration as functions of local temperature and pressure. As the liquid and gaseous phases of NH_3/H_2O are treated as the homogeneous phases, the concentration difference of NH_3 in liquid phase is supposed to be approximated as $\Delta x \approx x - x_{sat}$, where x and x_{sat} represent local NH_3 concentration and local saturated concentration of liquid mixture, respectively. In present work, the main operating temperature range is spanning from 30 to 50℃ and the length of heat sink is 6mm. Hence, it is assumed that the local concentration of the NH_3/H_2O solution undergoes minimal variation in this constrained scenario. Specifically, the local concentration of liquid mixture in microchannels is supposed to be equal to that of inlet concentration (x_{in}). This simplification helps mitigate computational complexity and reduce the demand on computational resources. The details are illustrated in section 3.4.2.

$$\begin{cases} S_g = -S_f = -r_i \alpha_g \rho_g \left| \dfrac{x - x_{sat}}{x_{sat}} \right|, & x < x_{sat} \\ S_g = -S_f = +r_i \alpha_f \rho_f \left| \dfrac{x - x_{sat}}{x_{sat}} \right|, & x > x_{sat} \end{cases}$$

Importantly, the relaxation factor (r_i) in the modified LEE model is an empirical coefficient which could be further optimized to accurately describe mass transfer and species diffusion in the zeotropic mixture, especially when relevant experimental data is available.

(3) Surface wettability of NH_3/H_2O on heated walls is assumed to be superhydrophilic with a contact angle set to zero in this chapter. Although limited studies have focused on the surface wettability effect of the zeotropic mixture flow boiling in microchannels, some experimental investigations in the literature on flow boiling of pure fluids in microchannels have indicated that a superhydrophilic surface could significantly enhance the HTC and the critical heat flux (CHF) in microchannels under the high heat flux conditions. This enhancement is primarily

attributed to the uniform distribution of a thin liquid film on heated surfaces and the resulting delay in partial dryout [297,299]. Currently, the contact angle is commonly used to quantify and characterize the surface wettability, where a smaller angle indicates higher wettability and vice versa. Therefore, the contact angle of the NH_3/H_2O mixture on the heated surfaces in the microchannel is set to 0, indicating the superhydrophilic characteristic.

(4) The Realizable k-ε model is adopted as the turbulence model in this chapter mainly due to its superior performance for complex flow and strong heat transfer process, as demonstrated in previous investigations on flow boiling heat transfer in microchannels [253,279]. The PISO algorithm is chosen for pressure-velocity coupling, the second-order upwind discretization is used for momentum and energy equations, and PRESTO and Geo-Reconstruct discretization are employed for pressure and volume fraction interpolation, respectively. The variable time step is controlled by the Global Courant number, set up to 0.25, and the absolute residuals of the continuity equation are maintained at 1×10^{-4}.

(5) Apart from assumed preconditions, the others are similar to those in section 5.2.

6.3-Grid independence and model validation

The computational domain in this study is illustrated in Figure.76. The schematic diagram of a classic experimental test section is depicted in Figure.76(a) for flow boiling in microchannel. The coolant flows inside a rectangular channel with three sides heated (left, right, and bottom), while the top is covered by a quartz plate for visual observation of bubbles and flow patterns.

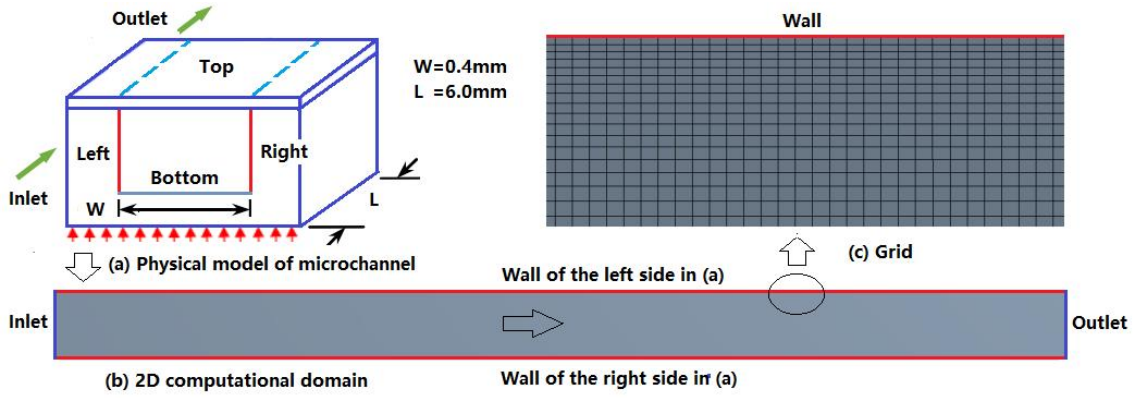
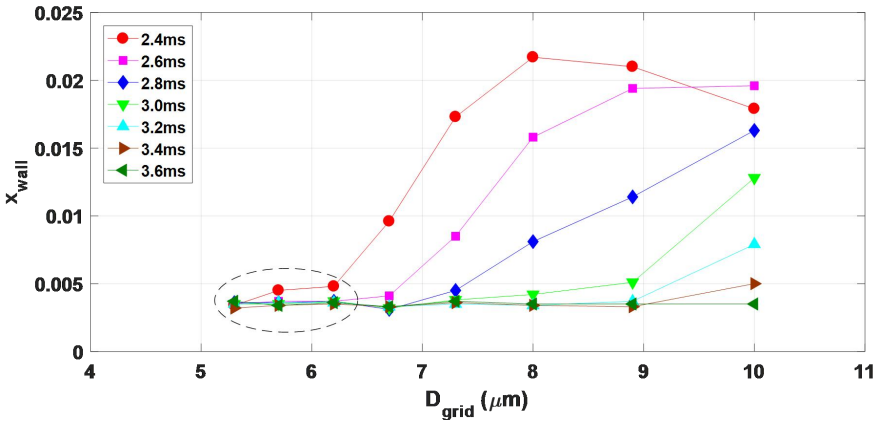


Figure.76 Schematic of numerical simulation construction on NH_3/H_2O flow boiling

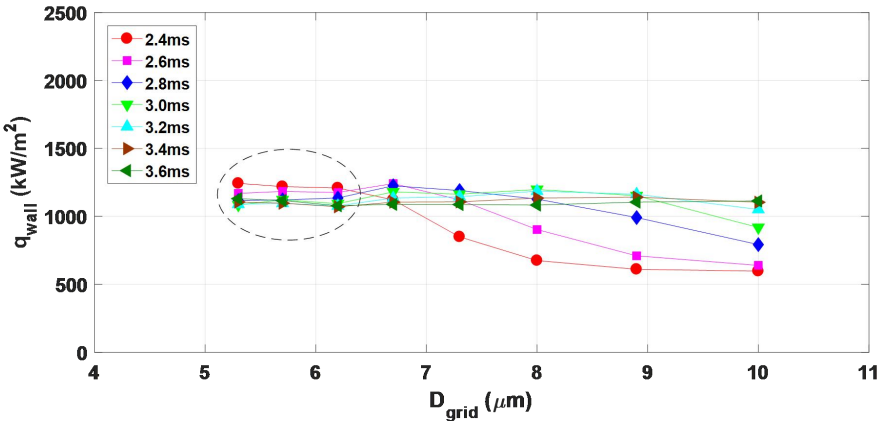
Therefore, the computational domain was simplified to a 2D rectangular horizontal domain with a width of 0.4mm and a length of 6mm in Figure.76 (b) and the gravity force is neglected in this work. As the length is only 6 mm, the interfaces between heated walls and fluids were assumed as constant temperature surfaces [244,262,280]. A non-uniform quadrilateral mesh was employed for the computational domain in Figure.76 (c). The mesh was gradually refined towards walls to accurately capture small-size nucleating bubbles in the boundary layers.

6.3.1-Mesh independence test

A mesh independence test was conducted in the computational domain, shown in Figure.77. Eight mesh sizes were evaluated at mass flux of 46 kg/(m^2·s), the NH_3 concentration of 30% mol. and heating wall temperature of 50 ˚C.



(a)



(b)

Figure.77 Grid independent tests based on vapor fraction (a) and heat flux (b) on heating wall

In Figure.77, the area-averaged vapor fraction on heated surfaces (x_{wall}) and the heat fluxes of heated walls (q_{wall}) are plotted against varying grid sizes to demonstrate the effect of grid size on the numerical results. It can be observed that when the average grid size was decreased to 6.2 μm and below, the variations in vapor fractions and heat fluxes among cases with different grid sizes were less than 3%. Therefore, the average grid size of 6.2 μm satisfactorily met the requirement for mesh independence and was selected for the present study.

6.3.2-Simulation model validation

Since there are limited experimental investigations available in the literature on the NH_3/H_2O mixture flow boiling in microchannels, the simulation methods were adopted in two separate steps as follows: (1) In section 4.3, the VOF-LEE model was validated with experimental data of subcooled water flow boiling heat transfer in microchannels. Since water can be considered as a special case of an NH_3/H_2O mixture with zero concentrations, this validation served as an indirect validation for the VOF-LEE model. (2) To further validate the VOF-modified LEE model, additional numerical simulations were conducted based on flow boiling heat transfer of an R134a/R245fa mixture (i.e., 70/30 by wt.%) in a 2D microchannel. The conditions were designed to duplicate the experimental conditions described in the literature [300], including a constant heat flux at 33 kW/m^2 and a saturating temperature of 18.5℃. The properties of the R134a/R245fa mixture were obtained by NIST REFPROP 9.1 [301].

In order to comply with experimental data in the literature [300], the same equation of outlet vapor quality X was employed as follows:

$$X = \frac{1}{h_{lv}}\left[\frac{Q}{\dot{m}} - c_{p,l}\left(T_{sat,in} - T_{in}\right)\right] \tag{6-1}$$

where, X is the vapor quality at channel outlet, Q is total heat input from the heating surfaces, h_{lv} is the evaporation latent heat of zeotropic mixture,$\dot{m}$,$c_{p,l}$, T_{in} and $T_{sat,in}$ are mass flux, liquid specific heat, inlet fluid temperature and saturation temperature, respectively.

Flow boiling HTC of the numerical results were calculated according to the equation below:

$$h = \frac{q}{T_{wall,ave} - T_{mix}} \tag{6-2}$$

where, h is the overall HTC in microchannels, q is the heat flux of heated walls, $T_{wall, ave}$ is the area-averaged temperature on surfaces, T_{mix} is temperature of the R134a/R245fa mixture.

The results of flow flowing HTCs and flow patterns of experimental and numerical simulation cases are compared and demonstrated in Figure.78 and Figure.79.

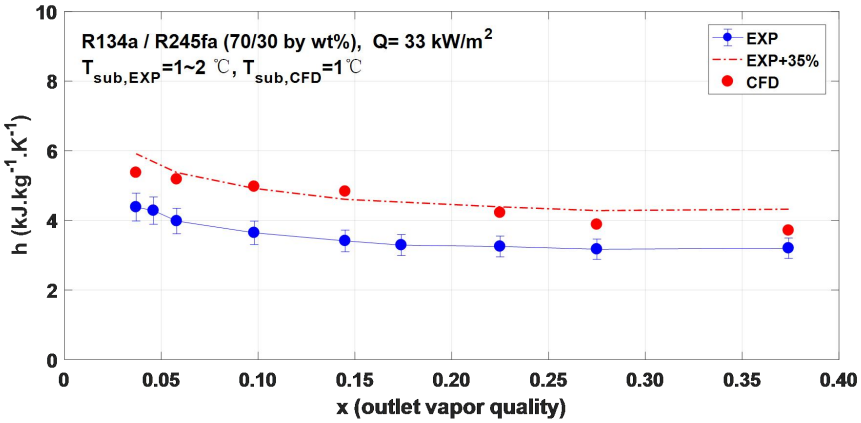
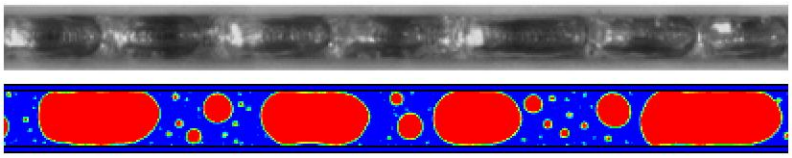
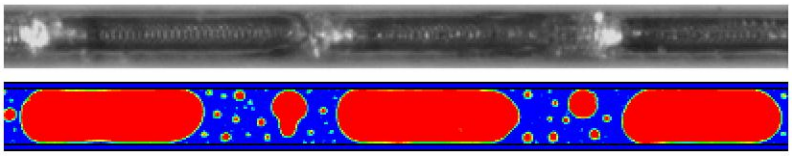


Figure.78 HTC result comparisons among numerical and referenced experimental cases of R134a/R245fa mixture (70/30 by wt.%) in the microchannel



(a) Confined flow



(b) Slug flow

Figure.79 Comparisons of corresponding confined bubble and slug flow patterns of R134a/R245fa mixture (70/30 by wt.%) between the experiment and numerical simulation

As depicted in Figure.78, the simulation results obtained using the VOF-modified Lee model successfully capture the trend of flow boiling HTCs as a function of outlet vapor quality (X_{out}) at a heat flux of 33 kW/m^2. In this graph, the dashed red line represents the curve of values with a positive deviation of +35% from experimental values at the same outlet vapor qualities, while the red dots denote the simulation results. Consequently, it is clear that the maximum deviations between the experimental and numerical results are around 35%, with an average

deviation of about 25.6% under the same conditions. Additionally, as shown in Figure.79, the simulated flow patterns (e.g., confined bubble in Figure.79(a) and slug flow in Figure.79(b)) closely correspond to the visually observed flow patterns in the experimental visualization of the R134a/R245fa mixture (70/30 by wt.%) flow boiling in the microchannels. In conclusion, the results indicate that this model is capable of predicting the heat transfer performance and flow patterns of the zeotropic mixture flow boiling in microchannels, meeting the anticipated requirements of this study.

Furthermore, as observed in Figure.78, the simulation results consistently over-predicted the relevant experimental values. This discrepancy can be attributed to the combined effects of assumptions and simplifications in the current numerical model. One possible reason could be the omission of mass diffusion equations in the present model, which is recognized as one of the primary factors leading to the degradation of heat transfer performance in the zeotropic mixture flow boiling compared to pure fluids [300].

As discussed in the section 3.4, selecting an appropriate coefficient is a significant challenge when adopting the LEE model as the phase change model. As there is almost no experimental data of NH_3/H_2O flow boiling in microchannels, this factor r in present work was referred to the values of pure refrigerants flow boiling in the literature in Table.14, and validated with the R134a/R245fa mixture flow boiling in microchannels as explained above. Hence, the same r value was used for the simulation of NH_3/H_2O flow boiling cases.

In conclusion, the numerical method adopted in this study, which includes the VOF/modified LEE model, has been validated and thus is appropriately utilized for investigations on the heat transfer of the NH_3/H_2O mixture flow boiling in microchannels.

6.4-Results and discussion

It is generally accepted that there are two main mechanisms for flow boiling heat transfer in microchannels, namely the convection boiling and nucleate boiling. Empirical correlations for flow boiling often combine the single-phase convection (h_{sp}) and pool nucleation boiling (h_{nb}) correlations, incorporating various enhancement or superposition factors (E, S) that capture

mutual effects shown in Equation 6-3 [302,303]. Among these correlations, the most important factors influencing flow boiling heat transfer performance are the mass flux (which dominates convection) and the heat flux (which is related to wall superheat).

$$h_{\mathrm{tp}} = \left[\left(Eh_{\mathrm{sp}}\right)^{n} + \left(Sh_{\mathrm{nb}}\right)^{n}\right]^{1/n} \tag{6-3}$$

In addition, the inlet concentration of the more volatile component in the zeotropic mixture is another significant parameter that distinguishes flow boiling of zeotropic mixtures from pure fluids [105,300,304,305]. Hence, the effects of inlet mass flux (G_{in}), inlet NH_3 concentration (x_{NH3}) and the heated wall temperature (T_{wall}) on flow boiling of NH_3/H_2O in microchannels were investigated and compared under a constant wall temperature, which was set below 85˚C to comply with the maximum sustainable temperature of electronic devices [13,306].

Accordingly, the relevant simulation conditions in this study are listed in Table.21. Figure.80 shows the phase diagram of NH_3/H_2O by the mole fraction and temperature at 0.1MPa. In the diagram, the left blue line represents the saturated liquid line of NH_3, while the right red line represents the saturated vapor curve of NH_3. To ensure the NH_3/H_2O mixture in a subcooled state (i.e., inlet temperature of 20˚C) before it entering the microchannel and undergoing flow boiling at a wall temperature of 50˚C, the mole fraction of NH_3 was selected within the range of 0.2 to 0.36, as determined from the phase diagram.

Table.21 The simulation conditions on flow boiling of NH_3/H_2O mixture in Chapter 6

Parameter	Values	G_{in}	x_{in}	T_{wall}
		kg/(m²·s)	-	℃
G_{in} (kg/(m².s))	46, 92, 138, 184, 230, 276, 368, 460, 552	-	0.15, 0.35	50
x_{in}	0.15, 0.19, 0.20, 0.25, 0.3, 0.35	46, 184, 276, 552	-	50
T_{wall} (K)	20.5, 21.5, 30, 50, 70	46, 184, 276, 552	0.35	-

Additionally, the surface wettability of microchannel for the NH_3/H_2O mixture were treated as the superhydrophilic with contact angle of 0 featuring optimum flow boiling performance.
The overall and local heat transfer performance of NH_3/H_2O flow boiling in the microchannel are analysed comparatively. When the average heat fluxes of the two heated surfaces fluctuate

regularly with flow time in a stability range, the averaged values of those parameters (e.g., heat fluxes in Figure.81) in the regular periods are considered dynamically stable after 22ms.

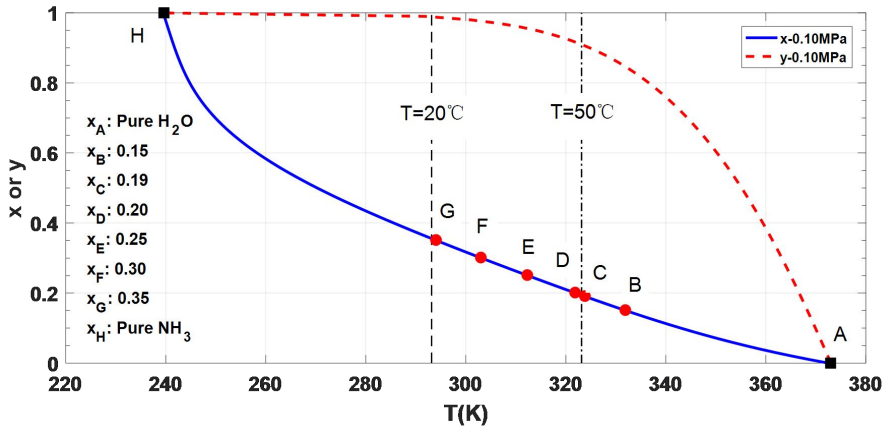


Figure.80 Simulation cases shown in saturated NH_3 solution properties plots at 0.1MPa

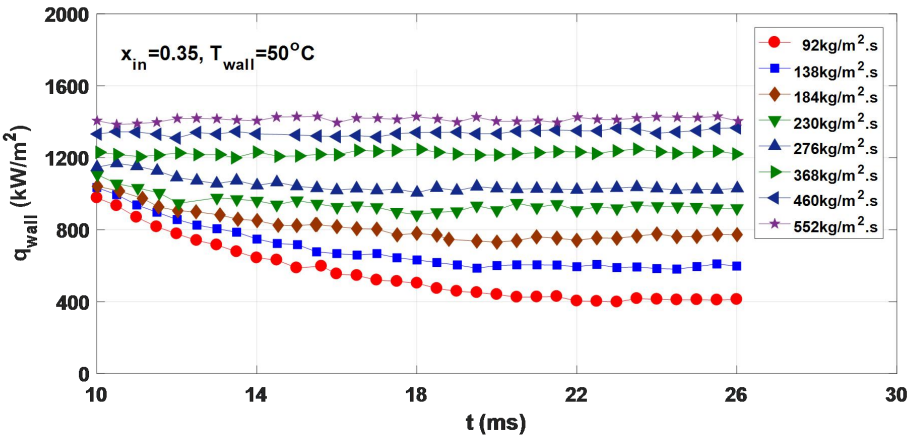


Figure.81 Relations of the area-averaged heat fluxes with flow time at different inlet mass fluxes

The overall HTC is calculated by

$$h_{\text{overall}} = \frac{\sum_{i=1}^{n}\left[\dfrac{\left(q_{\text{L,i}} + q_{\text{R,i}}\right)}{T_{\text{wall}} - \left(T_{in} + T_{\text{out,i}}\right)/2}\right]}{n} \tag{6-4}$$

Where h_{overall} is the overall HTC (kW/(m2·K)), q_L and q_R are the area-averaged heat fluxes (kW/m^2) at left and right heating wall in microchannel in Figure.82. T_{wall},$T_{in}$and $T_{\text{out,i}}$are the wall temperature, the mass-averaged inlet and outlet fluid temperature (K), respectively. The index "i" denotes an individual transient point in time after the dynamic equilibrium of flow

boiling. A total number of "n" individual time points were considered for evaluating the time-average HTC within the equilibrium state.

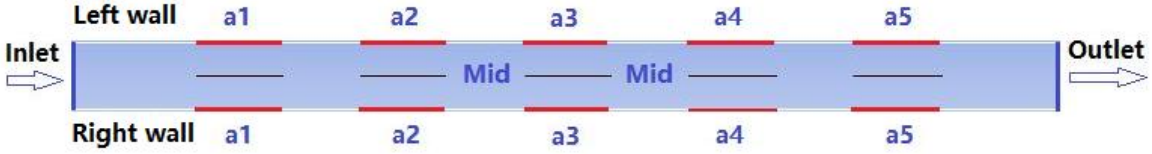


Figure.82 Schematic diagram of boundaries and local positions in domain

The local HTC is calculated by

$$h_{\text{local,j}} = \frac{\sum_{i=1,j}^{n}\left[\frac{\left(q_{\text{l,j,i}} + q_{\text{r,j,i}}\right)}{2} \Big/ \left(T_{\text{wall}} - T_{\text{fluid,j,i}}\right)\right]}{n} \tag{6-5}$$

Where h_{local} is the local HTC (kW/(m^2·K)), q_l and q_r are local area-averaged wall heat fluxes (kW/m^2) at left and right walls. The index "j" indicates the individual locations for where the local HTC investigated, shown as "a1…a5" in Figure.82. T_{fluid} is local mass-averaged fluid temperature (K) to the individual locations "a1…a5". The length of each area "a_j" is 0.5 mm.

6.4.1-Effect of inlet mass flux

In this section, the effect of inlet mass fluxes effect on the heat transfer performance of single-phase convection (i.e., cases with inlet mole concentration at 0, denoted as $x_{in,NH3}$=0) and subcooled flow boiling (i.e., with inlet concentration at 35%mol, denoted as $x_{in,NH3}$=35%mol.) is investigated and compared at the same wall temperature of 50˚C and pressure of 0.1 MPa.

6.4.1.1-The overall heat transfer performance

The effects of inlet mass fluxes on the overall HTCs ($h_{ave,m}$), flow patterns in the domain and wall heat fluxes (q_{wall}) of single-phase convection and flow boiling of NH_3/H_2O at 50℃ are plotted in Figure.83. As depicted in Figure.83(a), the HTC of single-phase convective flow (i.e., $x_{in,\ NH3}$=0, represented by the green line) exhibits a linear correlation with mass fluxes. On the other hand, the HTC of the NH_3/H_2O flow boiling (i.e., $x_{in,\ NH3}$=35% mol., represented by the blue line) initially increases linearly with inlet mass flux (A-B), followed by a gradual decrease in the growth rate (B-D), and eventually reaches a nearly constant value with further

increases in the inlet mass flux (D-E). Furthermore, it can be observed that the HTCs of the NH_3/H_2O flow boiling (i.e., $x_{in,\ NH3}$=35%mol.) surpass those for single-phase convection (i.e., $x_{in,NH3}$=0) at a consistent wall temperature of 50˚C. This indicates that the NH_3/H_2O mixture proves to be a more preferable choice compared to water (not be boiling at 50˚C and 0.1 MPa) for effectively managing heat in electronic devices that operate below 50˚C.

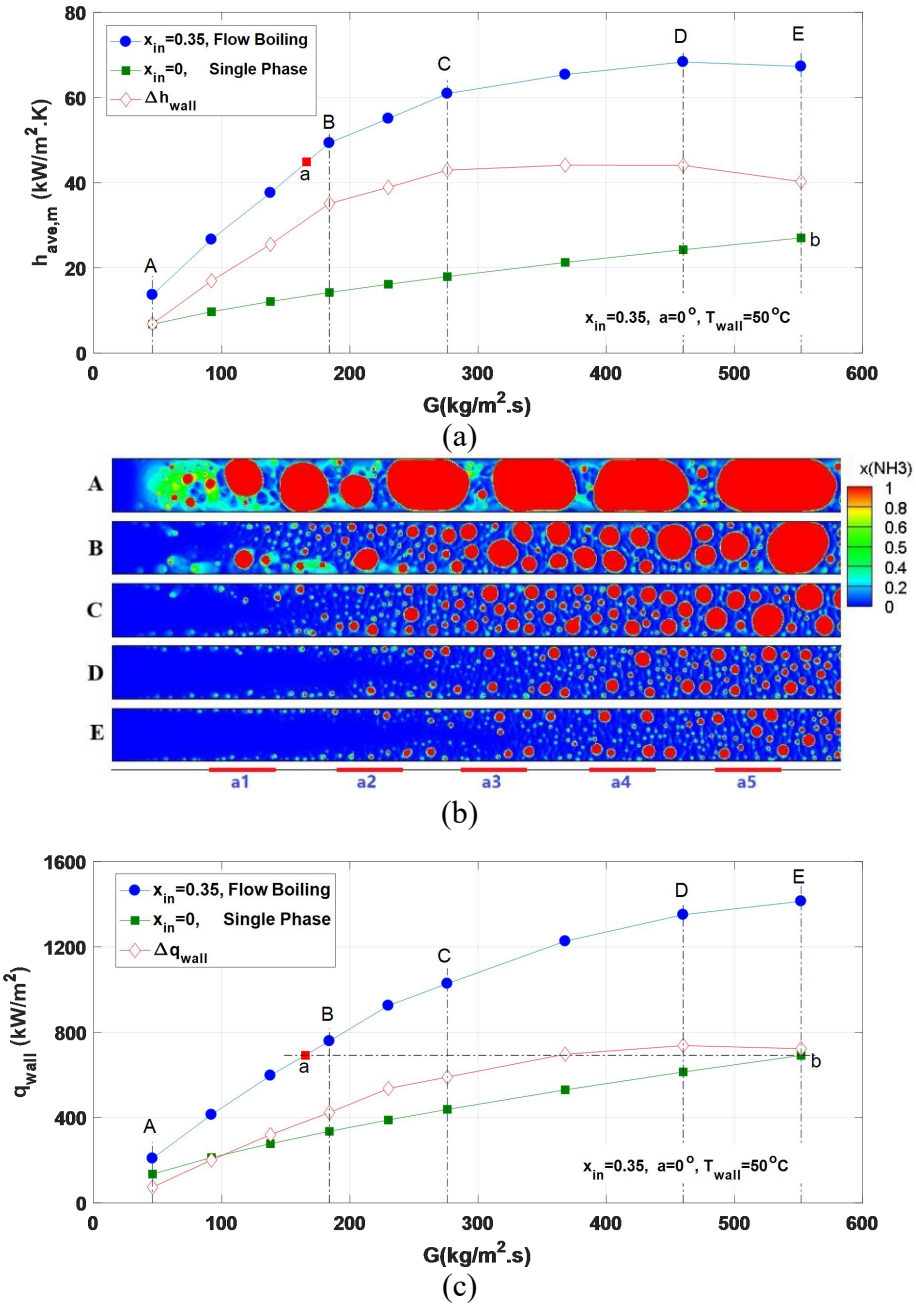
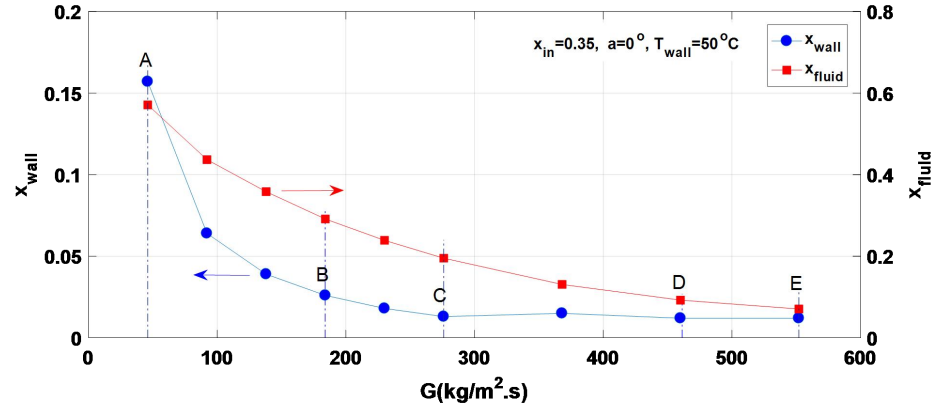
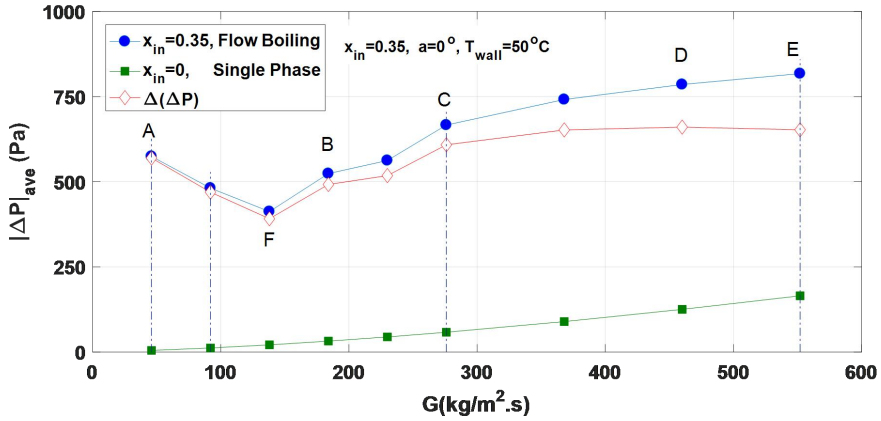


Figure.83 Effects of mass fluxes on (a) the overall heat fluxes, (b) vapor distribution in domain and (c) the overall HTC of NH_3/H_2O in microchannel at 50 ℃

Furthermore, the trend of the HTCs versus mass fluxes at 35% mol. exhibits a similarity to the well-known classic flow boiling behavior in microchannels. In the nucleated boiling dominant region, the HTC is primarily influenced by heat flux but shows less sensitivity to inlet mass flux and vapor quality. On the other hand, in the convective boiling dominant region, the HTC is dependent on mass flux and vapor quality but remains independent of heat flux [114,121].



(a)



(b)

Figure.84 Effects of mass fluxes on (a) the vapor fraction and (b) the overall pressure drop of NH_3/H_2O in microchannel at 50 ℃

The corresponding flow patterns (A-E) are illustrated in Figure.83(b), with Case A depicting the intermittent slug flow, Case B representing partial confined bubbly flow, Case C showing small bubbly flow, as well as Cases D and E indicating the nucleated flow. The area-averaged vapor fraction on the heated surfaces (x_{wall}) and in the domain (x_{fluid}) are plotted in Figure.84 (a). It can be observed that, for the same wall temperature (T_{wall}), higher inlet mass flux (G_{in})

leads to higher heat flux and HTC, but lower thermal equilibrium vapor quality as indicated by the vapor fractions x_{wall} and x_{fluid}. Specifically, when inlet mass flux exceeds 276 kg/ (m^2.s) from Case C to Case E, the x_{wall} remains constant in Figure.84 (a), and the HTC reaches its maximum value and becomes constant with a slight decrease in Figure.83 (a). Accordingly, the nucleated boiling region (e.g., Cases C-E) is typically associated with a low vapor quality, favoring the generation of relatively small bubbles on heated surfaces. On the other hand, the convective flow boiling region (e.g., Case A) features a high vapor quality with large bubbles attached to the heating surfaces, leading to the nucleation inhibition on the heated walls.

Additionally, the relationship between the absolute area-averaged pressure drops ($|\Delta P|_{ave}$) and the inlet mass flux (G_{in}) is plotted in Figure.84(b). The pressure drop in flow boiling is significantly higher than that in single-phase convection at the same wall temperature (T_{wall}) and mass flux (G_{in}). For single-phase convective flow under the same heated wall temperature, an increase in the inlet mass flux results in a higher fluid velocity, greater viscous losses and consequently a higher total pressure drop. However, for the flow boiling process under the given wall temperature condition, the pattern of variation in total pressure drop with respect to the inlet mass flux differs significantly from that of single-phase convective flow.

Generally, the pressure drops in flow boiling cases initially decrease with the increase of inlet mass fluxes within a small range of G_{in} (e.g., from Case A to Case F). Then they start to rise and eventually follow a trend similar to that of single-phase convection at high mass fluxes (e.g., from Case C to Case E) in Figure.84 (b). As shown in the corresponding flow patterns in Figure.83 (b), it is evident that the flow pattern transitions from the intermittent slug flow to the nucleating flow with the increase of inlet mass fluxes. Therefore, the decrease in pressure drops from case A to Case F with the increase of mass fluxes is primary due to the rapid decrease of vapor fractions in the domain (x_{fluid}). It is generally accepted that the pressure loss in gas-liquid flow is higher than that in liquid-phase flow under the same mass fluxes. This is because the gas-liquid interfaces introduce additional frictional resistance and surface tension between droplets and bubbles, resulting in greater energy dissipation and larger pressure loss. The larger the sizes and quantity of bubbles, the greater the increase in pressure drops. When

the sizes of bubbles in the domain are small (e.g., in Case D and Case E), the trend of pressure drop increment with inlet mass flux is similar to that of single-phase flow.

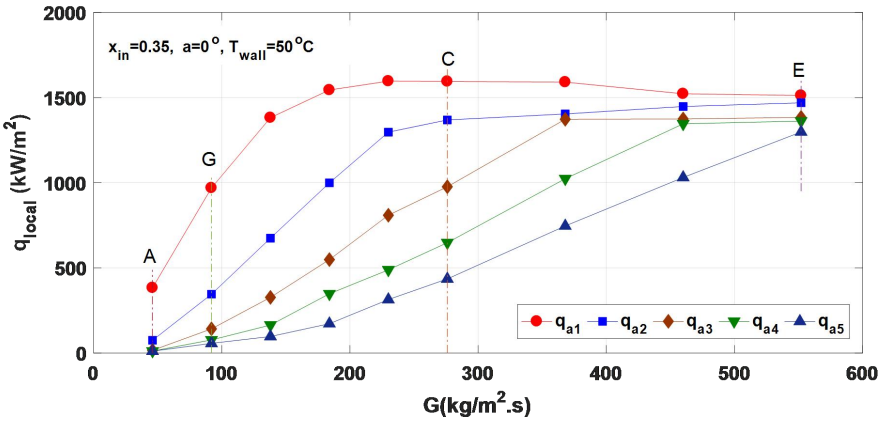
In order to evaluate the heat dissipation capability of NH_3/H_2O flow boiling in microchannels, the overall area-averaged heat flux at a constant heated wall temperature (T_{wall}) is plotted as a function of inlet mass flux in Figure.83(c). As shown, both single-phase and flow boiling heat transfer exhibit improved overall heat fluxes with increasing inlet mass fluxes. For cases at 552 kg/(m^2·s), the overall heat flux of NH_3/H_2O mixture flow boiling (Point E) can reach up to 1.41 MW/m^2, which is 2.05 times higher than that of single-phase convective heat transfer (e.g., the Case B of 0.69 MW/m^2 at x_{in} = 0). On the other hand, for the same heat dissipation rate of 0.69 MW/m^2 at the device temperature of 50˚C, the required mass flux of NH_3/H_2O in flow boiling case (e.g., the Case A) is 166.2 kg/(m^2·s), which is only 30% of the requirement in single-phase convection case (e.g., the Case B at x_{in} = 0). This indicates that less electrical power consumption is needed for circulating coolant in practical applications. Therefore, flow boiling of the NH_3/H_2O mixture in microchannels presents a promising alternative approach for cooling high power density electronics.

6.4.1.2-The local heat transfer performance

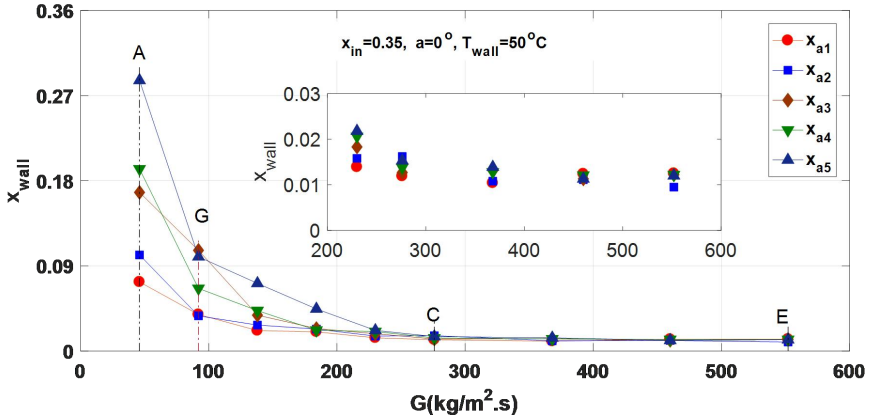
The effects of mass fluxes on local heat fluxes q_{local}, the vapor fraction on local surfaces x_{wall} and the HTCs of NH_3/H_2O flow boiling at various locations in microchannels, shown as “a1-a5” in Figure.82, are plotted in Figure.85, individually.

According to Figure.85(a), the local heat flux (q_{local}) at each position (e.g., q_{a1}-q_{a5}) follows the same trend as inlet mass flux (G_{in}) at a constant wall temperature. As the mass flux increases from 46 to 552 kg/(m^2·s), the local heat flux initially increases linearly and then stabilizes around 1.5 W/m^2 when the mass flux exceeds a certain value (referred to as a turning point). The turning point increases with the distance from the inlet position. Based on Figure.83(b) and Figure.85(b), the local vapor fraction on heated surfaces (x_{wall}) at each position decreases as the inlet mass flux increases at a constant wall temperature of 50℃. The closer the location is to the microchannel exit, the faster the decrease in local vapor fraction on heated surfaces (x_{wall}). This is because the evaporation process progresses in the flow direction, resulting in a

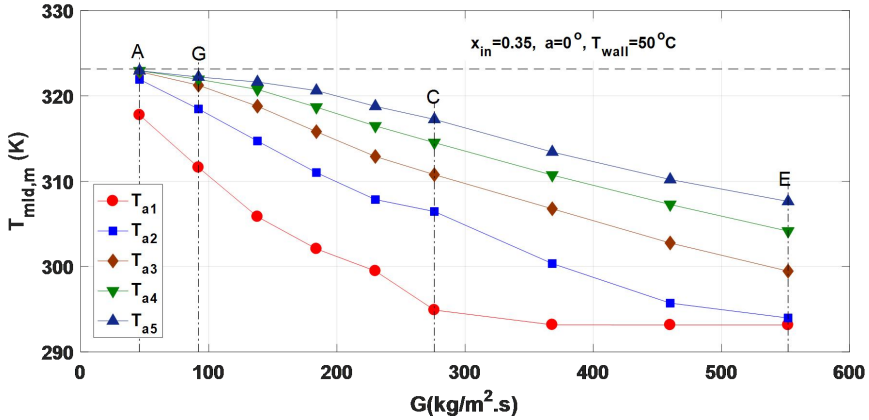
faster rate of bubble generation and growth on the heated surfaces with increasing inlet mass flux. This, in turn, leads to a cleaner local space available for nucleation at the same constant wall temperature. When local vapor fraction on the heated surfaces reaches its minimum level (e.g., the position a1 in Case C), the local heat flux remains stable as the mass flux increases.



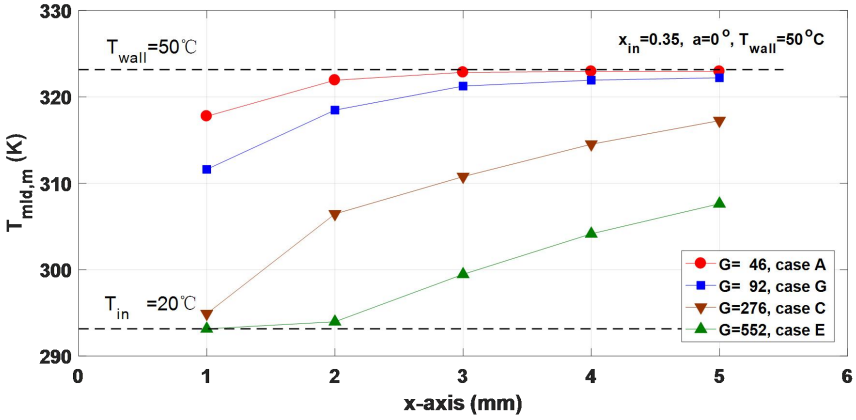
(a)



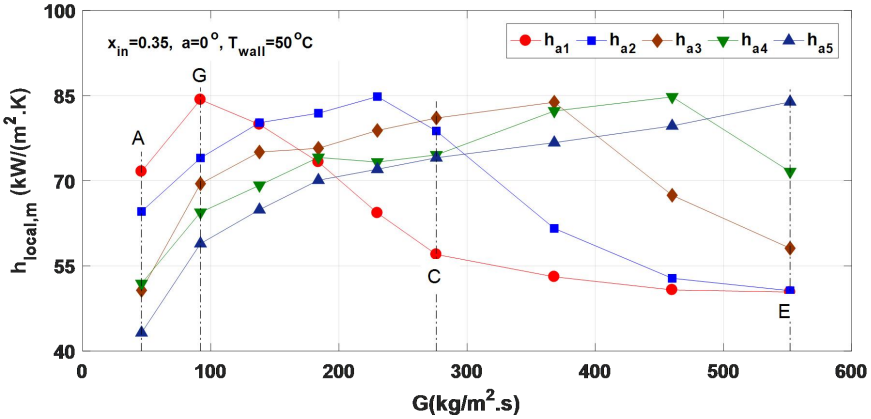
(b)



(c)



(d)



(e)

Figure.85 Effects of mass fluxes on (a) local heat fluxes, (b) vapor fraction on local surfaces, (c,d) fluid temperature in midsection and (e) local HTCs of NH_3/H_2O in flowing direction at 50 ℃

Figure.85(c) illustrates the effect of inlet mass flux on the mass-averaged fluid temperature in the local midsection of the microchannel ($T_{mid,\ m}$) at a constant wall temperature (T_{wall}). It is reasonable that the local temperature of the bulk fluid increases from the entrance to the outlet due to the development of the evaporation process.

In Figure.85(d), it is observed that the local wall temperature (T_{wall}) increases slowly from the inlet temperature (T_{in}) and then follows a regular increase at high inlet mass fluxes (e.g., Case E). However, at lower inlet mass fluxes (e.g., Case A), the local T_{wall} rises quickly and then approaches T_{wall} along the flow direction. This indicates the non-isothermal phase changing process of the NH_3/H_2O mixture. However, in the heat sink region, the fluid temperature at

the same location decreases with increasing inlet mass flux at a constant wall temperature. This is because the existence time of the fluid in the heat sink is reduced by the increased inlet mass flux (i.e., velocity). If the inlet mass flux is sufficiently high (resulting in an extremely short fluid residence time at a local position), the local fluid temperature tends to be the same as the inlet temperature (T_{in}). For example, the local temperature at a1 near the entrance (T_{local}) reaches inlet temperature (T_{in}), when inlet mass flux exceeds 368 kg/(m^2·s). Fundamentally, the local temperature of the NH_3/H_2O mixture in the domain depends on the combined effects of the fluid residence time in the domain and the non-isothermal phase change characteristics.

Based on the formula Eqn. (6-5), the local heat transfer coefficient (HTC) can be calculated and plotted in Figure.85 (e). The variation trend of the local flow boiling HTC (h_{local}) with the inlet mass flux (G_{in}) at a constant wall temperature shows a different pattern in Figure.85(e). Initially, local HTC increases and reaches a maximum value of approximately 85 kW/(m^2·K). Then, it starts to decrease and eventually stabilizes at around 50 kW/(m^2·K) as the flow boiling process becomes fully developed with increasing mass flux (e.g., at the local position a1 in Case E). The changing patterns and corresponding explanations near the inlet and outlet of the heat sink are discussed in detail as follows.

According to the curve of the local position a1, close to the inlet, the local flow boiling HTC initially increased from "A" to "G" and then decreased from "G" to "E" with increasing mass flux. For cases at low mass fluxes (e.g., A-G), the increment of G_{in} positively influenced the HTC values by enhancing the removal of large bubbles from hot surfaces at higher rates, thus facilitating local bubble growth. On the other hand, for cases at high values of G_{in} (e.g., G-E), the local flow boiling capability was suppressed due to insufficient time for the fluid to interact with the hot surfaces and undergo complete boiling, caused by the high inlet flow rate. As a result, there existed an optimum mass flux point at "F" where these two effects were well balanced. Furthermore, it can be observed that there was a common maximum value of local HTC for all locations (a1-a5), around 85 kW/(m^2·K), although occurring at different optimum mass fluxes. This indicates the presence of a consistent upper limit for the favorable effects of nucleation and convection on local flow boiling performance, primarily governed by the NH_3

concentration (i.e., the more volatile component in the binary mixture) at the constant wall temperature, regardless of the location in the microchannel.

However, local flow boiling behavior near the outlet (a5) is different and can be considered as the continuation of the flow boiling behavior at the inlet as shown in Figure.89 (e). This can be explained by the fact that the subcooled fluid just starts to boil at the inlet, while flow boiling is fully developed at the outlet, as the bulk fluid has already traversed the entire length of the heating surfaces. It is also important to note that the concentration of NH_3 in the bulk fluid decreases along the microchannel due to evaporation (from a1 to a5). Hence, the flow pattern at a5, close to the outlet, is fully developed slug flow at low mass fluxes and fully developed bubbly flow at high mass fluxes, at the constant wall temperature T_{wall}, as depicted in Figure.83(b). Accordingly, as shown in Figure.89 (e), the HTC value at a5 increases with mass flux. As flow boiling is fully developed and only a small amount of NH_3 is left in the bulk fluid, the heat transfer performance is mainly dependent on the convective part and mass flux. This is further supported by the near-zero vapor fraction on heated walls in Figure 83(b).

6.4.2-Effect of inlet concentration

Compared to pure fluids, the concentration of the more volatile component in binary mixture, which is related to thermal and mass diffusion, is one of the most essential factors governing flow boiling heat transfer in the mixture. Additionally, in the present work, the heated wall temperature is only above the saturated temperature of NH_3 and not H_2O throughout the entire domain. Furthermore, the degree of subcooling is also determined by the inlet concentration of NH_3 at a certain pressure. This concentration affects the temporal and spatial distributions of NH_3/H_2O flow boiling along the flow direction.

The effect of inlet concentration (x_{in}) on flow boiling heat transfer performance is complex. As discussed in section 3.4.2 regarding the modified LEE model for the zeotropic mixture, the difference between the local liquid concentration and the saturated concentration is considered as the driving force for the evaporation. Furthermore, the heat dissipation capacities of flow boiling in microchannels are strongly related to flow patterns, as depicted in Figure 10.

Therefore, the effect of inlet concentration of NH_3/H_2O on the heat transfer performance will be investigated. This includes one case of single-phase flow with an inlet concentration (x_{in}) of NH_3/H_2O at 0.19 and four cases of subcooled flow boiling with that at 0.2, 0.25, 0.3 and 0.35. The investigations will be conducted at a constant heated wall temperature of 50˚C and an operational pressure of 0.1 MPa. It is important to note that the saturated concentration of the NH_3/H_2O mixture is 0.194 under the corresponding conditions.

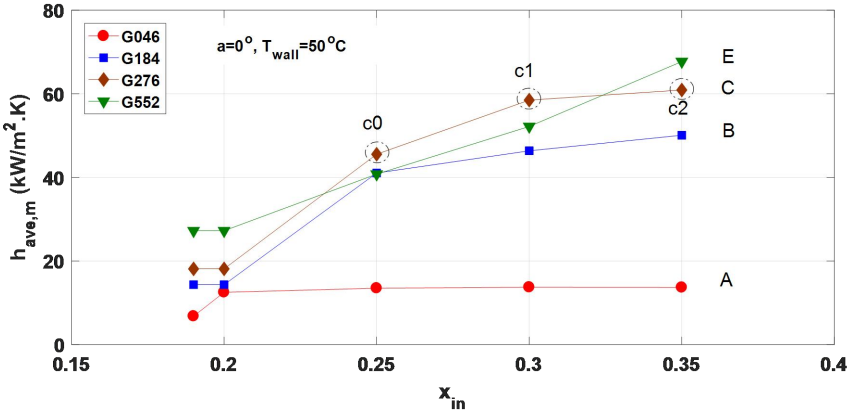
6.4.2.1-The overall heat transfer performance

The inlet concentration effect of the NH_3/H_2O mixture on the overall heat flux (q_{wall}) and the corresponding HTC at the same inlet temperature (T_{in}) of 20℃ and heated wall temperatures (T_{wal}) of 50℃ is shown in Figure.86 (a) and Figure.86 (c). Generally, the relation between the heat transfer performance (q_{wall} and HTC) and inlet concentration of NH_3/H_2O (x_{NH3}) can be divided into three stages: initial linear increase, followed by gradual degradation, and finally independence from x_{NH3}.

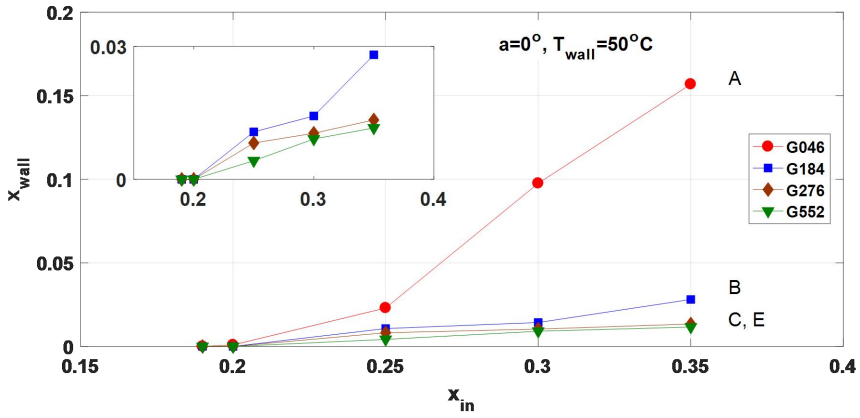
Taking the cases of an inlet mass flux at 276 kg/(m^2·s) as examples (represented by the brown line in Figure.86 (a)), the average flow boiling HTCs remained almost constant when the inlet concentrations (x_{in}) were below 0.2, as the degree of nucleate boiling was insignificant. Then, as the inlet concentrations (x_{in}) gradually increased (e.g., from c0 to c1), the HTCs started to increase gradually due to the enhancement of nucleation effects until flow boiling reached a nearly stable state (e.g., at c2).

The main reason for this behavior might be that the increase in inlet concentration (x_{in}) of the NH_3/H_2O mixture does not always benefit the overall flow boiling heat transfer performance. This is because the presence of large-sized bubbles attached to the surfaces could reduce the numbers of the effective nucleation sites. Additionally, the adverse effects of surface tension gradients, the dilution and dissolution of NH_3 caused by local concentration gradients in the microchannel, should also be considered to some extent. Finally, the HTCs reached a nearly constant level in cases c1 and c2. Furthermore, the trend curves of HTCs in Figure.86 (a) are different at different mass fluxes. The HTC reaches a steady value earlier for smaller inlet concentrations (x_{in}) in cases with lower inlet mass fluxes. This is observed by comparing the

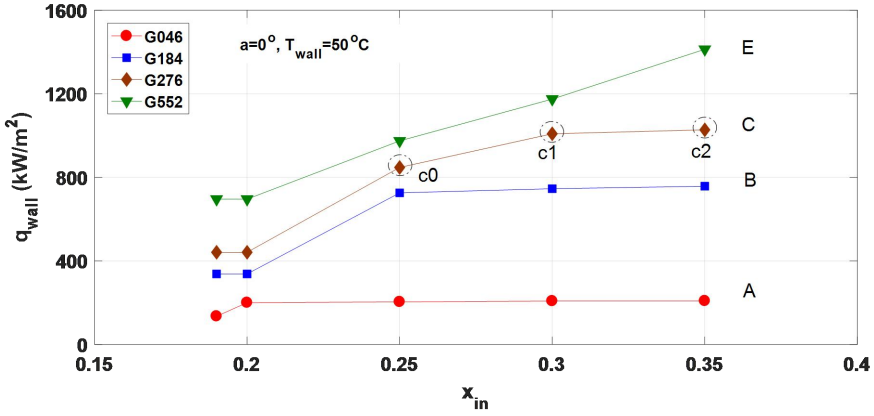
curves for a mass flux of 46 kg/(m^2·s) (red line) and that of 276 kg/(m^2·s) (brown line). Hence, inlet mass flux is another dominant factor, alongside the inlet NH_3 concentration, that affects the onset of nucleate boiling (ONB) and the development of flow boiling along the length of the channel. As mentioned previously, a higher fluid velocity implies less time for the fluid to interact with heated surfaces. This directly influences the initiation of nucleate boiling and the interactions of bubbles with the surfaces.



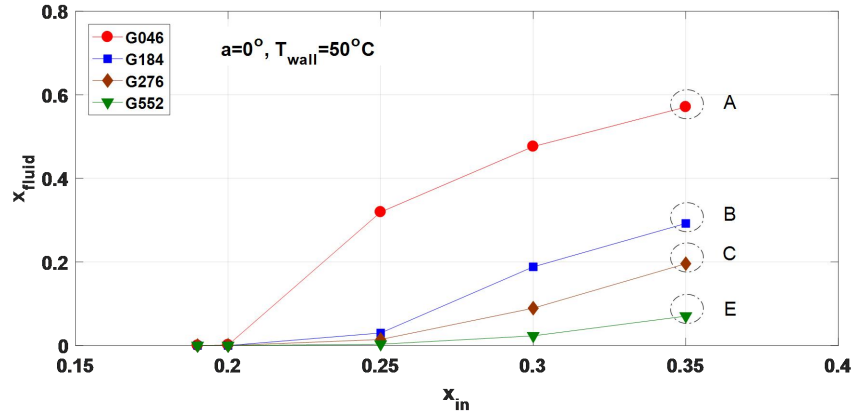
(a)



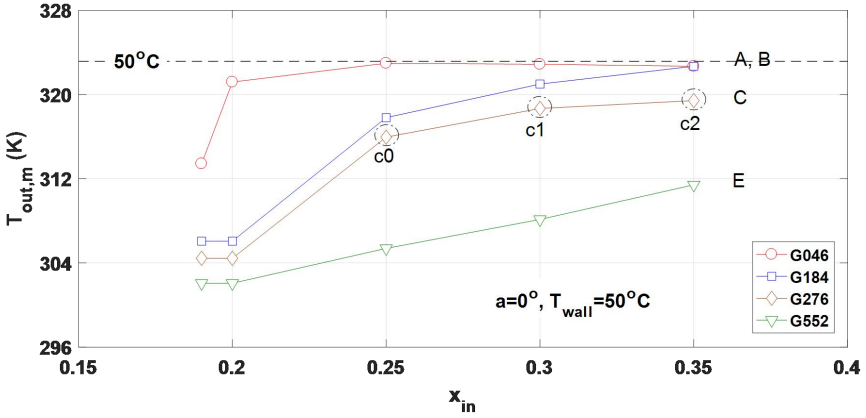
(b)



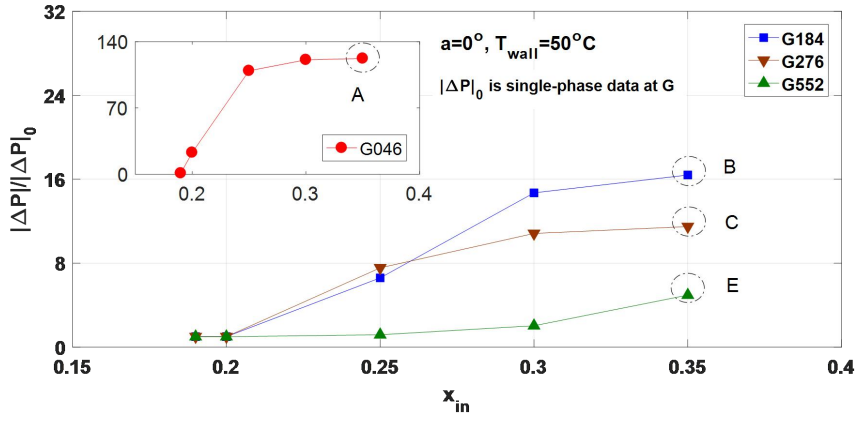
(c)



(d)



(e)



(f)

Figure.86 Effect of inlet concentration on (a) the overall HTC, (b) vapor fraction on surfaces, (c) heat fluxes, (d) vapor fraction in domain, (e) outlet temperature and (f) relative pressure drop ratio of the NH_3/H_2O mixture in microchannel

Generally, the overall HTC (i.e., $h_{ave,\ m}$) of NH_3/H_2O flow boiling in microchannels depends on the mutual effects of inlet mass flux (G_{in}) and inlet NH_3 concentration (x_{in}) at a constant heated temperature. Comparing the cases at 276 kg/(m^2·s) and 552 kg/(m^2·s), it is observed

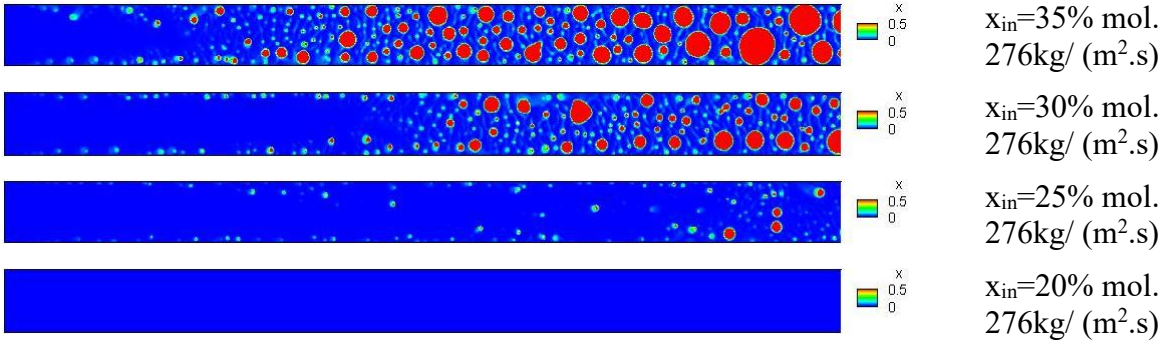
that the HTC for a higher inlet mass flux of 552 kg/(m^2·s) is larger than that for the lower mass flux of 276 kg/(m^2·s) under a small inlet concentration of 20%mol. and a high value of 35%mol.. However, the HTC for a higher mass flux is smaller than that for a lower mass flux at inlet concentration levels (e.g., x_{in}=25% and 30%mol.). The corresponding vapor fraction on heated walls (x_{wall}) is plotted in Figure.86 (c). It is found that, at a constant wall temperature (T_{wall}), the vapor fraction on heated walls (x_{wall}) increases with increasing inlet concentration (x_{in}) for the same inlet mass flux (G_{in}). Moreover, the increment rate of the vapor fraction on heated walls (x_{wall}) at a higher inlet concentration (x_{in}) of 35%mol. increases more rapidly as the inlet mass flux (G_{in}) decreases.

Similarly, the overall heat flux (q_{wall}) dissipated from the heated walls converges to a constant value as the inlet concentration (x_{in}) of NH_3/H_2O increases at different mass flow rates under the constant heated temperature (T_{wall}), as shown in Figure.86 (c) (e.g., red and blue lines). In other words, there is a threshold of inlet concentration (x_{in}) of NH_3/H_2O to maintain a certain level of heat dissipation capacity at a given mass flux. Additionally, it is evident that the value of q_{wall} increases with G_{in} at the same inlet concentration (x_{in}) and heated temperature (T_{wall}). This means that a higher mass flux results in a faster fluid velocity in the domain, leading to more efficient sweeping of bubbles from heated surfaces (as seen in x_{wall} in Figure.86 (b)) and in the heat sink (as seen in x_{fluid} in Figure.86 (d)). Furthermore, the HTC does not follow the same pattern as q_{wall}. For instance, the HTC (h_{wall}) at 276 kg/(m^2·s) is greater than that at 552 kg/(m^2·s) under the same inlet concentration (x_{in}) of 25%mol. The possible reason might be the variable outlet temperature ($T_{out,\ m}$) in Figure 86 (e), which tends towards the maximum value of T_{wall} due to the non-isothermal phase change characteristics of the NH_3/H_2O mixture.

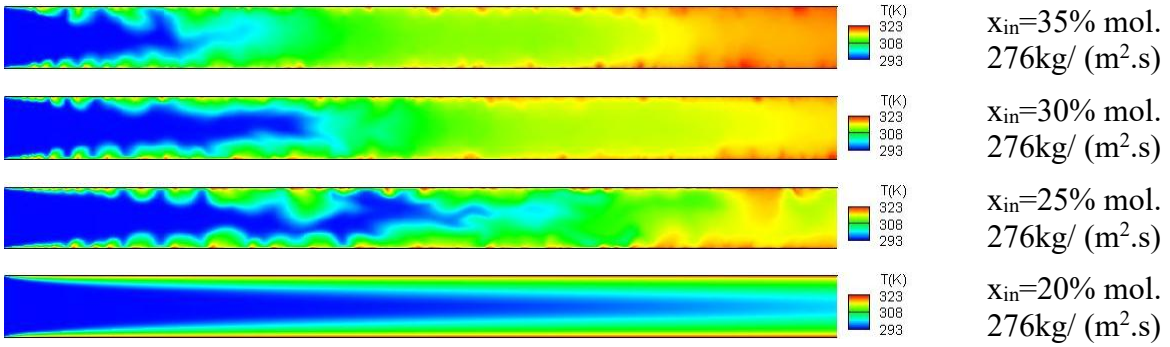
The relative ratio of pressure drops, defined as the ratio of total pressure drop in flow boiling to that in single-phase convective flow at the same conditions, is presented in Figure.86(f). It is evident that the inlet mass flux (G_{in}) plays a significant role in the pressure drop of single-phase convection and flow boiling in microchannels. Therefore, this relative parameter is used to assess the effect of inlet NH_3 concentration (x_{in}) on the pressure drop at the same heated wall temperature (T_{wall}). The value of this parameter increases with increasing the inlet NH_3

concentration (x_{in}) at the same mass flux, but this enhancement is weakened by increasing the inlet mass flux (G_{in}). This trend is roughly similar to that observed for x_{fluid} in Figure.86 (e).

In order to further investigate the effect of the concentration on flow boiling in microchannels, the dynamic stable distributions of bubbles and fluid temperature in the flow domain at 276 kg/(m^2·s) are presented in Figure.87, individually.



(a)



(b)

Figure.87 Effect of inlet concentration on dynamic stable distributions of (a) bubbles and (b) fluid temperature in domain at 276 kg/ (m^2.s)

Accordingly, for the case with an inlet concentration (x_{in}) at 20%vol, which is slightly higher than the saturated NH_3 concentration of 19.4%vol at a heated temperature (T_{wall}) of 50C° and 1 bar, a laminar single-phase convective flow is observed in Figure.87(b). When the inlet NH_3 concentration is increased to 25%vol, the corresponding saturation temperature of NH_3/H_2O decreases as shown in Figure.80. Consequently, the degree of subcooling (which is defined as the temperature difference between a liquid and its saturation temperature at a given pressure)

decreases and the nucleate boiling of fluid is triggered on the heated surfaces. Simultaneously, the temperature layer near the hot walls is disrupted by the small-sized bubbles generated and growing on the heated surfaces, even though the inlet liquid flow remains in a laminar state. This disturbance also enhances the heat transfer capability from the hot walls to the bulk fluid. Consequently, the overall heat flux is increased due to the combined effect of nucleation and local turbulent flow.

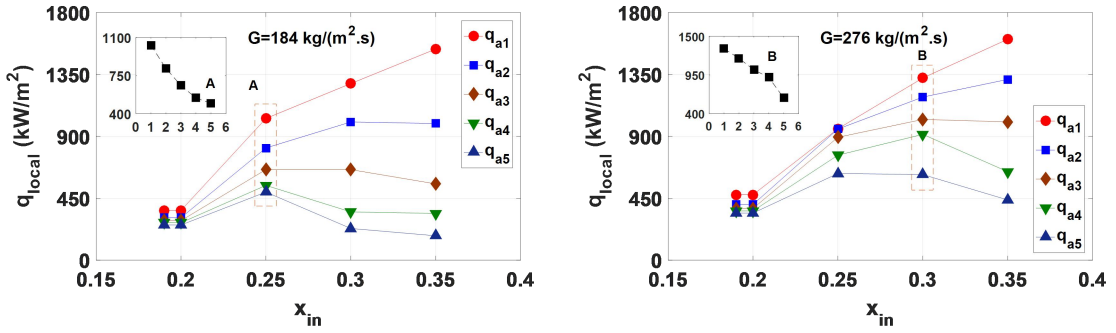
With a further increase in the inlet NH_3 concentration (x_{in}), the nucleate boiling intensity is also accelerated at the front part of microchannels due to the decreased subcooling. However, the heat transfer performance is degraded at the tail part due to the decreased temperature difference between the heating walls and the local fluid temperature. There exists a turning point where the local heat flux is equal to the overall heat flux under the given conditions, and this location moves towards the entrance as the concentration increases before the onset of evaporation at the entrance. This will be further discussed in the subsequent analysis of local heat transfer performance.

6.4.2.2-The local heat transfer performance

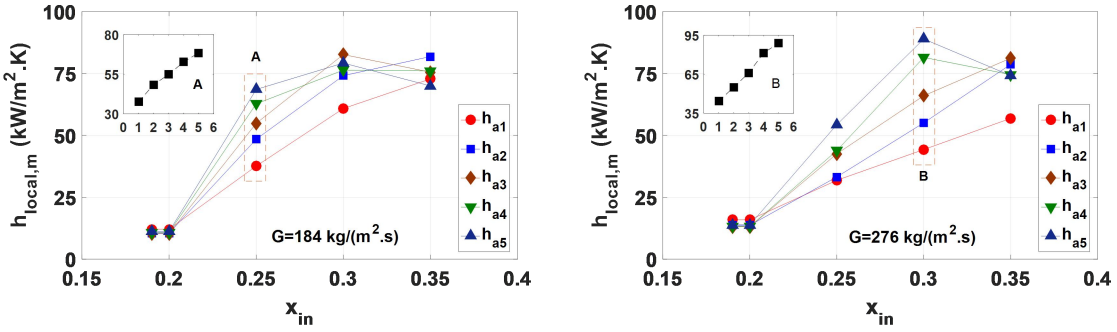
As discussed in section 6.4.2.1, the overall heat fluxes (q_{wall}) and HTC ($h_{ave,\ m}$) for cases with inlet mass fluxes of 184 and 276 kg/(m^2·s) exhibit three distinct stages with varying inlet NH_3 concentration (x_{in}) in Figure.86 (a) and (c). Therefore, in this section, we will investigate the local heat transfer performances of NH_3/H_2O mixture at mass fluxes of 184 and 276 kg/ (m^2·s) at different positions along the microchannels, indicated as a1 to a5 in Figure.82. The position a1 refers to the location near the entrance, while a5 represents the location near the exit.

Accordingly, the changing trend of the local heat flux (q_{local}) with inlet concentration (x_{in}) at the same heated temperature (T_{wall}) and inlet mass flux (G_{in}) can be divided into four stages, as shown in Figure.88 (a): an initial linear increase, followed by gradual improvement up to a maximum, then a decrease and finally reaching a constant value. Through the analysis of the flow patterns (i.e., bubble distribution) shown in Figure 87(a), it is found that the subcooled flow boiling process gradually develops along the flow direction with the same rules. This includes the transition from the single-phase flow at the inlet to nucleated flow, bubbly flow,

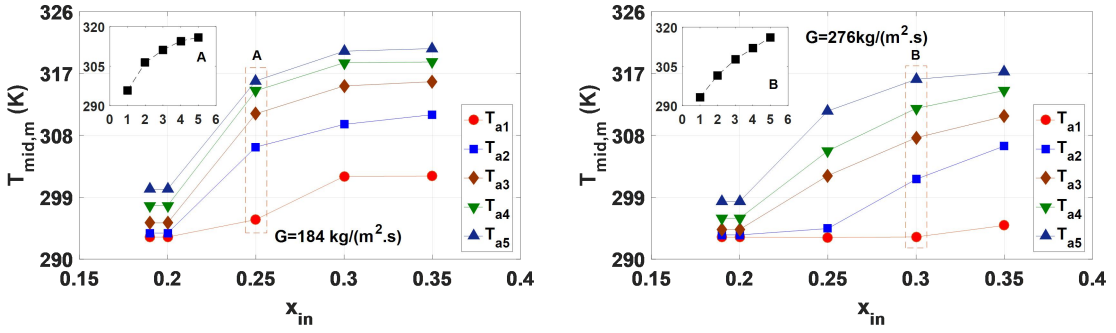
intermittent slug flow, and even local dryout at the exit. Correspondingly, the local heat flux (q_{local}) is the largest at the nucleated flow stage, followed by the bubbly flow stage, throughout the entire flow boiling process under the same conditions. In the case of local dryout, the local heat flux (q_{local}) is even smaller than that of the single-phase convective flow, as the thermal conductivity of coolants in the liquid state is generally larger than that in the gaseous state. Therefore, the values of local heat flux q_{local} for flow boiling, such as case A (i.e., x_{in}=25% mol., G_{in}=184 kg/(m^2·s)) and case B (i.e., x_{in}=30%mol., G_{in}=276 kg/(m^2·s)), decrease along the flow direction at the same heated wall temperature (T_{wall}) in Figure.88 (a).



(a)



(b)



(c)

Figure.88 Effect of inlet concentration on (a) local heat fluxes, (b) local HTCs and (c) local fluid temperatures in midsection at 184 and 276 kg/ (m^2.s)

Furthermore, both the inlet concentration (x_{in}) and inlet mass flux (G_{in}) have dominant effects on the boiling development process at the same wall temperature (T_{wall}). In the nucleated flow regime (e.g., red circle lines at a1 near the entrance), the values of local heat flux (q_{local}) are enhanced by increasing x_{in} and G_{in}. However, they decrease with a further increment of inlet concentration (e.g., x_{in} =25%-35%mol.) and/or a decrease in inlet mass flux (G_{in}) when larger-size bubbles exist near the heated walls (e.g., blue upper-triangle lines at a5 near the outlet). In general, the local heat fluxes (q_{wall}) are directly dependent on the flow patterns, which are mainly affected by the inlet concentration (x_{in}) and mass fluxes (G_{in}) in in flow boiling.

According to the formula of local HTC (h_{local}) in Eqn. (6.5), the local HTC (h_{local}) is mainly related to local heat flux (q_{local}) and local temperature in the midsection (T_{mid}) at a constant heated wall temperature (T_{wall}). Hence, it is merited to analyze inlet concentration (x_{in}) and inlet mass flux (G_{in}) effects on the local temperature in the midsection (T_{mid}), primarily.

$$h_{\mathrm{local,j}} = \frac{\sum_{i=1,j}^{n}\left[\dfrac{\left(q_{\mathrm{l,j,i}} + q_{\mathrm{r,j,i}}\right)}{T_{\mathrm{wall}} - T_{\mathrm{fluid,j,i}}}\right]}{n}$$

It is clear from Figure.88 (c) that the local mass-averaged temperature (T_{mid}) of the NH_3/H_2O mixture in the midsection increases with the distance from the entrance (i.e., from a1 to a5 in the sub-graph) and the inlet concentration (x_{in}). However, it decreases with an increase in the inlet mass flux (G_{in}) at a constant heated wall temperature (T_{wall}). The extent of influence on T_{mid} depends mainly on the combined effects of these factors within the range from the inlet fluid temperature (T_{in}) to the heated wall temperature (T_{wall}). Generally, the distinct curves of T_{mid} are determined by the inherent non-isothermal phase change characteristics of zeotropic mixtures (e.g., NH_3/H_2O), which differ from those observed during pure fluid evaporation.

Based on the aforementioned investigation of local heat flux (q_{local}) and local temperature in the midsection (T_{mid}), it is easy to analyze the complex effects on the local HTC (h_{local}) and

understand the corresponding flow boiling mechanism of the zeotropic mixture at a constant heated wall temperature (T_{wall}). Generally, the local HTC (h_{local}) increases linearly with inlet concentration (x_{in}) before local heat flux (q_{local}) begins to decline, followed by a small drop-off as shown in Figure.88 (b). The turning point of h_{local} occurs at a higher inlet concentration (x_{in}) (30%mol.) compared to local HTC (h_{local}) (i.e., 25%mol.), as observed in the cases at local positions b4 (green lower-triangle line) and b5 (blue upper-triangle line) at 184 kg/(m^2·s) shown in Figure.88 (b, left). In other words, although local heat flux (q_{local}) starts to decrease when inlet concentration (x_{in}) is increased from 25% to 30%mol., local HTC (h_{local}) continues to increase mainly due to the increment of local fluid temperature in the midsection (T_{mid}) of flow boiling in microchannels. Similarly, local HTC (h_{local}) increases along the flow direction, even though local heat flux (q_{local}) decreases, as local fluid temperature in the midsection (T_{mid}) also continues to rise under the same conditions.

Furthermore, the values and change patterns of local heat flux (q_{local}) and the HTC (h_{local}) with inlet concentration (x_{in}) differ significantly near the entrance (i.e., a1) and the exit (i.e., a5) in Figure.88. For instance, under the same conditions (i.e., inlet concentration of 35%vol, inlet mass flux of 184 kg/(m^2·s) and the heated wall temperature of 50℃), local heat flux (q_{local}) at location a1 is much larger than that at a5. Therefore, a comparative study of the combined effects on local heat flux (q_{local}) at locations a1 and a5 is conducted and presented in Figure.89.

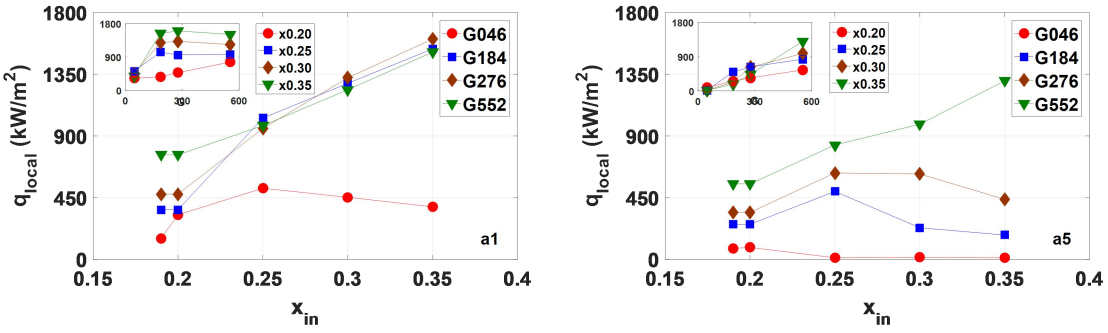


Figure.89 Effect of inlet concentration and mass flux on local heat flux near (a) the entrance at a1 and (b) the exit at a5 of microchannel

For the location a1 near the entrance, when the inlet mass flux (G_{in}) is equal to or greater than 184 kg/(m^2·s) and inlet concentration (x_{in}) is equal to or greater than 25% mol., the heat flux

(q_{local}) remains independent of inlet mass flux (G_{in}) at the same inlet concentration (x_{in}), but it linearly increases with the increase of inlet concentration (x_{in}) at the same G_{in} and T_{wall}. This is a typical characteristic of nucleation heat transfer dominant flow boiling in a microchannel. In the cases shown in Figure 87 at 276 kg/(m^2·s), it is observed that only tiny-size bubble nucleation occurs in the boundary layers near the entrance, resembling a homogeneous heat transfer process along the surfaces, similar to pool boiling. Furthermore, a higher x_{in} results in a more intense nucleation boiling of the NH_3/H_2O mixture on the hot surfaces, leading to larger values of q_{local} at the same heated wall temperature (T_{wall}). When inlet mass flux (G_{in}) is very small, such as 46 kg/(m^2·s), the local velocity is also low, causing larger-size bubbles to exist near the heating surfaces, which hinders heat transfer.

In contrast, the values of local heat flux (q_{local}) at a5 near the exit increase with increasing inlet mass flux (G_{in}) at the same inlet concentration (x_{in}), which is similar to the classic feature of convective heat transfer dominant flow boiling in microchannel. Considering the elongated slug flow as an example, the presence of large-size bubbles in the domain indicates significant liquid evaporation into vapor, resulting in a drastic velocity increase across the cross-section at the same inlet mass flux (G_{in}). A higher G_{in} at high vapor quality leads to a larger velocity increment, which enhances the convective effect on heat transfer significantly. Furthermore, the effects of inlet concentration (x_{in}) on local heat flux (q_{local}) at a5 vary at different values of G_{in}, similar to the effects observed for different local heat flux (q_{local}) at the same inlet mass flux (G_{in}) of 184 kg/(m^2·s) in Figure.88 (a). Therefore, the local heat flux (q_{local}) is primarily influenced by the local flow pattern (i.e., bubble numbers and sizes), which is adjusted by the combined effects of inlet concentration (x_{in}), inlet mass flux (G_{in}) and the local distance from the entrance (i.e., the degree of flow boiling development).

In general, local HTC (h_{local}) and local heat flux (q_{local}) are determined by the location, inlet mass flux (G_{in}) and inlet concentration (x_{in}). Heat transfer deterioration is more likely to occur closer to the entrance and with lower inlet mass flux (G_{in}) at the same inlet concentration (x_{in}) and heated wall temperature (T_{wall}). Unlike pure fluids, the inlet concentration (x_{in}) plays a crucial role as it not only influences the local fluid temperature in the non-isothermal phase

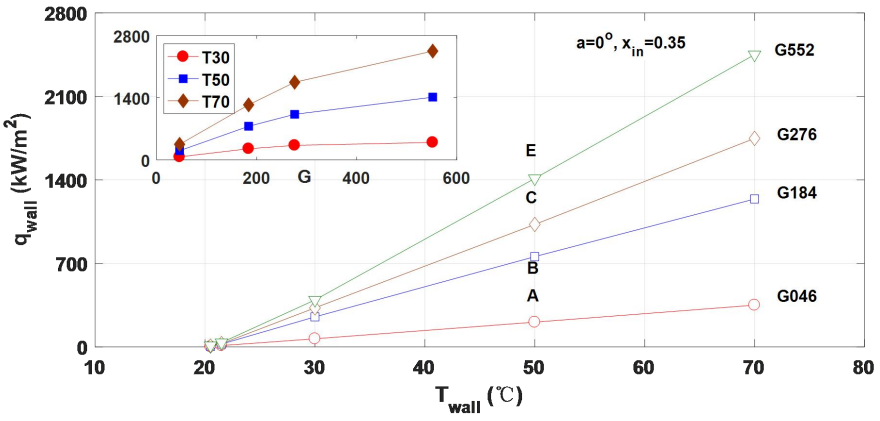
change process of zeotropic mixtures but also directly affects the effective bubble nucleation density on hot surfaces and the transition of flow patterns.

6.4.3-Effect of heating temperature

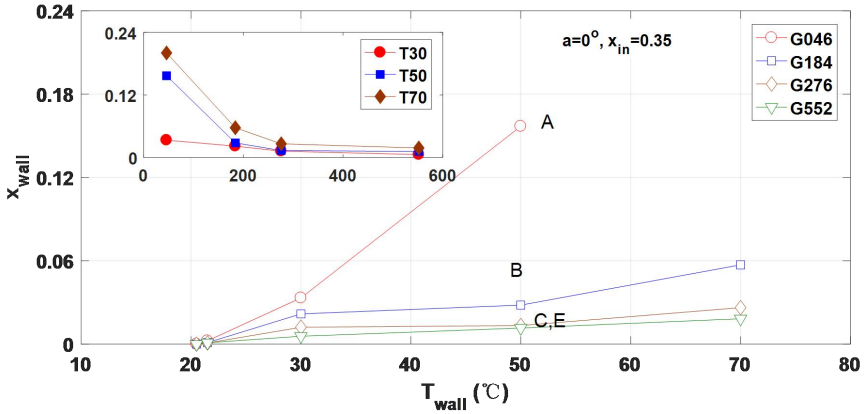
The above analysis of the heat transfer performance is conducted based on a constant heated temperature (T_{wall}) of 50℃. In this part, the effect of heated temperature on the heat transfer performance is investigated while maintaining a constant inlet concentration (x_{in}) of 35% mol..

6.4.3.1-The overall heat transfer performance

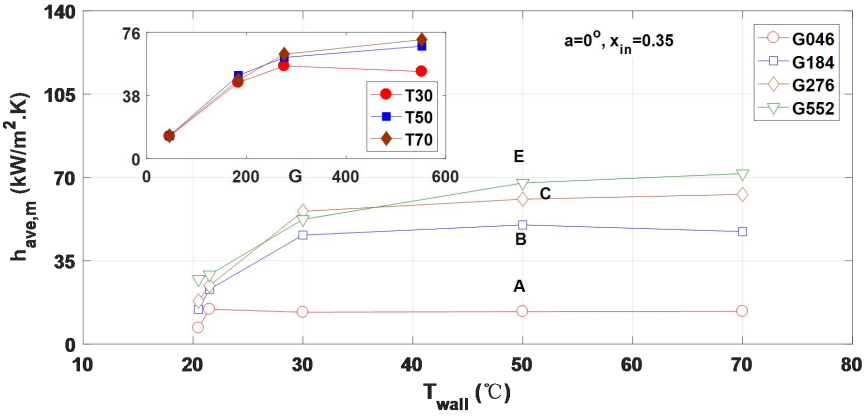
The relations between heat transfer performances (e.g., q_{wall}, h and ΔP) and some parameters (e.g., T_{out} and x_{wall}) with heated wall temperature (T_{wall}) and inlet mass flux (G_{in}) are plotted in Figure.90.



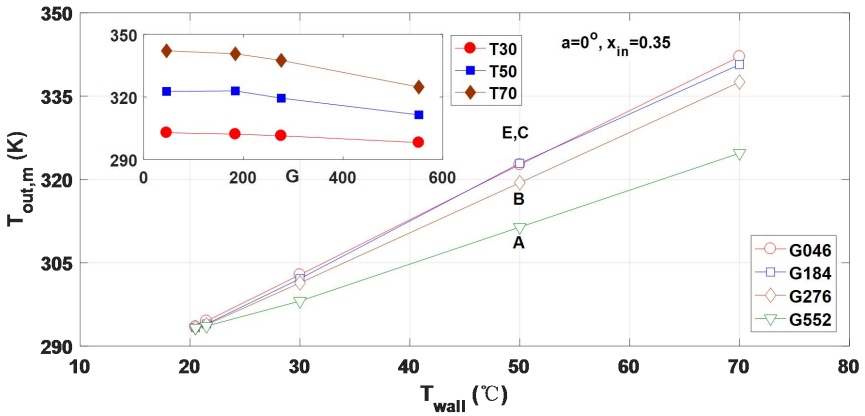
(a)



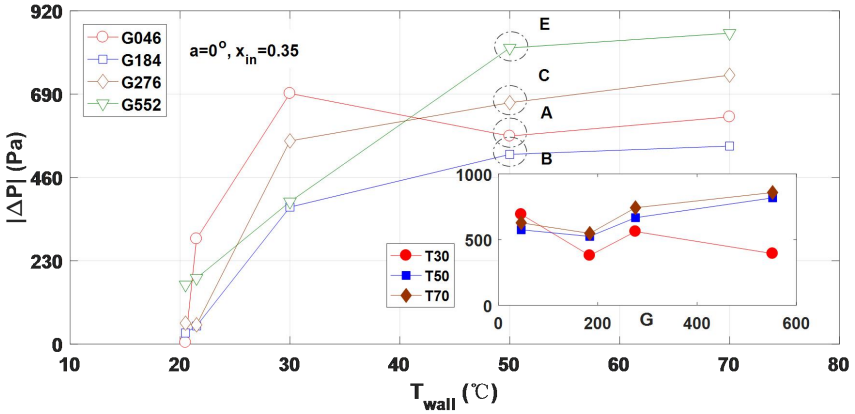
(b)


a=0°, x_in=0.35
G046
G184
G276
G552
T30
T50
T70
E
C
B
A
G
h_ave,m (kW/m².K)
T_wall (℃)

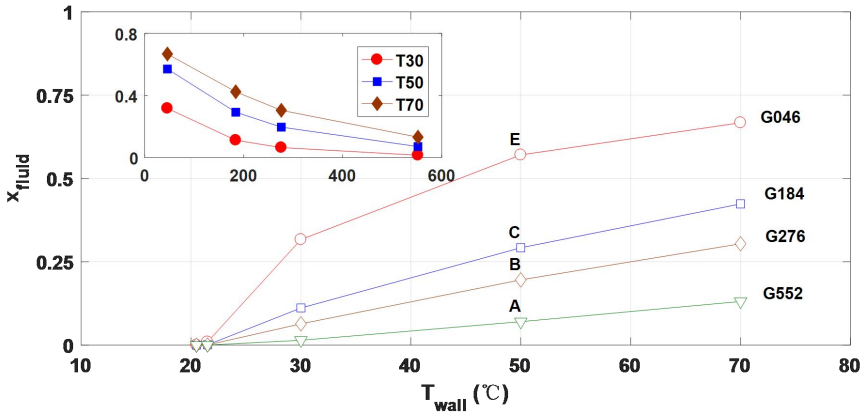
(c)


a=0°, x_in=0.35
T30
T50
T70
E,C
B
A
G046
G184
G276
G552
G
T_out,m (K)
T_wall (℃)

(d)


a=0°, x_in=0.35
G046
G184
G276
G552
E
C
A
B
T30
T50
T70
G
|ΔP| (Pa)
T_wall (℃)

(e)



(f)

Figure.90 Effect of heating temperature on (a) the overall heat flux, (b) HTC, (c) outlet temperature, (d) vapor fraction on walls, (e) pressure drop and (f) vapor fraction in domain at various G_{in}

According to Figure.90(a), it is evident that the heat flux (q_{wall}) increases linearly with heated temperature (T_{wall}) at the constant inlet mass flux (G_{in}) and inlet concentration (x_{in}). A larger G_{in} results in a higher enhancement of q_{wall}. This can be attributed to the increased nucleating effect by raising the heated wall temperature (T_{wall}) and the improved convection effect due to the increment of inlet mass flux (G_{in}), which collectively enhance the overall heat transfer capability such as the heat flux (q_{wall}).

In contrast, the vapor fraction on surfaces (x_{wall}) exhibits different behavior. It increases with the increment of the heated wall temperature (T_{wall}) at the same inlet mass flux, but decreases when inlet mass flux (G_{in}) is increased at the same heated wall temperature (T_{wall}) and inlet concentration (x_{in}), as shown in Figure.90(b). This means that both the reduction of the vapor faction on surfaces (x_{wall}) with increasing inlet mass flux (G_{in}) at the same wall temperature (T_{wall}) and the increase of vapor faction on surfaces (x_{wall}) by raising heated wall temperature (T_{wall}) at the same inlet mass flux (G_{in}) contribute to the enhancement of the heat flux (q_{wall}) at the same inlet concentration (x_{in}). In the case of nucleating flow at 552 kg/(m^2·s), the increase in the vapor faction on surfaces (x_{wall}) is relatively small when heated wall temperature (T_{wall}) is increased from 30 to 70℃, but it significantly enhances heat wall (q_{wall}). However, for the elongated slug flow at 46 kg/(m^2·s), although there is a larger increase in the vapor faction on surfaces (x_{wall}), it only leads to a small enhancement of heat flux under the same conditions.

Therefore, it is the combined effects of inlet mass flux (G_{in}), the heated wall temperature (T_{wall}) and flow boiling patterns determined by these factors that ultimately govern heat flux (q_{wall}) at the same inlet concentration (x_{in}).

However, the relationship between the HTC (h_{ave}) and heated wall temperature (T_{wall}) differs from that of the heat wall (q_{wall}) at the same mass flux (G_{in}). Importantly, the trend of the HTC (h_{ave}) with the heated wall temperature (T_{wall}), under the constant inlet NH_3 concentration (x_{in}) and inlet mass flux (G_{in}) as shown in Figure.90 (c), is similar to the trend observed with x_{in} at the constant T_{wall} and G_{in} in Figure.86 (a), as well as with inlet mass flux (G_{in}) at the constant x_{in} and T_{wall} in Figure 83(a). For instance, when considering cases where the inlet mass flux (G_{in}) is no less than 184 kg/(m^2.s), the HTC (h_{ave}) increases linearly when the heated wall temperature (T_{wall}) is below 30℃, and then stabilizes to a certain extent when it reaches 50℃ or higher in Figure.90 (c).

Similarly, this is also due to the non-isothermal phase change feature of the zeotropic mixture. As discussed in section 6.4.2, the fluid temperature of NH_3/H_2O tends to approach the heated wall temperature during the evaporation process. Consequently, the outlet temperature ($T_{out, m}$) increases linearly with the increment of heated wall temperature (T_{wall}), as shown in Figure.90 (d). Furthermore, the rate of increase in the outlet temperature ($T_{out, m}$) of mixture is weakened by increasing inlet mass flux (G_{in}) at the same inlet concentration (x_{in}), as the residence time of the coolant in the domain is shortened by raising inlet mass flux (G_{in}) (i.e., inlet velocity of u_{in}), thereby hindering the increase rate of outlet temperature ($T_{out, m}$) of mixture. According to Figure.90 (d), the outlet temperature ($T_{out, m}$) slightly decreases when inlet mass flux (G_{in}) is less than 184 kg/(m^2·s), and then decreases rapidly with further increases in inlet mass flux at the same conditions. However, the wall heat flux (q_{wall}) continues to increase with increasing inlet mass flux (G_{in}) under the same conditions in Figure 90(a). Therefore, it is the complex mutual effects of heat flux (q_{wall}), heated wall temperature (T_{wall}) and the outlet temperature ($T_{out, m}$) that ultimately determine the HTC (h_{ave}), as indicated by the calculation formula of the overall HTC in Equation (6-4).

$$h_{ave} = \frac{\sum_{i=1}^{n}\left[\frac{q_{\text{wall,i}}}{T_{\text{wall}} - \left(T_{\text{in}} + T_{\text{out,i}}\right)/2}\right]}{n}$$

Figure.90 (e) illustrates the effects of heated wall temperature (T_{wall}) and inlet mass flux (G_{in}) on the total pressure drop (ΔP) at a constant inlet concentration (x_{in}). Generally, the change patterns of ΔP are complex and depend on different factors. As discussed in section 2.2.1, the total pressure drop is influenced by factors such as inlet mass flux (liquid Reynolds number), the vapor fraction in the domain (x_{fluid}) and the strong interactions of bubbles in the thermal boundary layers, including local turbulence induced by bubble nucleation related to the vapor fraction on heated surfaces (x_{wall}).

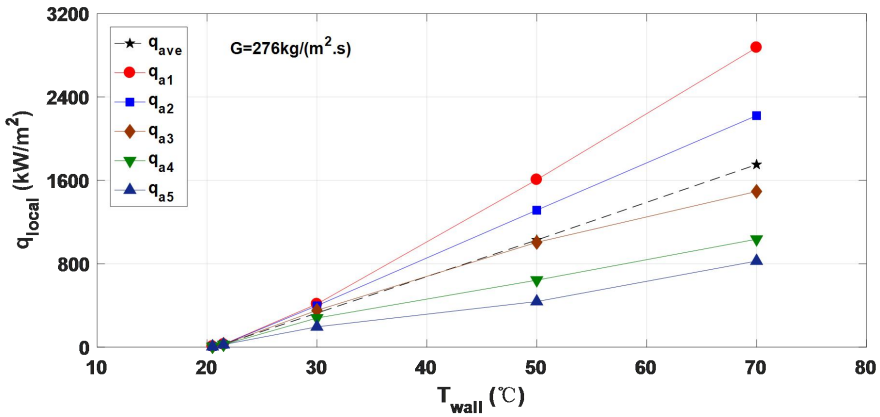
Furthermore, the evaporation degree of mixture is affected by mutual influence of inlet mass flux (G_{in}), inlet NH_3 concentration (x_{in}) and the heated wall temperature (T_{wall}), among others. For instance, the total pressure drop (ΔP) generally increases with the heated wall temperature (T_{wall}) at the same conditions, since the evaporation is enhanced and the bubble growth rate is accelerated by increasing the wall temperature (T_{wall}). However, in the case of T_{wall} at 50℃ or 70℃, the pressure drop (ΔP) initially decreases with increasing the inlet mass flux (G_{in}) from 46 to 184 kg/(m^2·s) since the vapor fraction in the domain (x_{fluid}) also decreases significantly in Figure.90 (e). However, the pressure drop (ΔP) starts to rise again with further increases in inlet mass flux (G_{in}), when some small-size bubbles are present and moving in the domain (i.e., the nucleating and bubbly flow), resembling the features of the single-phase convection. Therefore, it is the dynamic balance of factors that ultimately determines the total pressure drop (ΔP) in flow boiling of the NH_3/H_2O mixture in microchannels.

6.4.3.2-The local heat transfer performance

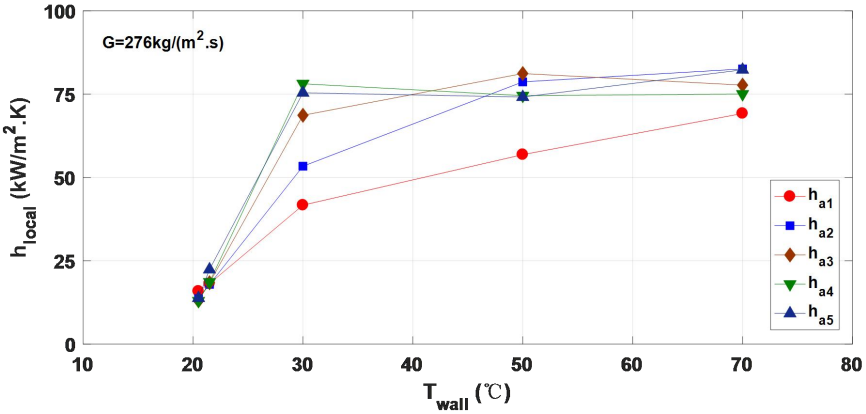
The local heat flux (q_{local}) and local HTC (h_{local}) of the NH_3/H_2O mixture at 276 kg/(m^2·s) are plotted at different heated wall temperatures (T_{wall}) in Figure.91. The distributions of fluid temperature (T_{fluid}) and the bubbles in the domain are shown in Figure.92.

Similar to the overall heat flux (q_{ave}) in Figure.90, the local heat flux (q_{local}) increases linearly with heated wall temperature (T_{wall}) under the same conditions in Figure.91(a). This indicates

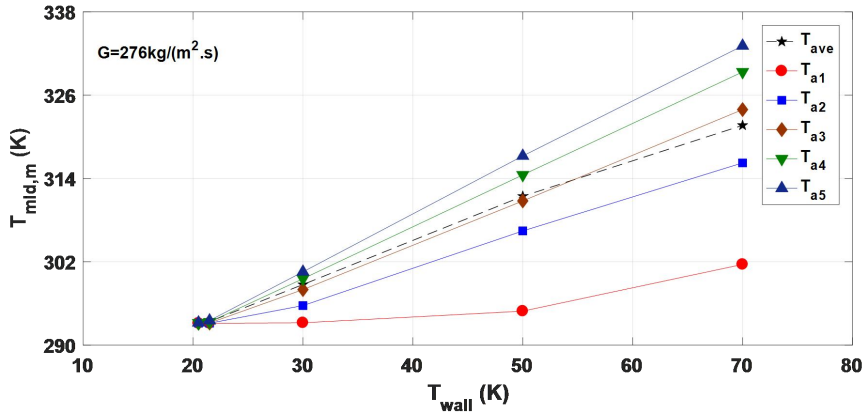
that T_{wall} serves as the driving force for flow boiling heat transfer. The closer the position is to the entrance (e.g., a1), the higher the local heat flux (q_{local}) at that local position. However, the rate of increase in q_{local} is not the same for different positions along the microchannel. Both the magnitude and slope of q_{local} versus T_{wall} decrease from a1 near the entrance to a5 near the exit. This is explained in Figure.92 (b), which shows the gradual development of NH_3/H_2O flow boiling along the flow direction, transitioning from a nucleated boiling dominant state (e.g., the bubbly flow) near the entrance (i.e., a1) to a convection boiling dominant state (e.g., large-size bubbly flow and slug flow) closer to the outlet (i.e., a5).



(a)

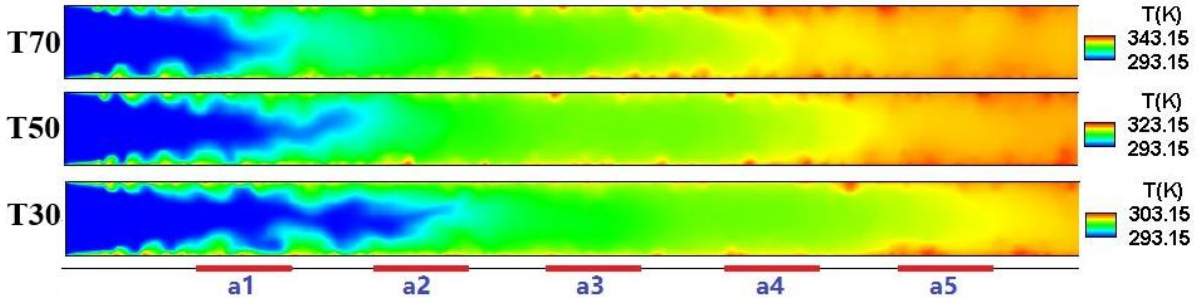


(b)

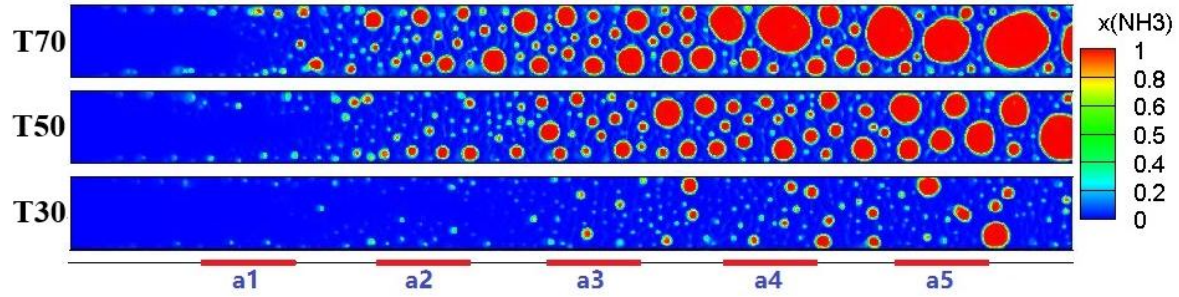


(c)

Figure.91 Effect of heating temperature on (a) local heat flux (b) local HTC and (c) fluid temperature in midsection at 276 kg/(m².s)



(a)



(b)

Figure.92 Effect of heating temperature on (a) fluid temperature distribution and (b) vapor fraction distribution of NH_3/H_2O flow boiling in microchannel at 276 kg/(m²·s)

Furthermore, with the increase in the heated wall temperature (T_{wall}), the local heat flux (h_{local}) shows a sharp improvement initially at locations near the entrance (e.g., a1) and increases with a tendency to stabilize at around 75 kW/(m²·K) along the flow direction (e.g., from a3 to a5) in Figure 91(b). In the case where the heated wall temperature (T_{wall}) is set at 30˚C, local

heat flux (h_{local}) increases from a1 to a5 as flow boiling of NH_3/H_2O progresses from the subcooled flow (e.g., a1) to nucleating flow (e.g., a2, a3, and a4), and finally to bubbly flow (e.g., a5) without any large bubbles attached to the heating surfaces, as illustrated in Figure.92 (b). However, when the heated wall temperature (T_{wall}) is increased to 50 and 70℃, the values of local heat flux (h_{local}) remain stable with slight fluctuations, except for h_{local} at a1. This is because the flow patterns at locations from a2 to a5 are characterized by bubbly flow without any significant bubbles blocking the channel in Figure.92 (b). In these cases, the local fluid temperatures (T_{mid}) increase with the same level of local heat flux (q_{local}) in Figure.91 (c).

6.4.4-General performance evaluation

According to aforementioned investigations, the local HTCs of NH_3/H_2O mixture flow boiling at different conditions (e.g., inlet mass flux (G_{in}), inlet concentration (x_{in})and heated temperature (T_{wall})) are summarized as a function of local vapor fraction on wall surfaces (x_{wall}), which is difficult to be measured actually in experimental studies, as plotted in Figure.93.

Based on the aforementioned investigations, the local HTCs of NH_3/H_2O flow boiling under different conditions (e.g., inlet mass flux G_{in}, inlet NH_3 concentration x_{in} and the heated wall temperature T_{wall}) are summarized as a function of the local vapor fraction on surfaces (x_{wall}). Nevertheless, it's worth noting that it is challenging to measure the vapor fraction on surfaces (x_{wall}) during experimental studies. The summary of the local HTCs is presented in Figure.93.

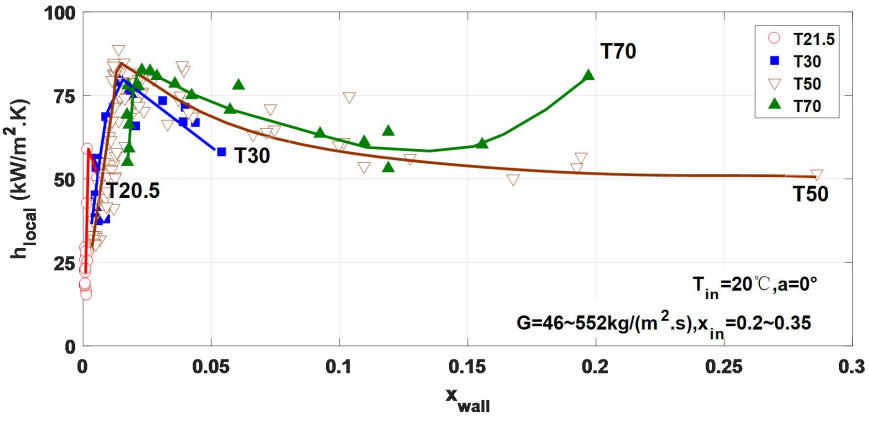


Figure.93 Local HTC with vapor fraction on heating wall surface of NH_3/H_2O in microchannel

As depicted in Figure.93, the simulation results of local HTC (h_{local}) versus the vapor fraction on heated surfaces (x_{wall}), regardless of inlet mass flux (G_{in}), inlet NH_3 concentration (x_{in}) and heated wall temperature (T_{wall}), follow the classic M-shaped curves observed for flow boiling HTCs versus the vapor quality in different refrigerants, as shown in Figure.9. Specifically, as the vapor fraction on heated surfaces (x_{wall}) increases, the local HTC (h_{local}) exhibits a linear increase at low values of x_{wall} (corresponding to the nucleating flow), followed by a decline at moderate value of the vapor fraction on heated surfaces (x_{wall}) (indicative of small-size bubbly flow) after reaching a maximum value of around 85 kW/(m^2·K). Subsequently, the local HTC (h_{local}) decreases slowly at high vapor fraction on heated surfaces (x_{wall}) associated with large-size bubbly and slug flow until it undergoes a sudden jump to a higher local HTC (h_{local}) (indicative of elongated slug flow and film evaporation flow), as observed in the "T70" curve in this study. Furthermore, as previously analyzed, the flow pattern (including the distribution of bubbles in the domain) in NH_3/H_2O flow boiling in microchannels is primarily determined by the combined and mutual effects of G_{in}, x_{in}, T_{wall}, and other factors.

In summary, it can be concluded that the flow boiling crisis and local dry-out are successfully prevented for NH_3/H_2O mixture at all the cases in this study (i.e., the wall temperature (T_{wall}) less than 70℃, inlet NH_3 concentration (x_{in}) less than 35% mol. and inlet mass flux (G_{in}) less than 552 kg/(m^2·s)).

6.5- Summary

In present work, numerical simulation was conducted to investigate flow boiling heat transfer performance of the binary mixture (i.e., NH_3/H_2O) in a horizontal microchannel with 0.4 mm width and 6mm length at the constant heated wall temperature condition. A novel approach, which couples the quasi-ideal properties of the NH_3/H_2O mixture, multiphase VOF and modified LEE method, has been introduced and adopted to simulate the non-isothermal phase changing process in microchannel. The combined effects of inlet mass flux (ranging from 46 to 552 kg/(m^2·K)), inlet NH_3 concentration (ranging from 15% mol. to 35%mol.) and heated wall temperature (ranging from 20.5℃ to 70℃) on heat transfer performance are investigated comparatively.

The main findings of this study are summarized as follows:

(1) The heat transfer performance of NH_3/H_2O flow boiling in microchannels is superior to that of water at a constant heated temperature of 50℃, making it a promising approach for thermal management of electronic devices. At the same inlet mass flux of 552 kg/(m^2·s), the overall heat dissipation rate of the NH_3/H_2O flow boiling can reach up to 1.41 MW/m^2, which is 2.05 times higher than that of water single-phase convective heat transfer. Moreover, for the same heat flux of 0.69 MW/m^2, the required inlet mass flux for the NH_3/H_2O flow boiling is only 166.2 kg/(m^2·s), which is just 30% of the demand for water single-phase convection. Additionally, the maximum values of local heat flux and HTC for the NH_3/H_2O flow boiling are approximately 1.52MW/m^2 and 85kW/(m^2·K), respectively, as observed in this study.

(2) Flow boiling heat transfer performance of the NH_3/H_2O mixture in microchannels follows the classic flow boiling characteristics observed in pure fluids, such as the M-shaped curve of HTC versus vapor quality. However, it is also important to note that the non-isothermal phase change behaviour of the zeotropic mixture introduces an additional factor, as the saturated temperature of the mixture is dependent on the concentration and pressure. This difference in behaviour is a distinct feature of the zeotropic mixture compared to pure fluids.

(3) It has been observed that the overall heat flux and HTC of the NH_3/H_2O mixture initially increase linearly and eventually become independent of inlet mass flux (G_{in}) or inlet NH_3 concentration (x_{in})) at a constant inlet concentration (x_{in}) or inlet mass flux (G_{in}) and heated wall temperature (T_{wall}). It suggests the presence of a threshold value of inlet concentration (x_{in}) or inlet mass flux (G_{in}) required to maintain a certain level of heat dissipation at the given conditions. Beyond this threshold, further increases in inlet concentration (x_{in}) or inlet mass flux (G_{in}) would not significantly benefit the dissipation of heat. For instance, the threshold inlet concentration is found to be 25% mol. for the case of an inlet mass flux at 184 kg/(m^2·s) and a heated wall temperature at 50℃.

(4) Based on the distributions of bubbles and fluid temperature in the domain, it is observed that flow patterns, such as the nucleating, bubbly and intermittent slug flow, are influenced by the combined and mutual effects of inlet mass flux (G_{in}), inlet concentration (x_{in}), and heated

wall temperature (T_{wall}). Furthermore, the flow patterns play a crucial role in determining the phase change behaviour of the NH_3/H_2O flow boiling heat transfer performance. Specifically, the convective boiling dominates the heat transfer performance during the bubbly flow stage, while nucleating boiling becomes prominent during the slug flow or partial dryout flow stages.

(5) Moreover, it is important to note that no local dry-out was observed in all the cases of the NH_3/H_2O mixture flow boiling in microchannels (i.e., the heated wall temperature less than 70℃, inlet concentration less than 35% mol. and inlet mass flux less than 552kg/(m^2·s)). This indicates that the NH_3/H_2O mixture has the ability to delay local dry-out even under high heat dissipation conditions. This makes it a promising fluid to cool the electronic components.

Chapter-7 Flow boiling heat transfer of the NH_3/H_2O/PCM slurries

7.1 Introduction

In this chapter, flow boiling of the NH_3/H_2O mixture based PCM slurries in microchannels is investigated to assess the mutual effects of two non-isothermal phase change phenomena on the enhancement of heat dissipation capacity for cooling electronic devices. The effects of the melting temperature ($T_{melting}$), the melting latent (q_m) of the PCM particles, as well as contact angle (α) of heated walls and PCM particles, are analyzed comparatively. It is conducted at a constant inlet NH_3 concentration (x_{in}) of 35%mol., an inlet fluid temperature (T_{in}) of 20℃ and a heated wall temperature (T_{wall}) of 50℃, along with various inlet mass fluxes (G_{in}) and inlet particle concentrations (y_{in}). The melting temperature of the particle is set as 1K in this work.

7.2-Basical assumption and treatment

The prerequisite hypotheses for simulating the multiphase flow of the NH_3/H_2O/PCM mixture in microchannels are similar to those of the R134a-based functional fluid in Chapter 5 and the NH_3/H_2O mixture in Chapter 6. They are listed briefly as follows.

(1) The NH_3/H_2O/PCM mixture is considered a Newtonian-like and incompressible fluid and is divided into three separated homogeneous phases: the liquid and gaseous NH_3/H_2O mixture and a suspended cloud of PCM particles. In present work, the NH_3/H_2O mixture is assumed to be a pure substance with the same equivalent thermal and transport properties of the saturated NH_3/H_2O mixture. Similarly, the particles are treated as a continuous medium rather than the discrete phase. These properties of this virtual fluids (e.g., density, temperature, velocity, etc.) are considered to exhibit the continuous distribution in the domain, facilitating the analysis of flow and heat transfer behaviors of nanoscale particles in simulations without considering the individual particle's position and movement at the nanoscale.

In the simulation, an inlet boundary condition with an average velocity is employed, which is determined by the mass balance equation. The mixture at the inlet is in a uniform mixed state, comprising the liquid phase of NH_3/H_2O (Phase-l), the gaseous phase of NH_3/H_2O (Phase-g)

and the virtual PCM phase (Phase-s). Since the mixture at the inlet is in a subcooled state, the volume fraction of gaseous phase (phase-g) at the inlet is set to 0. Additionally, the inlet PCM concentration (y_{PCM}) is set by specifying the volume fraction of the virtual phase (Phase-s) to represent the presence of particles in the NH_3/H_2O/PCM mixture. Therefore, the distribution and interactions of the particles with the liquid and gaseous NH_3/H_2O mixture are investigated without considering the individual positions and motions of individual particles.

(2) The multiphase VOF-modified LEE method and the quasi-ideal-mixture treatment of the NH_3/H_2O mixture are used to simulate the non-isothermal phase change in the microchannels. The effective heat capacity method with a rectangular profile as well as the effective dynamic viscosity method (VAND) are employed to consider the flow and melting effects of the PCM particles suspended in the mixture.

(3) The realizable k-ε model is chosen as the turbulence model. The PISO algorithm is chosen for pressure-velocity coupling, the second-order upwind discretization is used for momentum and energy equations, and PRESTO and Geo-Reconstruct discretization are employed for pressure and volume fraction interpolation, respectively. The variable time step is controlled by the Global Courant number, set up to a maximum of 0.25, and the absolute residuals of the continuity equation are set to $1e^{-4}$.

(4) As described in Chapter 3, the warm start approach is used in present work to simulate the subcooled flow boiling heat transfer in microchannels. Specifically, the convergent result of a steady-state laminar flow is utilized as the initial conditions for the multiple-phases changing process of the NH_3/H_2O/PCM mixture.

7.3-Grid independence and model validation

The computational domain is selected as a 2D rectangular horizontal channel with a width of 0.4 mm and a length of 6mm. Similar to the horizontal microchannels studied in the previous work, the gravity effect on flow boiling heat transfer performance is neglected in this chapter. Both of the hot walls in a 2D channel represent the left and right sides in an actual rectangular microchannel, as illustrated in Figure.76.

According to the grid independence tests conducted in the chapter 6, a grid size of 6.2 μm is selected in this part to simulate the NH_3/H_2O/PCM mixture. Similarly, since few experimental data of the NH_3/H_2O/PCM mixture flow boiling in microchannels is available in the literature, the model validation is carried out as introduced in those previous chapters.

7.4-Results and discussion

The major assessments were focused on the effects of properties (e.g., thermal conductivity and the latent heat) of various coolants (i.e., the R134a based functional fluid in chapter 5 and the NH_3/H_2O mixture in chapter 6) and boundary conditions (e.g., inlet mass flux, the wall heat flux and inlet particles concentration in chapter 5, the heated wall temperature and inlet NH_3 concentration in chapter 6) on multiphase heat transfer performance in microchannels. Therefore, this chapter aims to explore the effects of the melting temperature ($T_{melting}$) and the latent heat per unit temperature (q_m) of the PCM material, as well as the contact angle (α) of surfaces on the multiphase flow heat transfer of the NH_3/H_2O/PCM mixture. The properties of the PCM particle and the saturated NH_3/H_2O mixture at 1 bar are listed in Table.22.

Table.22 Physical properties of PCM and the saturated NH_3/H_2O solution at 50℃ and 1bar

	Density	Thermal conductivity	Viscosity	Specific heat	Specific latent heat
	kg/m^3	W/(m·K)	Pa·s	kJ/(kg.K)	kJ/kg
PCM	1304	0.48	1.72×10^{-5}	0.69	201
NH_3/H_2O	923	0.53	1.52×10^{-4}	4.22	1443

7.4.1-Effect of the PCM melting temperature

The impact of the PCM particle melting temperature ($T_{melting}$) on the single-phase convective heat transfer performance such as the heat flux (q_{wall}) and HTC (h_{ave}) of NH_3/H_2O based PCM slurries in microchannels are analyzed under the conditions of an inlet fluid temperature (T_{in}) of 20°C and a heated wall temperature (T_{wall}) of 50°C. The inlet concentration of NH_3 (x_{in}) is set at 15%mol. and that of the particles (y_{in}) is fixed at 5%mol. in the NH_3/H_2O/PCM mixture. According to Figure.42, the saturated concentration of the NH_3/H_2O mixture at 1 bar is about 19.4 %mol. at a saturated temperature of 50°C. Hence, the mixture with a NH_3 concentration

of 15%mol. remains in an undersaturated state under a maximum temperature of 50°C at 1bar. The results are presented comparatively in Figure.94.

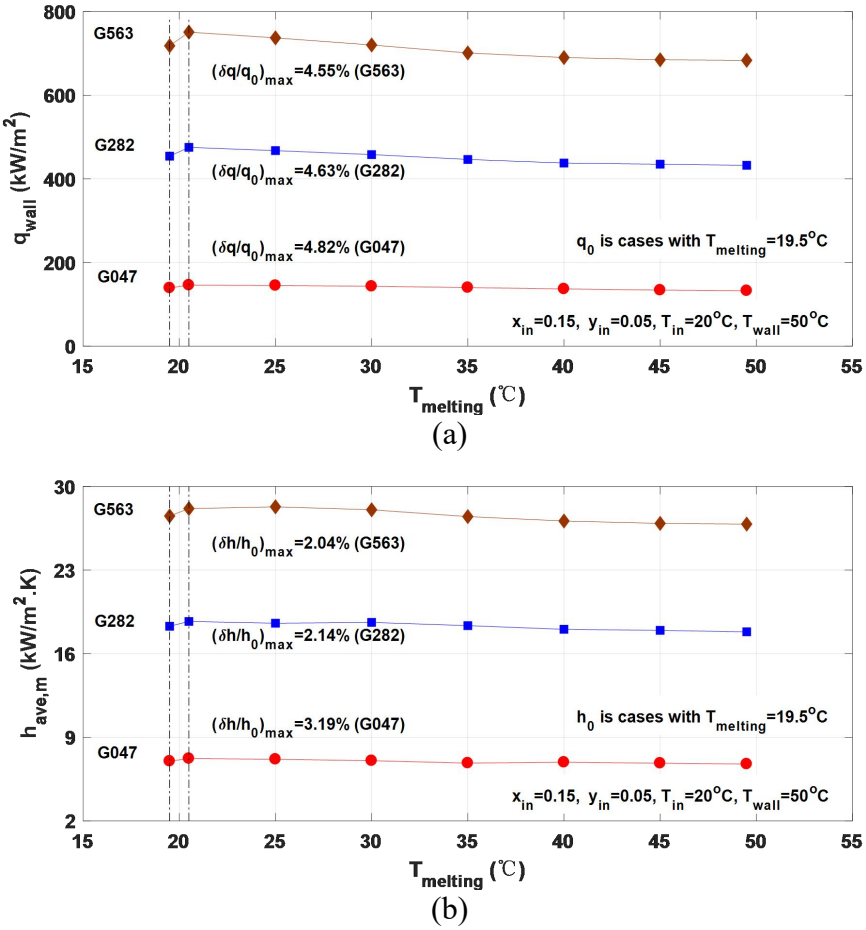
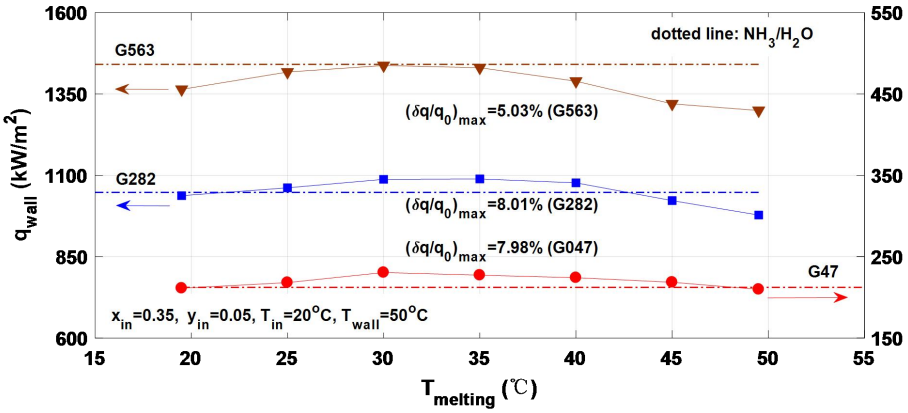


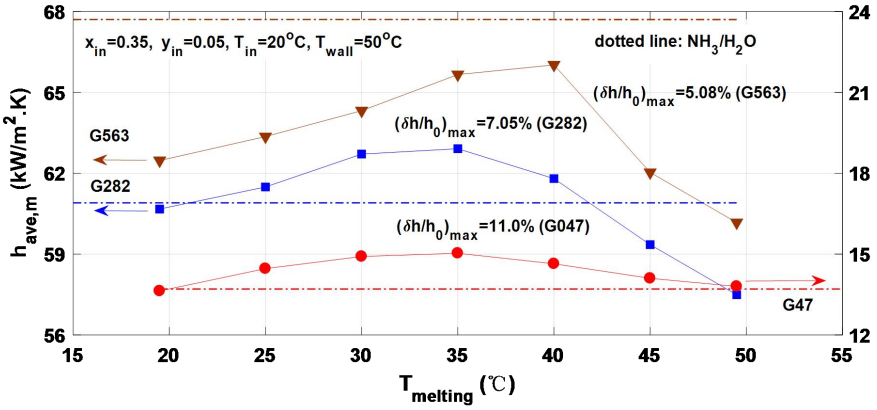
Figure.94 Effect of PCM melting temperature on (a) the overall heat flux and (b) HTC of single-phase convective heat transfer of NH_3/H_2O/PCM mixture in microchannel at a heated temperature 50 ℃

According to Figure.94, it is observed that the overall heat flux (q_{wall}) and HTC (h_{ave}) of the NH_3/H_2O/PCM mixture increase when the melting temperature ($T_{melting}$) of PCM particles is set between inlet temperature (T_{in}) and the wall temperature (T_{wall}). However, the maximum enhancement rates (δq/q and δh/h) are less than 5% compared to the cases without the PCM melting in microchannels. Additionally, the absolute increments of q_{wall} and HTC are slightly reduced by increasing inlet mass flux (G_{in}) from 47 to 563 kg/(m^2·s). This can be attributed to the expansion of the non-melted area in the domain, wherein the local temperature is below the melting point of PCM particles. This expansion occurs as the inlet mass flux is increased.

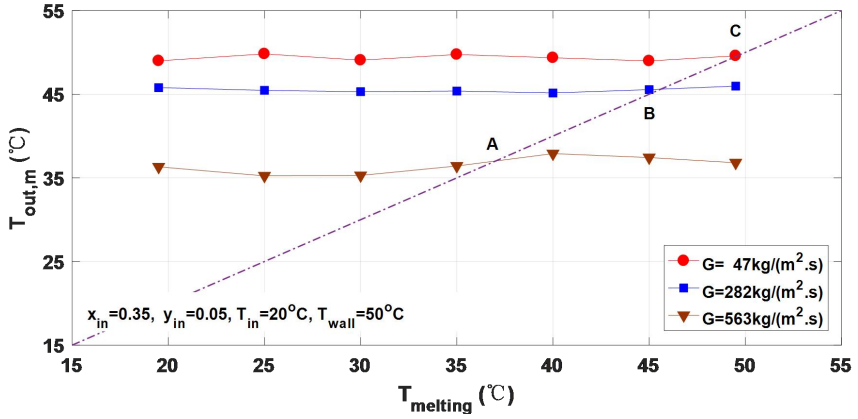
Furthermore, the results in Figure.95 illustrate the effects of the melting temperature ($T_{melting}$) of the PCM particles on the overall heat flux (q_{wall}), the HTC (h_{ave}), the fluid temperature at the exit ($T_{out,m}$) and the vapor fraction on the heated surfaces (x_{wall}) of the NH_3/H_2O mixture flow boiling with PCM melting in the microchannel, individually.



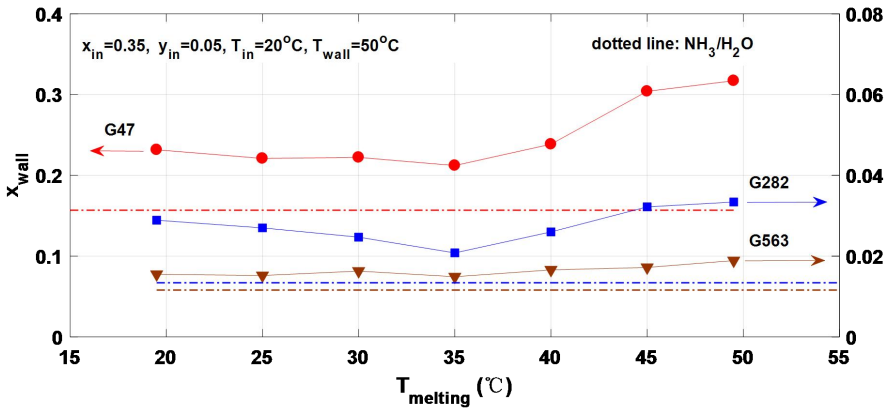
(a)



(b)



(c)



(d)

Figure.95 Effect of PCM melting temperature on (a) heat flux, (b) HTC, (c) the outlet temperature and (d) the vapor fraction on heated surfaces of the NH_3/H_2O/PCM mixture in microchannel

Based on Figure.95 (a) and Figure.95 (b), the result reveal that both the overall heat flux (q_{wall}) and HTC (h_{ave}) exhibit an initial increase, reaching their peak values, and then followed by a gradual decrease with the increment of the melting temperature ($T_{melting}$). This highlights the significance of choosing an appropriate PCM material with a melting temperature ($T_{melting}$) that matches well with the NH_3/H_2O flow boiling conditions. The incorporation of suspended PCM particles in the mixture presents both advantages and disadvantages for the NH_3/H_2O flow boiling heat transfer within a heat sink.

According to Figure.95 (c), the mass-averaged fluid temperature at the exit ($T_{out,m}$) decreases as inlet mass flux (G_{in}) is increased at the same conditions. This is mainly due to the increased inlet velocity (u_{in}), which reduces the residence time of the fluid flowing through the domain. Consequently, when the out temperature (T_{out}) is lower than the melting temperature ($T_{melting}$) at the intersection points such as A and B, it indicates that only a portion of the PCM particles near the heated surfaces can melt and absorb heat from the walls. As a result, the heat transfer enhancement effect of the PCM particles is significantly diminished.

Correspondingly, the vapor fraction on the heated surfaces (x_{wall}) initially decreases towards its minimum value and then starts to increase rapidly in Figure.95 (d). This suggests that the suspended particles in the mixture have both positive and negative effects on the generation and adhesion of bubbles on hot walls. The endothermic melting of the PCM materials in the

particles could mitigate the growth rate of bubbles by absorbing heat from the neighbor fluid. However, those suspended particles could physically impede the departures of bubbles from the wall surfaces, thereby increasing the vapor fraction on the heated surfaces (x_{wall}). Hence, it is the balance between these factors that finally determines the impact on the flow boiling and heat transfer performance of the NH_3/H_2O/PCM mixture.

In order to further understand the heat transfer mechanism affects by the melting temperature ($T_{melting}$) in the NH_3/H_2O/PCM mixture multiphase flow in microchannels. The distributions of fluid temperature and the PCM locations in the domain are presented in Figure.96 at the different melting temperature ($T_{melting}$ or T_m) ranging from 30℃ to 45℃. The same conditions are maintained at inlet temperature (T_{in}) of 20℃, the heated wall temperature (T_{wall}) of 50℃, inlet mass flux (G_{in}) of 282 kg/(m^2·s), inlet NH_3 concentration (x_{in} or x_{NH3}) of 35%mol. and inlet PCM particle concentration (y_{in} or y_{PCM}) of 5%vol.. Hence, in order to clearly illustrate the melted areas of PCM particles in the flow domain, the contour values are set between inlet temperature and the melting temperature in ranges of 30-45℃ in Figure.96.

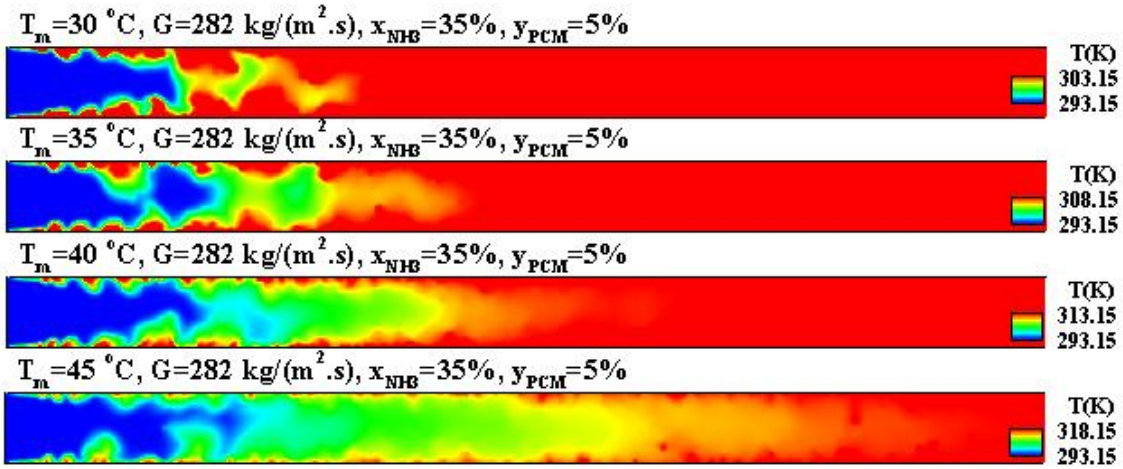


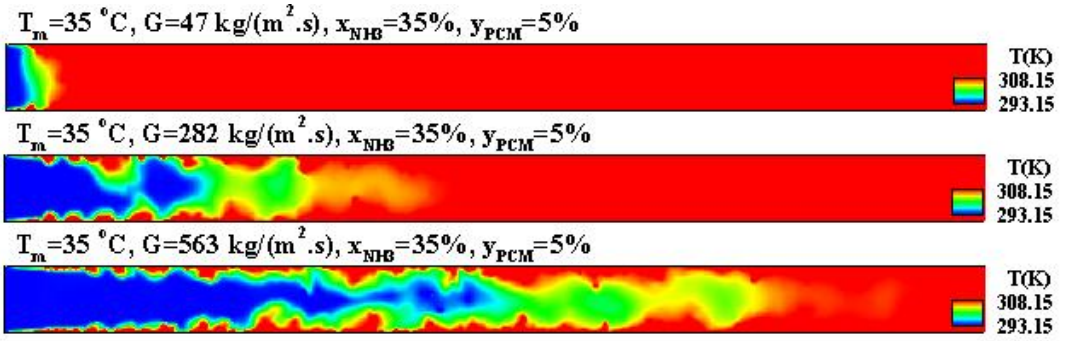
Figure.96 Effect of PCM melting temperatures on fluid temperature distribution of NH_3/H_2O/PCM mixture flow boiling in microchannel at heating temperature 50 ℃

As an example, in the case where the melting temperature of the PCM particles is 30°C, the upper temperature limit is defined as 303.15K, as depicted in the first cloud chart in Figure.96. This chart illustrates the PCM melting region through the red-shaded area when the particles are present in the flow domain. Consequently, it is clear that the melting temperature ($T_{melting}$)

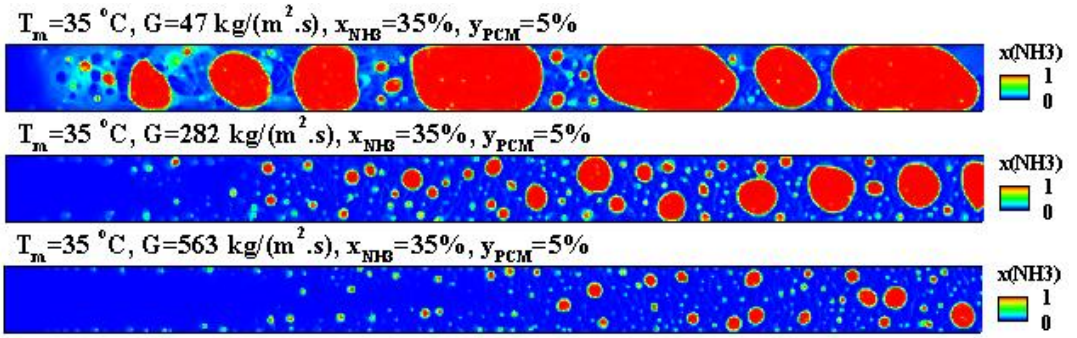
exerts a notable influence on local fluid temperature in the domain, directly determining the extent of the endothermic melting of PCM particles. Lower values of the melting temperature ($T_{melting}$) correspond to larger PCM melting areas within the domain.

Additionally, inlet mass flux (G_{in}) has a significant impact on the heat transfer performance of the NH_3/H_2O/PCM mixture. Comparing the case without PCM melting (i.e. $T_{melting}>T_{wall}$), the maximum relative enhancement of the heat fluxes (q_{wall}) and the HTC (h_{ave}) at 47kg/(m^2·s)) is larger than that at 47 kg/(m^2·s) in Figure.95 (a) and (b). Furthermore, both heat fluxes and the HTCs of the NH_3/H_2O/PCM mixture are larger than those of the NH_3/H_2O mixture at 47 kg/(m^2·s) but smaller at 563 kg/(m^2·s) under the conditions of inlet NH_3 concentration (x_{in}) of 35%mol., inlet particle concentration (y_{PCM}) of 5%vol. and the heated wall temperature (T_{wall}) of 50°C. For a moderate inlet mass flux of 282 kg/(m^2·s), it is necessary to select a suitable value of the PCM melting temperature ($T_{melting}$) below 40°C for enhancing the heat dissipation.

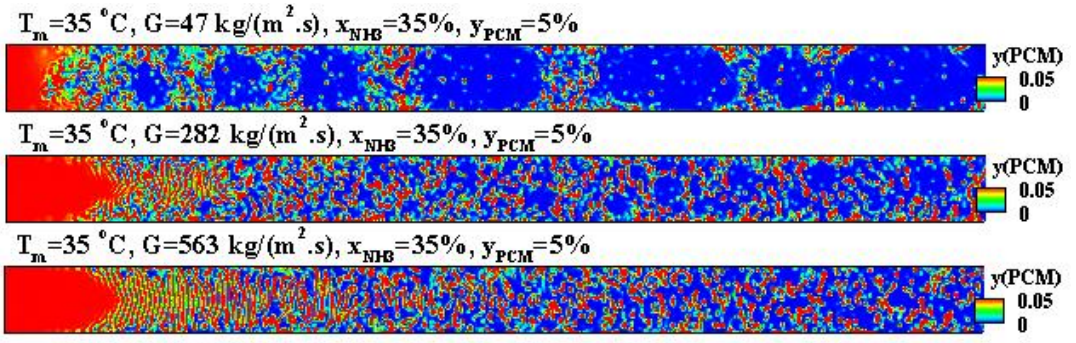
Figure.97 illustrates the effects of inlet mass flux (G_{in}) on the distribution of fluid temperature, the gaseous phase of the NH_3/H_2O mixture and the virtual phase of the PCM particle between the melting temperature ($T_{melting}$) of 35°C and the heated wall temperature (T_{wall}) of 50°C.



(a)



(b)



(c)

Figure.97 Effect of inlet mass fluxes on (a) fluid temperature, (b) vapors and (c) PCM distributions of NH_3/H_2O/PCM mixture flow boiling in microchannel at T_{wall} of 50 ℃

In order to provide a clear representation for the distributions of the gaseous phase, the virtual phase of the PCM particles and the melting areas of the PCM particles in the microchannel, some special treatments have been applied to the upper limit values in these aforementioned cloud charts in Figure.97. For the cloud chart of gas phase in Figure.97 (b), the upper limit of the vapor concentration (x_{NH3}) is set as unit. Consequently, the red region corresponds to the bubble area. For the cloud chart of the virtual PCM phase in Figure.97 (c), the upper limit of the particle concentration (y_{PCM}) is defined as the inlet concentration value of 5%vol.. As a result, the blue region in this chart roughly represents the area where PCM particles are absent, while the red region represents the areas that the concentration remains stable or aggregates, as the concentration is no less than the inlet value. For the cloud chart of the fluid temperature distribution in Figure.97 (a), the upper limit of fluid temperature (T) is chosen as the melting temperature ($T_{melting}$) of the PCM particles. Clearly, the red region indicates the area where the PCM particles can undergo the melting phase change, whereas the blue region represents the area where phase change cannot occur.

As introduced in Section 7.2, the liquid NH_3/H_2O/PCM mixture is treated as a Newtonian-like fluid and is divided into three distinct homogeneous phases: the liquid phase of the NH_3/H_2O mixture (Phase-l), the gaseous phase of the NH_3/H_2O mixture (Phase-g) and the virtual phase of the PCM particles (Phase-s). In this chapter, the inlet mixture in each case is in a subcooled state, which means that the volume fraction of gaseous phase (phase-g) at the inlet is set to 0. Moreover, the inlet PCM concentration (y_{PCM}) is determined by setting the volume fraction of

the virtual phase (Phase-s) to represent the suspension of particles in the mixture. Therefore, the flow boiling heat transfer of the NH_3/H_2O/PCM mixture could be explained as follows.

For the case of an inlet mass flux (G_{in}) of 282kg/(m^2·s) and a constant wall temperature (T_{wall}) of 50℃, it is the laminar flow near the entrance, since the corresponding inlet liquid Reynolds number is about 288. Consequently, the fluid temperature near the entrance remains relatively uniform, with a gradual increase near the walls, as depicted in Figure.97 (a). In this scenario, the virtual phase of the PCM particles (Phase-s) near the inlet continues to be uniform with a concentration (y_{PCM}) of 5%vol. as shown in Figure.97(c). When the fluid temperature near the walls reaches the saturation point of the NH_3/H_2O mixture, the nucleate boiling occurs on the heated surfaces, leading to the disruption (e.g., the fluid temperature) in the thermal boundary layer of the laminar flow shown in Figure.97(a). During the transient flow and heat transfer process, small bubbles start to grow, collide and merge with others, detach from the heated walls, and eventually exit the channel along with the bulk fluid. Meanwhile, these bubbles begin to occupy the positions previously held by the liquids of the NH_3/H_2O mixture and the particles, resulting in the particle aggregation and the completed disruption of flow field. For the same case before, the maximum values of velocity, liquid and gaseous Reynolds number in the fluid domain could reach 2.52 m/s, 2529 and 121910, respectively. Furthermore, when the fluid temperature (T) in the flow domain reaches the melting point ($T_{melting}$) as shown in Figure.97 (a), the PCM particles at that location will undergo the endothermic melting process. At this moment, the absorbed heat is described by the increase in specific heat capacity of the virtual PCM particle phase.

Generally, the PCM particle distribution is primarily determined by the evaporation degree of the NH_3/H_2O mixture. It indicates that the inlet mass flux (G_{in}) effect on the flow boiling heat transfer performance is complex mainly due to the mutual effects of flow patterns, the PCM locations and the melting degrees in the domain. For example, compared to the slug flow at an inlet mass flux of 47 kg/(m^2·s), the PCM particles are more uniformly suspended in fluid but with the fewer melting areas in the nucleated flow boiling at a mass flux of 563 kg/(m^2·s).

Basically, the PCM melting theoretically enhances the heat dissipation rate from hot surfaces, suppresses bubble collision and coalescence, decreases the vapor fraction in the domain (x_{fluid}), and directly improves heat transfer performance. However, it can also accelerate the bubble-wall adhesion effects due to the tendency of the small-size particles to be pushed towards thin boundary layers near walls during the bubble growth. As a result, this hinders the movement of small bubbles nucleated near the walls and flowing out along with the bulk in the channel. Consequently, the vapor fraction on hot surfaces (x_{wall}) increases, reducing the density of the active nucleation sites and the effective thermal conductivity (λ) of the NH_3/H_2O mixture. It is worth noting that the thermal conductivity of the gaseous saturated NH_3/H_2O mixture (λ_{vapor}) is smaller than that of the liquid-phase mixture (λ_{liquid}) at the same condition.

To accurately assess the potential heat transfer enhancement of the NH_3/H_2O/PCM mixture in microchannels at a heated wall temperature of 50°C, the values of heat flux (q_{wall})are plotted in Figure.98. While the cases A and case B represent single-phase convective flow and flow boiling heat transfer of the NH_3/H_2O mixture respectively, the cases C and case D correspond to the cases involving the PCM particles melting in the microchannel.

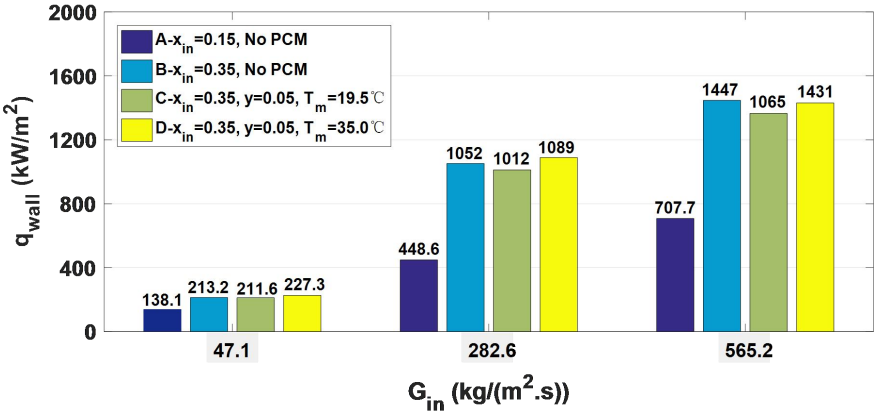


Figure.98 The overall heat fluxes comparison of the NH_3/H_2O/PCM mixture flow boiling with and without PCM melting in microchannel at a constant T_{wall} of 50 ℃

As depicted in Figure.98, the heat dissipation capacity could be significantly enhanced by considering the NH_3/H_2O mixture based functional fluids as alternative coolants to water for the cooling applications, particularly in the situation operating at a temperature below 100°C. Furthermore, the heat dissipation capacity experiences the further enhancement only when the

PCM particles fully melt in the NH_3/H_2O mixture during flow boiling, as observed in case D. However, the extent of improvement is limited. As observed in the results of R134a-based functional fluid flow boiling discussed in Chapter 5, the heat flux (q_{wall}) can be increased by selecting PCM materials with higher thermal conductivity and melting latent heat compared to those of the NH_3/H_2O mixture. The latent heat of the PCM particles is 201 kJ/kg, while that of the NH_3/H_2O mixture is 1443 kJ/kg at 1 bar.

In conclusion, the melting temperature ($T_{melting}$) impact on the heat transfer performance of the NH_3/H_2O/PCM mixture is primarily determined by its influence on the melting degree of the suspended PCM particles flowing through the microchannel. This melting degree, in turn, is affected by various factors, including inlet concentration of NH_3 (x_{in}), and the PCM (y_{PCM}), inlet mass flux (G_{in}), the heated wall temperature (T_{wall}) and the ratio of latent heat between the NH_3/H_2O evaporation and the PCM melting, among others.

7.4.2-Effect of the PCM melting latent heat

The effects of the melting latent heat (q_m) and inlet concentration (y or y_{PCM}) of the PCM particles on the heat flux (q_{wall}) at an inlet NH_3 concentration (x_{in}) of 35%mol. and a heated wall temperature (T_{wall}) of 50℃ are investigated in Figure.99. The melting temperature of the PCM particles is set as 1K.

It is observed in Figure.99 (a) that the overall heat flux (q_{wall}) exhibits an approximately linear enhancement with the increase in the melting latent (q_m) under the same conditions. Moreover, the rate of increase in the overall heat flux (q_{wall}) becomes higher with a larger inlet mass flux (G_{in}). For instance, when q_m is six times higher than the original PCM material as referenced in this study, and considering the same magnitude of NH_3/H_2O mixture boiling latent heat, the overall heat flux (q_{wall}) can be increased by 52.8% at a G_{in} of 47.1 kg/(m^2·s) and by 28.6% at a G_{in} of 565.2 kg/(m^2·s), with a PCM concentration of 5%vol.

Moreover, the heat flux (q_{wall}) can also be improved by increasing the PCM concentration (y), while keeping the heat flux (q_{wall}) constant (e.g., case D and E, case F and G) in Figure.99 (b). The enhancement of the heat flux (q_{wall}) becomes larger with higher values of inlet mass flux

(G_{in}) and/or the melting latent heat (q_m). Additionally, for cases with the same product of the PCM concentration (y) and the melting latent heat (q_m) (e.g., case E and F), the positive effect of the melting latent heat (q_m) on the heat flux (q_{wall}) is more pronounced than that of the concentration (y) at a lower inlet mass flux (G_{in}) (e.g., 47.1 kg/(m^2·s)), and the relative impact of the PCM concentration (y) becomes more significant with increasing inlet mass flux (G_{in}) (e.g., 565.2 kg/(m^2·s)). This observation is consistent with the previously discussed concept of the actual absorbed heat, which is closely related to the melting degree of the PCM particles suspended in the liquid/vapor mixture flowing through the microchannel.

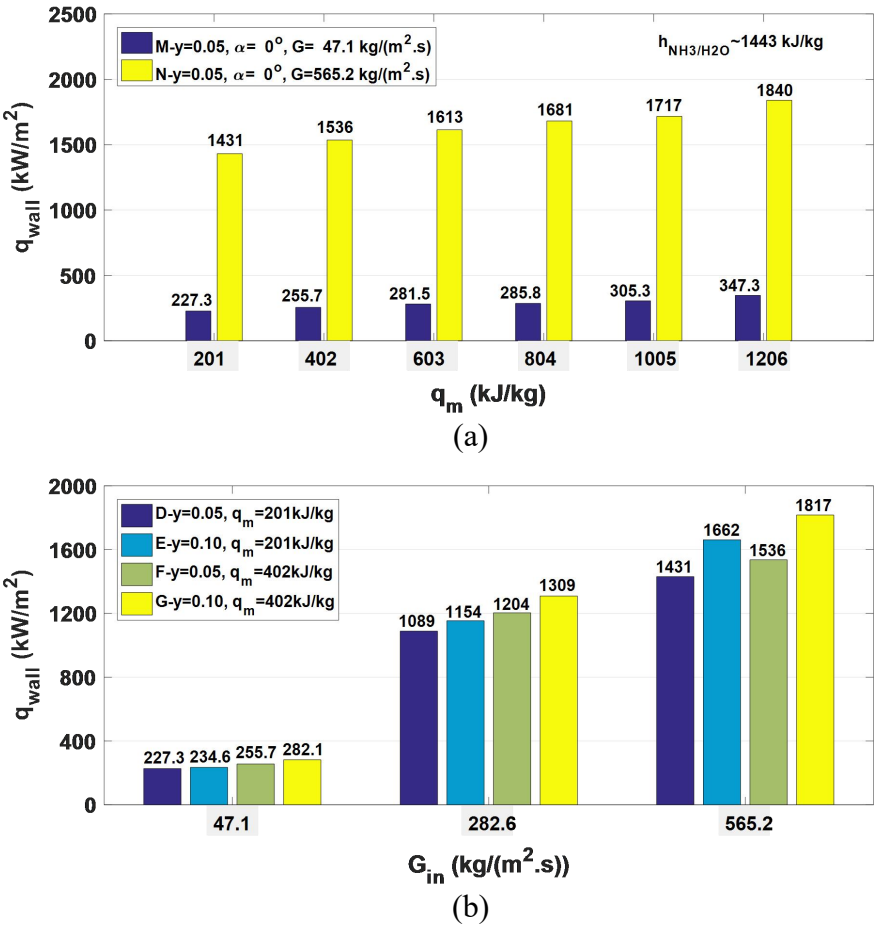


Figure.99 The overall heat fluxes comparison of the NH_3/H_2O/PCM mixture flow boiling at different (a) the melting latent heat and (b) inlet concentration of PCMs at a constant T_{wall} of 50 ℃

7.4.3-Effect of surface wettability

As reviewed in section 2.2.4, the surface wettability (i.e., contact angle) has important effects on flow boiling heat transfer performance in microchannel. For example, the HTC at low heat flux could be improved by reducing the wettability (i.e., increasing contact angle), while the CHF phenomenon could be delayed and therefore to improve the CHF at high heat fluxes by increasing it. Additionally, it is accepted that the nanosize particles deposited or coated on surfaces could also change the wettability in Figure.29. Therefore, the wettability effect on flow boiling heat transfer of NH_3/H_2O/PCM mixture will be investigated in this part. The contact angles of heating walls and PCM particles surfaces are set as 45°.

As discussed in section 2.2.4, the surface wettability, characterized by the contact angle, plays a crucial role in flow boiling heat transfer in microchannels. Lowering the wettability (i.e., increasing the contact angle) can improve the HTC at low heat fluxes, while increasing the wettability can delay the critical heat flux (CHF) phenomenon, thereby enhancing the CHF at high heat fluxes. Additionally, it is known that the wettability can be altered by depositing or coating nanosize particles on surfaces, as shown in Figure.29. In this section, the effect of wettability (represented by α) on the flow boiling heat transfer of the NH_3/H_2O/PCM mixture will be investigated. The contact angles of the heated walls and PCM particles are set to 45°.

The contact angle effects on the heat flux (q_{wall})and the HTC (h_{ave}) of the NH_3/H_2O/PCM mixture flow boiling at different melting temperature ($T_{melting}$) under the same conditions of inlet NH_3 concentration (x_{in}) of 35%mol., inlet PCM particle concentration (y) of 5%vol., inlet mass flux (G_{in}) of 82.6kg/(m^2·s) and heated wall temperature (T_{wall}) of 50℃ is shown in Figure.100.

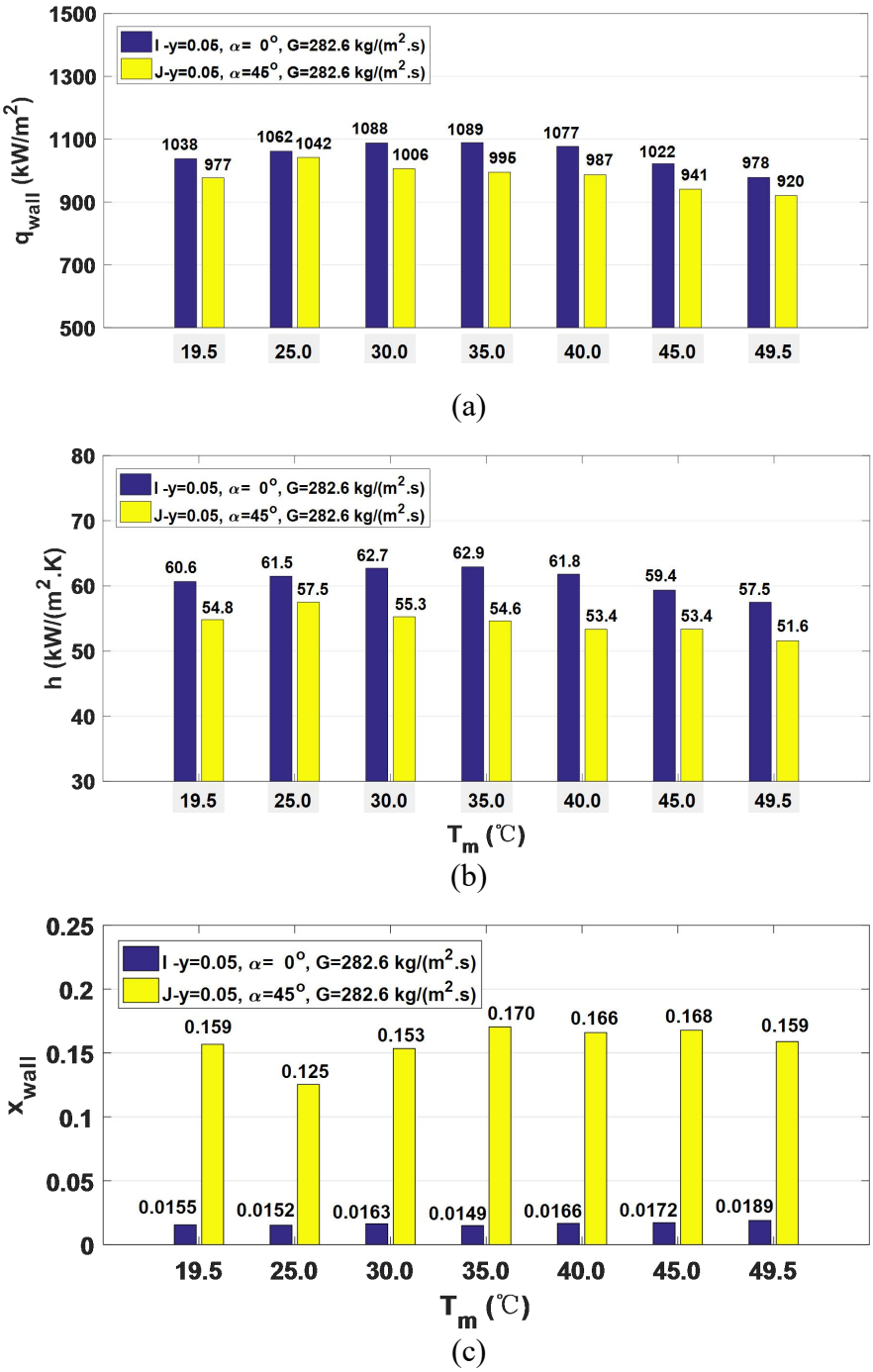


Figure.100 Effect of surface wettability on (a) the overall heat flux, (b) HTC and (c) vapor fraction on surfaces of NH_3/H_2O/PCM mixture flow boiling in microchannel at T_{wall} of 50 ℃

It is found that the increase of the contact angle (α) from 0° to 45° under the same conditions results in a decrease in the heat flux (q_{wall}) and the HTC (h_{ave}), while the vapor fraction on surfaces (x_{wall}) increases rapidly. For the hydrophobic surface (α=45°) at a temperature of

35°C, the heat flux (q_{wall}) and the HTC (h_{ave}) decrease by 8.6% and 13.2% respectively, while the vapor fraction on surfaces (x_{wall}) increases quickly from 1.5 to 17% by volume compared to the superhydrophilic surface at 0°. Some experimental studies in the literature [127,155,156] generally support the idea that increasing surface wettability (i.e., decreasing contact angle) can enhance flow boiling heat transfer performance, such as the CHF at high heat dissipation rates. The high-wettability surfaces (e.g., α=0°) exhibit strong liquid affinity, generate thin film boiling flow patterns, and effectively rewet hot surfaces under high heat flux conditions (q_{wall}). Therefore, the decrease in the heat flux (q_{wall}) shown in Figure.100 (a) by reducing the contact angle at a constant wall temperature (T_{wall}) leads to higher HTCs at high vapor quality conditions depicted in Figure.100 (b).

The distributions of bubbles (i.e., gaseous NH_3/H_2O) and PCMs are displayed in Figure.101.

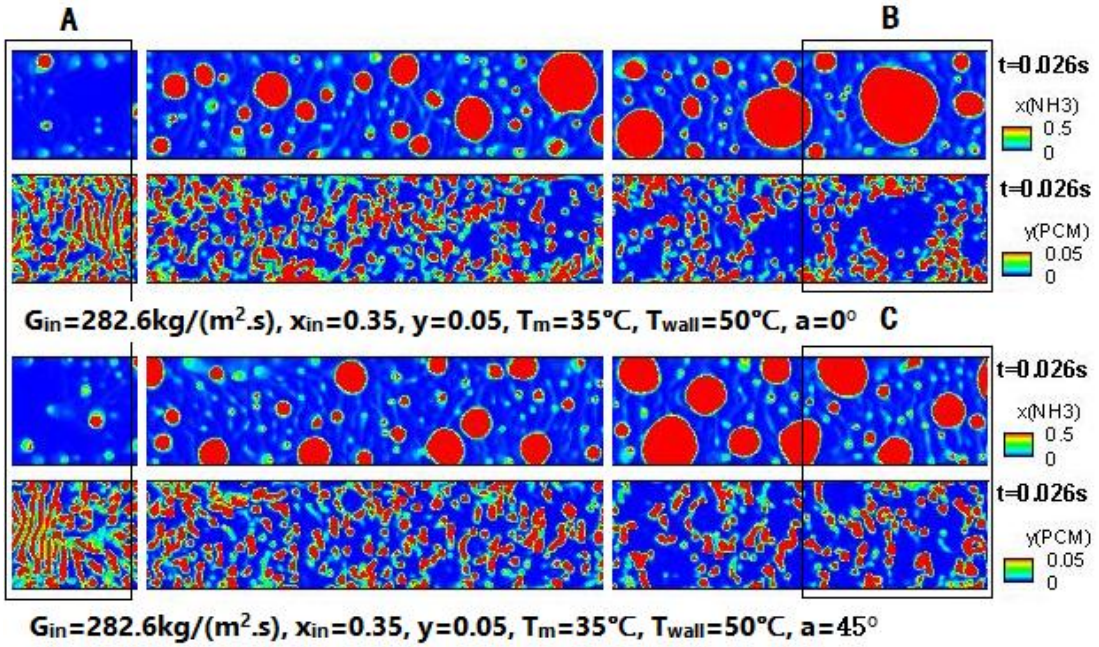


Figure.101 Distributions of bubbles and PCM in domain at different surface wettability conditions

It is evident that the spatial distributions of bubbles and the PCM particles near surfaces and in the domain strongly are strongly influenced with each other. During the initial evaporating stage of the NH_3/H_2O mixture (e.g., A), the particles are uniformly suspended throughout the domain. However, as the process progresses, they become unevenly dispersed within the liquid, occupying spaces between the large-sized bubbles and heating walls (e.g., B and C).

Consequently, the surface properties, such as wettability of the heating walls and particles, play a crucial role in determining the heat dissipation capacity by directly affecting the mutual interactions between the heating walls, bubbles and particles.

7.5-Summary

In this chapter, the multiphase flow heat transfer performance of NH_3/H_2O/PCM mixture was investigated by CFD methods based on basic assumptions, validations and results before. The effects of the melting temperature ($T_{melting}$) and the latent heat of PCM particle (q_m) as well as the surface wettability were evaluated comparatively. It is found that:

(1) There are both positive and negative effects on flow boiling heat transfer of the NH_3/H_2O mixture when PCM particles are added and undergo melting and movement in a microchannel. The endothermic phase change action of PCM melting can enhance the overall heat transfer capability. However, the presence of PCM particles sedimented on the heated surfaces can increase the vapor fraction on surfaces, thereby impeding heat transfer between the walls and coolants, especially under high heat flux conditions (e.g., low patterns of large-size bubbly, slug flow and partial dryout). Therefore, whether the inclusion of suspended PCM particles in the NH_3/H_2O mixture enhances the heat dissipation capability depends on finding a balance between the advantageous and adverse effects in practical conditions. For instance, a larger PCM melting latent heat and better surface wettability at high heat dissipation rates would result in a greater enhancement of the heat transfer performance. Conversely, an increase in the number and size of bubbles attached to the heating surfaces at the same temperature would lead to a deterioration in heat transfer performance.

(2) Furthermore, it is necessary to implement measures to ensure the PCM particles melted completely before exiting the heat sink. This can be achieved by optimizing the physical and practical parameters and aligning controllable variables (e.g., inlet mass flux) with the actual heat-dissipating requirements.

Chapter-8 Conclusion and future work

8.1 General conclusions

In conclusion, this study has introduced a promising approach to enhance flow boiling heat transfer performance in microchannels by using functional fluids as the coolants. Additionally, the heat transfer performance has been systematically compared and evaluated by numerical simulation methods. The main aim is to gain a comprehensive understanding of the critical factors influencing heat transfer performance and to devise effective strategies for improving thermal management in electronic devices and fuel cells. Through the evaluation of the heat transfer capabilities, the following findings have been established:

Chapter 1: Background

(1) The urgent requirement and limitations for cooling the advanced electronics and fuel cells is to dissipate the high-level non-uniform heat effectively for ensuring the peak temperature lower than 85℃ and maintaining the largest temperature difference of less than 30℃.

(2) Flow boiling of refrigerant in microchannels was chosen as an effective method according to the comprehensive experimental performance comparisons of available passive and active cooling approaches at the maximum temperature less than 85℃ in the literature. The addition of functional particles in coolants is a promising approach to further enhance the heat transfer performance of R134a and the NH_3/H_2O mixture flow boiling in microchannels.

Chapter 2: Literature review

(1) According to an extensive literature review on flow boiling heat transfer in microchannels, some methods including the modification of coolants, the structures and geometric parameters of sinks and the surfaces morphology were identified as the promising approaches for further enhancing flow boiling heat transfer performance individually or in combination.

(2) The VOF model, when combined with some specialized treatments, is generally accepted and adopted as a promising option for simulating flow boiling of pure fluid and single-phase convective heat transfer of functional fluids in microchannels. Consequently, it is selected to be hybrid utilized with the LEE model and the equivalent properties treatments of fluids for predicting multiphase flow heat transfer performance of functional fluids in microchannels.

Chapter 3: Simulation methods for multiphase flow heat transfer

(1) Based on some reasonable simplification and assumptions, these mathematic models and computational methods utilized in present study have been determined by theoretical analysis and comprehensive assessment, including the vapor-liquid equilibrium state, thermodynamic and transport properties of the NH_3/H_2O mixture, the capturing method of multiple interfaces (i.e., VOF), the mass and heat transfer models in the liquid-vapor interfacial surfaces (e.g., the LEE model for pure fluid, the modified LEE model for the zeotropic mixture), the melting of PCM materials (i.e., the enthalpy-porosity method and the equivalent heat capacity method), the initial and boundary conditions (e.g. dynamic meshing method and fully developed flows treatment at outlet). Furthermore, the warm start approach is utilized by using the convergent results of a steady-state single phase laminar flow as the initial conditions for the subsequent transient simulation of flow boiling heat transfer.

(2) All the relevant models and methods are compiled and processed using the User-Defined Function (UDF) approach in ANSYS.

Chapter 4: Flow boiling heat transfer of water with a PCM particle

(1) The impact of a PCM particle melting and moving on water flow boiling heat transfer in a vertical microchannel was explored through the utilization of by using the VOF, the enthalpy-porosity and dynamic meshing methods. The effects of surface wettability and particle density, along with the interactions between the particle and the surrounding fluid, were analyzed at various flow patterns to assess their influence on transient heat transfer performance.

(2) Surface wettability plays a significant role in influencing vapor fraction on heated surfaces, especially under high heat dissipation rates. This factor is crucial in affecting the heat transfer performance. Regarding a PCM particle, the melting and movement within a confined domain exert both beneficial and detrimental effects on the neighboring heat transfer performance during flow boiling in microchannels. While it could increase local heat dissipation due to the extra absorbed melting heat and local turbulence enhancement of a moving particle, it also has

risks to deteriorate the performance as the particle in a confined domain could impede bubbles departing from hot walls.

Chapter 5: Flow boiling heat transfer of R134a based functional fluid

(1) Multiphase flow heat transfer performance of R134a-based functional fluid was revealed in a horizontal microchannel. The effects of particle properties and some thermal parameters on the heat transfer performance were comparatively investigated and discussed by the VOF-LEE and the effective heat capacity methods.

(2) Flow boiling HTCs of R134a in microchannels could be enhanced by adding functional particles with different mechanisms related to the particle types. While the equivalent thermal conductivity of coolants could be enhanced by adding functional particles with high thermal conductivity, flow boiling patterns could be shifted to that with a higher HTC (e.g., from slug flow to nucleated flow at the same heat flux) by the melting of PCM particles. Differently, the pressure drops could be increased as the increment of fluid viscosity by adding particles, but it also could be declined significantly attributed to the favorable flow pattern changes induced by adding the melting latent particles. The FOMs of latent heat functional fluids (e.g., PCM emulsion and slurries) were greater than those of the non-melting fluids (e.g., nanofluid) at the same conditions, indicating that the additions of PCM particles in R134a could increase the heat transfer performance comprehensively.

Chapter 6: Flow boiling heat transfer of the NH_3/H_2O mixture

(1) The non-isothermal flow boiling of the NH_3/H_2O mixture in a horizonal microchannel was investigated by adopting a novel simplified calculating approach (i.e., the VOF-modified LEE model coupled with the quasi-ideal properties treatment of NH_3/H_2O). The proposed approach was validated with the published experimental data (i.e., the HTCs and flow patterns) of the R134a/R245fa mixture flow boiling in microchannels.

(2) It is found that there is existing a threshold value of inlet NH_3 concentration to maintain a certain of heat dissipation rate at a given inlet mass flux and a maximum heated temperature.

For a case with an inlet mass flux at 552 kg/(m^2·s) and an NH_3 concentration at 35%mol., the overall and the local heat fluxes could reach up to 1.41 and 1.52 MW/m^2, respectively.

(3) Flow boiling of the NH_3/H_2O mixture obeys classic flow boiling characteristics of pure coolants except for the non-isothermal phase change feature. There is no local dry-out existed in microchannels in present study. Therefore, the NH_3/H_2O mixture could delay local dry-out at a high heat dissipation and is a promising coolant for maintaining a certain temperature of electronic components.

Chapter 7: Flow boiling heat transfer of the NH3/H2O/PCM slurries

(1) The multiphase flow heat transfer performance of a NH_3/H_2O/PCM mixture was evaluated in a horizontal microchannel. The effects are taken into consideration including the melting temperature and melting latent heat of PCM materials, inlet concentrations of PCM particles and NH_3, and the surface wettability, etc.

(2) Similar to that of R134a based functional fluid, there are positive and negative effects on flow boiling heat transfer performance of the NH_3 /H_2O mixture by adding PCM particles. Furthermore, it is necessary to take measures to ensure the PCM particles melted completely before exiting the sink, such as optimizing particle properties (e.g., the melting temperature) and thermal parameters (e.g., inlet concentrations of NH_3 and particles), as well as matching the controllable variables (e.g., mass flux) with the actual heat-dissipating demands.

In general, the utilization of flow boiling heat transfer of the NH_3/H_2O mixture and functional fluids (characterized with high thermal conductivity and melting latent heat) in microchannels is promising for cooling the high-heat dissipation electronic devices and fuel cells under the operational temperature below 85℃. However, it also has inherent risks that could potentially compromise cooling performance. Therefore, it is necessary to take measures to mitigate the adverse cases occurred in applications such as the non-melted particles exiting the sinks and the deposition of particles on the heated surfaces.

8.2 Future work

Building upon the investigation conducted in this study, the evaluation of multiphase flow heat transfer performance of functional fluids in microchannels was accomplished by the CFD method grounded in some rational assumptions and simplified treatments. In order to gain a deeper comprehension of the interactive mechanisms governing multiphase flow heat transfer performance in microchannels and to provide more advanced thermal management solutions for cooling electronics and fuel cells, the suggestions for future research, encompassing both experimental and numerical studies, are listed as follows.

Experimental test aspects

The primary objective of future experimental work is to validate the results obtained through the CFD method in this study and to achieve reliable outcomes regarding the multiphase flow heat transfer performance of functional fluids in microchannels. To achieve this, the design and construction of an experimental setup are crucial. It should have the capability:

(1) To accurately measure the dominant transient and spatial parameters (e.g., the velocity and temperature) within the nano/micro-scale spaces without interrupting the original flow.

(2) To capture the entire processes of the bubble formation and development in different flow patterns, including the nucleation near the entrance, growth, elongation, collision, coalescence and the departure from the domain.

The proposed experimental work should encompass the analysis of individual and combined effects of various factors (e.g., the geometric parameters and functional fluids) in a broader range of parameters and conditions on heat transfer performance and flow pattern.

Numerical simulation aspects

The refinement and optimization of the mathematical models and calculating methods should be pursued to increase their accuracy and predictive capabilities, leading to more reliable and effective simulations. For flow boiling of the NH_3/H_2O mixture with functional particles in microchannels, it is noteworthy to consider the effects of species diffusion, bubble nucleation

and department in the boundary layers of the mixture, the mutual effects of particles with bubbles and walls, as well as the mass and heat transfer in multiphase interfaces.

Appendix-1 Flow boiling heat transfer in literature

Table.23 Flow boiling heat transfer in microchannel (T_{wall} <85 ℃) -Experimental literature review

Shape	T_{wall}	T_{in}	T_{sat}	W×H-L	G	q	dP	year
	℃	℃	℃	μm×μm-mm	kg/(m^2.s)	W/cm^2	kPa	
FC-72								
Straight	66.3	54.1	56.1	225×276-16	531	12.8	/	2012 [148]
Straight	81.0	23.3	56.5	220× 55-10	578	32.8	67	2019 [57]
Straight	83.2	23.3	56.5	220× 55-10	2311	65.7	109	2019 [57]
Straight fins	83.8	29.5	/	350×1190-25	349	38.4	3.0	2015 [149]
Oblique fins	70.7	26.5	56.5	300×1190-25	394	70.4	5.8	2016 [58]
Oblique fins	82.2	29.5	/	340×1170-25	349	59.1	5.1	2015 [149]
HFE7100								
Straight	76.0	54.6	59.6	700×350-25	250	33.5	/	2019 [151]
Straight	78.9	25.0	61.0	220× 52-10	1561	46.8	37	2021 [152]
Straight	83.8	25.0	61.0	220×250-10	1600	57.0	/	2018 [153]
Straight	84.5	15.0	61.0	200×573-20	550	37.9	/	2021 [59]
Straight	83.1	0.0	63.0	260×1041-10	1682	278.3	7.4	2008 [60]
Manifold	68.7	35.0	61.0	60×250-0.8	1290	140.4	52.2	2020 [307]
Nano structured	82.6	25.0	61.0	220×250-10	1300	111.8	/	2018 [153]
Micro cavities	74.4	18.0	61.0	200×250-10	1155	175.2	/	2018 [61]
R134a								
Straight	43.6	20.0	29.1	381×953-9.5	334	29.5	/	2009 [186]
Straight	38.5	/	32.2	500×500-45	994	43.6	/	2019 [308]
Straight	35.3	28.0	28.0	470×382-30	1200	48.7	/	2018 [185]
Straight	30.0	/	24.0	300×700-20	300	28.7	/	2017 [309]

Straight	34.8	15.0	25.0	100×500-15	400	30.5	/	2013 [62]
Straight	28.3	20.0	20.0	382×470-40	1000	52.4	/	2020 [310]
Straight	85.0	22.0	25.0	199×756-39	3000	197.7	/	2010 [63]
R245fa								
Straight	52.1	20.0	26.0	381×953-9.5	334	27.6	/	2009 [186]
Straight	38.0	25.0	30.0	123×494-15	500	23.8	18.7	2015 [311]
Straight	39.5	20.0	30.0	123×494-15	300	28.4	/	2015 [311]
Pin fins microgap	84.4	13.0	/	200×200-11	2632	148.5	201.4	2018 [312]
Pin fins microgap	84.1	13.0	/	200×200-11	7896	219.0	450	2018 [312]

Table.24 Single phase convection in microchannel (T_{wall} <85 ℃) -Experimental literature review

Shape	T_{wall}	T_{in}	T_{sat}	W×H-L	G	q	dP	year
	℃	℃	℃	μm×μm-mm	kg/(m^2.s)	W/cm^2	kPa	
Air								
Radical micro	80	20	/	10×40-D4	/	4.5	345	2008 [313]
H_2O								
Micro-slot	84.9	22.0	100	200×250-10	430	105.5		2020 [39]
Plain	82.4	30.0	100	80×200-10	815	108.9	39.2	2021 [40]
Straight	67.0	30.0	100	1000×490-40	1188	32.7	3.7	2019 [41]
Nanowire Manifold	81.7	35.0	100	250×250-/	1250	79.3		2019 [42]
Interconnected	85.0	60.0	100	80×200-10	963	56.0		2021 [43]
Groove	80.7	60.0	100	80×200-10	815	39.1	13.2	2021 [40]

Table.25Heat transfer performance of water heat pipes (T_{wall} <85 ℃) -Experimental literature review

Types	T_{wall}	T_{in}	Shape and size	q	Q	R	year
	℃	℃	/	W/cm^2	W	℃/W	
Air-based HP	35.0	27.7	4 U-shape, 8mm	9.4	150	0.074	2020 [314]

Air-based embedded HP	63.5	25.0	3 U-shape	85.0	/	0.170	2017 [315]
Air-based sintered wick HP	41.4	30.0	10cm×8cm	81.6	360	0.032	2011 [316]
Ultra-thin plate HP	57.0	25.0	12cm×12cm	22.7	160	0.156	2019 [317]

Table.26 Heat transfer of two phase impingement (T_{wall} <85 ℃) -Experimental literature review

Shape	Twall	Tin	Tsat	H	dj	q	dP	Other	year
	℃	℃	℃	mm	mm	W/cm^2	kPa		
FC-72									
Smooth	68.9	47.0	50.0	5	0.24	40.8	241	Re4977	2011 [47]
Pin fins	63.8	47.0	50.0	5	0.24	84.5	241	Re4977	2011 [47]
Smooth	82.2	21.0	56.0	/	/	77.8	/	2m/s	2011 [49]
Submerged pin fins	75.2	21.0	56.0	/	/	166.5	/	2m/s	2011 [49]
Microchannel	68.4	30.0	50.0	1.5	0.24	133.0	/	450ml	2014 [50]
H_2O									
Smooth-0.176bar	85.0	57.3	57.3	H/dj=6		76.7		Re8844	2012 [318]
Smooth-0.176bar	85.0	40.3	57.3	H/dj=6		162.2		Re5966	2012 [318]
HFE7100									
Smooth	68.0	56.0	61.0	20	0.76	69.0	210	7.15cc/s	2014 [51]
Minichannel	81.6	0.0		3	0.3	285.6	16.7	23.3cm^3/s	2009 [53]
Pin fins	78.5	51.0	61.0	2.5	0.75	77.2	1.7	10.5g/s	2015 [52]
Pin fins & Porous	69.0	51.0	61.0	2.5	0.75	95.4	2.7	10.5g/s	2015 [52]
R134a									
Submerged micro jet	67.3	20.1	29.1	4.7	2.1	218.6	/	4m/s	2021 [319]
Submerged micro jet	55.2	17.0	47.0	/	0.11	335.0	/	10m/s	2010 [48]
Smooth	42.5	26.0	31.0	/	2.0	113.7	/	4m/s	2012 [46]
Circular micro pins	44.5	26.0	31.0	/	2.0	209.0	/	2.2m/s	2012 [46]
Hydrofoil micro pins	68.6	26.0	36.0	/	2.0	277.1	/	1.7m/s	2012 [46]

R245fa									
Pin fins & Porous	61.1	40.0	45.0	0.5	0.75	218.0	6.4	/	2017 [320]
Flat porous	57.2	40.0	45.0	0.5	0.75	145.3	4.1	/	2017 [320]

Table.27 Heat transfer of two phase spray cooling (T_{wall} <85 ℃) -Experimental literature review

Shape	Twall	Tin	Tsat	H	dj	q	dP	Other	year
	℃	℃	℃	mm	mm	W/cm^2	kPa		
FC-72									
Multi-nozzle plate	77.8	>51	53.0	9	3.18	50.3	241	/	2003 [321]
Smooth flat	85.0	23.5	56.0	10	0.20	59.6	/	0.67cm^3/s	2006 [322]
H2O									
Sinlge-nozzle-30°	84.7	28.0	100.0	2	/	250.4	500	5.2L/h	2010 [37]
Flat	80.3		100.0	15	1.0	178.5	/	41.6L/h	2013 [323]
Micro groove-30°	81.0		100.0	15	1.0	267.9	/	41.6L/h	2013 [323]
HFE7100									
Plain	79.9	30.4	60.4	9.4	0.76	44.3	/	4.7cm^3/s	2014 [324]
Micro porous	74.1	30.4	60.4	9.4	0.76	140.7	/	4.7cm^3/s	2014 [324]
Horizontal fins-75°	51.1	16.0	61.0	80	0.4	81.6	/	5.2L/h	2015 [325]
Vertical fins-75°	57.8	16.0	61.0	80	0.4	56.0	/	5.2L/h	2015 [325]
R134a									
Smooth flat	44.2	/	10.0	8.8	0.3	8.8	123.5	480.0	2013 [326]
Square pins flat	44.8	/	10.0	7.8	0.3	7.8	211.7	480.0	2013 [326]
Rough surface	47.6	20.3	20.3	12	0.76	12	167.1	107.0	2013 [327]

Table.28 Single phase convection of air and water in microchannel (T_{wall} <85 ℃) -Experimental literature review

Shape	T_{wall}	T_{in}	T_{sat}	W×H-L	G	q	dP	year
	℃	℃	℃	μm×μm-mm	kg/(m^2.s)	W/cm^2	kPa	
Air								
Radical micro	80	20	/	10×40-D4	/	4.5	345	2008 [313]
H_2O								

Appendix-1 Flow boiling heat transfer in literature

Patterned	79.5	24.0	100	750×200-20	203	53.2		2019 [328]
Micro-slot	84.9	22.0	100	200×250-10	430	105.5		2020 [39]
Plain	82.4	30.0	100	80×200-10	815	108.9	39.2	2021 [40]
Straight	67.0	30.0	100	1000×490-40	1188	32.7	3.7	2019 [41]
Nanowire Manifold	81.7	35.0	100	250×250-/	1250	79.3		2019 [42]
Interconnected	85.0	60.0	100	80×200-10	963	56.0		2021 [43]
Groove	80.7	60.0	100	80×200-10	815	39.1	13.2	2021 [40]

Appendix-2 Calculation mathematical model of NH_3/H_2O mixture

A2.1-Vapor-liquid equilibrium and thermodynamic properties

Assuming gas phase is an ideal mixture of real components, the specific enthalpy $h_g(T,y)$ can be calculated from the enthalpy of pure ammonia and water.

$$h_g(T,y) = (1-w)\cdot h_w(T,p) + w\cdot h_A(T,p) \tag{A2-1}$$

$$w = \frac{yM_A}{yM_A + (1-y)M_W} \tag{A2-2}$$

The value corresponding to the phase equilibrium state has to be substituted for pressure. The functions reproducing the selected experimental data are shown as the following structure:

$$T(p,x) = T_0 \sum_i a_i (1-x)^{m_i} \left[ln\left(\frac{p_0}{p}\right)\right]^{n_i} \tag{A2-3}$$

$$T(p,y) = T_0 \sum_i a_i (1-y)^{m_i/4} \left[ln\left(\frac{p_0}{p}\right)\right]^{n_i} \tag{A2-4}$$

$$y(p,x) = 1 - exp\left[ln\,(1-x) \sum_i a_i \left(\frac{p}{p_0}\right)^{m_i} x^{n_i/3}\right] \tag{A2-5}$$

$$h_l(T,x) = h_0 \sum_i a_i \left(\frac{T}{T_0} - 1\right)^{m_i} x^{n_i} \tag{A2-6}$$

$$h_g(T,y) = h_0 \sum_i a_i \left(1 - \frac{T}{T_0}\right)^{m_i} (1-y)^{n_i/4} \tag{A2-7}$$

Where, h and M are specific enthalpy (kJ/kg) and molar weight (kg/mol), p and T are pressure (MPa) and temperature (K), x and y are the ammonia mole fraction in the liquid and gaseous phases, respectively.

Table.29 Parameters of T(p,x) and T(p,y)

$T(p,x)=T_0\sum_i a_i(1-x)^{m_i}\left[ln\left(\frac{p_0}{p}\right)\right]^{n_i}$				$T(p,y)=T_0\sum_i a_i(1-y)^{m_i/4}\left[ln\left(\frac{p_0}{p}\right)\right]^{n_i}$			
i	m_i	n_i	a_i	i	m_i	n_i	a_i
1	0	0	+0.322302e+1	1	0	0	+0.324004e+1
2	0	1	-0.384206e0	2	0	1	-0.395920e0
3	0	2	+0.460965e-1	3	0	2	+0.435624e-1
4	0	3	-0.378945e-2	4	0	3	-0.218943e-2
5	0	4	+0.135610e-3	5	1	0	-0.143526e+1
6	1	0	+0.487755e0	6	1	1	+0.105256e+1
7	1	1	-0.120108e0	7	1	2	-0.719281e-1
8	1	2	+0.106154e-1	8	2	0	+0.122362e+2
9	2	3	-0.533589e-3	9	2	1	-0.224368e+1
10	4	0	+0.785041e+1	10	3	0	-0.201780e+2
11	5	0	-0.115941e+2	11	3	1	+0.110834e+1
12	5	1	-0.523150e-1	12	4	0	+0.145399e+2
13	6	0	+0.489596e+1	13	4	2	+0.644312e0
14	13	1	+0.421059e-1	14	5	0	-0.221246e+1
				15	5	2	-0.756266e0
				16	6	0	-0.135529e+1
				17	7	2	+0.183541e0
$T_0=100K,\ p_0=2\text{MPa}$				$T_0=100K,\ p_0=2\text{MPa}$			

Table.30 Parameters of y(p,x)

$$y(p,x)=1-exp\left[ln(1-x)\sum_i a_i\left(\frac{p}{p_0}\right)^{m_i}x^{n_i/3}\right]$$

i	m_i	n_i	a_i	i	m_i	n_i	a_i
1	0	0	+1.98022017e+1	8	3	2	-3.42198402e+3
2	0	1	-1.18092669e+1	9	4	3	+1.19403127e+4
3	0	6	+2.77479980e+1	10	5	4	-2.45413777e+4
4	0	7	-2.88634277e+1	11	6	5	+2.91591865e+4
5	1	0	-5.91616608e+1	12	7	6	-1.84782290e+4
6	2	1	+5.78091305e+2	13	7	7	+2.34819434e+1
7	2	2	-6.21736743e0	14	8	7	+4.80310617e+3
$p_0=2\text{MPa}$							

Table.31 Parameters of $h_l(T,x)$ and $h_g(T,y)$

$h_l(T,x)=h_0\sum_i a_i\left(\frac{T}{T_0}-1\right)^{m_i}x^{n_i}$				$h_g(T,y)=h_0\sum_i a_i\left(1-\frac{T}{T_0}\right)^{m_i}(1-y)^{n_i/4}$			
i	mi	ni	ai	i	mi	ni	ai
1	0	1	-0.761080e+1	1	0	0	+0.128827e+1
2	0	4	+0.256905e+2	2	1	0	+0.125247e0
3	0	8	-0.247092e+3	3	2	0	-0.208748e+1
4	0	9	+0.325952e+3	4	3	0	+0.217696e+1
5	0	12	-0.158854e+3	5	0	2	+0.235687e+1
6	0	14	+0.619084e+2	6	1	2	-0.886987e+1
7	1	0	+0.114314e+2	7	2	2	+0.102635e+2
8	1	1	+0.118157e+1	8	3	2	-0.237440e+1
9	2	1	+0.284179e+1	9	0	3	-0.670515e+1
10	3	3	+0.741609e+1	10	1	3	+0.164508e+2
11	5	3	+0.891844e+3	11	2	3	-0.936849e+1
12	5	4	-0.161309e+4	12	0	4	+0.842254e+1
13	5	5	+0.622106e+3	13	1	4	-0.858807e+1
14	6	2	-0.207588e+3	14	0	5	-0.277049e+1
15	6	4	-0.687393e+1	15	4	6	-0.961248e0
16	8	0	+0.350716e+1	16	2	7	+0.988009e0
				17	1	10	+0.308482e0
$h_0=100\text{kJ}\cdot\text{kg}^{-1}, T_0=273.16K$				$h_0=1000\text{kJ}\cdot\text{kg}^{-1}, T_0=324K$			

Table.32 Comparison between reference data and calculated results

P	x	T	T_{cal}	dT	h_{liq}	$h_{liq,cal}$	dh_{liq}	h_{gas}	$h_{gas,cal}$	dh_{gas}
MPa		℃	℃	%	kJ/kg	kJ/kg	%			%
2.0	0.111	180.0	180.7	0.15	691.9	698.6	0.96	2200.0	2201.7	0.08
	0.152	170.0	170.1	0.01	621.8	627.5	0.90	2039.0	2044.3	0.26
	0.191	160.0	160.5	0.11	557.8	566.1	1.48	1920.2	1927.3	0.37
	0.232	150.0	150.5	0.12	496.9	504.0	1.42	1818.0	1824.0	0.33
	0.277	140.0	139.9	0.02	432.9	438.6	1.31	1728.0	1729.3	0.07
	0.319	130.0	130.3	0.06	372.0	379.8	2.11	1661.5	1654.9	0.40
	0.364	120.0	120.4	0.11	314.1	321.4	2.32	1607.6	1589.5	1.14
	0.413	110.0	110.3	0.07	259.3	264.0	1.84	1565.3	1532.4	2.14
0.002	0.212	-30.0	-30.3	0.12	-281.8	-285.1	1.17	1294.3	1293.2	0.08
	0.283	-40.0	-39.7	0.12	-367.1	-369.1	0.56	1252.2	1238.3	1.12
0.006	0.132	0.0	0.3	0.12	-95.8	-98.3	2.67	1483.8	1476.7	0.49
	0.193	-10.0	-9.7	0.11	-184.1	-184.8	0.35	1367.0	1354.0	0.96
	0.257	-20.0	-19.4	0.25	-266.4	-267.6	0.44	1314.9	1289.3	1.99

A2.2-Mixture critical temperature and pressure

$$T_{c,m} = \sum_{i=0}^{4} a_i x^i \qquad p_{c,m} = \sum_{i=0}^{4} b_i x^i \qquad \text{(A2-8)}$$

Table.33 Data of the mentioned constant factors

i	0	1	2	3	4
a_i	647.14	-199.822371	109.035522	-239.626217	88.689691
b_i	220.64	-37.923795	36.424739	-41.851597	-63.805617

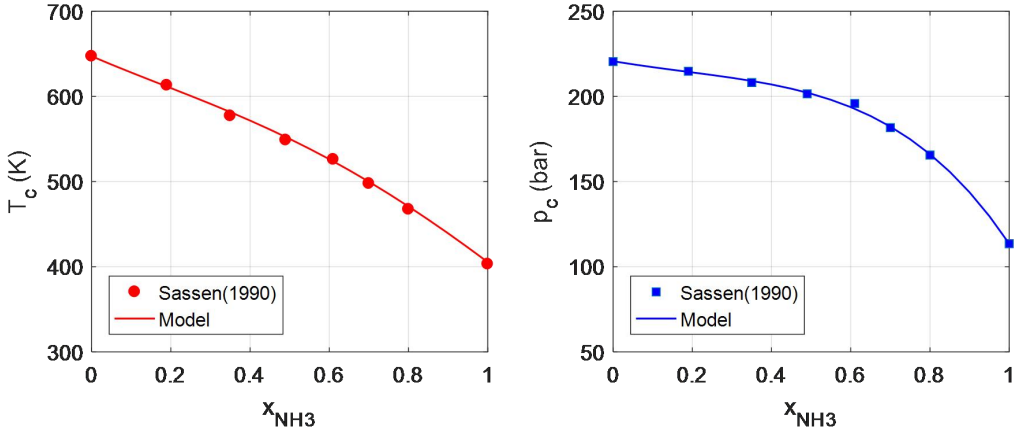


Figure.102 Comparisons between the mentioned calculated and experimental data

A2.3-Specific thermal capacity of saturated liquid mixtures at constant pressure

$$c_{pm}(T^*, x) = x c_{p_{\mathrm{NH_3}}}\left(T^*_{\mathrm{NH_3}}\right) + (1-x) c_{pH_2O}\left(T^*_{H_2O}\right) \qquad \text{(A2-9)}$$

$$c_p(T^*) = A_{cp} + B_{cp}\tau^{-1} \qquad \text{(A2-10)}$$

$$\tau = 1 - \theta = 1 - \frac{T^*}{T_c} \qquad \theta = \frac{T_m}{T_{c,m}} = \frac{T^*_{\mathrm{NH_3}}}{T_{c,\mathrm{NH_3}}} = \frac{T^*_{H_2O}}{T_{c,H_2O}}$$

$$T^*_{\mathrm{NH_3}} = T_{c,\mathrm{NH_3}} \cdot \theta = T_m \cdot \frac{T_{c,\mathrm{NH_3}}}{T_{c,m}} \qquad T^*_{H_2O} = T_{c,H_2O} \cdot \theta = T_m \cdot \frac{T_{c,H_2O}}{T_{c,m}}$$

Table.34Data of the mentioned constant factors

	A_{cp}	B_{cp}		A_{cp}	B_{cp}
NH_3	3.875648	0.242125	H_2O	3.665785	0.236312

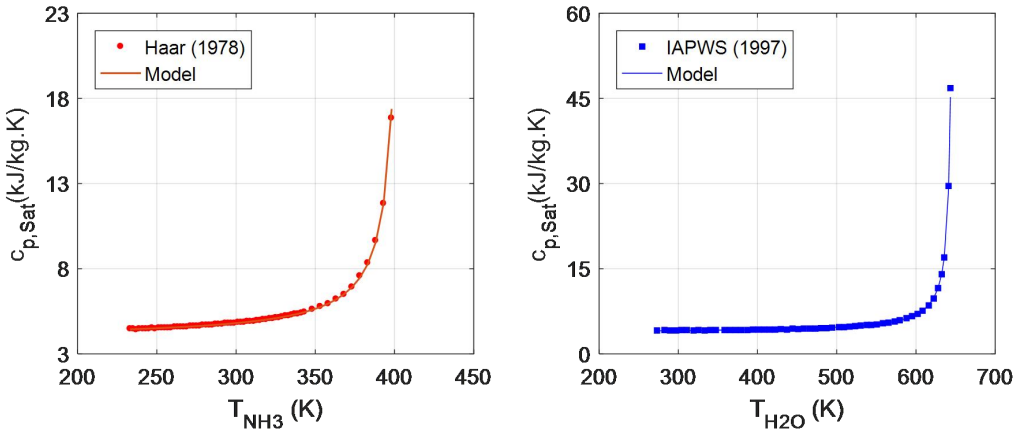


Figure.103 Comparisons between the mentioned calculated and experimental data

A2.4-Thermal conductivity of liquid mixtures

A formulation for a quasi-ideal mixture is proposed on the basis of the corresponding values of thermal conductivity of pure substances.

$$\lambda_m = x\lambda_{\mathrm{NH_3}}\left(\rho^{+}_{\mathrm{NH_3}}\right) + (1-x)\lambda_{H_2O}\left(T^{*}_{H_2O}\right) \tag{A2-11}$$

$$\rho^{+}_{\mathrm{NH_3}} = \rho_{\mathrm{NH_3}}\left(T^{*}_{\mathrm{NH_3}}\right)x^{0.425} \tag{A2-12}$$

$$\lambda_{\mathrm{NH_3}}\left(\rho^{+}_{\mathrm{NH_3}}\right) = \sum_{i=0}^{7} a_i \left(\rho^{+}_{\mathrm{NH_3}}\right)^i \qquad \lambda_{\mathrm{NH_3}}\left(T^{*}_{H_2O}\right) = \sum_{i=0}^{7} b_i \left(T^{*}_{H_2O}\right)^i \tag{A2-13}$$

Table.35 Data of the mentioned constant factors

i	a_i	b_i
0	+4.337955277951E+01	+1.393817844866E+04
1	+2.977570649380E-01	-2.290029884326E+02
2	+1.201385831428E-03	+1.574616703210E+00
3	+6.690272416636E-06	-5.703760390821E-03
4	-6.385698179523E-08	+1.186140465478E-05
5	+1.748929658112E-10	-1.418455074425E-08
6	-1.993882238051E-13	+8.992400966905E-12
7	+8.431881950442E-17	-2.310804485420E-15

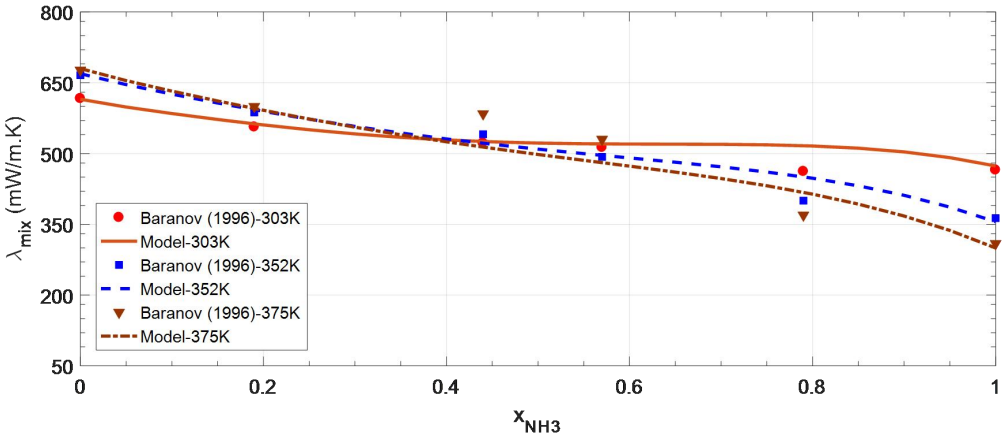


Figure.104 Comparisons between the mentioned calculated and experimental data

A2.5-Dynamic viscosity of liquid mixtures

$$\ln\mu_m = x \cdot \ln\mu_{\mathrm{NH_3}}\left(T^*_{\mathrm{NH_3}}\right) + (1-x)\mu_{H_2O}\left(T^*_{H_2O}\right) + \Delta\mu_{mix,x} \tag{A2-14}$$

$$\Delta\mu_{mix,x} = \left(0.534 - 0.815\frac{T_m}{T_{c,H_2O}}\right) \cdot F(x) \tag{A2-15}$$

$$F(x) = 6.38 \cdot (1-x)^{1.125x} \cdot \left[1 - e^{-0.585x(1-x)^{0.18}}\right] \cdot ln\left[\mu^{0.5}_{\mathrm{NH_3}}\left(T^*_{\mathrm{NH_3}}\right) \cdot \mu^{0.5}_{H_2O}\left(T^*_{H_2O}\right)\right] \tag{A2-16}$$

$$\eta_{\mathrm{NH_3}}\left(T^*_{\mathrm{NH_3}}\right) = \sum_{i=0}^{7} a_i\left(T^*_{\mathrm{NH_3}}\right)^i \qquad \eta_{H_2O}\left(T^*_{H_2O}\right) = \sum_{i=0}^{7} b_i\left(T^*_{H_2O}\right)^i \tag{A2-17}$$

Table.36 Data of the mentioned constant factors

i	a_i	b_i
0	+1.313855631536E+05	+6.553381577055E+05
1	-2.963607788649E+03	-9.797988524738E+03
2	+2.898320250404E+01	+6.252789912829E+01
3	-1.582768545381E-01	-2.203671360114E-01
4	+5.194840712025E-04	+4.627538225879E-04
5	-1.022531596503E-06	-5.786969589318E-07
6	+1.116009925788E-09	+3.989469497756E-10
7	-5.204716001922E-13	-1.169518240457E-13

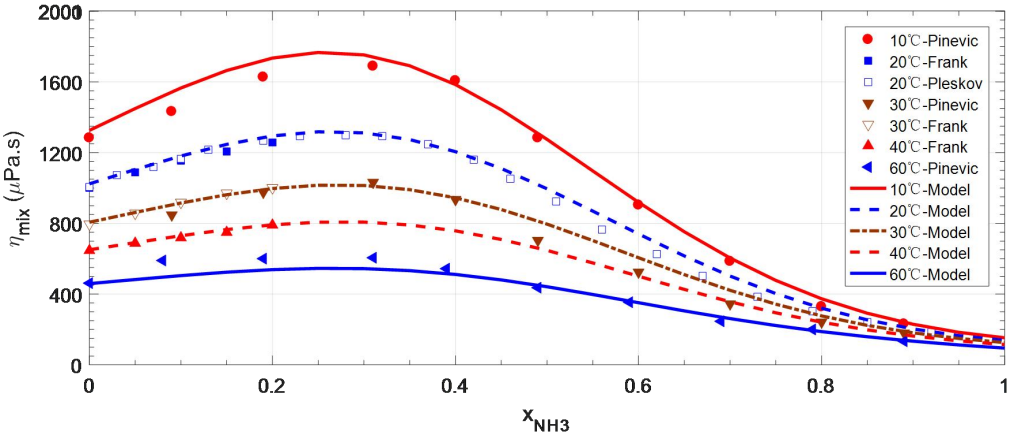


Figure.105 Comparisons between the mentioned calculated and experimental data

A2.6 Liquid Mixture density

$$\rho_m = x \cdot \rho_{\mathrm{NH_3}}\left(T^*_{\mathrm{NH_3}}\right) + (1-x) \cdot \rho_{H_2O}\left(T^*_{H_2O}\right) \tag{A2-18}$$

$$\rho_L = \rho_c \cdot \sum_{i=0}^{6}\left(A_i \cdot \tau^{b_i}\right) \qquad \tau = 1 - \theta = 1 - \frac{T^*}{T_c} \qquad \theta = \frac{T_m}{T_{c,m}} = \frac{T^*_{\mathrm{NH_3}}}{T_{c,\mathrm{NH_3}}} = \frac{T^*_{H_2O}}{T_{c,H_2O}}$$

	H_2O			NH_3	
i	A	b	i	A	b
0	1	0	0	1	0
1	+1.993771843	1/3	1	+2.02491283	1/3
2	+1.0985211604	2/3	2	+0.84049667	2/3
3	-0.5094492996	5/3	3	+0.30155852	5/3
4	-1.761912427	16/3	4	-0.20926619	16/3
5	-44.9005480267	43/3	5	-74.60250177	43/3
6	-723692.2618632	110/3	6	+4089.79277506	70/3

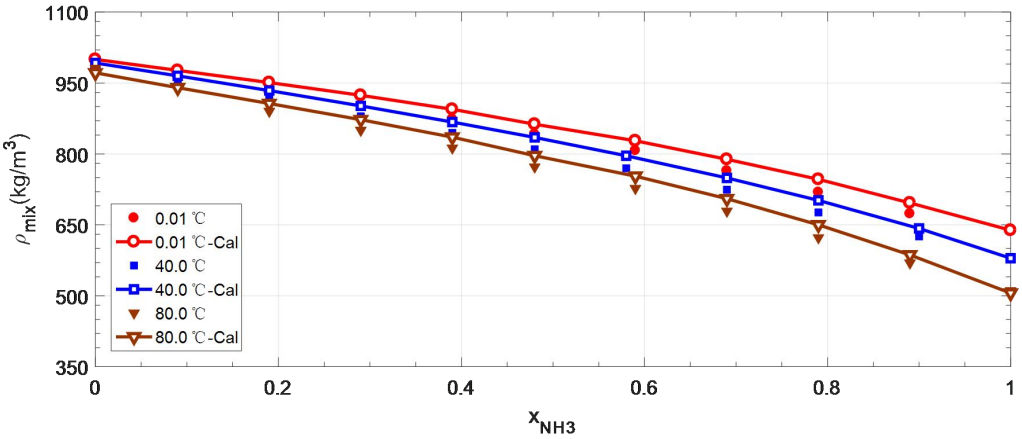


Figure.106 Comparisons between the mentioned calculated and experimental data

References

[1] K. Ebrahimi, G.F. Jones, A.S. Fleischer, A review of data center cooling technology, operating conditions and the corresponding low-grade waste heat recovery opportunities, Renew. Sustain. Energy Rev. 31 (2014) 622–638.

[2] Y.Liu,X.Wei,J. Xiao,Z.Liu,Y.Xu,Y Tian, Energy consumption and emission mitigation prediction based on data center traffic and PUE for global data centers, Glob. energy interconnect. 3 (2020) 272-282.

[3] X Yuan, X Zhou, Y Pan, R Kosonen, H Cai, Y Gao, Phase change cooling in data centers: A review, Energy Build. 236 (2021) 110764.

[4] J. Cho, T. Lim, B.S. Kim, Viability of data center cooling systems for energy efficiency in temperate or subtropical regions: case study, Energy Build. 55 (2012) 189–197.

[5] C. Nadjahi, H. Louahlia, S. Lemasson, A review of thermal management and innovative cooling strategies for data center, Sustain. Comput. Inf. Syst. 19 (2018) 14–28.

[6] J. Lee, I. Mudawar, Critical heat flux for subcooled flow boiling in microchannel heat sinks, Int. J. Heat Mass Transfer 52 (13–14) (2009) 3341–3352.

[7] T.G. Karayiannis, M.M. Mahmoud, Flow boiling in microchannels: Fundamentals and applications, Appl. Therm. Eng. 115 (2017) 1372–1397.

[8] https://www.intel.com/content/www/us/en/products/details/processors/core.html.

[9] S.M. Sohel Murshed, C.A. Nieto de Castro, A critical review of traditional and emerging techniques and fluids for electronics cooling, Renew. Sustain. Energy Rev. 78 (2017) 821–833.

[10] T. Brunschwiler, B. Smith, E. Ruetsche, B. Michel, Toward zero-emission data centers through direct reuse of thermal energy, IBM Journal of Research and Development 53 (2009) 476.

[11] C. Bachmann, A. Bar-Cohen, Hotspot remediation with anisotropic thermal interface materials, in: 11th IEEE Intersociety Conference on Thermal and Thermomechanical Phenomena in Electronic Systems, Orlando, USA, 2008.

[12] P. Wang, B. Yang, A. Bar-Cohen, Mini-contact enhanced thermoelectric coolers for on-chip hot spot cooling, Heat Transfer Eng. 30 (9) (2009) 736–743.

[13] J.B. Marcinichen, J.A. Olivier, N. Lamaison, J.R. Thome, Advances in electronics cooling, Heat Transfer Eng. 34 (5–6) (2013) 434–446.

[14] Shankar Krishnan, et al., Towards a thermal Moore's law, IEEE Trans. Adv. Packag. 30 (3) (2007) 462–474.

[15] A. Ibrahim, F, Jiang, The electric vehicle energy management: An overview of the energy system and related modeling and simulation, Renew. Sust. Energ. Rev.144 (2021) 111049.

[16] Q Chen, G Zhang, X Zhang, C Sun, K Jiao, Y Wang, Thermal management of polymer electrolyte membrane fuel cells: A review of cooling methods, material properties, and durability, Appl. Energy 286 (2021) 116496.

[17] Y. Wang, D.F. Ruiz Diaz, K.S. Chen, Z. Wang, X.C. Adroher, Materials, technological status, and fundamentals of PEM fuel cells–A review, Mater. Today 32 (2020) 178–203.

[18] Y. Wang, P.P. Mukherjee, J. Mishler, R. Mukundan, R.L. Borup, Cold start of polymer electrolyte fuel cells: Three-stage startup characterization, Electrochim. Acta 55 (2010) 2636-2644.

[19] C. Chellaiah, R. Ramesh, Future renewable energy option for recharging full electric vehicles, Renew Sustain Energy Rev, 76 (2017) 824-838

[20] J. Lin, X. Liu, S. Li, C. Zhang, S. Yang, A review on recent progress, challenges and perspective of battery thermal management system, Int. J. Heat Mass Transfer 167 (2021) 120834.

[21] M Shahjalal, T Shams, ME Islam, W Alam, et al., A review of thermal management for Li-ion batteries: Prospects, challenges, and issues, J Energy Storage 39 (2021) 102518.

[22] C. Curry, Bloomberg New energy Finance: Lithium-ion battery cost and market (2017).

[23] G. Zhao, X. Wang, M. Negnevitsky, H. Zhang, A review of air-cooling battery thermal management systems for electric and hybrid electric vehicles, J. Power Sources 501 (2021) 230001.

[24] Y. Chen, Y. Kang, Y. Zhao, L. Wang, J. Liu, et al., A review of lithium-ion battery safety concerns: the issues, strategies, and testing standards,J. Energy Chem. 59 (2021) 83–99.

[25] Q. Wang, B. Jiang, B. Li, Y. Yan, A critical review of thermal management models and solutions of lithium-ion batteries for the development of pure electric vehicles, Renewable Sustainable Energy Rev. 64 (2016) 106–128.

[26] R. Zhao, S. Zhang, J. Liu, J. Gu, A review of thermal performance improving methods of lithium ion battery: Electrode modification and thermal management system, J. Power Sources 299 (2015) 557–577.

[27] C.G. Motloch, J.P. Christophersen, J.R. Belt, R.B. Wright, High-Power Battery Testing Procedures and Analytical Methodologies for HEV's, SAE Transactions, 111(2002) 797-802.

[28] V.G. Choudhari, D.A.S. Dhoble, T.M. Sathe, A review on effect of heat generation and various thermal management systems for lithium ion battery used for electric vehicle, J. Energy Storage 32 (2020) 101729.

[29] S.-W. Kang, Y.T. Chen, G.-S. Chang, The manufacturing and test of (110) orientated silicon based micro heat exchanger, Tamkang J. Sci. Eng. 5 (3) (2002) 129–136.

[30] M.C. Riofrío, N. Caney, J.A. Gruss, State of the art of efficient pumped two-phase flow cooling technologies, Appl. Therm. Eng. 104 (2016) 333–343.

[31] P. Smakulski, S. Pietrowicz, A review of the capabilities of high heat flux removal by porous materials, microchannels and spray cooling techniques, Appl. Therm. Eng. 104 (2016) 636–646.

[32] A.H. Khalaj, S.K. Halgamuge, A Review on efficient thermal management of air-and liquid-cooled data centers: from chip to the cooling system, Appl. Energy 1 (205) (2017) 1165–1188.

[33] Y. Wang, B. Wang, K. Zhu, H. Li, W. He, S. Liu, Energy saving potential of using heat pipes for CPU cooling, Appl. Therm. Eng. 143 (2018) 630–638.

[34] M.S. El-Genk, J.L. Parker, Nucleate boiling of FC-72 and HFE-7100 on porous graphite at different orientations and liquid subcooling, Energy Convers. Manage. 49 (2008) 733–750.

[35] D.B. Tuckerman, R.F.W. Pease, High-performance heat sinking for VLSI, IEEE Electron. Dev. Lett. EDL-2 (1981) 126–129.

[36] J.F. Tullius, R. Vajtai, Y. Bayazitoglu, A review of cooling in microchannels, Heat Transfer Eng. 32 (7–8) (2011) 527–541.

[37] W.L. Cheng, Q.N. Liu, R. Zhao, H.L. Fan, Experimental investigation of parameters effect on heat transfer of spray cooling, Heat Mass Transfer 46 (8–9) (2010) 911–921.

[38] B. Agostini, M. Fabbri, J.E. Park, L. Wojtan, J.R. Thome, B. Michel, State of the art of high heat flux cooling technologies. Heat Transfer Engineering 28 (2007) 258-281.

[39] G. Huang , W. Li , J. Ma , C. Ren , C. Li , High-frequency alternating nucleate boiling of water enabled by microslot arrays in microchannels, Int. J. Heat Mass Transf. (2020) 150.

[40] X. Cheng , H. Wu , Enhanced flow boiling performance in high-aspect-ratio groove-wall microchannels, Int J Heat Mass Transfer 164 (2021) 120468.

[41] B. Ramesh, P. Jayaramu, S. Gedupudi, Subcooled flow boiling of water in a copper microchannel: Experimental investigation and assessment of predictive methods, Int. Commun. Heat Mass Transfer 103 (2019) 24–30.

[42] S.Wang, H.H. Chen, C.L. Chen, Enhanced flow boiling in silicon nanowire – coated manifold microchannels, Appl. Therm. Eng. 148 (2019) 1043–1057.

[43]X.Cheng, H. Wu, Improved flow boiling performance in high-aspect-ratio interconnected microchannels, Int J Heat Mass Transfer 165 (2021) 120627.

[44] www.3M.com/electronics.

[45] B. Platzer, A. Polt, G. Maurer, Thermophysical Properties of Refrigerants, Springer-Verlag, Berlin, 1990.

[46] S. Ndao, Y. Peles, M.K. Jensen, Experimental investigation of flow boiling heat transfer of jet impingement on smooth and micro structured surfaces, Int. J. Heat Mass Transfer 55 (2012) 5093–5101.

[47] L.-H. Chien, C.-Y. Chang, An experimental study of two-phase multiple jet cooling on finned surfaces using a dielectric fluid, Appl. Therm. Eng. 31 (2011) 1983–1993.

[48] E.A. Browne, G.J. Michna, M.K. Jensen, Y. Peles, Microjet array single-phase and flow boiling heat transfer with R134a, Int. J. Heat Mass Transfer 53 (2010) 5027–5034.

[49] D. Guo, J.J. Wei, Y.H. Zhang, Enhanced flow boiling heat transfer with jet impingement on micro-pin-finned surfaces, Appl. Therm. Eng. 31 (2011) 2042–2051.

[50] L.H. Chien,W.R. Liao, H.Y. Liu, An experimental study of two-phase convection in micro-channels with impinging FC-72 jets, Appl. Therm. Eng. 67 (2014) 159–167.

[51] W. Wu, L.C. Chow, C.M. Wang, M. Su, J.P. Kizito, Jet impingement heat transfer using a Field's alloy nanoparticle – HFE7100 slurry, Int. J. Heat Mass Transfer 68 (2014) 357–365.

[52] S.N. Joshi, E.M. Dede, Effect of sub-cooling on performance of a multi-jet two phase cooler with multi-scale porous surfaces, Int. J. Therm. Sci. 87 (2015) 110–120.

[53] M.K. Sung, I. Mudawar, Effects of jet pattern on two-phase performance of hybrid micro-channel/micro-circular-jet-impingement thermal management scheme, Int. J. Heat Mass Transfer 52 (13–14) (2009) 3364–3372.

[54] S.T. Kadam, R. Kumar, Twenty first century cooling solution: Microchannel heat sinks, Int. J. Therm. Sci. 85 (2014) 73-92.

[55] Y.K. Prajapati, P. Bhandari, Flow boiling instabilities in microchannels and their promising solutions – A review, Exp. Therm. Fluid Sci. 88 (2017) 576–593.

[56] T. Harirchian, S.V. Garimella, Boiling heat transfer and flow regimes in microchannels – a comprehensive understanding, J. Electron. Packag. 133 (1) (2011) 011001–011010.

[57] Y. Lv , G. Xia , L. Cheng , D. Ma, Experimental study on the pressure drop oscillation characteristics of the flow boiling instability with FC-72 in parallel rectangle microchannels, Int. Commun. Heat Mass Transf. 108 (2019) 104289.

[58] M. Law, P.-S. Lee, Effects of varying secondary channel widths on flow boiling heat transfer and pressure characteristics in oblique-finned microchannels, Int. J. Heat Mass Transf. 101 (2016) 313–326.

[59] P.Cui, Z.Liu, Enhanced flow boiling of HFE-7100 in picosecond laser fabricated copper microchannel heat sink,Int. J. Heat Mass Transfer 175 (2021) 121387.

[60] J. Lee, I. Mudawar, Fluid flow and heat transfer characteristics of low temperature two-phase micro-channel heat sinks – Part 2. Subcooled boiling pressure drop and heat transfer, Int. J. Heat Mass Transfer 51 (2008) 4327–4341.

[61] W. Li, J. Ma, T. Alam, F. Yang, J. Khan, C. Li, Flow boiling of HFE-7100 in silicon microchannels integrated with multiple micro-nozzles and reentry microcavities, Int. J. Heat Mass Transfer 123 (2018) 354–366.

[62] F.J.D. Nascimento, H.L.S.L. Leão, G. Ribatski, An experimental study on flow boiling heat transfer of R134a in a microchannel-based heat sink, Exp. Therm. Fluid Sci. 45 (2013) 117–127.

[63] J. Park, J. Thome, Critical heat flux in multi-microchannel copper elements with low pressure refrigerants, Int. J. Heat Mass Transfer 53 (2010) 110–122.

[64] S. Xie, M. Shahmohammadi, J. Cai, J. Zhao, Review of critical-heat-flux enhancement methods, Int. J. Heat Mass Transfer 122 (2018) 275–289.

[65] H.J. Lee, D.Y. Liu, S. Yao, Flow instability of evaporative micro-channels, Int. J. Heat Mass Transfer 53 (2010) 1740–1749.

[66] Y. Kuang, W. Wang, J. Miao, X. Yu, R. Zhuan, Theoretical analysis and modeling of flow instability in a mini-channel Evaporator, Int. J. Heat Mass Transfer 104 (2017) 149–162.

[67] D.S. Saidina, M.Z. Abdullah, M. Hussin, Metal oxide nanofluids in electronic cooling: a review, J. Mater. Sci. Mater. Electron. 31 (6) (2020) 4381–4398.

[68] F.Rubbi, L.Das, K.Habib, N.Aslfattahi, R.Saidur, A comprehensive review on advances of oil-based nanofluids for concentrating solar thermal collector application, J. Mol. Liq. Xxx.

[69] B. Bakthavatchalam, K. Habib, R. Saidur, B.B. Saha, K. Irshad, Comprehensive study on nanofluid and ionanofluid for heat transfer enhancement: A review on current and future perspective, J. Mol. Liq. 305 (2020) 112787.

[70] N. Pradhan, H. Duan, J. Liang, G. Iannacchione, The specific heat and effective thermal conductivity of composites containing single-wall and multi-wall carbon nano tubes, Nanotechnology 20 (24) (2009) 245705.

[71] Guodong Xia, Huanming Jiang, Ran Liu, Yuling Zhai, Effects of surfactant on the stability and thermal conductivity of Al2O3/de-ionized water nanofluids, Int. J. Therm. Sci. 84 (2014) 118–124.

[72] G.J. Tertsinidou, C. Tsolakidou, M. Pantzali, M.J. Assael, L. Colla, L. Fedele, S. Bobbo, W.A. Wakeham, New measurements of the apparent thermal conductivity of nanofluids and investigation of their heat transfer capabilities, J. Chem. Eng. Data 62 (2017) 491 – 505.

[73] X. Zhang, H. Gu, M. Fujii, Effective thermal conductivity and thermal diffusivity of nanofluids containing spherical and cylindrical nanoparticles, Exp. Therm. Fluid Sci. 31 (6) (2007) 593 – 599.

[74] B. Buonomo, O. Manca, L. Marinelli, S. Nardini, Effect of temperature and sonication time on nanofluid thermal conductivity measurements by nano-flash method, Appl. Therm. Eng. 91 (2015) 181 – 190.

[75] H.A. Mintsa, G. Roy, C.T. Nguyen, D. Doucet, New temperature dependent thermal conductivity data for water-based nanofluids, Int. J. Therm. Sci. 48 (2) (2009) 363 – 371.

[76] B. Barbés, R. Páramo, E. Blanco, M.J. Pastoriza-Gallego, M.M. Piñeiro, J.L. Legido, C. Casanova, Thermal conductivity and specific heat capacity measurements of Al2O3 nanofluids, J. Therm. Anal. Calorim. 111 (2) (2013) 1615 – 1625.

[77] S. Halelfadl, T. Maré, P. Estellé, Efficiency of carbon nanotubes water based nanofluids as coolants, Exp. Thermal Fluid Sci. 53 (2014) 104 – 110.

[78] K.J. Lee, S.H. Yoon, J. Jang, Carbon nanofibers: a novel nanofiller for nanofluid applications, Small 3 (7) (2007) 1209 – 1213.

[79] M.R. Sohel, S.S. Khaleduzzaman, R. Saidur, A. Hepbasli, M.F.M. Sabri, I.M. Mahbubul, An experimental investigation of heat transfer enhancement of a minichannel heat sink using Al2O3 – H2O nanofluid, Int. J. Heat Mass Transfer 74 (2014) 164 – 172.

[80] H. Zhang, S. Shao, H. Xu, C. Tian, Heat transfer and flow features of Al_2O_3-water nanofluids flowing through a circular microchannel- Experimental results and correlations, Appl. Therm. Eng. 61 (2013) 86 – 92.

[81] S.M. Peyghambarzadeh, S.H. Hashemabadi, A.R. Chabi, M. Salimi, Performance of water based CuO and Al_2O_3 nanofluids in a Cu – Be alloy heat sink with rectangular microchannels, Energy Convers. Manage. 86 (2014) 28 – 38.

[82] J.Y. Jung, H.S. Oh, H.Y. Kwak, Forced convective heat transfer of nanofluids in microchannels, Int. J. Heat Mass Transf. 52 (2009) 466 – 472.

[83] C.J. Ho, L.C. Wei, Z.W. Li, An experimental investigation of forced convective cooling performance of a microchannel heat sink with Al2O3/water nanofluid, Applied Thermal Engineering 30 (2009) 96 – 103.

[84] B. Jacqueline, D. Brutin, and L. Tadrist. A review on boiling heat transfer enhancement with nanofluids. Nanoscale research letters 6.1 (2011) 1-16.

[85] M. Boudouh, H.L. Gualous, M. De Labachelerie, Local convective boiling heat transfer and pressure drop of nanofluid in narrow rectangular channels, Appl. Therm. Eng. 30 (2010) 2619–2631.

[86] L. Xu, J. Xu, Nanofluid stabilizes and enhances convective boiling heat transfer in a single microchannel, Int. J. Heat Mass Transfer 55 (2012) 5673–5686.

[87] A.A. Chehade, H.L. Gualous, S.L. Masson, F. Fardoun, A. Besq, Boiling local heat transfer enhancement in minichannels using nanoflfluids, Nanoscale Res. Lett. 8 (2013) 130.

[88] J. Lee, I. Mudawar, Assessment of the effectiveness of nanofluids for single-phase and two-phase heat transfer in micro-channels, Int. J. Heat Mass Transfer 50 (2007) 452–463.

[89] T.A. Moreira, F.J.d. Nascimento, G. Ribatski, An investigation of the effect of nanoparticle composition and dimension on the heat transfer coefficient during flow boiling of aqueous nanofluids in small diameter channels (1.1mm), Exp. Therm. Fluid Sci. 89 (2017) 72–89.

[90] C. Zhang, L. Zhang, H. Xu, D. Wang, B. Ye, Investigation of flow boiling performance and the resulting surface deposition of graphene oxide nanofluid in microchannels, Exp. Therm. Fluid Sci. 86 (2017) 1–10.

[91] Y.H. Diao, Y. Liu, R. Wang, Y.H. Zhao, L. Guo, X. Tang, Effects of nanofluids and nanocoatings on the thermal performance of an evaporator with rectangular microchannels, Int. J. Heat Mass Transfer 67 (2013) 183–193.

[92] K. Henderson, Y.-G. Park, L. Liu, A.M. Jacobi, Flow-boiling heat transfer of R-134a-based nanofluids in a horizontal tube, Int. J. Heat Mass Transfer 53 (2009) 944–951.

[93] F. Ma, J. Chen, P. Zhang, Experimental study of the hydraulic and thermal performances of nano-sized phase change emulsion in horizontal mini-tubes, Energy 149 (2018) 944–953.

[94] H. Nazir, M. Batool, F.J. Bolivar Osorio, M. Isaza-Ruiz, X. Xu, K. Vignarooban, et al., Recent developments in phase change materials for energy storage applications: a review, Int. J. Heat Mass Transf. 129 (2019) 491–523.

[95] W. Lan, B. Shang, R. Wu, X. Yu, R. Hu, X. Luo, Thermally-enhanced nanoencapsulated phase change materials for latent functionally thermal fluid, Int. J. Therm. Sci. 159 (2021) 106619.

[96] Al-Shannaq, J. Kurdi, S. Al-Muhtaseb, M. Farid, Innovative method of metal coating of microcapsules containing phase change materials, Sol. Energy 129 (2016) 54–64.

[97] T. Khadiran, M.Z. Hussein, H.W. Syamsi, Z. Zainal, R. Rusli, Laboratory-scale studies on smart gypsum composite boards incorporated with nano-encapsulated organic phase change material for thermal comfort building application, J. Mater. Civil Eng. 28 (2015) 04015137.

[98] G.H. Zhang, S.A.F. Bon, C.Y. Zhao, Synthesis, characterization and thermal properties of novel nanoencapsulated phase change materials for thermal energy storage, Sol. Energy 86 (2012) 1149–1154.

[99] Y.L. Zhu, Y. Chi, S.E. Liang, X. Luo, K.P. Chen, C.R. Tian, J.H. Wang, L. Zhang, Novel metal coated nanoencapsulated phase change materials with high thermal conductivity for thermal energy storage, Sol. Energy Mater. Sol. Cell. 176 (2018) 212–221.

[100] M.R. Kærn, A. Modi, J.K. Jensen, J.G. Andreasen, F. Haglind, An assessment of in-tube flow boiling correlations for ammonia-water mixtures and their influence on heat exchanger size, Appl. Therm. Eng. 93 (2016) 623–638.

[101] R. Xu, C. Zhang, H. Chen, Q. Wu, R. Wang, Heat transfer performance of pulsating heat pipe with zeotropic immiscible binary mixtures, Int. J. Heat Mass Transfer 137 (2019) 31–41.

[102] C. Dang, L. Jia, M. Xu, Q. Huang, Q. Peng, Experimental study on flow boiling characteristics of pure refrigerant (R134a) and zeotropic mixture (R407C) in a rectangular micro-channel, Int. J. Heat Mass Transf. 104 (2017) 351–361.

[103] C. Guo, J. Wang, X. Du, L. Yang, Experimental flow boiling characteristics of R134a/R245fa mixture inside smooth horizontal tube, Appl. Therm. Eng. 103(2016) 901–908.

[104] C. Dang, L. Jia, X. Zhang, Q. Huang, M. Xu, Experimental Investigation on Flow Boiling Characteristics of Zeotropic Binary Mixtures (R134a/R245fa) in a Rectangular Micro-channel, Int. J. Heat Mass Transf. 115 (2017) 782–794.

[105] C. Dang, L. Jia, Q. Peng, L.F. Yin, Z.L. Qi, Experimental study on flow boiling heat transfer for pure and zeotropic refrigerants in multi-microchannels with segmented configurations, Int. J. Heat Mass Transf. 127 (2018) 758–768.

[106] S. Szczukiewicz, M. Magnini, J.R. Thome, Proposed models, ongoing experiments, and latest numerical simulations of microchannel two-phase flow boiling, Int. J. Multiphase Flow 59 (2014) 84-101.

[107] F. Táboas, M. Valles, M. Bourouis, A. Coronas, Flow boiling heat transfer of ammonia/water mixture in a plate heat exchanger, Int. J. Refrig. 33 (2010) 695–705.

[108] F. Taboas, M. Valles, M. Bourouis, A. Coronas, Assessment of boiling heat transfer and pressure drop correlations of ammonia/water mixture in a plate heat exchanger, Int. J. Refrig. 35 (2012) 633-644.

[109] H. Arima, J.H. Kim, A. Okamoto, Y. Ikegami, Local boiling heat transfer characteristics of ammonia in a vertical plate evaporator, Int. J. Refrig. 33 (2010) 359-370.

[110] H. Arima, A. Okamoto, Y. Ikegami, Local boiling heat transfer characteristics of ammonia/water binary mixture in a vertical plate evaporator, Int. J. Refrig. 34 (2011) 648–657.

[111] D.M. van de Bor, C. Vasilescu, C.I. Ferreira, Experimental investigation of heat transfer and pressure drop characteristics of ammonia–water in a mini-channel annulus, Exp. Therm. Fluid Sci. 61 (2015) 177-186.

[112] S.M. Fan, F. Duan, A review of two-phase submerged boiling in thermal management of electronic cooling, International Journal of Heat and Mass Transfer150 (2020) 119324.

[113] J.L. Xu, J.J. Zhou, Y.H. Gan, Static and dynamic flow instability of a parallel microchannel heat sink at high heat flux, Energy Convers. Manage. 46 (2005) 313–334.

[114] M. Cortina-Diaz, J. Schmidt, Flow boiling heat transfer of n-hexane and n-octane in a minichannel. In: Proceedings of the 13th International Heat Transfer Conference, Sydney, Australia, 2006.

[115] Y. Yang, Y. Fujita, Flow Boiling Heat Transfer and Flow Pattern in Rectangular Channel of Mini-Gap, in: ASME. International Conference on Nanochannels, Microchannels, and Minichannels, ASME 2nd International Conference on Microchannels and Minichannels. (2004) 573-580.

[116] K. Balasubramanian, M. Jagirdar, P.S. Lee, C.J. Teo, S.K. Chou, Experimental investigation of flow boiling heat transfer and instabilities in straight microchannels. Int. J. Heat Mass Transfer 66 (2013) 655-671.

[117] S.-M. Kim, I. Mudawar, Review of databases and predictive methods for heat transfer in condensing and boiling mini/micro-channel flows, Int. J. Heat Mass Transfer 77 (2014) 627–652.

[118] M. Jagirdar, P.S. Lee, Study of transient heat transfer and synchronized flow visualizations during sub-cooled flow boiling in a small aspect ratio microchannel, Int. J. Multiph. Flow 83 (2016) 254–266.

[119] W. Li, J. Li, Z. Feng, K. Zhou, Z. Wu, Local heat transfer in subcooled flow boiling in a vertical mini-gap channel, Int. J. Heat Mass Transf. 110 (2017) 796–804.

[120] E. Sobierska, R. Kulenovic, R. Mertz, Heat transfer mechanism and flow pattern during flow boiling of water in a vertical narrow channel-experimental results, Int. J. Therm. Sci. 46 (11) (2007) 1172–1181.

[121] W. Qu, I. Mudawar, Flow boiling heat transfer in two-phase microchannel heat sinks – II. Annular two-phase flow model, Int. J. Heat Mass Transfer 46 (2003) 2773–2784.

[122] B. Markal, O. Aydin, M. Avci, Effect of aspect ratio on saturated flow boiling in microchannels, Int. J. Heat Mass Transf. 93 (2016) 130–143.

[123] E. Galvis, R. Culham, Measurements and flow patterns visualization of two phase flow boiling in single channel microevaporator, Int. J. Multiphase Flow 42 (2012) 52–61.

[124] W. Li, R. Dai, M. Zeng, Q. Wang, Review of two types of surface modification on pool boiling enhancement: Passive and active, Renew. Sustain. Energy Rev. 130 (2020) 109926.

[125] D.L. Saums, S. Gill, et al. Vaporizable dielectric fluid cooling of IGBT power semiconductors for vehicle powertrains. Fifth IEEE Vehicle Power and Propulsion Conference (VPPC'09), Dearborn MI USA. 2009.

[126] Y. Madhour, J. Olivier, E. Costa-Patry, S. Paredes, B. Michel, J.R. Thome, Flow boiling of R134a in a multi-microchannel heat sink with hotspot heaters for energy-efficient microelectronic CPU cooling applications, IEEE Trans. Compon. Packag. Technol. 1 (2011) 873–883.

[127] G. Liang, I. Mudawar, Review of pool boiling enhancement by surface modification, Int. J. Heat Mass Transfer 128 (2019) 892–933.

[128] K.C. Leong, J.Y. Ho, K.K. Wong, A critical review of pool and flow boiling heat transfer of dielectric fluids on enhanced surfaces, Appl. Therm. Eng. 112 (2017) 999–1019.

[129] W. Wu, H. Bostanci, L.C. Chow, Y. Hong, M. Su, J.P. Kizito, Nucleate boiling heat transfer enhancement for water and FC-72 on titanium oxide and silicon oxide surfaces, Int. J. Heat Mass Transfer 53 (2010) 1773–1777.

[130] B. Vadgama, D.K. Harris, Measurements of the contact angle between R134a and both aluminum and copper surfaces, Exp. Therm. Fluid Sci. 31 (8) (2007) 979–984.

[131] G. Wang, P. Cheng, An experimental study of flow boiling instability in a single microchannel, Int. Comm. Heat Mass Transfer 35 (2008) 1229–1234.

[132] Z.J. Edel, A. Mukherjee, Experimental investigation of vapor bubble growth during flow boiling in a microchannel, Int. J. Multiphase Flow 37 (2011) 1257–1265.

[133] D. Bogojevic, K. Sefiane, G. Duursma, A.J. Walton, Bubble dynamics and flow boiling instabilities in microchannels, Int. J. Heat Mass Transfer 58 (1–2) (2013) 663–675.

[134] D. Bogojevic, K. Sefiane, A. Walton, H. Lin, G. Cummins, Two-phase flow instabilities in a silicon microchannels heat sink, Int. J. Heat Fluid Flow 30 (2009) 854–867.

[135] D. Bogojevic, K. Sefiane, A.J. Walton, H. Lin, G. Cummins, D.B.R. Kenning, T.G. Karayiannis, Experimental investigation of non-uniform heating effect on flow boiling instabilities in a microchannel-based heat sink, Int. J. Therm. Sci. 50 (3) (2011) 309–324.

[136] T. Alam, W. Li, F. Yang, W. Chang, J. Li, Z. Wang, J. Khan, C. Li, Force analysis and bubble dynamics during flow boiling in silicon nanowire microchannels, Int. J. Heat Mass Transf. 101 (2016) 915–926.

[137] G. Wang, P. Cheng, H. Wu, Unstable and stable flow boiling in parallel microchannels and in a single microchannel, Int. J. Heat Mass Transfer 50 (21–22) (2007) 4297–4310.

[138] G. Wang, P. Cheng, A.E. Bergles, Effects of inlet/outlet configurations on flow boiling instability in parallel microchannels, Int. J. Heat Mass Transfer 51 (2008) 2267–2281.

[139] C.T. Lu, C. Pan, Convective boiling in a parallel microchannels heat sink with a diverging cross-section and artificial nucleation sites, Exp. Therm. Fluid Sci. 35 (2011) 810–815.

[140] K. Balasubramanian, P.S. Lee, L.W. Jin, S.K. Chou, C.J. Teo, S. Gao, Experimental investigations of flow boiling heat transfer and pressure drop in straight and expanding microchannels – a comparative study, Int. J. Therm. Sci. 50 (2011) 2413–2421.

[141] S. Szczukiewicz, N. Borhani, J.R. Thome, Two-phase flow operational maps for multi-microchannel evaporators, Int. J. Heat Fluid Flow 42 (2013) 176–189.

[142] F. Yang, et al., Flow boiling phenomena in a single annular flow regime in microchannels (I): characterization of flow boiling heat transfer, Int. J. Heat Mass Transfer 68 (2014) 703-715.

[143] Y.K. Prajapati, M. Pathak, Mohd.K. Khan, A comparative study of flow boiling heat transfer in three different configurations of microchannels, Int. J. Heat Mass Transfer 85 (2015) 711–722.

[144] D. Deng, W. Wan, Y. Tang, Z. Wan, D. Liang, Experimental investigations on flow boiling performance of reentrant and rectangular microchannels – A comparative study, Int. J. Heat Mass Transfer 82 (2015) 435–446.

[145] S. Zhang, Y. Tang, W. Yuan, J. Zeng, Y. Xie, A comparative study of flow boiling performance in the interconnected microchannel net and rectangular microchannels, Int. J. Heat Mass Transfer 98 (2016) 814–823.

[146] D. Deng, Y. Xie, Q. Huang, W. Wan, On the flow boiling enhancement in interconnected reentrant microchannels, Int. J. Heat Mass Transfer 108 (2017) 453–467.

[147] W. Wan, D. Deng, Q. Huang, T. Zeng, Y. Huang, Experimental study and optimization of pin fin shapes in flow boiling of micro pin fin heat sinks, Appl. Therm. Eng. 114 (2017) 436–449.

[148] A. Megahed, Local flow boiling heat transfer characteristics in silicon microchannel heat sinks using liquid crystal thermography, Int. J. Multiphase Flow 39 (2012) 55–65.

[149] M. Law, P.-S. Lee, A comparative study of experimental flow boiling heat transfer and pressure characteristics in straight- and oblique- finned microchannels, Int. J. Heat Mass Transfer 85 (2015) 797–810.

[150] B.R. Fu, C.R. Lee, C. Pan, The effect of aspect ratio on flow boiling heat transfer of HFE-7100 in a microchannel heat sink, Int. J. Heat Mass Transfer 58 (1–2) (2013) 53–61.

[151] A.H. Al-Zaidi, M.M. Mahmoud, T.G. Karayiannis, Flow boiling of HFE-7100 in microchannels: Experimental study and comparison with correlations, Int. J. Heat Mass Transf. 140 (2019) 100–128.

[152] Y.Lv, G.Xia, L.Cheng, D.Ma, Experimental investigation into unstable two phase flow phenomena during flow boiling in multi-microchannels, Int. J. Therm. Sci. 166(2021) 106985.

[153] T. Alam, W.M. Li, W. Chang, F.H. Yang, J. Khan, C. Li, A comparative study of flow boiling HFE-7100 in silicon nanowire and plainwall microchannels, Int. J. Heat Mass Transf. 124 (2018) 829–840.

[154] X.J. Wang, Z.H. Liu, Y.Y. Li, Experimental study of heat transfer characteristics of high-velocity small slot jet impingement boiling on nanoscale modification surfaces, Int. J. Heat Mass Transfer 103 (2016) 1042–1052.

[155]N.A. Patankar, Supernucleating surfaces for nucleate boiling and dropwise condensation heat transfer, Soft Matter 6 (2010) 1613–1620.

[156] B. Bourdon, E. Bertrand, P. Di Marco, M. Marengo, R. Rioboo, J. De Coninck, Wettability influence on the onset temperature of pool boiling: experimental evidence onto ultra-smooth surfaces, Adv. Colloid Interface Sci. 221 (2015) 34–40.

[157] C.C. Hsu, P.H. Chen, Surface wettability effects on critical heat flux of boiling heat transfer using nanoparticle coatings, Int. J. Heat Mass Transfer 55 (13) (2012) 3713–3719.

[158] H.T. Phan, N. Caney, P. Marty, S. Colasson, J. Gavillet, Surface wettability control by nanocoating: the effects on pool boiling heat transfer and nucleation mechanism, Int. J. Heat Mass Transfer 52 (23) (2009) 5459–5471.

[159] Y.-Y. Li, Z.-H. Liu, B.-C. Zheng, Experimental study on the saturated pool boiling heat transfer on nano-scale modification surface, Int. J. Heat Mass Transfer 84 (2015) 550–561.

[160] R. Chen, M.C. Lu, V. Srinivasan, Z. Wang, H.H. Cho, A. Majumdar, Nanowires for enhanced boiling heat transfer, Nano Lett. 9 (2009) 548–553.

[161] H. Jo, H.S. Ahn, S. Kang, M.H. Kim, A study of nucleate boiling heat transfer on hydrophilic, hydrophobic and heterogeneous wetting surfaces, Int. J. Heat Mass Transfer 54 (2011) 5643–5652.

[162] P. Xu, Q. Li, Y. Xuan, Enhanced boiling heat transfer on composite porous surface, Int. J. Heat Mass Transfer 80 (2015) 107–114.

[163] M. Golubovic, H.D.M. Hettiarachchi, W.M. Worek, W.J. Minkowycz, Nanofluids and critical heat flux, experimental and analytical study, Appl. Therm. Eng. 29 (2009) 1281–1288.

[164] R.K. Cheedarala, E. Park, K. Kong, Y.B. Park, H.W. Park, Experimental study on critical heat flux of highly efficient soft hydrophilic CuO–chitosan nanofluid templates, Int. J. Heat Mass Transf. 100 (2016) 396–406.

[165] H.S. Jo, S. An, H.G. Park, M.W. Kim, S.S. Al-Deyab, S.C. James, et al., Enhancement of critical heat flux and superheat through controlled wettability of cuprous-oxide fractal-like nanotextured surfaces in pool boiling, Int. J. Heat Mass Transf. 107 (2017) 105–111.

[166] C. Choi, J.S. Shin, D.I. Yu, M.H. Kim, Flow boiling behaviours in hydrophilic and hydrophobic microchannels, Exp. Therm. Fluid Sci. 35 (2011) 816–824.

[167] A.K. Sadaghiani, N.S. Saadi, S.S. Parapari, T. Karabacak, M. Keskinoz, A. Kosar, Boiling heat transfer performance enhancement using micro and nanostructured surfaces for high heat flux electronics cooling systems, Appl.Therm. Eng. 127 (2017) 484–498.

[168] T.Y. Liu, P.L. Li, C.W. Liy, C. Gau, Boiling flow characteristics in microchannels with very hydrophobic surface to super-hydrophilic surface, Int. J. Heat Mass Transfer 54 (2011) 126–134.

[169] W. Zhang, Y. Chai, J. Xu, G. Liu, Y. Sun, 3D heterogeneous wetting microchannel surfaces for boiling heat transfer enhancement, Appl. Surf. Sci. 457 (2018) 891–901.

[170] Alam T, Lee P S, Yap C R. Effects of surface roughness on flow boiling in silicon microgap heat sinks[J]. International Journal of Heat and Mass Transfer, 2013, 64: 28-41.

[171] P. Jayaramu, S. Gedupudi, S.K. Das, Influence of heating surface characteristics on flow boiling in a copper microchannel: Experimental investigation and assessment of correlations, Int. J. Heat Mass Transfer 128 (2019) 290–318.

[172] H. Jo, S. Kim, H.S. Park, M.H. Kim, Critical heat flux and nucleate boiling on several heterogeneous wetting surfaces: controlled hydrophobic patterns on a hydrophilic substrate, Int. J. Multiphase Flow 62 (2014) 101–109.

[173] A.R. Betz, J. Xu, H. Qiu, D. Attinger, Do surfaces with mixed hydrophilic and hydrophobic areas enhance pool boiling?, Appl Phys. Lett. 97 (2010) 141909.

[174] A.R. Motezakker, A.K. Sadaghiani, S. Çelik, T. Larsen, L.G. Villanueva, A. Kosar, Optimum ratio of hydrophobic to hydrophilic areas of biphilic surfaces in thermal fluid systems involving boiling, Int. J. Heat Mass Transfer 135 (2019) 164–174.

[175] J.D. Bernardin, I. Mudawar, C.B. Walsh, E.I. Franses, Contact angle temperature dependence for water droplets on practical aluminum surfaces, Int. J. Heat Mass Transfer 40 (1997) 1017–1033.

[176] J.M. Kim, S.H. Kang, D.I. Yu, H.S. Park, K. Moriyama, M.H. Kim, Smart surface in flow boiling: spontaneous change of wettability, Int. J. Heat Mass Transf. 105 (2017) 147–156.

[177] X. Lu, J. Liu, X. Xu, Contact angle measurements of pure refrigerants, Int. J. Heat Mass Transfer 102 (2016) 877–883.

[178] M.M. Mahmoud, T.G. Karayiannis, D. Kenning. Surface effects in flow boiling of R134a in microtubes. Int. J. Heat Mass Transfer, 54(15–16) (2011) 3334-3346.

[179] T. G. Karayiannis, M.M. Mahmoud, D. Kenning. A study of discrepancies in flow boiling results in small to microdiameter metallic tubes. Exp. Therm. Fluid Sci. 36.1(2012) 126-142.

[180] C.L. Ong, J.R. Thome, Flow boiling heat transfer of R134a, R236fa and R245fa in a horizontal 1.03 mm circular channel, Exp. Therm. Fluid Sci. 33 (2009) 651– 663.

[181] R.Jafari, et al. Experimental investigation of surface roughness effects on the flow boiling of R134a in microchannels. Exp. Therm. Fluid Sci. 79 (2016) 222-230.

[182] H. Han, X. Cui, Y. Zhu, T. Xu, Y. Sui, S. Sun, Experimental study on a closed-loop pulsating heat pipe (CLPHP) charged with water-based binary zeotropes and the corresponding pure fluids, Energy 109 (2016) 724–736.

[183] B. Agostini, J.R. Thome, M. Fabbri, B. Michel, D. Calmi, U. Kloter, High heat flux flow boiling in silicon multi-microchannels: Part II. Heat transfer characteristics of refrigerant R245fa, Int. J. Heat Mass Transfer 51 (2008) 5415–5425.

[184] P. Thiangtham et al., An experimental study on two-phase flow patterns and heat transfer characteristics during boiling of R134a flowing through a multimicrochannel heat sink, Int. J. Heat Mass Transf. 98 (2016) 390–400.

[185] A.S. Dalkilic, C. Ozman, K. Sakamatapan, S. Wongwises, Experimental investigation on the flow boiling of R134a in a multi-microchannel heat sink, Int. Commun. Heat Mass Transfer 91 (2018) 125–137.

[186] S.S. Bertsch, E.A. Groll, S.V. Garimella, Effects of heat flux, mass flux, vapor quality, and saturation temperature on flow boiling heat transfer in microchannels, Int. J. Multiphase Flow 35 (2009) 142–154.

[187] C.B. Tibiriçá, G. Ribatski, Flow patterns and bubble departure fundamental characteristics during flow boiling in microscale channels, Exp. Therm. Fluid Sci. 59 (2014) 152–165.

[188] F.T. Kanizawa, C.B. Tibiriçá, G. Ribatski, Heat transfer during convective boiling inside microchannels, Int. J. Heat Mass Transfer 93 (2016) 566–583.

[189] L. Consolini, J.R. Thome, Micro-channel flow boiling heat transfer of R-134a, R-236fa, and R-245fa, Microfluid Nanofluid 6 (2009) 731–746.

[190] M.H. Maqbool, B. Palm, R. Khodabandeh, Boiling heat transfer of ammonia in vertical smooth mini channels: experimental results and predictions, Int. J. Therm. Sci. 54 (2012) 13–21.

[191] B.M. Fronk, S. Garimella, Condensation of ammonia and high-temperature glide ammonia/water zeotropic mixtures in minichannels–Part I: measurements, Int. J. Heat Mass Transf. 101 (2016) 1343–1356.

[192] Y.W. Kuang, W. Wang, J.Y. Miao, X.G. Yu, H.X. Zhang, R. Zhuan, Flow boiling of ammonia and flow instabilities in mini-channels, Appl. Therm. Eng. 113 (2017) 831–842.

[193] G.B. Abadi, E. Yun, K.C. Kim, Flow boiling characteristics of R134a and R245fa mixtures in a vertical circular tube, Exp. Therm. Fluid Sci. 72 (2016) 112–124

[194] D.S. Jung, M. McLinden, R. Radermacher, D. Didion, A study of flow boiling heat transfer with refrigerant mixtures, Int. J. Heat Mass Transfer 32 (9) (1989) 1751–1764.

[195] T. Khir, R.K. Rahim, N. Ghaffour, A.B. Brahim, Experimental study on forced convective boiling of ammonia–water mixtures in a vertical smooth tube, Arab. J. Sci. Eng. 30 (1B) (2005) 47–63. ISSN 1319-8025.

[196] W. Rivera, R. Best, Boiling heat transfer coefficients inside a vertical smooth tube for water/ammonia and ammonia lithium nitrate mixtures, Int. J. Heat Mass Transf. 42 (5) (1999) 905–921.

[197] Y. Ding, H. Alias, D. Wen, R.A. Williams, Heat transfer of aqueous suspensions of carbon nanotubes (CNT nanofluids), Int. J. Heat Mass Transfer 49 (2006) 240–250.

[198]X.Wu, H.Wu ,P. Cheng, Pressure drop and heat transfer of Al2O3-H2O nanofluids through silicon microchannels. J. Micromech. Microeng. 19.10 (2009) 105020.

[199]S.Vafaei, D.Wen, Flow boiling heat transfer of alumina nanofluids in single microchannels and the roles of nanoparticles,J. Nanopart. Res.13.3(2011) 1063-1073.

[200]S.Vafaei, R. Wen , Critical Heat Flux (CHF) of Subcooled Flow Boiling of Alumina Nanofluids in a Horizontal Microchannel,J. Heat Transfer 132.10(2010) 369-380.

[201]S.Vafaei, D. Wen, Critical heat flux of nanofluids inside a single microchannel: Experiments and correlations, Chem. Eng. Res. Des. 92.11(2014) 2339-2351.

[202]G.Duursma, K. Sefiane, A. Dehaene, S. Harmand et al, Flow and Heat Transfer of Single-and Two-Phase Boiling of Nanofluids in Microchannels, Heat Transfer Eng.36.13-15(2015) 1252-1265.

[203]F.D. Nascimento, T. A. Moreira, G.Ribatski, Flow boiling critical heat flux of DI-water and nanofluids inside smooth and nanoporous round microchannels, Int. J. Heat Mass Transfer 139(2019) 240-253.

[204]L.Yu, A. Sur, and L. Dong, Flow Boiling Heat Transfer and Two-Phase Flow Instability of Nanofluids in a Minichannel, J. Heat Transfer 137.5(2015) 51502-51501.

[205] Z. Jin, Y. Wang, J. Liu, Z. Yang, Synthesis and properties of paraffin capsules as phase change materials, Polymer 49 (2008) 2903–2910.

[206] L. Chai, R. Shaukat, L. Wang, H.S. Wang, A review on heat transfer and hydrodynamic characteristics of nano/microencapsulated phase change slurry (N/MPCS) in mini/ microchan -nel heat sinks, Appl. Therm. Eng. 135 (2018) 334–349.

[207]K.Pielichowska, K. Pielichowski, Phase change materials for thermal energy storage, Prog. Mater. Sci. 65(2014) 67-123.

[208]B.Nrja, B. Mc, A review of phase change materials for vehicle component thermal buffering, Appl. Energy 113(2014) 1525-1561.

[209]A.As,B.Vvt,A.Crc, Review on thermal energy storage with phase change materials and applications, Renewable Sustainable Energy Rev.13.2(2009) 318-345.

[210]L.F. Cabeza, A.Castell, C, Barreneche, A.D. Gracia,Materials used as PCM in thermal energy storage in buildings: A review, Renewable Sustainable Energy Rev.15.3(2011) 1675-1695.

[211]A.Dinker, M.Agarwal, G.D. Agarwal, Heat storage materials, geometry and applications: A review, J. Energy Inst.(2017):1-11.

[212]Z.Khan,Z. Kha, A. Ghafoor, A review of performance enhancement of PCM based latent heat storage system within the context of materials, thermal stability and compatibility, Energy Convers. Manage.115.5(2016) 132-158.

[213]A.Aj, A.Sms, B.Mf, A review of microencapsulation methods of phase change materials (PCMs) as a thermal energy storage (TES) medium, Renewable Sustainable Energy Rev.31(2014)531-542.

[214]M.M. Farid, A.M. Khudhair, S. Razck, A review on phase change energy storage: materials and applications,Energy Convers. Manage.45.9-10(2004) 1597-1615.

[215] C.-J. Ho, W.-C. Chen, W.-M. Yan, Experimental study on cooling performance of minichannel heat sink using water-based MEPCM particles, Int. Commun. Heat Mass Transf. 48 (2013) 67–72.

[216] Y. Wang, Z. Chen, X. Ling, An experimental study of the latent functionally thermal fluid with micro-encapsulated phase change material particles flowing in microchannels, Appl. Therm. Eng. 105 (2016) 209–216.

[217] W. Wu, et al., Heat transfer enhancement of PAO in microchannel heat exchanger using nano-encapsulated phase change indium particles, Int. J. Heat Mass Transf. 58 (1–2) (2013) 348–355.

[218] L. Min, C. Meirong, W. Zhishen, Enhancement in thermal property and mechanical property of phase change microcapsule with modified carbon nanotube, Appl. Energy 127 (2014) 166–171.

[219] X. Jiang, R.L. Luo, F.F. Peng, Y.T. Fang, T. Akiyama, S.F. Wang, Synthesis, characterization and thermal properties of paraffin microcapsules modified with nano Al2O3, Appl. Energy. 137 (2015) 731–737.

[220] Y.Y. Yang, J. Kuang, H. Wang, G.L. Song, Y. Liu, G.Y. Tang, Enhancement in thermal property of phase change microcapsules with modified silicon nitride for solar energy, Solar Energy Mater. Solar Cells 151 (2016) 89–95.

[221] C. Li, H. Yu, Y. Song, H. Liang, X. Yan, Preparation and characterization of PMMA/ TiO2 hybrid shell microencapsulated PCMs for thermal energy storage, Energy 167 (2019) 1031–1039.

[222] H. Zhang, X. Wang, D. Wu, Silica encapsulation of n-octadecane via sol–gel process: a novel microencapsulated phase-change material with enhanced thermal conductivity and performance, J. Colloid Interface Sci. 343 (2010) 246–255.

[223] F. He, X. Wang, D. Wu, New approach for sol–gel synthesis of microencapsulated n-octadecane phase change material with silica wall using sodium silicate precursor, Energy 67 (2014) 223–233.

[224] S. Yu, X. Wang, D. Wu, Microencapsulation of n-octadecane phase change material with calcium carbonate shell for enhancement of thermal conductivity and serving durability: synthesis, microstructure, and performance evaluation, Appl. Energy 114 (2014) 632–643.

[225] H. Liu, X. Wang, D. Wu, Fabrication of graphene/TiO2/paraffin composite phase change materials for enhancement of solar energy efficiency in photocatalysis and latent heat storage, ACS Sustain. Chem. Eng. 5 (2017) 4906–4915.

[226] W. Wang, C. Wang, T. Wang, W. Li, L. Chen, R. Zou, et al., Enhancing the thermal conductivity of n-eicosane/silica phase change materials by reduced graphene oxide, Mater. Chem. Phys. 147 (2014) 701–706.

[227] C. Liu, Z. Rao, J. Zhao, Y. Huo, Y. Li, Review on nanoencapsulated phase change materials: preparation, characterization and heat transfer enhancement, Nano Energy 13 (2015) 814–826.

[228]S. Dhivya, S.I. Hussain, S. Kalaiselvam, Novel metal coated nanocapsules of ethyl esters fatty acid eutectic mixture as phase change material with enhanced thermal conductivity for energy storage applications, Thermochim. Acta 687(2020) 178581.

[229] Y. Zhu, Y. Qin, S. Liang, K. Chen, C. Tian, J. Wang, X. Luo, L. Zhang, Graphene/ SiO2/n-octadecane nanoencapsulated phase change material with flower like morphology, high thermal conductivity, and suppressed supercooling, Appl. Energy 250 (2019) 98–108.

[230] H.I. Mohammed, D. Giddings, G.S. Walker, CFD simulation of a concentrated salt nanofluid flow boiling in a rectangular tube, Int. J. Heat Mass Transf. 125 (2018) 218–228.

[231] B.A. Nichita, J.R. Thome, A level set method and a heat transfer model implemented into FLUENT for modeling of microscale two phase flows, in: AVT-178 Specialists ' Meeting on System Level Thermal Management for Enhanced Platform Efficiency, Bucharest, Romania, 2010.

[232] R.Yang, Y. Wang, and Y. Li. Numerical investigations on flow boiling heat transfer of ammonia water binary solution (NH3/H2O) in a horizontal microchannel. Int. J. Heat Mass Transfer 171 (2021) 121091.

[233] M. Akbari, N. Galanis, A. Behzadmehr, Comparative analysis of single and two phase models for CFD studies of nanofluid heat transfer, Int. J. Therm. Sci. 50 (2011) 1343-1354.

[234] E.L. Alisetti, S.K. Roy, Forced convection heat transfer to phase change material slurries in circular ducts, J. Thermophys. Heat Transfer 14 (1) (2000) 115–1180.

[235] S.C.P. Cheung, S. Vahaji, G.H. Yeoh, J.Y. Tu, Modeling subcooled boiling flow in vertical channels at low pressures – Part 1: Assessment of empirical correlations, Int. J. Heat Mass Transfer 75 (2014) 736–753.

[236] M. Colombo, M. Fairweather, Accuracy of Eulerian-Eulerian, two-fluid CFD boiling models of subcooled boiling flows, Int. J. Heat Mass Transf. 103 (2016) 28-44.

[237] C.R. Kharangate, I. Mudawar, Review of computational studies on boiling and condensation, Int. J. Heat Mass Transfer 108 (2017) 1164-1196.

[238] J. Gu, Q. Wanga, Y. Wub, J. Lyu, S. Li, W. Yao, Modeling of subcooled boiling by extending the RPI wall boiling model to ultra-high pressure conditions, Appl. Therm. Eng. 124 (2017) 571–584.

[239] X. Wang, Y. Wang, H. Chen, Y. Zhu, A combined CFD/visualization investigation of heat transfer behaviors during geyser boiling in two-phase closed thermosyphon, Int. J. Heat Mass Transf. 121 (2018) 703–714.

[240]Lee, Jeongmin, et al. Experimental and computational investigation on two-phase flow and heat transfer of highly subcooled flow boiling in vertical upflow. Int. J. Heat Mass Transf. 136(2019) 1199-1216.

[241] W.H. Lee, A pressure iteration scheme for two-phase flow modeling, in:T.N. Veziroglu (Ed.), Multiphase Transport Fundamentals, Reactor Safety, Applications, vol. 1, Hemisphere Publishing, Washington, DC, 1980.

[242] C. Fang, M. David, A. Rogacs, K. Goodson, Volume of fluid simulation of boiling two-phase flow in a vapor venting microchannel, Front. Heat Mass Transfer 1 (2010) 013002.

[243] K.C. Wong, J.H. Chong, Hydrodynamics and heat transfer prior to onset of nucleate boiling in a rectangular microchannel heat sink, Int. Commun. Heat Mass. 64 (2015) 34–41.

[244] N. Cheng, Y. Guo, C.H. Peng, A numerical simulation of single bubble growth in subcooled boiling water, Ann. Nucl. Energy 124 (2019) 179–186.

[245] J. Wei, L. Pan, D. Chen, H. Zhang, J. Xu, Y. Huang, Numerical simulation of bubble behaviors in subcooled flow boiling under swing motion, Nucl. Eng. Des. 241 (2011) 2898–2908.

[246]Y.K. Prajapati, M. Pathak, M.K. Khan, Numerical investigation of subcooled flow boiling in segmented finned microchannels, Int. Commun. Heat Mass, 86(2017) 215-221.

[247] Y.Luo, J.Z.Zhang,W.Li, A comparative numerical study on two-phase boiling fluid flow and heat transfer in the microchannel heat sink with different manifold arrangements, Int. J. Heat Mass Transfer. 156 (2020) 119864.

[248] J. Kim, J.S. Lee, Numerical study on the effects of inertia and wettability on subcooled flow boiling in microchannels, Appl. Therm. Eng 152 (2019) 175–183.

[249] S. Hardt, F. Wondra, Evaporation model for interfacial flows based on a continuum-field representation of the source terms, J. Comput. Phys. 227 (2008) 5871–5895.

[250] L.Y. Xie, Y.Q. Xie, J.Z. Yu, Phase distributions of boiling flow in helical coils in high gravity, Int. J. Heat Mass Transfer 80 (2015) 7–15.

[251] H.I.Mohammed,D.Giddings,G.S.Walker. CFD multiphase modelling of the acetone condensation and evaporation process in a horizontal circular tube, Int. J. Heat and Mass Transfer 134 (2019) 1159-1170.

[252] X. Yin, Y. Tian, D. Zhou, N. Wang, Numerical study of flow boiling in an intermediate-scale vertical tube under low heat flux, Appl. Therm. Eng. 153 (2019) 739–747.

[253] M. Bahreini, A. Ramiar, A.A. Ranjbar, Numerical simulation of subcooled flow boiling under conjugate heat transfer and microgravity condition in a vertical mini channel, Appl. Thermal Eng. 113 (2017) 170–185.

[254] J. Lee, L.E. O'Neill, I. Mudawar, 3-D computational investigation and experimental validation of effect of shear-lift on two-phase flow and heat transfer characteristics of highly subcooled flow boiling in vertical upflow, Int. J. Heat Mass Transfer 150 (2020) 119291.

[255]Z. Yang, X.F. Peng, P. Ye, Numerical and experimental investigation of two phase flow during boiling in a coiled tube, Int. J. Heat Mass Transfer 51 (2008) 1003–1016.

[256]J. Kim, J.Y. Cho, J.S. Lee, Flow boiling enhancement by bubble mobility on heterogeneous wetting surface in microchannel, Int. J. Heat Mass Trans. 153 (2020) 119631.

[257]G.Hedau,P.Dey,R.Raj,S.K.Saha, Experimental and numerical investigation of the effect of number of parallel microchannels on flow boiling heat transfer, Int. J. Heat Mass Trans. 158 (2020) 119973.

[258] S.M.A.N.R. Abadi, M. Mehrabi, J.P. Meyer, J. Dirker, Effect of saturation temperature on the condensation of R134a inside an inclined smooth tube, Int. J. Refrig. 94 (2018) 186-204.

[259] H. Lee, C.R. Kharangate, N. Mascharehnas, I. Park, I. Mudawar, Experimental and computational investigation of vertical downflow condensation, Int. J. Heat Mass Transfer 85 (2015) 865–879.

[260] ANSYS FLUENT Theory Guide, ANSYS Inc., Canonsburg, PA, 2009.

[261] R. Banerjee, Turbulent conjugate heat and mass transfer from the surface of a binary mixture of ethanol/iso-octane in a countercurrent stratified two-phase flow system, Int. J. Heat Mass Transfer 51.25-26 (2008) 5958-5974.

[262] J.Y. Zhang, J. Wen, S. Deng, J.J. Bao, L. Zhao, 2D numerical study on flow boiling of zeotropic mixture isobutane/pentane in internal countercurrent flow system, Appl. Therm. Eng. 114 (2017) 1247-1255.

[263] A.A.S. Lima, A.A.V. Ochoa, J.A.P. Da Costa, J.R. Henriquez, CFD simulation of heat and mass transfer in an absorber that uses the pair ammonia/water as a working fluid, Int. J. Refrig. 98 (2019) 514-525.

[264] D. Liu, P.S. Lee, S.V. Garimella, Prediction of the onset of nucleate boiling in microchannel flow, Int. J. Heat Mass Transfer 48 (2005) 5134-5149.

[265] M. Haghshenas Fard, M.N. Esfahany, M. Talaie, Numerical study of convective heat transfer of nanofluids in a circular tube two-phase model versus single-phase model, Int. Commun. Heat Mass Transfer 37 (1) (2010) 91–97.

[266] M.K. Moraveji, R.M. Ardehali, CFD modeling (comparing single and two-phase approaches) on thermal performance of Al2O3/water nano fluid in mini-channel heat sink, Int. Commun. Heat Mass Transf 44 (2013) 157–164.

[267] M. Ghalambaz, A.J. Chamkha, D. Wen, Natural convective flow and heat transfer of Nano-Encapsulated Phase Change Materials (NEPCMs) in a cavity, Int. J. Heat Mass Transfer 138 (2019) 738–749.

[268] A. Soleimani, A. Sattari, P. Hanafizadeh, Thermal analysis of a microchannel heat sink cooled by two-phase flow boiling of Al2O3 HFE-7100 nanofluid, Therm Sci Eng Prog. 20 (2020) 100693.

[269] Patek, J., and J. Klomfar. Simple functions for fast calculations of selected thermodynamic properties of the ammonia-water system. Int. J. Heat Mass Transfer 18.4 (1995) 228-234.

[270]Sassen, C.L.Vapor-liquid equilibria for the system ammonia+ water up to the critical region. J. Chem. Eng. Data 35.2 (1990) 140-144.

[271]Tillner-Roth, Reiner, and Daniel G. Friend. Survey and assessment of available measurements on thermodynamic properties of the mixture {water+ammonia}. J. Phys. Chem. Ref. Data 27.1 (1998) 45-61.

[272]M. Conde-Petit, Thermodynamic properties of NH3+H2O mixtures for the industrial design of absorption refrigeration equipment, Zurich, Switzerland, 2006.

[273] R. Revellin, V. Dupont, T. Ursenbacher, J.R. Thome, I. Zun, Characterization of diabatic two-phase flows in microchannels: Flow parameter results for R-134a in a 0.5 mm channel, Int. J. Multiphase Flow 32 (2006) 755-774.

[274]J.U. Brackbill, D.B. Kothe, C. Zemach, A continuum method for modeling surface tension, J. Comput. Phys. 100 (1992) 335-354.

[275] W.H. Lee, A Pressure Iteration Scheme for Two-Phase Flow Modeling, Multiphase Transport Fundamentals, Reactor Safety, Applications, Hemisphere Publishing, Washington D.C., 1980.

[276] L. Yang, W. Li, J.Z. Zhang, W.J. Minkowycz. Analysis of thermal performance and pressure loss of subcooled flow boiling in manifold microchannel heat sink. Int. J. Heat Mass Transfer 162 (2020) 120362.

[277]Voller, Vaughan R., and C. Prakash. A fixed grid numerical modelling methodology for convection-diffusion mushy region phase-change problems. Int. J. Heat Mass Transfer 30.8 (1987) 1709-1719.

[278]Q. Liu, W. Wang, B. Palm, A numerical study of the transition from slug to annular flow in micro-channel convective boiling, Appl. Therm. Eng. 112 (2017) 73–81.

[279] R. Banerjee, K.M. Isaac, Evaluation of turbulence closure schemes for stratified two phase flow, in: 2003 ASME International Mechanical Engineering Congress and Exposition, Washington, DC, 2003.

[280]Y. Tomohide, and O. Nakabeppu. Microscale wall heat transfer and bubble growth in single bubble subcooled boiling of water. Int. J. Heat Mass Transfer 100 (2016) 851-860.

[281] Y.K. Prajapati, M. Pathak, M.K. Khan, A comparative study of flow boiling heat transfer in three different configurations of microchannels, Int. J. Heat Mass Transfer 85 (2015) 711-722.

[282] W. Qu, I. Mudawar, Flow boiling heat transfer in two-phase microchannel heat sinks – I. Experimental investigation and assessment of correlation methods, Int. J. Heat Mass Transfer 46 (2003) 2755–2771.

[283] W. Su, J. Darkwa, G. Kokogiannakis, Review of solid−liquid phase change materials and their encapsulation technologies, Renew. Sustain. Energy Rev. 48 (2015) 373–391.

[284]Morshed, A. K. M. M., et al. Enhanced flow boiling in a microchannel with integration of nanowires. Appl. Therm. Eng. 32 (2012) 68-75.

[285] J.B. Marcinichen, J.A. Olivier, N. Lamaison, J.R. Thome, Advances in electronics cooling, Heat Transfer Eng. 34(5-6) (2013) 434-446.

[286] X. Wang, J. Niu, Y. Li, X. Wang, B. Chen, R. Zeng, Q. Song, Y. Zhang, Flow and heat transfer behaviors of phase change material slurries in a horizontal circular tube, Int. J. Heat Mass Transf. 50 (2007) 2480-2491.

[287] G.H. Zhang, C.Y. Zhao, Thermal and rheological properties of microencapsulated phase change materials, Renew. Energ. 36 (2011) 2959-2966.

[288] H. Dai, W. Chen, Q. Cheng, Y. Liu, X. Dong, Analysis of thermo-hydraulic characteristics in the porous-wall microchannel with microencapsulated phase change slurry, Int. J. Heat Mass Transf. 165 (2021) 120634.

[289] L. Liu, G. Alva, Y. Jia, X. Huang, G. Fang, Dynamic thermal characteristics analysis of microencapsulated phase change suspensions flowing through rectangular minichannels for thermal energy storage, Energy Build. 134 (2017) 37-51.

[290] S. Chen, Z. Yang, Y. Duan, Y. Chen, D. Wu, Simulation of condensation flow in a rectangular microchannel, Chem. Eng. Process.: Process Intens. 76 (2014) 60-69.

[291] R. Ali, B. Palm, M.H. Maqbool, Flow boiling heat transfer of refrigerants R134a and R245fa in a horizontal micro-channel, Exp. Heat Transf. 25 (2012) 181–196.

[292] M. Veerappan, S. Kalaiselvam, S. Iniyan, R. Goic, Phase change characteristic study of spherical PCMs in solar energy storage, Sol. Energy 83 (2009) 1245-1252.

[293] D. Shiferaw, T.G. Karayiannis, D.B.R. Kenning, Flow boiling in a 1.1 mm tube with R134a: experimental results and a comparison with model, Int. J. Therm. Sci. 48 (2009) 331–341.

[294] T.G. Karayiannis, D. Shiferaw, D.R. Kenning, V.V. Wadekar, Flow patterns and heat transfer for flow boiling in small to micro diameter tubes, Heat Transfer Eng. 31 (2010) 257–275.

[295] M.M. Mahmoud, T.G. Karayiannis, D.B.R. Kenning, Flow boiling pressure drop of R134a in microdiameter tubes: Experimental results and assessment of correlations, Heat Transf. Eng. 35 (2) (2014) 178–192.

[296] M. Bahiraei, N. Mazaheri, Y. Hosseini, H. Moayedi, A two-phase simulation for analyzing thermohydraulic performance of Cu – water nanofluid within a square channel enhanced with 90° V-shaped ribs, Int. J. Heat Mass Transfer 145 (2019) 118612.

[297] K. Zhou, C. Coyle, J. Li, J. Buongiorno, W. Li, Flow boiling in vertical narrow microchannels of different surface wettability characteristics, Int. J. Heat Mass Transfer 109 (2017) 103–114.

[298] W. Li, K. Zhou, J. Li, Z. Feng, H. Zhu, Effects of heat flux, mass flux and two-phase inlet quality on flow boiling in a vertical superhydrophilic microchannel, Int. J. Heat Mass Transfer 119 (2018) 601–613.

[299] W. Li, K. Zhou, J. Li, Z. Feng, H. Zhu, Effects of heat flux, mass flux and two phase inlet quality on flow boiling in a vertical superhydrophilic microchannel, Int. J. Heat Mass Transfer 119 (2018) 601–613.

[300]C. Dang, L. Jia, X. Zhang, Q. Huang, M. Xu, Experimental investigation on flow boiling characteristics of zeotropic binary mixtures (R134a/R245fa) in a rectangular micro-channel, Int. J. Heat Mass Transfer 115 (2017) 782-794.

[301] Lemmon, Eric W., Marcia L. Huber, and Mark O. McLinden. NIST standard reference database 23. Reference fluid thermodynamic and transport properties (REFPROP), version 9.1 (2010).

[302]S. Yuan, W.L. Cheng, et al. Evaluation of prediction methods for heat transfer coefficient of annular flow and a novel correlation. Appl. Therm. Eng. 114 (2017) 10-23.

[303]S.M. Kim, I. Mudawar. Universal approach to predicting saturated flow boiling heat transfer in mini/micro-channels–Part II. Two-phase heat transfer coefficient. Int. J. Heat Mass Transfer 64 (2013) 1239-1256.

[304] M. Azzolin, S. Bortolin, D.D. Col, Flow boiling heat transfer of a zeotropic binary mixture of new refrigerants inside a single microchannel, Int. J. Therm. Sci. 110 (2016) 83-95.

[305] S. In, S. Baek, L.Jin, S. Jeong, Flow boiling heat transfer of R123/R134a mixture in a microchannel, Exp. Therm. Fluid Sci. 99 (2018) 474-486.

[306] B. Yang, P. Wang, A. Bar-Cohen, Mini-contact enhanced thermoelectric cooling of hot spots in high power devices, IEEE Trans. Compon. Packag. Technol. 30 (3) (2007) 432-438.

[307] K.P. Drummond , J.A. Weibel , S.V. Garimella , Two-phase flow morphology and local wall temperatures in high-aspect-ratio manifold microchannels, Int. J. Heat Mass Transf. 153 (2020) 119551.

[308] Q.Yan, L.Jia, Z.An, Q.Peng, A comprehensive criterion for slug-annular flow transition based on flow boiling of R134a in microchannels, Int. Commun. Heat Mass Transf.105 (2019) 1–9.

[309] E.M. Fayyadh, M.M. Mahmoud, K. Sefiane, Flow boiling heat transfer of R134a in multi microchannels, Int. J. Heat Mass Transf. 110 (2017) 422–436.

[310] A.S. Dalkılıç, A. Celen, M. Erdoğan, Effect of saturation temperature and vapor quality on the boiling heat transfer and critical heat flux in a microchannel, Int. Commun. Heat Mass Transf.117 (2020) 104768.

[311] H.L.S.L. Leao, C.A. Chávez, F.J. Nascimento, G. Ribatski, An analysis of the effect of the footprint orientation on the thermal-hydraulic performance of a microchannels heat sink during flow boiling of R245fa, Appl. Therm. Eng. 90 (2015) 907–926.

[312] P. Asrar, X. Zhang, C.E. Green, M. Bakir, Y.K. Joshi, Flow boiling of R245fa in a microgap with staggered circular cylindrical pin fins, Int. J. Heat Mass Transfer 121 (2018) 329–342.

[313] Y. Joo, H.C. Yeh, K. Dieu, C.J. Kim, Air cooling of a microelectronic chip with diverging metal microchannels monolithically processed using a single mask, Journal of Micromechanics and Microengineering 18 (2008) 115022.

[314] M. Moze, A. Nemanic, P. Poredos, Experimental and numerical heat transfer analysis of heat-pipe-based CPU coolers and performance optimization methodology, Appl. Therm. Eng. 179 (2020) 115720.

[315] K. Zhu, M.Z. Zheng, B. Wang, B.M. Dai, Y.B. Wang, J. Wei, X.Q. Chen, Experimental study of energy saving performances in chip cooling by using heat sink with embedded heat pipe, Energy Procedia 105 (2017) 5160–5165.

[316] S.C. Wong, S.F. Huang, K.C. Hsieh, Performance tests on a novel vapor chamber, Appl. Therm. Eng. 31 (2011) 1757–1762.

[317] G. Chen, Y. Tang, Z. Wan, G. Zhong, H. Tang, J. Zeng, Heat transfer characteristic of an ultra-thin flat plate heat pipe with surface-functional wicks for cooling electronics, Int. Commun. Heat Mass. 100 (2019) 12–19.

[318] R. Cardenas, V. Narayanan, Submerged jet impingement boiling of water under subatmospheric conditions, J. Heat Transfer 134 (2) (2012) 020909.

[319] V.S. Devahdhanush, I. Mudawar, Critical heat flux of confined round single jet and jet array impingement boiling, Int. J. Heat Mass Transfer 169 (2021) 120857.

[320] S.N. Joshi, E.M. Dede, Two-phase jet impingement cooling for high heat flux wide band-gap devices using multi-scale porous surfaces, Appl. Therm. Eng. 110 (2017) 10–17.

[321] L. Lin, R. Ponnappan, Heat transfer characteristics of spray cooling in a closed loop, Int. J. Heat Mass Transfer 46 (2003) 3737–3746.

[322] E.A. Silk, J. Kim, K. Kiger, Spray cooling of enhanced surfaces: impact of structured surface geometry and spray axis inclination, Int. J. Heat Mass Transf. 49 (2006) 4910–4920.

[323] Z. Zhang, J. Li, P. Jiang, Experimental investigation of spray cooling on flat and enhanced surfaces, Appl. Therm. Eng. 51 (1–2) (2013) 102–111.

[324] S.J. Thiagarajan, S. Narumanchi, R. Yang, Effect of flow rate and subcooling on spray heat transfer on microporous copper surfaces, Int. J. Heat Mass Transf. 69 (2014) 493–505.

[325] W.-L. Cheng, W.-W. Zhang, S.-D. Shao, L.-J. Jiang, D.-L. Hong, Effects of inclination angle on plug-chip spray cooling in integrated enclosure, Appl. Therm. Eng. 91 (2015) 202–209.

[326] J.L. Xie, Y.B. Tan, F. Duan, K. Ranjith, T.N. Wong, K.C. Toh, K.F. Choo, P.K. Chan, Study of heat transfer enhancement for structured surfaces in spray cooling, Appl. Therm. Eng. 59 (2013) 464–472.

[327] E. Martínez-Galván, R. Antón, J.C. Ramos, R. Khodabandeh, Influence of surface roughness on a spray cooling system with R134a. Part I: heat transfer measurements, Exp. Therm. Fluid Sci. 46 (2013) 183–190.

[328] H. Wang , Y. Yang , M. He , H. Qiu , Subcooled flow boiling heat transfer in a microchannel with chemically patterned surfaces, Int. J. Heat Mass Transf. 140 (2019) 587–597.